THE EFFECTS OF NANO-TITANIUM DIOXIDE ON DURABILITY AND MECHANICAL PROPERTIES OF CEMENT COMPOSITE

Davood Shafaei

October 2022

A dissertation submitted for the Degree of Doctor of Philosophy

Strathclyde University Engineering Department

Dedicated to my family, my son Keyan and my daughter Rosha,

I will always love all of you to the infinity and beyond…

Acknowledgement

This thesis represents a culmination of the adventure that has taken place over a period of almost three years and a half when I took the decision, after 2 years of working in the oil industry, to make a career step to pursue a PhD degree and provide a better life for my family. During the development of my PhD, I had the opportunity to learn and to grow as a professional and become a better person and researcher. To live and work in a foreign country as Scotland with a family was not easy but it gave me the chance to interact with other cultures and different ways of thinking. I am leaving a lot of colleagues and friends that I am going to miss, especially during our soccer games. Without the support of my family, colleagues and friends, it would have been almost impossible to complete and successfully finish my PhD degree. For that reason, I want to thank all of you for your patience, love, advice, and cooperation during the good and bad moments spent during the past years. I would like to address some people in particular. I would like to firstly thank my supervisor Dr. Shangtong yang who allowed me to join his research group and to start my PhD research. I am incredibly grateful to him not only for directing my dissertation, but also for the invaluable moral support I received throughout this project. His guidance and supervision enabled me to complete my work successfully. In addition, I wish to acknowledge the support of the lab technicians Mr. Christopher Bonner and Mr. Gavin Gibson. With their support I was able to conduct the experiments and obtain the results for the following research work. I also want to express my gratitude to Dr Leonard Berlouis and Dr James Minto for reading and commenting on my thesis. I could not have completed this thesis without the fantastic friends who have inspired, distracted, and kept me sane. I have been blessed with loving and loyal parents who have supported me from my first steps to the conclusion of this thesis. I owe them the greatest thanks of all. This research has been made possible through funding by Engineering & Physical Sciences Research Council (EPSRC) and Additional financial support from Strathclyde University Engineering Department, is also gratefully acknowledged.

Davood Shafaei,

5 Oct 2022

Abstract

Summary Application of nano-titanium in cement paste to ensure the future competitiveness of concrete as a building material, it is essential to improve the sustainability of concrete infrastructures. Recent developments in nanotechnology show a significant promise in addressing many of the challenges to produce environmentally friendly concrete. In this context and in the scope of this thesis, the environmental impact and sustainability of concrete was improved by the combined use of nano-titanium dioxide and supplementary cementitious materials (SCM). In particular, the effects of SCM such as FA and MK as by-product materials and NT as a high surface area additive on the permeability as well as pore structure properties of cementitious materials were investigated and analysed in this PhD thesis. The main properties and characteristics of nano-titanium were obtained using different techniques such as X-ray computed tomography (XCT), Brunauer-Emmett-Teller (BET), scanning electron microscopy (SEM), X-ray diffraction (XRD), thermogravimetric/derivative thermogravimetric analysis (TG/DTG), and energy-dispersive X-ray spectroscopy (EDAX®). To examine the pore configuration in the matrix, 2D and 3D porosity calculations had been carried out in order to find the pores and their exact sizes, positions and distributions from the pore network using a Nikon XT H 225/320 LC X-ray computed tomography system. In addition, reconstructed tomography images were used to extract the main parameters of porosity. The number of pores in the scanned volume, as well as the volumes and shapes of individual pores were determined and based on these recommendations, design guidelines were suggested. A novel direct tensile were conducted to quantify and characterise the mechanical properties of the NT cement composite. Furthermore, the impact of increasing the amount of NT on the mechanical properties of NT-modified geopolymer were investigated. This test method covers the determination of the fracture energy (G_f) of composites using the disk-shaped compact tension geometry. Numerical results were validated with the existing experimental data specifically on the CMOD responses and von Mises stresses. Finally, we investigated different amounts of nano-TiO_2 on the sulfate attack resistance of pure Portland cement pastes. The distributions of internal pore structures of hardened mortars were measured by MIP method. The corrosion progression of a steel bar in concrete was investigated by X-ray computed tomography (i.e., XCT) and accelerated corrosion process of reinforcing steel with impressed current was traced by X-ray micro-computed tomography (μCT) with high accuracy and the mass loss of steel over different accelerated corrosion periods was analysed. This PhD thesis included a significant experimental phase and an associated analytical phase. The experimental phase focused on determining the material behaviours of the NT cement composite from the testing on over 900 individual specimens, with an emphasis toward determining the compressive and tensile behaviours, the long-term stability, and the durability of composite. Many of the material characterization tests were completed according to the British standard test procedures. However, in some instances these tests were modified, or new tests were devised to accurately capture the relevant behaviours of the NT cement. The analytical phase of this research combined, analysed, and explained upon the results from the experimental phase. This results in concrete with better performance, lower costs and improved ecological footprint. The final outcome is a methodology to design concrete and a practical framework which allows the optimum application of NT in concrete, given the available raw materials and the desired properties of the end-product. In summary, it can be concluded that adding a certain amount of NT (around 2.5 wt%) and FA/MK (10 wt%) can modify the pore structure of cement mortars by changing the harmful microscale pores to the nano-sized benign pores, leading to a

much stronger durability of cement-based materials. The results demonstrate that the photovoltaic waste can be used as a potential NT-SCM composite to partly replace cement in concrete, thereby decreasing the CO_2 footprint of concrete and the environmental impact associated with landfill.

CONTENTS

List of Tables

List of Figures

The major figures used in this Guide are listed below for reference purposes. Other are described where used.

Notation

The major symbols used in this Guide are listed below for reference purposes. Other are described where used.

- A (m^2) : Surface area
- b (m): Cross section dimension of the beam
- C_w (LT^2/M): Compressibility of water
- C_{eff} (LT^2/M): Compressibility of the porous skeleton
- D (nm, µm, m): Particle size or sphere diameter
- $\mathrm{D_{BET}}$ (nm): Average particle size by BET method
- $\mathrm{D_{min}}$ (nm, µm, m): Minimum diameter
- d (nm): Interplanar spacing between rows of atoms
- d_i (nm): Diameter
- $\mathrm{d_p}$ (nm): Pore diameter
- f_{cf} (MPa): Flexural strength
- GF (N/mm): Average fracture energy
- K (m^2 or ft^2): Permeability of the medium
- L (m): Sample length
- $\mathrm{m_c}$ (g): Mass of cement
- $\mathrm{m_w}$ (g): Mass of water
- $p_b - p_a$ (N/m^2): Pressure drops
- ρ (kg/m ^{3}): Density
- σ (MPa): Compressive and tensile strength
- Q $(\frac{m^3}{s})$: Flow rate
- ϕ (nm): Capillary condensation
- R (-): Gas constant
- SSA_{t-plot} $[m^2$/g]: Total specific surface area
- SSA_i $[m^2$/g]: Specific surface area determined by the BET
- T (°C): Absolute temperature
- T_R(L^2/T): Transmissivity of the tested interval
- µ [Pa·s]: Dynamic viscosity of the fluid
- u (-): Size ratio
- V (Cm^3): Volume
- V_{MP}[cm^3/m^2. nm]: Adsorption in saturated micropores
- V_N [mol/ml]: Molar volume of liquid nitrogen
- w/b (-): Water/binder ratio
- w/c (-): Water/cement ratio
- Δ^2 (-): Radially symmetric coordinate system
- δ_{Fu} (-): Limit of proportionality load

Abbreviations

- ASR: Alkali-silica reaction
- ASTM: American Society for Testing and Materials
- BET: Brunauer-Emmett-Teller
- BJH: Barret-Joyner-Halenda
- BRE: Building Research Establishment
- C.S: Compressive strength
- CEM: Cement
- CMOD: Crack Mouth Opening Displacement
- C-A-S-H gel: Calcium aluminate silicate hydrate
- C-S-H gel: $xCaO.ySiO_2.zH_2O$ gel
- DM-water: Demineralized water
- DTG: Derivative thermal gravimetric analysis
- EDS: X-ray energy dispersive spectroscopy
- F.S: Flexural strength
- FA: Fly ash
- FEG: Field emission gun
- FPZ: Fracture Process Zone
- Fu: Limit of Proportionality Load
- FW: Percentage of free water
- HL: Hydrated lime
- LEFM: Linear Elastic Fracture Mechanics.
- LOI: Loss on ignition
- LVDT: Toni Linear Variable Differential Transducer
- M: Mid-span Moment
- MIP: Mercury intrusion porosimetry
- MK: Metakaolin
- Mu: Mid-span Moment, at proportional limit
- NT: Nano titanium dioxide
- N/D: Not determined
- N/S: Not specified
- NLFM: Non-Linear Fracture Mechanics
- OPC: Ordinary Portland Cement
- PSD: Particle size distribution
- PV: Plastic viscosity
- PFA: Pulverized Fuel Ash.
- RILEM: International Union of Testing and Research Laboratories for Materials and Structures
- SCM: Supplementary cementitious materials
- SE: Secondary electron

- SEM: Scanning electron microscopy
- SF: Slump-flow
- Sf: Silica fume
- SSA: Specific surface area
- TG/TGA: Thermal gravimetric analysis
- W/B: Water/binder ratio.
- W/C: Water to cement ratio
- W/CM: Water/cementitious material ratio or water/’equivalent cement’ ratio
- XCT: X-ray computed tomography
- XRD: X-ray diffraction
- XRF: X-ray fluorescence

Chapter 1

Introduction

1.1 Overview

The cement industry is estimated to be responsible for 5–7 % of the global CO_2-emissions, as a result of the calcination and grinding process (Proske et al., 2013). In addition, it produces sulfure dioxide (SO_2) and mono-nitrogen oxides (NOx). In 2013, about 3.98 billion tons of cement was produced around the world (Global cement report, 2013). Based on this estimated value and considering average cement content of 10% and 70% of the cement-based product shared market, the worldwide production of concrete is about 32 billion tons. This amount is about twice as much as the combination of steel, wood, plastics, and aluminium. Therefore, reducing the cement clinker content might have positive effects on the environmental aspects of concrete. The amount of CO_2-emissions depends on the concrete type (strength class, binder, etc.), and the production process (self-compacting, precast, vibrated, etc.) which also affects the embodiment energy used for production (Hammond and Jones, 2011).

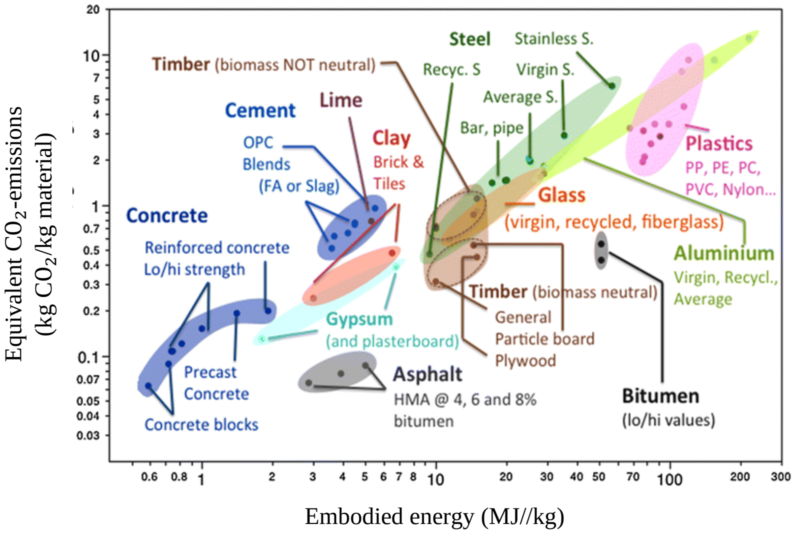

Figure 1.1: Equivalent CO_2-emissions and embodied energy of different construction materials (Kline and Barcelo, 2012). Data adapted from Hammond and Jones (2008).

In Figure 1.1 it is possible to observe that even though concrete is associated with high CO_2 footprint, it is still a material with a relatively low relation between the equivalent CO_2 and the energy required for production compared to other building materials (e.g. aluminium or steel). Because of extensive use of concrete worldwide, it is essential to evaluate the environmental impact of this material. Additionally, to ensure the future affordability of concrete as a building material, it is necessary to improve the sustainability of concrete structures.

Different approaches or potential opportunities for reducing the environmental impact and consumption of scarce resources have been already identified in the field of concrete construction, especially in the production of raw materials, concrete technology, and structures. One approach is to replace the percentage of Ordinary Portland Cement (OPC) with Green cements, such as fly ash (FA), silica fume (SF), hydrated lime (HL) and metakaolin (MK) (Barbhuiya et al., 2009; Güneyisi et al., 2008), to reduce the environmental consequences, mainly by reducing the CO_2-emissions. When these materials are combined with Portland cement through either pozzolanic or hydraulic activity, a contribution towards the properties of hardened concrete is made. As a result, the emission of greenhouse gases is reduced, whilst creating a more economical solution than Portland cement. As per engineering properties, it also increases the strength of the concrete over time, reduces permeability, increase durability, and minimises heat of hydration.

Another approach to reduce the environmental impact of concrete includes the use of nano particles, which modify the hydration performance. By using nano particles in concrete, less steel reinforcement is required, and the concrete offers a lighter weight and longer serviceable life, which are all crucial issues in the eco-efficiency of construction materials. Despite the growing importance of nanotechnology, investigations into the incorporation of nanoparticles into concrete are limited. It therefore remains to be seen how research in this area will contribute to concrete eco-efficiency. In the following chapters, it is explained how the sustainability and durability of cement composite can be improved using different approaches and the combined use of nano particles and green cement in concrete mix.

1.2 Nanotechnology in Construction

Nanotechnology can be considered as the latest field of science and technology. Because nanotechnology has great market potential and economic impact, the need for research and exploration in this field and of its applications has been growing during the last few years. US engineering group AECOM estimates by 2025 more than 50 per cent of building materials will contain nanomaterials as manufacturers take advantage of lighter, stronger and more energy efficient materials (Bill Looney, 2019). The nanotechnology concept was introduced for the first time by Feynman (1960) with his famous work entitled ‘‘There’s plenty of room at the bottom”. Nanotechnology is the re-engineering of materials through controlling the matter at the atomic level. In general, nanotechnology can be referred to understanding of matter on the nano scale (from 0.1 nm to 100 nm). A more accurate definition of nanotechnology was emphasized by Drexler (1981), such as the production with dimensions and precisions between 0,1 and 100 nm. Another accepted term is that nanotechnology involves the study at nano-range (1nm = $1\text{x}10^{-9}$m).

The report of the RILEM Technical Committee 197-NCM, ‘‘Nanotechnology in construction materials” (Bartos et al., 2002), is one of the first documents that clearly highlight the potential of nanotechnology in terms of the development of construction and building materials. The extremely high specific surface area is one of the most important characteristics of nanoparticles because this facilitates more interphase in a composite and thereby, a strong interaction between the fillers and the matrix even at a rather low nano-filler loading (Zhang et al., 2009). For heterogenous composites such as concrete composites, addition of nanoparticles makes them an ideal candidate for the application of nanotechnology. In general, nanoparticles influence concrete in many ways such as densifying the structure of the hydration products and the interparticle transition zone (ITZ) and promoting nucleation sites for the cement hydration products and also active reactants in the hydration process (Sanchez and Sobolev, 2010). The processes that occur at the nanoscale in concrete define its properties at the macroscale. The main cement hydration product, the C-S-H gel, is a nano-structured phase (Richardson, 2008). This phase is mainly responsible for the strength of concrete as well as its durability.

To date, numerous nanomaterials, such as nano-silica (nano-SiO_2), nano-alumina (nano-Al_2O_3), nano-iron oxide (nano-Fe_2O_3), nano-clay, nano-titanium dioxide (nano-TiO_2), carbon nanotubes and graphene oxide, have been used in cementitious composites. Nano-SiO_2 readily reacts with the free lime available in mix to produce additional calcium silicate hydrate (C–S–H) gel, thereby significantly contributing towards early strength development (Li et al, 2004(b)). In addition, it helps in refining the pore structure (Zhang et al., 2011), which is highly beneficial for the enhancement of the durability of mortar/concrete.

Nano-Al_2O_3 has been added to concrete to improve its modulus of elasticity and to improve the compressive strength (Nazari et al., 2010; Oltulu and Sahin, 2011). Nano-Fe_2O_3 was found to significantly improve the strength of concrete and mortars (Li et al, 2004a; Li et al, 2004b) and additionally, to provide concrete/mortar with a self-sensing ability (Li et al., 2004a). This ability is related to the change of the electrical resistivity of concrete with nano-Fe_2O_3 at different stress levels under each specific applied load.

The application of natural or calcined nano-clays (e.g., metakaolin) in cementitious materials has also shown positive effects, such as the improvement of the compressive and flexural strengths and the reduction of permeability (Poon et al., 2006; Sabir et al., 2001; Kim et al., 2007; Antoni et al., 2012). Nano-$CaCO_3$ has been proven to increase the hydration rate of cement at early age, acting as nucleation sites for hydration products (Kawashima et al., 2013; Raki et al., 2010).

Amongst these materials, nano-TiO_2 (NT) have shown significant potential to be utilised in cementitious materials, due to its safety, chemical stability, self-cleaning and air purifying properties (Chen et al., 2009). Due to the lack of quantitative research conducted towards the effects of NT on the characteristics of cementitious materials such as durability, there is an effort in the industry to carry out studies that focuses on inspecting these properties by using and comparing different dosages of NT, to maintain a durable structure, which is also the main topic of the present PhD research. In the following section an extended summary of NT used in cement mortar is provided.

1.3 Production Method of Nano-Titanium Dioxide (NT)

Titanium dioxide (TiO_2) is a molecule composed of one atom of titanium and two atoms of oxygen. TiO_2 mainly exists in three crystalline polymorphs, namely anatase, rutile and brookite. These three polymorphs have different crystalline structures. Anatase and Rutile have tetragonal structure, whereas brookite is orthorhombic. TiO_2 in the form of anatase has received considerable attention in the construction industry in recent years due to their potential to add new functionalities to infrastructures, i.e., self-cleaning properties and the ability to remove air pollutants through photocatalysis. Under ultraviolet light and humidity, TiO_2 can decompose a wide range of organic and inorganic air pollutants, providing cleaner air and better health for humans and other living creatures. The process of photodecomposition through light absorption is known as photocatalysis and $\mathrm{TiO_2}$ is considered one of the most powerful photocatalysts available. Nowadays, there are different methods to produce $\mathrm{TiO_2}$ products. The two main production methods are the sulfate process and the chloride process. The main production method is the sulfate process. In this process, ilmenite ($\mathrm{FeTiO_3}$), a common iron/titanium oxide material, is used. It is treated with the concentrated sulfuric acid ($\mathrm{H_2}SO_4$) and the titanium oxygen sulfate ($\mathrm{TiOSO_4}$) is selectively extracted and converted into titanium dioxide. Ilmenite is treated (digested) with a 60% excess of concentrated sulfuric acid at a temperature around 105°C. The reaction can be summarized as:

$$\mathrm{FeTiO_3(s) + 2H_2SO_4(aq) \longrightarrow FeSO_4(s) + TiOSO_4(aq) + 2H_2O(l)} \tag{1.1}$$

In the next stage, the waste product iron (II) sulfate is removed. As $\mathrm{FeSO_4}$ is not very soluble at low temperatures, the solution is cooled to around 12°C and $\mathrm{FeSO_4}$ crystallises out. It can then be removed by filtration. The remaining aqueous digestion products are heated to around 110°C to hydrolyse the titanium oxygen sulphate. The reaction can be summarized as:

$$\mathrm{TiOSO_4(aq) + (n+1)\,H_2O(l) \longrightarrow TiO_2}(s)\mathrm{ + nH_2O(l) + H_2SO_4(aq)} \tag{1.2}$$

The hydrolysis stage of the process produces sulfuric acid waste and a precipitate gel containing titanium dioxide. In the last stage, the titanium dioxide is heated in large rotary kilns to drive off the water and produce crystals of anatase by following reaction:

$$\mathrm{TiO_2}(s) + \mathrm{nH_2O(aq) \longrightarrow TiO_2}(s) + \mathrm{nH_2O(l)} \tag{1.3}$$

In the next stage of the process water is removed at temperatures about 250 °C and seed crystals are added to start the crystallisation process. Depending on the final heating temperature (800−850°C or 900−930 °C), either anatase or rutile is formed, respectively. An alternative production method is called chloride process. In this process, titanium dioxide is reduced with carbon and then oxidised again with chlorine. The reaction can be summarized as:

$$\mathrm{TiO_2(s) + C(g) \rightarrow Ti(s) + CO_2(g)} \tag{1.4}$$

$$\mathrm{Ti(s) + 2Cl_2(g) \rightarrow TiCl_4(aq)} \tag{1.5}$$

Liquid $\mathrm{TiCl_4}$ is distilled off and converted back into $\mathrm{TiO_2}$ in a pure oxygen flame or in plasma at temperatures of 1200–1700 °C. The majority of chlorine is recovered by following reaction:

$$\mathrm{TiCl_4(g) + O_2(g) \rightarrow TiO_2(s) + 2Cl_2(g)} \tag{1.6}$$

The chloride process has been favoured on financial and environmental grounds since the early 1990s. In order to produce nano-structured titanium dioxide, pure $\mathrm{TiCl_4}$ liquid is vaporised by heating and mixed with air and hydrogen. The gases are heated in a burner at high temperatures between 1000 and 2400 °C, where they react. Titanium chloride is converted to titanium oxide and hydrogen gas combines with chlorine to form HCl by following reaction:

$$\mathrm{TiCl_4(aq) + 2H_2(g) + O_2(g) \rightarrow TiO_2(s) + 4HCl(g)} \tag{1.7}$$

The titanium dioxide formed is pure and contains nano-sized particles with a diameter of approximately 21 nm.

1.4 Effect of nano-titanium dioxide addition in cement mortar

Currently, the application of nanomaterials and the investigation of concrete at the nanoscale are considered as emerging topics of interest and have become a focus for many researchers. In the last decade, $\mathrm{TiO_2}$ cement has been applied in a number of laboratories and real civil engineering projects, *e.g.*, the Jubilee Church in Rome as illustrated in Figure 1.2. The decomposition of the pollutants leads to the formation of water, $\mathrm{CO_2}$ and other harmless compounds which can be naturally washed away by rainwater and thus it is a completely green and environmental-friendly procedure. When mixing with cement, the “self-cleaning” property of TiO_2 can be utilised on a large-scale, *e.g.*, to help urban cities improve their air quality. Moreover, the white colour of titanium dioxide cement/concrete is generally appealing in terms of architectural needs. NT addition in cement paste and concrete can result in different effects (Figure 1.3). NT has been applied into concrete (Hüsken, 2010; Hunger et al., 2010; Ballari and Brouwers, 2013) to promote the self-cleaning and air-purifying properties, as the TiO_2 and its modification can be activated by UV light and act as a catalyst in the photocatalytic oxidation of various air pollutants.

Figure 1.2: Jubilee Church in Rome: (Source: quartiermagazin.com/quartier08/ der-weise-riese).

Demeestere et al. (2008) evaluated the potential of heterogeneous photocatalytic removal of toluene from outdoor air using ceramic building materials incorporating TiO_2 under different ambient conditions. Though there are still a number of outstanding issues that need to be addressed in order to increase the efficiency of air pollutants removal by TiO_2 enriched building materials, it did demonstrate a very promising potential as a future smart city feature. Apart from the photocatalytic properties, the mechanical properties, microstructures, and hydration of the TiO_2 cement composites have also been studied.

Lee and Kurtis (2010) pointed out that NT is chemically inert in the process of cement hydration, but it can provide crystal nuclei to promote the cement hydration process, leading to the increases of the compressive strengths of mortars. Lee et al. (2013) reported that the compressive strength increased by 10 wt% NT replacement at a relatively low water-to-cement ratio (0.4). There are also some studies showing that the NT accelerates the early-age strength (Jayapalan et al, 2009), due to the high specific surface area of NT particles.

The influence of NT on the hydration of cementitious materials was examined by several researchers (Lee et al, 2010). It was found that NT enhanced the hydration of cement by increasing the nucleation sites for the hydration reaction due to their high specific surface area. The addition of NT can result in the decreased water permeability and improved durability properties, such as chloride penetration and capillary adsorption (Jayapalan et al, 2009).

Compared with the photocatalytic and mechanical properties of the TiO_2 cement, the influence of NT on the inherent performance of hardened mortars/concretes, including high brittleness and durability, has not received attention, which leads to a decline in performance and service life of the building materials. This casts doubts or uncertainty in the widespread application of the NT-cement composite for construction. When a structural element tends to crack under load, nano particles bridge the cracks. Such bridging action provides the nano concrete greater ultimate tensile strength and, more importantly, huge toughness.

The main functions of the nano particles in members subjected to tension are to resist the opening of cracks due to micro-cracking, to increase the ability of the composite to withstand loads, and to allow large strains. The permeability of concrete is of significant concern and this is of particular concern in harsh and aggressive environments.

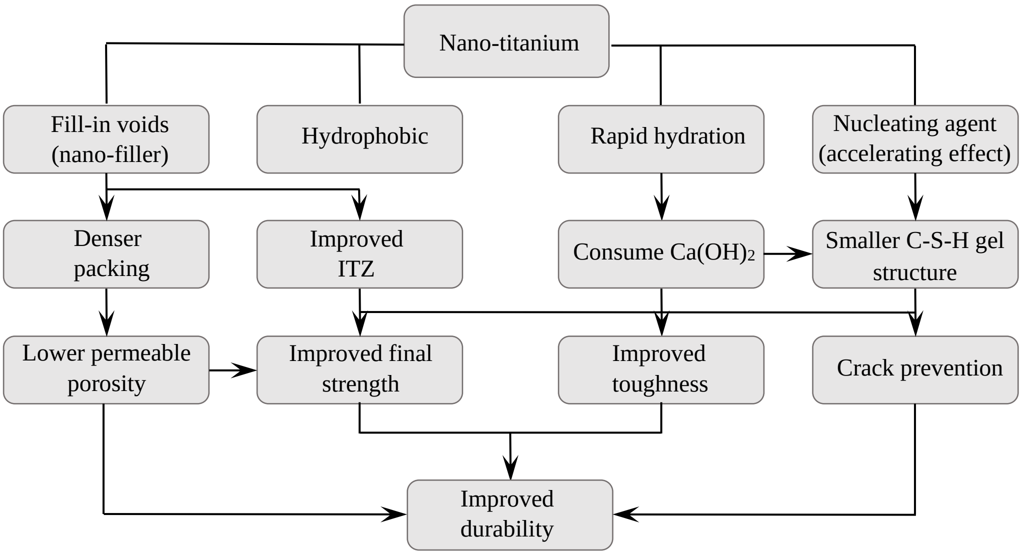

Figure 1.3: Schematic representation of the effects of adding NT in mortar and concrete

Most durability problems, such as the corrosion of steel reinforcement, damage by freeze-thaw cycles, attack by sulphates and acids, and alkali aggregate reaction, are controlled or affected by the pore system of the concrete. In fact, due to the nano particle size and hydrophilic property, NT can change the pore system of cement paste across different length scales. Another application of NT is the use as an additive in eco-concrete mixtures. Eco-concretes are mixtures where cement is replaced by waste materials mainly sludge ash, incinerated sludge ash, fly ash (FA) or others supplementary waste materials. Amongst these various supplementary cementitious materials, FA is the most abundantly available material worldwide (Heidrich et al., 2013). Palomo et al. (1999) showed the great potential of FA as an alternative to cement for the future. However, the majority of global FA production falls into the low calcium class F category which has very low reactivity (Wang et al., 2007) and very slow hydration characteristics, thus providing a little contribution to the early age strength (Boukni et al., 2009). This disadvantage may be solved by adding NT to eco-concrete mixes to obtain an accelerated setting and higher compressive strength. The properties of cement-based materials containing fly ash or NT have been reported in the literature. Kalpana et al. (2016) studied the influence of NT on early and higher age strengths of fly ash concrete. It was observed that a 0.5 wt.% substitution of NT gave an appreciably higher strength and also an increase in percentage of NT particles showed an increase in strength (with maximum at 3%). Most of the investigations evaluated the effects of specific percentages of NT on the hydration, setting and compressive strength of concrete but there has been limited progress on the effect of addition of NT in combination with fly ash in terms of durability properties. In particular, the effects of FA as by-product materials and NT as a high surface area additive on the permeability as well as pore structure properties of cementitious materials need to be studied in detail. The author hypothesized that, as NT has a high surface area to volume ratio and provides high reactivity, can be employed as growth points to facilitate the FA hydration, and modify the structure of hydration products at molecular level, which in turn improves the mechanical performance of fly ash cement. Considering NT as a potentially highly effective additive for the improvement of the concrete's durability and sustainability, its application and effects are investigated and analysed in this PhD thesis.

1.5 Research Aim and Strategy

The aim of this research is to develop durability and mechanical characteristics of concrete mixtures by incorporating nano-engineering practices. The research is performed based on the experimental and multidisciplinary point of view to obtain concrete with better properties and lower environmental impact. The outcome is a methodology to design concrete and a practical framework which allows the optimum application of NT in cementitious materials, given the available raw materials and the desired properties of the end-product. Five main objectives to increase the durability and suitability of concrete can be drawn as follows:

1. To examine the micro/nano-scales pore system of NT cement mortars across length scales with different NT dosages in order to increase the quality as well as the overall

properties of cement composites, allowing the use of lower amount of cement for the same functionality.

2. To determine the effect of NT on the inherent performance of hardened mortars/concretes, including high brittleness and changes in phase compositions, which lead to a decline in performance and service life of the building materials.
3. To explore the effect of NT on microstructures and morphology of cement mortars to achieve a densely packed material and lead to improved durability and strength.
4. To determine the change in calcium silicate hydrates (C-S-H gel) and the other phases of cement mortars (*e.g.*, Ettringite, Portlandite, Alite and Belite), before and after the addition of NT in the cement mortar.
5. To add NT to enhance the use of other supplementary cementitious materials (SCM) such as fly ash, metakaolin and the incorporation of other waste materials and recycled products.

1.6 Outline of the Thesis

The durability and sustainability of concrete are continuously becoming of an increasing importance for the construction industry. Nevertheless, only a limited amount of information can be found regarding the durability of concrete with NT. The goal of this research is to explore microstructural characteristics, multiscale pore system and morphology of cement mortars modified with NT particles by advanced physical and chemical methods on micro and nanoscales. Thus, it obviously leads to investigating a variety of complex topics starting from NT characteristics and properties to concrete full scale testing. The research is performed based on the experimental and multidisciplinary point of view to obtain concrete with better properties and lower environmental impact. The underlying research framework and the correlation between eight chapters of this thesis are presented in Figure 1.4. The content of the chapters is explained in the following sections.

1.6.1 Chapter 2

This chapter gives an overview of material characterization techniques with relevance to this research. Based on this overview, the properties of the applied materials and the hardened cement matrix were characterized. The mineralogical phases and chemical compositions of the raw materials used were obtained from the X-ray diffraction (XRD) and X-ray fluorescence (XRF) analyses. The obtained characteristics, such as shape, particle size, specific surface area, density and pore-size distribution were compared.

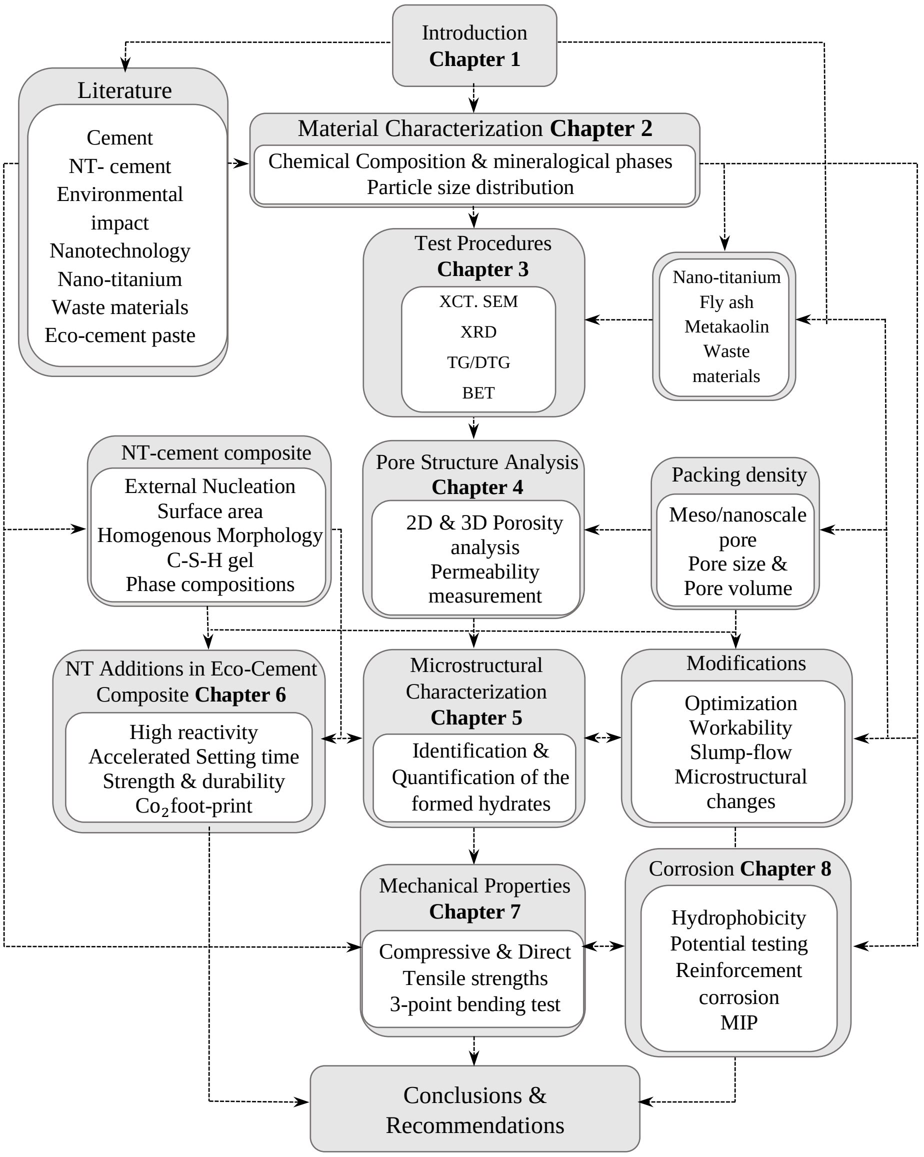

Figure 1.4: Outline of this thesis

1.6.2 Chapter 3

This chapter addresses the theoretical background and experimental procedures and the suitable test methods for evaluating the properties of NT cement mortars using different techniques such as X-ray computed tomography (XCT), Brunauer-Emmett-Teller (BET), scanning electron microscopy (SEM), X-ray diffraction (XRD), thermogravimetric/derivative thermogravimetric analysis (TG/DTG), and energy-dispersive X-ray spectroscopy (EDAX®).

1.6.3 Chapter 4

This chapter attempts to determine the pore system of NT cement mortars across length scales with different NT dosages. X-ray computed tomography (XCT) was used to analyse the micro scale pore structures of NT mortars with NT percentages of 0 wt%, 2.5 wt%, 3.5 wt%, 5 wt% and 10 wt%. 3D pore structures of the NT mortars were obtained and evaluated. In addition, the scanning electron microscopy (SEM) was used to compare the morphologies of the samples with different NT inclusions. Meanwhile, elementary analysis was performed using an energy-dispersive X-ray spectroscopy (EDAX®). Moreover, the nanoscale surface areas and the nano pore volume and shapes of the NT mortar samples were obtained by Brunauer-Emmett-Teller (BET) and Barrett-Joyner-Halenda (BJH) analysis. Furthermore, the permeability of the NT mortars was measured using a high-pressure core holder with a sensitive and automated measurement capability.

1.6.4 Chapter 5

In this chapter, the effects of NT on the crystalline phases of the cement mortars were investigated. The characterization of the cement hydration process, hydration products and morphology of the cement mortars were conducted by scanning electron microscopy (SEM) and X-ray diffraction (XRD) with different NT inclusions. The changes in calcium silicate hydrates (C-S-H gel) and the other phases of cement mortars (*e.g.*, Ettringite, Portlandite, Alite and Belite), before and after the addition of NT in cement mortar specimens, were detected using thermo-gravimetric method (TG). Derivative thermogravimetric (DTG) curves were plotted from the TG data to identify the extent of cement hydration and the exact boundaries of various phases or group of phases present in the hydrated samples. Meanwhile, elementary analysis was performed using an energy-dispersive X-ray spectroscopy (EDAX®).

1.6.5 Chapter 6

This chapter focuses on the addition of NT as an additive in eco-concrete mixtures. In particular, the effects of supplementary cementitious materials (SCM) such as FA and MK as by-product materials and NT as a high surface area additive on the permeability as well as pore structure properties of cementitious materials were studied in detail. The NT-modified geopolymer samples were analysed by X-ray computed tomography (XCT) to examine the pore configuration in the matrix. 2D and 3D porosity calculations were carried out to find the pores and their exact sizes, positions and distributions from the pore network using a Nikon XT H 225/320 LC X-ray computed tomography system. In addition, reconstructed tomography images were used to extract the main parameters of porosity. The numbers of pores in the scanned volume, as well as the volume and the shape of individual pores, were determined.

1.6.6 Chapter 7

In this chapter, novel direct tensile tests were conducted to quantify and characterise the mechanical properties of the NT cement composites. Furthermore, the impact of increasing the amount of NT on the mechanical properties of NT-modified geopolymer was investigated. This test method covered the determination of the fracture energy (G_f) of the composites using the disk-shaped compact tension geometry. Numerical results were validated with the existing experimental data specifically on the CMOD responses and von Mises stresses. In this analysis, manually random sizes of particles were considered to simulate 2D section distributions of NT with FA and MK particles in the ABAQUS CAE Environment. Firstly, according to particle volume fractions, the average radius of particles were assumed and secondly, positions of particles were posed in ABAQUS sketch.

1.6.7 Chapter 8

In this Chapter, different amounts of nano-TiO_2 on the sulfate attack resistance of pure Portlnad cement pastes were investigated. The distributions of internal pore structures of hardened mortars were measured by MIP method. Furthermore, the corrosion progression of steel bars in concrete was investigated by X-ray computed tomography (i.e., XCT). Finally, an accelerated corrosion process of reinforcing steel with impressed current was traced by X-ray micro-computed tomography (μCT) with high accuracy and the mass losses of steel at different accelerated corrosion periods were analysed.

1.6.8 Chapter 9

This chapter gives the conclusions of the research with general recommendations for the use of NT in cementitious materials. Practical applications for the design of sustainable eco-concrete mixes were proposed and starting points for further research being continuation of this work were outlined. The research included a significant experimental phase and an associated analytical phase. The experimental phase focused on determining the material behaviours of cement mortars from the testing on over 1600 individual specimens, with an emphasis toward determining the compressive and tensile behaviours, the long-term stability, and the durability of the composites to obtain concrete with better mechanical properties and lower environmental impact. The results demonstrated that the photovoltaic waste can be used as a potential NT-SCM composite to partly replace cement in concrete, thereby decreasing the CO_2 footprint of concrete and the environmental impact associated with landfill.

Chapter 2

Material Characterization of Nano Engineered Cement Composites

2.1 Introduction

At some structural level, the behaviour of every material is related to its microstructure. The understanding of these relationships between structure and properties forms the basis of materials science. Concrete with nanoparticles is composed of granular materials of different sizes, the smallest particle size of the finest component, i.e., Titanium (IV) oxide, anatase and brookite are less than 25 nm and 100 nm, respectively, whereas the largest particle of the coarsest component, gravel, can usually be 10-32 mm. The combination of all the individual particle size distributions (PSDs) of all granular materials used results in an overall PSD of the mixture.

The fresh state properties, i.e., the flow properties and workability, are governed by the particle size distribution (Hüsken and Brouwers, 2008). Moreover, the hardened state properties of concrete, such as durability and strength, are also determined by the particle size distribution (Neville, 2002). Therefore, in industrial production processes, the grading of concrete, which follows from the individual components, is of utmost importance.

An accurate description of the mixture and its particle size distribution is essential to understand the material behaviour and accurately predict the product properties (Hüsken, 2010). To apply nanomaterials in concrete, several chemical and physical properties need to be determined for the material to be fitted in a concrete mix design. These properties include specific surface area, particle size distribution (PSD), agglomerated state, chemical composition, impurities, and internal porosity (Sobolev et al., 2006). In this chapter, a brief description of the chemistry and structure of the conventional concrete components such as cement, fillers, sand, and gravel are characterized by standard methods. The mineralogical phases and chemical compositions of the raw materials used were obtained from the X-ray diffraction (XRD) and X-ray fluorescence (XRF) analyses. PSDs among the various types of concrete components are compared and the specific surface areas of the powders were determined using Brunauer-Emmett-Teller (BET) method. The density of the samples was measured according to BS EN ISO 8655-4:2022, using a calibrated glass pycnometer. Finally, different procedures and characterization techniques, carried out to determine the properties of various materials used to formulate different types of concretes and mortars, are fully explained.

2.2 Characterization Techniques for Aggregates, Powders, and Nano-Titanium Particles

The properties of concrete aggregates, powder, and fine additives are important for the design of concrete mixtures. The aimed composition of concrete mixtures in terms of workability, strength, durability, and sustainability requires a thorough analysis of both physical and chemical material properties by adequate characterization techniques. Therefore, a brief overview of relevant characterization techniques used for determining the physical and chemical properties is given in this section and at each stage the importance of quantitative characterization and methods of achieving this are discussed.

2.2.1 Particle size distribution

The particle size distribution (PSD) or so-called grading of aggregates and powders is an important parameter for the mix design of concrete as the workability of concrete mixtures is influenced by the particle grading and the resulting paste requirements (Hüsken, 2010). Decent aggregate gradation corresponds to high packing density, workable and uniform concrete, without any segregation of the particles (Erdoğan and Turhan, 2009). There are specific techniques available to characterize the PSD of aggregates and fines and the selection of each one depends on the particle size range and the limitation of the selected technique. In this chapter, the grading of aggregates is determined by sieve analysis and described in standards, i.e. ASTM C117 (ASTM, 2004) and ASTM C136 (ASTM, 2006). In the sieve analysis, the aggregate samples pass through a stack of sieves that are arranged in the order of decreasing sieve openings. The sieve openings are standardized by different norms as specified in ISO 3310-1 (ISO, 2000) and BS410 (BSI, 1986). An overview of varying sieve sizes and designations used in the present research is given in Table 2.1. The grading is usually expressed as a percentage of material passing through each sieve, which is also referred to as the cumulative finer fraction.

Table 2.1: Sieves used in the present study according to ISO 3310-1 and BS 410-1.

ISO 3310-1 / BS 410-1 (sieves sizes)			
(mm)	(inch)	(μm)	(inch)
40	1.575	600	0.024
20	0.787	500	0.020
18	0.709	250	0.010
16	0.630	180	0.007
12.5	0.492	125	0.005
10	0.394	90	0.004
4.75	0.187	63	0.002
2.36	0.093	53	0.002
1.18	0.046	36	0.001

2.2.2 Morphology

Morphology, in the field of materials science, is the study of size, shape and phase distribution of physical objects. For the design of a nano concrete mix, it is important to consider the properties of concrete aggregates, powder, and fine additives (nano particles) such as crystallinity, purity, and size, as they have influences on the concrete properties such as permeability, porosity, and mechanical strength. In addition, the geometry and shape of the particles and their surface roughness affect the bonding behaviour, absorption capacity, etc. The morphology of a material often has a greater impact on its macroscopic properties than its chemical compositions. The techniques available to establish the morphological characteristics of fines include scanning electron microscopy (SEM), scanning and transmission electron microscopy (STEM and TEM, respectively) and elemental analysis by energy-dispersive X-ray spectrometry (EDS).

Based on these, the size and morphology of fines in the present research were analysed using a scanning electron microscope (HITACHI SU-6600, S-3700) and a transmission electron microscope (Tecnai model 20FEG), both equipped with a Schottky field emission gun operated at 20 keV and 200 keV, respectively. Furthermore, an elementary analysis was performed using an EDAX® energy-dispersive spectroscopy (EDS) device with EDS measurements arranged in rectangular grids of 10×20 points at the vertical and horizontal distances of 5 mm.

A Micromeritics ASAP2020 equipment, using N2 and an evacuation time of 14 h at 130 °C, was used for the gas physisorption analysis. Using the BET theory [Brunauer et al., 1938] and the standard procedure described in BS ISO 9277 (BSI, 2005), the specific surface areas (SSA_{BET}) of the cement, sand, SCMs and NT powders were determined. Finally, the BJH method was applied for the adsorption and desorption isotherms to derive the pore-sizes and their distribution. It is known that this method considers several assumptions (Groen et al., 2003). However, it is still extensively used to characterize the pores in the size range of 1-50 nm.

2.2.3 Density measurements

The specific density of the raw materials was measured using an automatic helium pycnometer AccuPyc® II 1340 from Mircromiretics®. Before the density measurements, the samples were dried and degassed at 110 °C for 18 hours. Helium was used as the displacement medium. In order to determine the density and to assure equilibrium and to complete a total degassing of the sample, ten purges of the system were performed followed by 8 successive volume measurements to obtain an average density value.

2.2.4 Mineralogy and chemical composition

To characterize the phase contents and chemical compositions of the concrete raw materials and the hydrated system, the X-ray diffraction (XRD) and X-ray fluorescence (XRF) analyses were performed to characterize the phases content and chemical compositions of the concrete raw materials and the hydrated system.

XRD is a commonly used technique which allows identification of crystalline phases. XRD method was performed using a Bruker D8 Advance. Powder samples were loaded in an aluminium circular holder with a diameter of 25 mm, Cu-Kα X-rays of wavelength λ=1.5406 and the data was taken over the 2θ range of 5° to 70° with a step of 0.02° under an operating voltage of 40 kV and a working current of 40 mA.

2.3 Characteristic of Aggregates and Powder Materials

Aggregate shape, texture and gradation qualities affect the workability, finishing, bleeding and segregation of fresh concrete, and they also affect the strength, stiffness, retraction, permeability, and durability of hardened concrete. Because aggregates occupy between 70% and 80% of concrete volume, it is not surprising that their quality is of considerable importance. The properties of concrete aggregates, powder, and fine additives are important for the design of concrete mixtures.

To create dense mixtures, aggregates are used in two major different sizes, fine and coarse aggregates. According to BS EN 12620 (BSI, 2008), aggregates passing through a 4 mm sieve are called fine aggregate and those retained on such sieve are called coarse aggregates. Coarse aggregates consist of gravels or crushed stones with particle size more than 4 mm up to 65 mm.

The coarse aggregates form the main matrix of concrete and the fine aggregates form the filler matrix between the coarse aggregate (Duggal, 2008). Not only may the aggregate limit the strength of concrete, as aggregates with undesirable properties cannot produce strong concrete, but the properties of aggregates greatly affect the durability and structural performance of concrete.

Fines and powder materials have also large impacts on the properties of concrete because their physical and chemical characteristics affect the paste layer that covers the aggregates in concrete. This paste layer is mainly composed of smaller particles (less than 120 μm) and water. The aimed composition of concrete mixtures in terms of workability, strength, durability, and sustainability requires a thorough analysis of both physical and chemical properties by acceptable characterization techniques. An overview of the most relevant material characteristics of the aggregates used in this research is given in the following subsections.

2.3.1 Coarse aggregates

Single forms of coarse crushed aggregates of fluvial gravel and crushed granite were used in the experimental study, with diameters of 0-10 mm, 5-20 mm and 2-16 mm respectively. In Figure 2.1 the PSD of all coarse aggregates is shown, taking into account the sieve sizes (ISO sieves) presented in Table 2.1.

All the river gravels and broken granite that have been used in this study were certified for the use in concrete and fulfil the requirements on concrete aggregates according to BS EN 12620 (BSI, 2008). The most relevant physical properties of aggregates were quoted from the work by Hunger (2010). An overview of the chemical properties is given in Tables 2.2 and 2.3 for all the coarse river and crushed granite aggregates used.

Table 2.2: Chemical composition of the used coarse gravel by XRF.

Type of aggregate	Fluvial		Granite
Size	5-20 mm	0-10 mm	2-16 mm
Content	(%)	(%)	(%)
SiO_2	92.7	93.8	61.8
Al_2O_3	3.9	3.6	13.9
Fe_2O_3	0.52	0.61	2.9
CaO	0.51	0.42	6.1
MgO	-	-	1.8
Na_2O	-	-	2.6
K_2O	0.78	0.87	2.9
SO_3	-		0.4
TiO_2	0.07	0.07	0.4
Mno	-	-	0.1
P_2O_5	0.32	0.37	-
NiO	-	-	-
ZnO	-	-	-
SrO	-	-	-
ZrO_2	0.01	0.01	-
BaO	0.01	0.01	0.3
LOI	1.19	0.24	6.8
Total	100	100	100

Values were quoted from the work by Hunger (2010).

Table 2.3: Physical properties of the used coarse gravel.

Type of aggregate	Fluvial		Granite
Size	5-20 mm	0-10 mm	2-16 mm
Specific density (g/cm^3)	2.81	2.80	2.650
D_{min}(mm)	0.170	0.160	0.980
D_{max}(mm)	18.6	10.6	15.4
Shape factor (ξ)[1]	1.10	1.10	1.26
Loose packing density (g/cm^3)[1]	1.590	1.567	1.361
Vibrated packing density(g/cm^3)[1]	1.754	1.728	1.523
Specific surface area (m^2/m^3)	1,110 (BET)	6,411 (BET)	1,761 (BET)

1). Referencial values were quoted from the work by Hunger (2010).

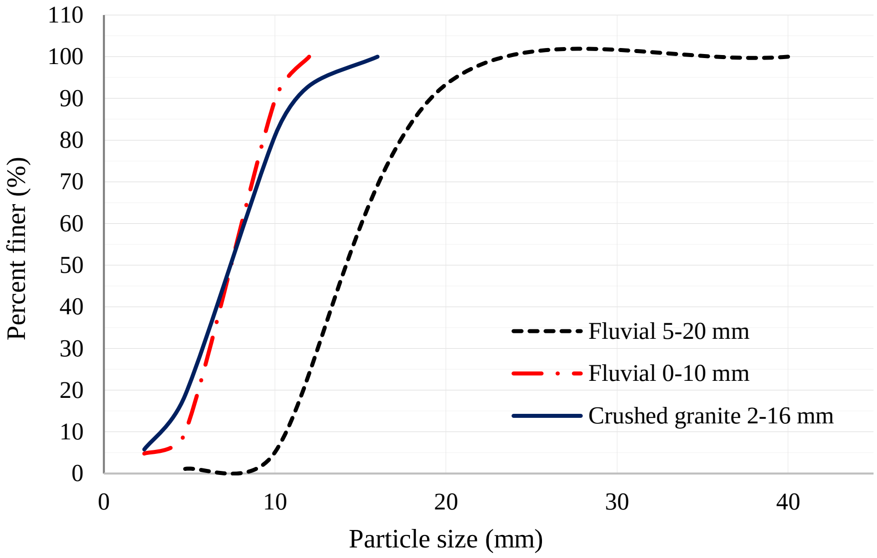

Figure 2.1: Grading curves of the coarse aggregates determined by sieve analysis.

2.3.2 Fine aggregates

Similar to the coarse aggregates, two types of fine aggregates (fluvial sand 0-4 mm and CEN-standard sand 0-2 mm) used in the present research. In Figure 2.2 the PSD of all fine aggregates is shown, considering the sieve sizes (ISO sieves) presented in Table 2.1. The mineralogical phases and chemical compositions of the fine aggregates used were obtained from the X-ray diffraction (XRD) and X-ray fluorescence (XRF) analyses. Fluvial sand was expected to have the same mineralogical composition as the coarse aggregates discussed before. An overview of the physical and chemical properties of fine aggregates is given in Tables 2.4 and 2.5 for all the types of sand used.

Table 2.4: Physical properties of the used sand.

Type of aggregate	Fluvial sand	CEN- standard sand
Size	0-4 mm	0-2 mm
Specific density (g/cm^3)	2.81	2.80
D_{min} (mm)	0.170	0.160
D_{max} (mm)	8.6	9.3
Shape factor (ξ)^1	1.10	1.10
Loose packing density (g/cm^3)^1	1.590	1.567
Vibrated packing density(g/cm^3)^1	1.754	1.728
Specific surface area (m^2/m^3)	17,568 (BET)	18,512 (BET)

1). Referencial values were quoted from the work by Hunger (2010).

Table 2.5: Chemical composition of the used sand by XRF.

Type of aggregate	Fluvial sand	CEN- standard sand
Size	0-4 mm	0-2 mm
content	(%)	(%)
SiO_2	93.2	93.6
Al_2O_3	3.7	3.9
Fe_2O_3	0.53	0.49
CaO	0.18	0.24
MgO	-	-
Na_2O	-	-
K_2O	1.34	1.43
SO_3	-	-
TiO_2	-	-
Mno	-	0.02
P_2O_5	0.25	0.1
NiO	-	-
ZnO	-	-
SrO	-	-
ZrO_2	-	-
BaO	0.01	0.01
LOI	0.79	0.21
Total	100	100

The values were quoted from the work by Hunger (2010).

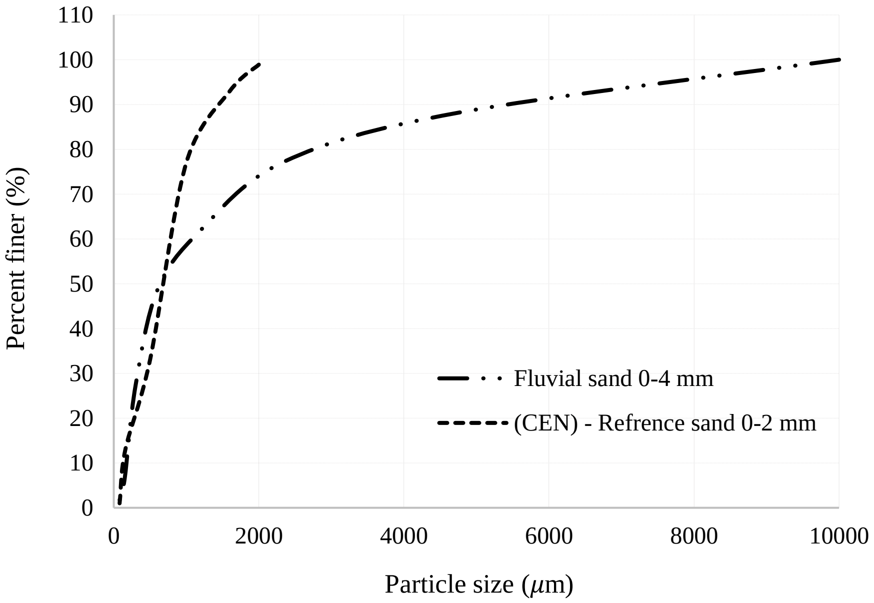

Figure 2.2: Grading curves of the sands determined by sieve analysis.

2.3.3 Binders

Portland cement is the most common example of a hydraulic binder. The four principal minerals found in ordinary Portland cement are alite, impure tricalcium silicate (C_3S); belite, impure dicalcium silicate (C_2S); and the aluminate and ferrite phases which have average compositions of C_3A and C_4AF, respectively. These compounds are formed in a kiln by a series of reactions at temperatures as high as 1500°C between lime, silica, alumina, and iron oxide. The calcium silicates react to give calcium hydroxide and calcium silicate hydrate and the aluminate and ferrite phases react with the added calcium sulfate to give two groups of products referred to as AFt and AFm.

Calcium hydroxide (CH) is the only hydration product to have a well-defined stoichiometry and crystal structure and normally forms as massive, relatively pure crystals with a euhedral hexagonal habit. In the manufacturing process, selected raw materials are ground to fine powders, and proportioned in such a way that the resulting mixture has a desired chemical composition. After blending, the raw material mixture is fed into a kiln and converted to cement clinker. The clinker is cooled, a small amount of gypsum (3% to 6%) is added, and the mixture is pulverized. The finished pulverized product is Portland cement.

The two main clinker phases, C_3S and C_2S, react with water to form fibrous calcium silicate hydrates (C-S-H gel) that give the strength to the hardened concrete (Mindess et al., 2002). Such a binder sets and develops compressive strength as a result of hydration, which involves chemical reactions between water and the mixtures present in the cement. The development of strength is predictable, uniform and relatively fast. Based on the previous notation, two type I cements of different grades (CEM I 52.5N and CEM I 42.5N) were used in the experiments performed in this study, which complied with BS EN197 part 1 (BSI, 2000). The mineralogical phases and chemical composition of the raw materials used were quoted from the work by Hunger (2010). An overview of the physico-chemical properties of binders is given in Table 2.6 and Table 2.7. In Figure 2.3, the PSDs of both cements are shown, considering the sieve sizes (ISO sieves) presented in Table 2.1. Main phase composition of the examined cements by XRD is provided in Table 2.8.

Table 2.6: Chemical composition of the used cement by XRF.

Properties	(OPC) CEM I 42.5 N	(OPC) CEM I 52.5
Content	(%)	(%)
SiO_2	20.62	21.41
Al_2O_3	3.52	3.22
Fe_2O_3	2.98	2.91
CaO	63.21	64.1
MgO	1.92	1.80
Na_2O	-	-
K_2O	0.74	0.91
SO_3	3.12	3.98
TiO_2	0.45	0.65
Mno	-	-
P_2O_5	-	-
NiO	-	-
ZnO	-	-
SrO	-	-
ZrO_2	-	-
BaO	-	-
LOI	3.44	1.02
Total	100	100

The values were quoted from the work by Hunger (2010).

Table 2.7: Physical properties of the cement used.

Properties	(OPC) CEM I 42.5 N	(OPC) CEM I 52.5
Specific density (g/cm^3)	3.11	3.32
D_{min}(µm)	0.27	0.360
D_{max}(µm)	160	155
Shape factor (ξ)[1]	1.70	1.70
Loose packing density (g/cm^3)[1]	1.590	1.567
Vibrated packing density(g/cm^3)[1]	1.754	1.728
Specific surface area (m^2/m^3)	992,145(BET)	942,115(BET)

1). Referencial values were quoted from the work by Hunger (2010).

Table 2.8: Main Phase composition of the examined cements by XRD.

Type of cement	(OPC) CEM I 42.5 N	(OPC) CEM I 52.5 N
Phase content	(%)	(%)
Alite (C_3S)	50.83	50.03
Belite(C_2S)	21.21	21.05
Ferrite (C_4AF)	8.700	9.260
Aluminate (C_3A)	6.010	5.240
Calcite	2.590	3.010
Ca-Langbeinite	0.550	0.550
Anhydrite	0.160	0.190
Bassanite	0.910	1.160
Syngenite	0.010	0.940
Free lime (CaO)	0.290	0.970
Periclase (MgO)	1.330	0.970
Gypsum	2.100	2.200
Others	5.320	4.470
Total content	100	100

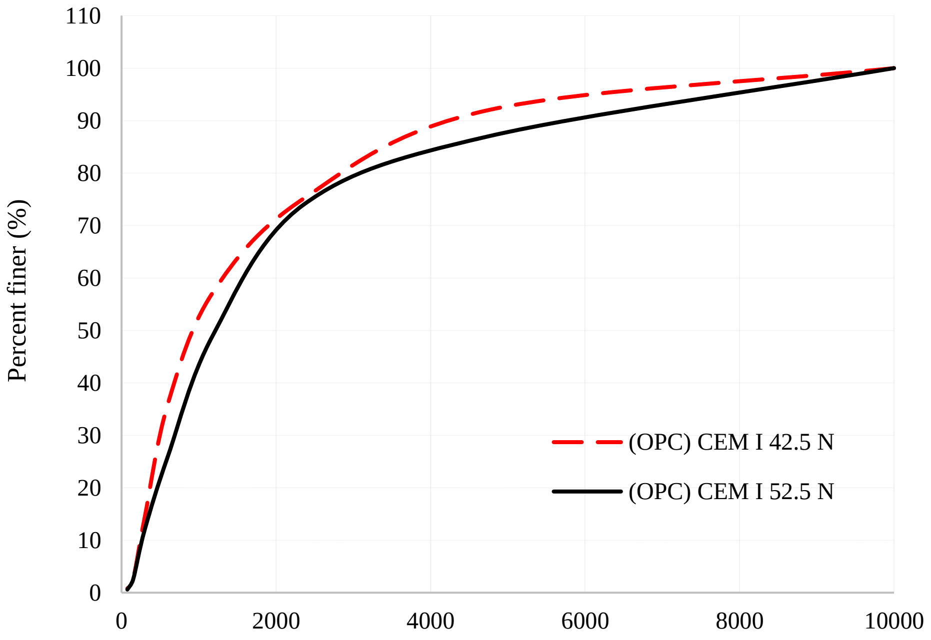

Figure 2.3: Grading of cement determined by sieve analysis.

2.3.4 Supplementary cementitious materials (SCMs)

Supplementary cementitious materials (SCMs) are widely used in concrete either in blended cements or added separately. The use of SCMs such as fly ash (FA), silica fume (SF), hydrated lime (HL) and metakaolin (MK), currently represents a viable solution to partially substitute Portland cement clinker. When these materials are combined with Portland cement through either pozzolanic or hydraulic activity, a contribution towards the properties of hardened concrete is made. As a result, the emissions of greenhouse gases are reduced, whilst creating a more economical solution than Portland cement.

SCMs are also considered as reactive fines and are added to concrete to improve or influence certain properties, such as workability, strength development or heat release during hydration. SCMs may be divided into natural materials and artificial ones. The natural materials are true pozzolans and volcanic tuffs. The artificial materials are comprised of siliceous by-products and wastes, such as fly ashes, silica fume and other new waste products such as photovoltaic waste sludge originating from the manufacturing process of solar panels and electronics. Fly ash is a by-product from the thermal power industry by burning coal, which is widely available in the world. Fly ashes consist mainly of silicate (SiO_2) but can contain also significant quantities of alumina (AL_2O_3). Fly ashes are spherical in nature. Besides the pozzolanic activity, FA plays a role of a micro filler, water reducing agent and prevents the formation of micro-cracks at early ages due to the relatively slow release of the hydration heat (Spiesz, 2013). The amount of CaO in FA is limited for some applications, and it is highly variable depending on the origin. Several standards differentiate and classify fly ashes like BS EN 450-1 (BSI, 2012), ASTM C618 (ASTM, 2019), etc., in high calcium (Class C) and low-calcium (Class F) ashes. Class F fly ashes contain between 10% and 35% alumina, so the blending of OPC with such fly ash results in high amounts of Al-rich phases and therefore increased durability of concrete is obtained. Fly ash Superpozz SV80 of class F was utilised in the present research, which complies with BS EN 450-1 (BSI, 2002). In recent years, there has been a growing interest in the use of metakaolin (MK) as a mineral admixture to enhance the strength and durability of concretes. Metakaolin has been widely studied for its highly pozzolanic properties, suggesting that metakaolin could be used as an SCM. Unlike other SCMs that are secondary products or by-products, metakaolin is a primary product, obtained by calcining kaolin clay within a temperature range of 650 to 800 C° (Ramezanianpour et al., 2012; Guneyisi et al., 2012). Metakaolin is increasingly being used to produce materials with higher strength, denser microstructure, lower porosity, higher resistance to ions, and improved durability (Paiva et al., 2012; Güneyisi et al., 2013; Nadeem et al., 2013). An overview of the physico-chemical properties determined for all SCMs applied in this study are given in Tables 2.9 and 2.10. Additionally, Figure 2.4 shows their PSDs considering the sieve sizes (ISO sieves) presented in Table 2.1.

Table 2.9: Chemical compositions of the used SCMs.

Properties	Metakaolin	(Fly ash, class F)
Content	(%)	(%)
SiO_2	53.67	55.68
Al_2O_3	37.32	19.92
Fe_2O_3	2.11	8.65
CaO	0.76	5.35
MgO	0.21	1.44
Na_2O	0.23	1.15
K_2O	0.65	2.13
SO_3	2.73	0.25
TiO_2	-	-
Mno	-	-
P_2O_5	-	0.34
NiO	-	-
ZnO	-	-
SrO	-	-
LOI	3.55	5.1
Total	100	100

Table 2.10: Physical properties of the used SCMs.

Properties	Metakaolin	(Fly ash, class F)
Specific density (g/cm^3)	2.728	2.382
D_{min}(µm)	0.170	0.160
D_{max}(µm)	18.6	10.6
Shape factor (ξ)[1]	1.15	1.09
Loose packing density (g/cm^3)[1]	1.590	1.567
Vibrated packing density(g/cm^3)[1]	1.754	1.728
Specific surface area (m^2/m^3)	792,145(BET)	989,183(BET)

1). Referencial values were quoted from the work by Hunger (2010).

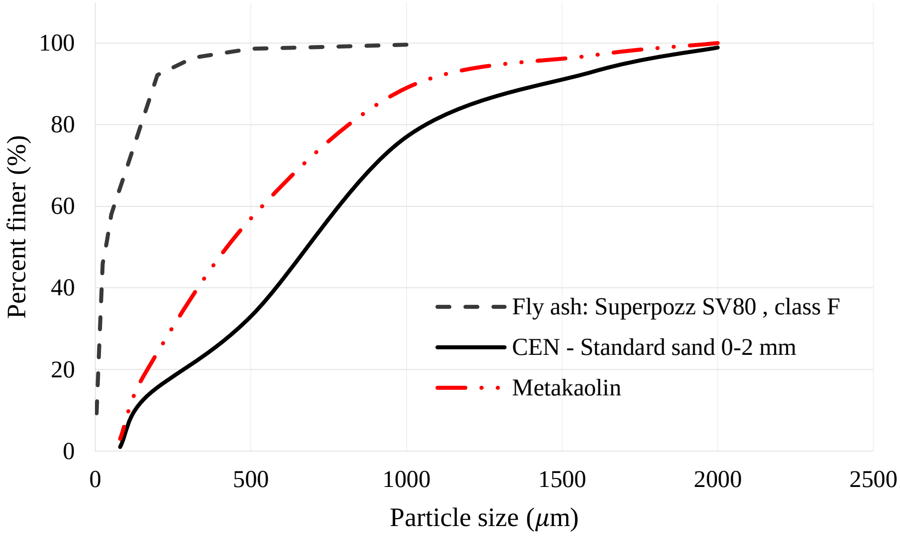

Figure 2.4: Grading curves of the SCMs determined by sieve

2.3.5 Nano titanium particles

The NT used in this research was obtained from ALDRICH and had a specific surface area of 55 m^2/g, a specific gravity of 2.1-2.3 at 25 °C, a bulk density of 0.054 g.mL^{-1}, and an average particle size of 19 nm. A summary of the physical properties of the NT is given in Table 2.11.

Table 2.11: Properties of Nano Titanium Dioxide TiO_2 .

Properties	Nano Titanium Dioxide
Particulates	Anatase based
PH	3.5-4.5
Particle size (nm)[1]	21
Moisture content [1]	0.42
Melting point [1]	1850°, > 350 °C(lit.)
Poisson's ratio	0.27
Density (g/cm^3)[1]	4.23
Surface area (m^2/g)[1]	55 (BET)
Mw (g/mol)	79.8

1). Referencial values were quoted from ALDRICH.

2.4 Water to ´Equivalent Cement/Binder´ Ratio

Abrams' law is used to predict the compressive strength of cementitious materials based on water/cement ratio (W/C). Abram observed that as the W/C ratio decreases, the strength of the concrete increases, accordingly, proposed a relationship between W/C ratio and compressive strength of concrete (Abram, 1919). This law contributed a significant progress in the history of cementitious materials and concrete technology. However, Abrams' law of water/cement ratio does not contribute to pozzolanic materials and supplementary cementitious materials as stated by Rao (2001). Therefore, an alternative water/cementitious materials ratio law was proposed for designing mix proportions, incorporating different cement replacement materials known as water/´equivalent cement´ ratio or water/cementitious material ratio expressed at Abraham's law and Abram's law with application of 'equivalent cement' (Rao, 2001), presented in Equations (2.1) and (2.2), respectively.

$$\sigma c = A/B^{w/c} \tag{2.1}$$

$$\sigma c = A/B^{w/c_{eq}} \tag{2.2}$$

where σc is the compressive strength, A and B are constants as per the material age and test, w/c is the water cement ratio and C_{eq} is the equivalent cement. Referring to BRE (Teychenne et al., 1997), the water/'equivalent cement' ratio is as following:

$$w/c = \frac{m_w}{m_c} \tag{2.3}$$

where m_w is the weight of water and m_c is the weight of the ordinary Portland cement. The water/binder ratio is utilised to compare the maximum or minimum content of cement, or the water/cement ratio as specified in BS 8110-2 (BSI, 1985). The water/binder ratio is expresses as following as per BRE:

$$w/b = \frac{m_w}{m_c + k.m_{add}} \tag{2.4}$$

where m_w is the weight of water, the amount of addition (m_{add}) is reduced by a factor k (cementing efficiency factor) and added to the cement content (m_c) to form a new equivalent water/binder ratio (*w/b*). Minimum cement content and maximum *w/b* ratio are important design parameters using exposure classes as defined in BS 8110-2 (BSI, 1985). In this way the k-value concept can be used to achieve certain *w/c* (or *w/b*) ratio limits by actually using less cement. The applied k-values are hereby depending on the type of reactive powder and cement type. The k-value concept has been first established for fly ash and silica fume (amorphous silica), but other type II additions can be applied by following the equivalent concrete performance concept as given in BS 8110-2 (BSI, 1985). It usually varies from 0.2 to 0.45. For a 28-day strength concrete BRE, Teychenne et al. (1997) suggest setting the “k” factor at 0.3. In the present research, the k-value of 0.3 was used for the design of different mortars and concrete mixes.

2.5 Workability tests

In practice, there are several testing devices to measure workability such as the slump or the slump-flow test, flow table test, mini-cone test, and some others. The workability properties of fresh concrete mixes were investigated during this PhD thesis through three main experiments Slum test, Slump-flow test and vebe test based on BS EN 12350-2 (BSI, 2009a), BS EN 12350-5 (BSI, 2009c) and BS EN 12350-3 (BSI, 2009b) respectively. Brief descriptions of the conducted tests are given in this section.

2.5.1 Slump test

Slump test was conducted following the guidelines of BS EN 12350-2 (BSI, 2009), to examine the fresh concrete consistence. The test consists of a cone, a tamping rod, a base plate, a funnel, a shovel, and a timer. The cone is 300 mm height, and it has a diameter of 200 mm and 100 mm at its base and top, respectively. The tamping rod, also known as the compaction rod, has a length of 600 mm and a diameter of 16 mm. Thereafter, the metal cone was lifted, leaving the concrete sample behind, which slumped down by the action of gravity. Slump was measured from the highest point according to the standard BS EN 12350-2 (BSI, 2009a). In the present research, the mix proportion design resulted with a slump ranging from 100 mm to 230 mm and vebe time ranging from 8 and 16 seconds which met the required workability based on BS EN 12350-2 (BSI, 2009a). The recorded mix design, water/´equivalent cement´ ratio and water/binder ratio for samples, are presented in chapters 4, 5 and 6.

2.5.2 Slump flow test

The slump flow test has become more widely used in recent years, as it is appropriate for concrete of high and exceedingly high workability including flowing concrete, which would exhibit a collapse slump. The apparatus consists of a flow table over which concentric circles are marked. A standard mould made from smooth metal in the form of a frustum cone (dimensions are different from the Abram’s cone) was kept at the centre of the table, firmly held and was filled in two equal layers, by compacting with a wooden bar (50 mm × 50 mm). Each layer was compacted 15 times as in slump test. After lifting the mould, the table was jolted 25 times and the average diameter of the spread was noted. The flow diameter was measured according to the standard BS EN 12350-5 (BSI, 2009c). The Vebe test was conducted with regards to BS EN 12350-3 (BSI, 2009b). The test measured the required time to compact the fresh concrete mix.

2.6 Hydration of Portland Cement

Ordinary Portland cement and clinker are extraordinarily complex materials consisting of several crystalline phases. The four major components of OPC cement are silicate or Alite (C_3S– Ca_3SiO_5), dicalcium silicate or Belite ($C_2S - Ca_2SiO_4$), tricalcium aluminate (C_3A–$Ca_3Al_2O_6$), and tetracalcium alumino-ferrite ($C4AF - 4CaO.Al_2O_3.Fe_2O_3$), while the minor components are gypsum, calcium sulphate hemihydrate, etc. An overview of the main phase composition of the examined cement using X-Ray diffractometer (XRD) is given in Table 2.8. In Portland cement, C_3S and C_2S are the two major clinker phases, which take up around 60 to 80% of the total mass of cement. These two compounds will react with water to form fibrous calcium silicate hydrates (C-S-H gel) that give the strength to the hardened concrete (Mindess et al., 2002). C-S-H gel is the principal hydration product from cement hydration, and it occupies around 50 to 60% of the solid volume of the hydrated cement paste. The hydration of C_3S can be accelerated by the addition of anhydrite, gypsum, or fine inert calcium carbonates (Hewlett, 2004). In contrast, the hydration of C_2S does not normally proceed to a significant extent until 28 days. The C-S-H gel produced by both C_3S and C_2S has a typical Ca to Si ratio of approximately 1.7 (Richardson and Groves, 1993; Taylor et al., 2010; Myers et al., 2014). This is considerably lower than the 3:1 ratio in C_3S and the excess Ca^{+2} is precipitated as Portlandite $Ca(OH)_2$ crystals. C_2S hydration also results in some CH formation. The following equations approximately summarize the hydration reactions of silicates (estimated in dried samples):

$$C_3S + 3.9H \longrightarrow C_{1.7}SH_{2.6} + 1.3CH + \Delta H\uparrow\ (\sim 550\ kJ/mol) \quad (2.5)$$

$$C_2S + 2.9H \longrightarrow C_{1.7}SH_{2.6} + 0.3CH + \Delta H\uparrow\ (\sim 250\ kJ/mol) \quad (2.6)$$

The morphology of the C-S-H gel is also changing during the hydration process. In first few days, C-S-H gel is found to have acicular and honeycomb morphologies (Diamond and Lachowski, 1983; Thomas et al., 1998). After several days, small disks or spheres are observed (Stutzman, 2001). Another type of C-S-H gel with a very dense structure is also found as the “inner” hydration product in the cement paste at late age (Kjellsen and Lagerblad, 1997). Figure 2.5 shows an example of C-S-H gel observed under the SEM investigation. Calcium hydroxide is another product formed from the calcium silicates hydration and it occupies around 20 to 25% of the solid volume in the hydrated cement paste. CH is the only hydration product to have a well-defined stoichiometry and crystal structure and normally forms as massive, relatively pure crystals with a euhedral hexagonal habit. Different from the C-S-H gel, this hydration product is detrimental to the concrete strength because it is brittle in nature. It has definite stoichiometry and morphology and tends to be crystalized in empty pores as large crystals (10 µm or larger) that exhibit plate-like shape as illustrated in Figure 2.5.

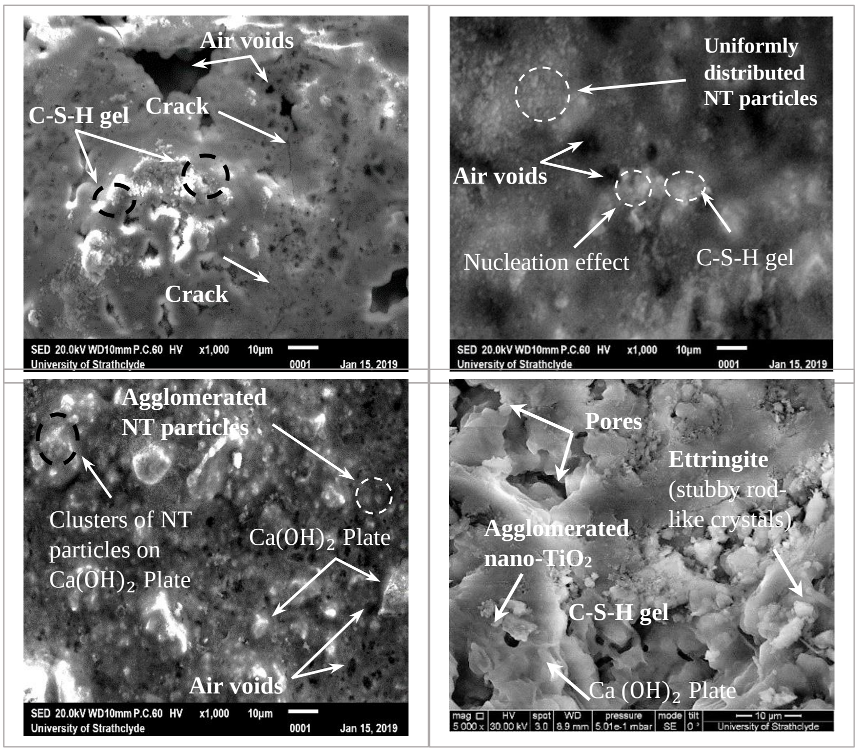

Figure 2.5: Typical SEM images of the specimens with different additions of NT at 28 days curing.

Equations (2.5) and (2.6) illustrates that the hydration of C_3S and C_2S produces the same hydration products (C-S-H gel and CH). However, the amounts of C-S-H gel and CH produced by C_2S are much less than C_3S due to their lower contents in the Portland cement (60-65% C_3S and 16-21% C_2S). The chemical reactivities of C_3S and C_2S are also different. C_3S is more reactive and able to react with water in the first few hours after mixing. Its hydration can cause the paste setting and determines the early-age strength of the concrete. On the contrary, C_2S starts to hydrate at late age (normally after

7 days). Therefore, the reaction of C_2S mainly increases late-age strength. Besides C_3S and C_2S, the reactions of C_3A and C_4AF with water are complex phenomena and are still under investigation. Nevertheless, Odler (1998) briefly studied the hydration of laboratory prepared samples alone or in the presence of calcium sulfate and calcium hydroxide. The finding can be used to explain the complex mechanism of hydration of these phases; however, this should be explained with caution as the composition of the aluminate phases in industrial clinker differs considerably from that prepared synthetically. Generally, the reaction between C_3A and gypsum (shown in Eq. (2.7)) produces ettringite (AFt) in the presence of water:

$$C_3A + 3C + 3\bar{S} + 32H \rightarrow C_3A{\cdot}3C\bar{S}{\cdot}32H + \Delta H \uparrow \ (\sim 866\ kJ/mol) \tag{2.7}$$

where $\bar{s}$ represents SO_3, H represents H_2O (see Appendix 1) and *ΔH* is the heat released due to hydration.

In the absence of soluble calcium sulfate, C_3A reacts rapidly with water to form the C_2AH_8 and C_4AH_{19} phases, which subsequently convert to C_3AH_6. This is a rapid and highly exothermic reaction (~856 kJ/mol). The hydration product, AFt, does not contribute significantly to the concrete strength in long term. However, the formation of ettringite influences the setting of the cement paste. This is because AFt is formed as the needle-like structure (Figure 2.5) at the early age. These needles interlock with each other, which can accelerate the setting of the cement paste. When gypsum depletes and C_3A remains, C_3A can react with the previously formed ettringite to generate monosulfate (AFm) (shown in Eq. (2.8)).

$$C_3A{\cdot}3C\bar{S}{\cdot}32H + 2C_3A + 4H \rightarrow 3[C_3A{\cdot}C\bar{S}{\cdot}12H] + \Delta H \uparrow \tag{2.8}$$

Monosulfate (AFm), together with ettringite, comprises 18 to 25% of the solid volume of the hydrated cement paste. Similarly, to ettringite, monosulfate does not contribute much to the concrete strength. The last clinker phase introduced in this section is C_4AF . It has two subsequent reactions with gypsum. Firstly, it reacts with gypsum and water to form ettringite, aluminium hydroxide and calcium hydroxide:

$$C_4AF + 3C\bar{S}H_2 + 30H \longrightarrow C_6(A,F)\bar{S}_3H_{32} + (A,F)H_3 + CH \qquad (2.9)$$

Then, C_4AF can further react with the formed AFt to produce garnets:

$$C_4AF + C_6(A,F)\,\bar{S}_3H_{32} + 2\,CH + 23H \longrightarrow 3C_4 + (A,F)\bar{S}_3H_{18} + (A,F)H_3 \qquad (2.10)$$

In these two equations, the use of the formulae, such as, $C_6(A,F)SH_{32}$ indicates that iron oxide and alumina occur interchangeably in the compounds. It can be seen that C_4AF forms the similar hydration products to C_3A . However, it should be pointed out that the reaction of C_4AF is much slower than C_3A and C_3S during the first few days. The quick hydration of C_3A consumes gypsum rapidly after mixing, which will retard C_4AF reaction. Therefore, most of C_4AF remains unreacted at late age (Scrivener, 2004). As a result, the influence of C_4AF on the hydration behaviour of cement paste at the early ages is not as significant as C_3A and C_3S. It was not considered as an important clinker phase that contributes to cement hydration at early age. In this research, an isothermal calorimetric analysis of cement pastes and mortars with w/c ratio of 0.3-0.5 was performed to study the hydration kinetics of pastes and mortars.

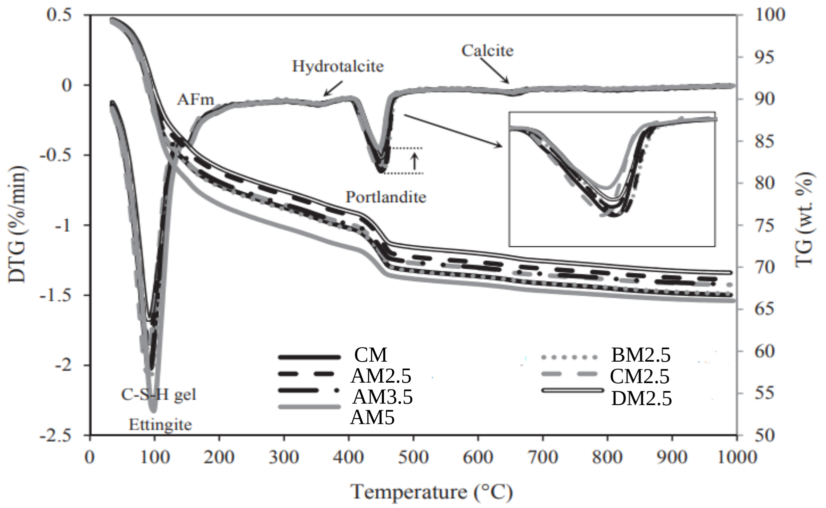

Figure 2.6: Typical TG/DTG analysis of hydrated NT-cement mortars, including the control mix, with different dosages of NT.

For this purpose, the characterization of the cement hydration process, hydration products and morphology of the cement mortars were performed by scanning electron microscopy (SEM) and X-ray diffraction (XRD) with different NT inclusions and to be presented in Chapters 5 and 6. The change in calcium silicate hydrates (C-S-H gel) and the other phases of cement mortars (*e.g.*, Ettringite, Portlandite, Alite and Belite), before and after the addition of NT in cement mortar specimens was detected using thermo-gravimetric method (TG) and to be explained in detail in Chapter 5.

Derivative thermogravimetric (DTG) curves were plotted from the TG data to identify the extent of cement hydration and the exact boundaries of various phases or group of phases present in the hydrated samples. Meanwhile, elementary analysis was performed using an energy-dispersive X-ray spectroscopy (EDAX®). Figure 2.6 illustrate typical TG/DTG analysis of hydrated NT-cement mortars, including the control mix, with different dosages of NT.

2.7 Remarks

Numerous procedures and material characterization techniques have been discussed in this chapter and will later be applied to obtain the main physico-chemical properties of the materials used in this research. In several cases, there are physical properties that can be evaluated by more than one technique. Different strengths and limitations of each technique complicate the choice of the most suitable method, while often a combinatorial characterization approach is needed. The materials used cover different particle sizes from nanoparticles to coarse aggregates develop mortars and concrete mixtures. Furthermore, applicable test procedures for the evaluation of the rheology and workability of concrete have been introduced and discussed. Based on this, the present chapter can be summarised as follows:

1. To characterize the phases content and chemical composition of the concrete raw materials and the hydrated system, the X-ray diffraction (XRD) and X-ray fluorescence (XRF) analyses were performed to characterize the phases content and chemical composition of the concrete raw materials and the hydrated system.
2. The characterization techniques to determine the PSD for aggregates, powders and amorphous nanoparticles are specific and the selection of each one depends on the particle size range (nanometric, micrometric or millimetric range) and the limitation of the selected technique.
3. PSDs among the various types of concrete components were compared and the specific surface areas of the powders were determined using Brunauer-Emmett-Teller (BET) method. In addition, the densities of the samples were measured using a calibrated glass pycnometer.
4. As for all the other experimental techniques, XRF analysis proved to be sensitive to the sample preparation or form of the sample (liquid, loose powder, or tablet). In addition, it is demonstrated that XRF analysis was the faster technique to estimate the mineralogical composition of cement using the Bogue methodology.
5. The workability of a concrete depends on many parameters such as the water to binder ratio, specific surface areas of the cement and powders, the size and shape of the coarse and fine aggregates, chemical composition, and PSD of the SCMs used, type of admixtures and the mixing and testing procedures.
6. The various aspects which contribute to the hydration of Portland cement were considered and illustrated, from the microstructure of the anhydrous cement to the microstructure of mature concrete. At each stage, the importance of quantitative characterization was discussed.

Chapter 3

Experimental Procedures

3.1 Introduction

This chapter addresses the theoretical background, and the experimental procedures for evaluating the properties of composites using different techniques such as X-ray computed tomography (XCT), Brunauer-Emmett-Teller (BET), scanning electron microscopy (SEM), and X-ray diffraction (XRD).

There are many techniques which have been used to study microstructure; they can be divided broadly into two categories. Bulk or indirect techniques give information on the average features of the whole microstructure. Examples of indirect techniques are BET, thermogravimetry (TG) and X-ray diffraction (XRD), which can be used to determine the amounts of certain phases in the sample. The other group of techniques are direct or microscopical techniques which provide information about the way in which the component phases are arranged in the microstructure.

Examples of direct techniques are XCT and SEM. The advantage of the indirect techniques is that they provide information in a quantitative form so that different samples can be compared objectively. In contrast, information derived from direct techniques usually takes the forms of images. Images are extremely valuable in conveying a vivid impression of the microstructure but comparisons between different samples are more subjective and rely on the experience and interpretation of the observer. Recent advances in imaging techniques, especially the 3D micro-X-ray computed tomography (XCT) technique, have made it possible to characterise microstructures for various composite materials with high resolution but without destruction of the materials.

For example, it has been applied to characterisation of steel fibres in self-compacting concrete (Ponikiewski et al., 2015), measurement of porosity and aggregate properties in porous concrete (Agar et al., 2013), shape and surface analyses of coarse aggregates in normal and lightweight concrete (Masad et al., 2005; Erdogan et al., 2006).

Brunauer-Emmett-Teller (BET) theory aims to explore the physical adsorption of gas molecules on a solid surface and serves as the basis for an important analysis technique for the measurement of the specific surface areas of materials. Moreover, gas adsorption has been one of the most popular techniques used for the study of pore structure in materials that contain micropores and mesopores, or mainly pores in cement pastes with radii between 2 nm and approximately 50 nm.

Therefore, gas adsorption technique can mainly characterize gel pores and small and medium capillary pores. Gas adsorption methods are based on measurements of the amount of gas adsorbed on the surface of a powder on the monomolecular depth of the particle’s surface. BJH the method of Barrett, Joyner, and Halenda is a procedure for calculating pore size distributions from experimental isotherms using the Kelvin model of pore filling. However, it applies only to the mesopore and small macropore size range.

In recent years, the application of scanning electron microscopy (SEM) to characterizing cement clinker and ground cements has increased. SEM and X-ray microanalyses have been utilized to identify the four major phases in Portland cement clinker (Stutzman et al., 1991). SEM is also used to investigate the pores or voids inside concrete specimens, and this helps to assess the concrete samples´ porosity. Moreover, EDS can be used to provide elemental information and identify phases observed from X-ray CT analysis.

X-ray powder diffraction (XRD) powder studies on cement paste have been reported by many investigators (Taylor, 1997; Mechling et al., 2009; Kim et al., 2014). XRD has been used for several decades to identify and measure the mass fractions of various crystalline phases in Portland cement. XRD analysis is also able to provide the quantitative determination of the phase compositions in the hydrating paste. XRF is the emission of characteristic secondary (or fluorescent) X rays from a material that has been excited by bombarding with high-energy X-rays or gamma rays. The phenomenon is widely used for elemental analysis and chemical analysis, particularly in the investigation of cementitious materials.

TG is a method for the determination of the composition by detecting the sample’s mass loss with increasing temperature and the comparison with the thermal data for pure phases, possibly present in the sample. The obtained mass loss curve is later transformed into derivative form (DTG), where the mass loss effects are more visible. In the cement research TG/DTG is mostly used for hydration reaction, phase identification and studying the effects of pozzolanic additives (Ramachandran et al., 2002). This method is extremely useful for studying the hydration of calcium silicates, which can only be marked by CH detection in the XRD pattern. This is due to the amorphous structure of C-S-H gel, which is normally undetectable by XRD.

3.2 2D and 3D Porosity Analysis Using X-Ray Computed Tomography (XCT)

X-ray computed tomography is a method of forming three-dimensional (3D) representations of an object by taking many x-ray images around an axis of rotation and using algorithms to reconstruct a 3D model (Kruth et al., 2011; De Chiffre et al., 2014). Three main methods of XCT have been developed over time and each development iteration has increased the speed of data collection.

The first XCT method uses a pencil beam of x-rays translated linearly opposite an x-ray detector to capture density data along each beam. The scanner is then rotated by a small increment and the process repeated until data from a full 360° arc are acquired. The second method uses a two-dimensional (2D) fan of x-rays, spanning the full width of the object, with a one-dimensional (1D) detector array that corresponds to the outer edges of the fan beam. The third method which is adopted in this PhD thesis, utilises a full 3D cone of x-rays with a 2D detector. Figure 3.1 illustrates each of the methods of XCT. In order to investigate the nature of the pore structure configuration of the composite mortar matrix, XCT, tests were carried out. The use of cylindrical samples allows minimization of beam hardening artefacts due to the X-ray penetration length being equal from all angles as the cylinder rotates around its axis in the scan.

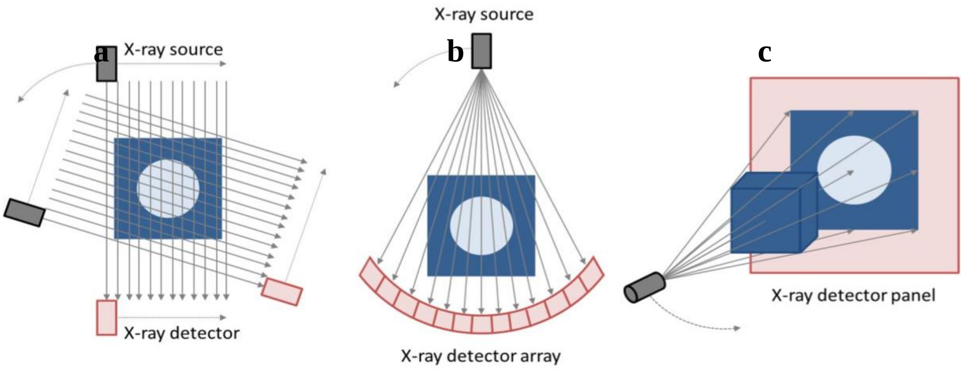

Figure 3.1: Schematics of: a). pencil, b). fan and c). cone beam XCT methods, respectively.

Unlike the more traditional methods for characterization of microstructure, e.g., mercury intrusion porosimetry (MIP) and scanning electron microscope (SEM), XCT provides a more complete picture of the pore distribution, including interconnected and isolated pores, with 3D images and no need of any prior drying preparation. Drying cementitious samples under high vacuum might produce irreversible changes in the microstructure (Rattanasak et al., 2005; Gallucci et al., 2007; Diamond et al., 2000). X-ray tomography can thus be well employed in understanding the meso-structure of building materials (Bentz et al., 2006) and the porosity of concrete (Lu et al., 2006).

The cement mortar samples were subjected to CT scans with a Nikon XT H 225/320 LC in the Advanced Materials Research Laboratory (AMRL) CT scanner facility at the University of Strathclyde. Scans of 20.0 μm resolution were achieved at an operating voltage of 145 kV, a current of 100 μA, and with 3141 projections recorded during one full rotation of the sample. This operating condition resulted in approximately 37 minutes per scan, excluding sample setup and background detector calibration. The 3141 2D projections were reconstructed into a 3D volume with CT PRO 3-D (Nikon Metrology). Further discussion regarding the XCT test is discussed in Chapters 4 and 6.

3.3 Nanoscale Pore System Analysis by Brunauer-Emmett-Teller (BET)

BET analysis provides precise specific surface area evaluation of materials by nitrogen multilayer adsorption measured as a function of relative pressure using a fully automated analyser. The technique encompasses external area and pore area evaluations to determine the total specific surface area in m^2/g, yielding important information in studying the effects of surface porosity and particle size in many applications.

BET analysis gives a more completed picture of the pore distribution compared to the MIP method, as liquid mercury is hydrophobic to most solids, it cannot invade into pores spontaneously without sufficient external pressures. The surface forces of the mercury fronts in pores, inversely depending on the pore curvatures, will resist the forces applied.

A Micromeritics ASAP2020 (Figure 3.2) equipment, using N2 and an evacuation time of 14 h at 130 °C, was used for the gas physisorption analysis. Using the BET theory (Brunauer et al., 1938) and the standard procedure described in DIN ISO 9277 (DIN, 2005), the specific surface areas (SSA_{BET}) of the cement and NT powders were determined.

The nitrogen sorption data was used to compute the total specific surface area (SSA_{t-plot}), the external specific surface area (SSA_{ext}) and the pores volume (V_{MP}) following the t-plot method described by De Boer and Lippens (1964). The statistical thickness (t_l) of the adsorbed gas layer at a given value of x =P/P$_0$, calculated using the model proposed by Harkins and Jura (1944), was plotted against the volume of liquid taken up (n_v). The external specific surface area (SSA_{ext}) in m^2/g, defined here as the surface area of pores larger than micropores, was determined from the slope of the first linear segment within the pressure region $0.10 < P/P_0 < 0.25$ using the following equation:

$$n_{vx} = V_{MP} + k_1 \times SSA_{ext} \times t_l\ (x) \qquad (3.1)$$

where, V_{MP} is the adsorption in saturated condition of micropores (micropore volume), and k_1 is a constant that depends on the units and is equal to the inverse value of 1.546 [cm^3/m^2. nm].

The total specific surface area (SSA_{t-plot}), that includes all pores, was determined from the slope of the linear segment passing through the origin at the pressure region (P/P$_0$) lower than 0.10, using the following equation:

$$n_{vx} = V_{MP} + k_1 \times SSA_{t-plot} \times t_l\ (x) \qquad (3.2)$$

Finally, using the different specific surface areas, the sizes of the primary and agglomerated particles were calculated based on (Thiele et al., 2007) as follows:

$$d_i = \frac{6000}{\rho \times SSA_i} \qquad (3.3)$$

where d_i is the diameter [nm] of the particle, ρ is the density and SSA_i is the specific surface area determined by the BET method SSA_{BET} .

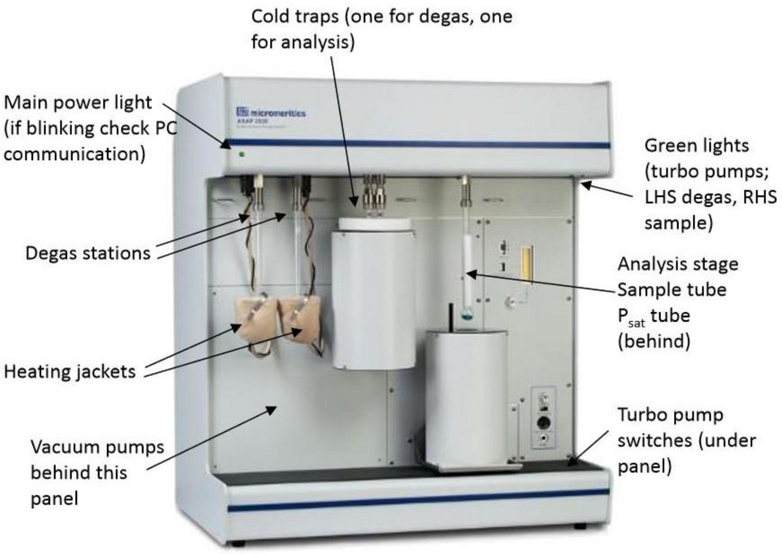

Figure 3.2: The diagram of the experimental apparatus of the Micromeritics ASAP2020 (BET)

3.4 Pore-Size and Distribution (BJH Method)

BJH analysis can also be employed to determine pore area and specific pore volume using adsorption and desorption techniques. This technique characterizes pore size distribution independent of external area due to particle size of the sample. The data obtained from the physical adsorption isotherms of nitrogen was used to determine the pore-size distribution and the surface area of the pores of a specific radius (r_p) of the amorphous micro and nano-titanium samples. For this purpose, the Kelvin equation, which describes the pore radius considering the pore as a cylinder, was used (Barret et al., 1951):

$$log\left(\frac{p}{p_0}\right)=\frac{-2\sigma V_N}{RT}\times\frac{1}{r_p} \tag{3.4}$$

where is σ the surface tension, V_N is the molar volume of liquid nitrogen, R is the gas constant and T is the absolute temperature in K. Furthermore, taking into account the thickness (t_l) in nm of the liquid nitrogen condensated in the wall of the pores in a relative pressure interval, gives as described by Halsey in (Gregg and Sing, 1952):

$$t_l = 3.54\left[\frac{-5}{ln\left(\frac{p}{p_0}\right)}\right]^{0.33} \tag{3.5}$$

The pore diameter in nm (d_p) is defined for each interval of the relative pressure as:

$$d_p = 2\,(r_p + t_l) \tag{3.6}$$

Inserting Equations (3.4) and (3.5) into (3.6) and using the BJH method described by Barret et al. (1951), the pore diameter for each relative pressure interval where condensation of liquid nitrogen occurred was derived. The BJH method was applied for the adsorption and desorption isotherms to derive the pore-sizes and their distribution, however, for comparison purpose. It is known that this method takes into account several assumptions (Groen et al., 2003; Sing, 2004). However, it is still extensively used to characterize the pores in the size range of 2-50 nm.

3.5 Permeability Measurement Using High Pressure Core Holder

Permeability can be defined as that property of a porous material which governs the rate at which fluid moves through the pore structure. The terms absolute permeability and intrinsic permeability are often used to describe the permeability, K, of a porous medium which is independent of the properties of the fluid migrating through the pore structure. The units associated with permeability are length squared (e.g., m^2 or ft^2).

The term hydraulic conductivity, k, describes the ease with which a specific fluid migrates through a porous medium. The units associated with hydraulic conductivity are length per unit time (e.g., m/s or ft/s). Occasionally, the term permeability has unfortunately been used to refer to the hydraulic conductivity of a porous material with respect to a specific fluid. Throughout this PhD thesis the term permeability will be used to signify the absolute permeability.

A general view of the experimental setup for conducting water-permeability measurement using a high-pressure Hassler type core holder is presented in Figure 3.3. For the purposes of the experimentation, specimens in cylindrical geometry with a diameter of 35 mm and thickness of 70 mm were extracted using a diamond precision cutter from the samples.

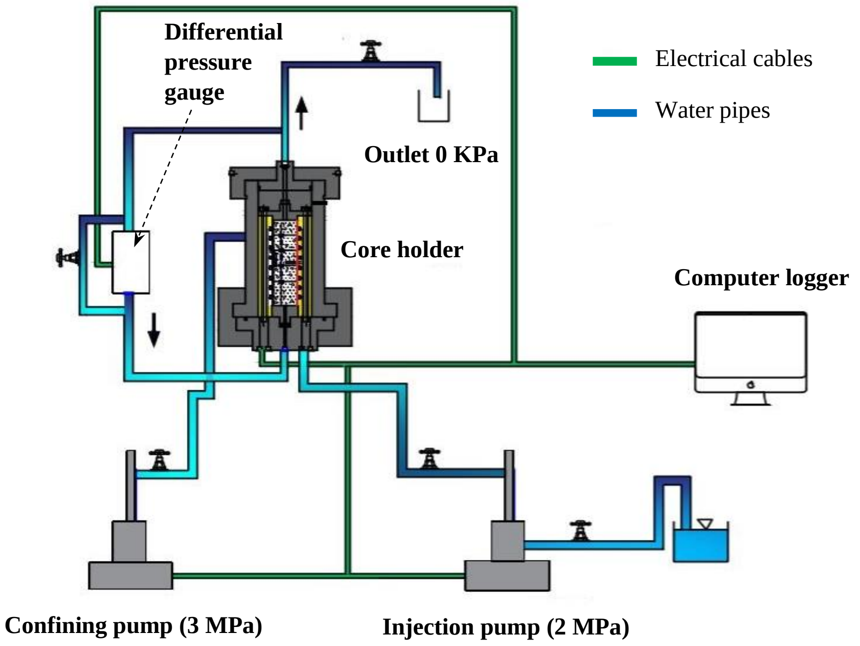

Figure 3.3: A general view of the experimental setup for conducting the water permeability measurement of the cement mortars using high pressure core holder.

The vacuum saturated core sample was mounted in the core holder and then placed under a suitable confining pressure (3 MPa) to ensure a tight seal around the sample and minimal bypass of injected fluid around the sample. The water was then flowed through the sample under a constant pressure gradient (max 2 MPa) until steady-state flow was reached. The flow rate and the pressure drop were then recorded. The test was repeated at different sets of flow rate and inlet pressure and the data were recorded. Controlling the temperature of the environment surrounding the permeability set-up contributes to pressure stability, so the test temperature was maintained at 22 ± 1.0 °C. Finally, de-aired water was used for the experiment as well as for applying the confining pressure.

A constant pressure was applied to the inlet of the sample and the pressure drop from inlet to outlet was recorded with a differential pressure transducer. The cumulative volume injected in order to maintain this constant pressure was recorded at ten second intervals, accurate to ± 0.5 mm^3, and was used to calculate flow rate. We assume that the flow of water in the porous medium is governed by Darcy's law:

$$Q = -\frac{kA(p_b - p_a)}{\mu L} \tag{3.7}$$

where A is the cross-sectional area of the sample (m^2), Q is the flow rate ($\frac{m^3}{s}$), k is the permeability of the medium (m^2), μ is dynamic viscosity of the fluid, L is the sample length and $(p_b - p_a)$ is the measured pressure drop. The pore fluid is assumed to be compressible. We also assume that the porosity of the medium is influenced by only the bulk compressibility of the medium. The volume of solids composing the porous medium is assumed to be incompressible in comparison with the pore fluid and the porous skeletal fabric. By considering equations of continuity and Darcy's law, it can be shown (Freeze and Cherry 1979; Fetter 1988; Barenblatt et al. 1990) that the differential equation governing the transient variation of head, h, (dimension L) in the region due to pressurization is given by:

$$\Delta^2 h = \frac{S}{T_R} \times \frac{\delta h}{\delta t} \tag{3.8}$$

where $\Delta^2 = \frac{\delta^2}{\delta r^2} + \frac{\delta}{\delta r^2}$ is Laplace's operator referred to the radially symmetric coordinate system. In Equation (3.8), S (non-dimensional) is the storage coefficient of the tested interval, l (dimension L) defined by:

$$S = l\gamma_w\left(nC_w + C_{eff}\right) \tag{3.9}$$

where γ_w is the unit weight of water (dimension M/T^2L^2), C_w is the compressibility of water (dimension LT^2/M), C_{eff} is the compressibility of the porous skeleton (dimension

LT^2/M), n is the porosity (non-dimensional), T_R is the transmissivity of the tested interval (dimension L^2/T) (Haimson and Doe 1983) which is related to k, the hydraulic conductivity of the porous medium (dimension L/T), by the relationship:

$$T_R = \frac{kl\gamma_w}{\eta} \tag{3.10}$$

where K is the permeability of the porous medium (dimension L^2), and η is the kinematic viscosity of water (dimension M/LT). Equation (3.10) is an approximation to the more generalized situation involving full coupling between the deformations of the pore fluid and the deformations of the porous skeleton (Biot 1941; Rice and Cleary 1976; Selvadurai and Yue 1994). Although the porous skeleton is assumed to be non-deformable, account is made for a bulk volume change of the porous skeleton.

An alternative to this approach is to assume that the porous skeleton is perfectly rigid, where C_{eff} is set equal to zero. In this research, the transient tests were conducted for 18 hours, but only the first 2100 seconds of data were used to determine the permeability of the samples. An initial injecting pressure of 2 MPa was adopted and ordinary tap water at room temperature was used as the permeating fluid.

3.6 Microstructural Analysis Using Scanning Electron Microscopy (SEM)

SEM is used to examine micro-scale topography and elemental compositions, and as the technique depends on the transfer of electrons both from filled states and to unoccupied states it is particularly surface sensitive. SEM uses a high-energy beam of electrons in a raster scan pattern to produce images of the surface topography of a sample. The high-energy electron beam is directed on the sample surface where the electrons interact with surface atoms. Signals produced from these interactions provide information about the surface topography, composition, and other properties, such as electrical conductivity. The signals produced can be in the form of secondary electrons

(SE), or backscattered electrons (BSE) (Insight Experts., 2008). The primary imaging mode uses signals produced in the form of secondary electrons. This method can produce extremely high resolution between 1-5 nm in size (Goldstein., 2003). Figure 3.4 shows a schematic diagram of an SEM column for the generation of images. SEM analysis was carried out in the secondary electron mode using the field emission scanning electron microscope (FE-SEM). A HITACHI SU-6600 was operated with an acceleration voltage of 20 keV.

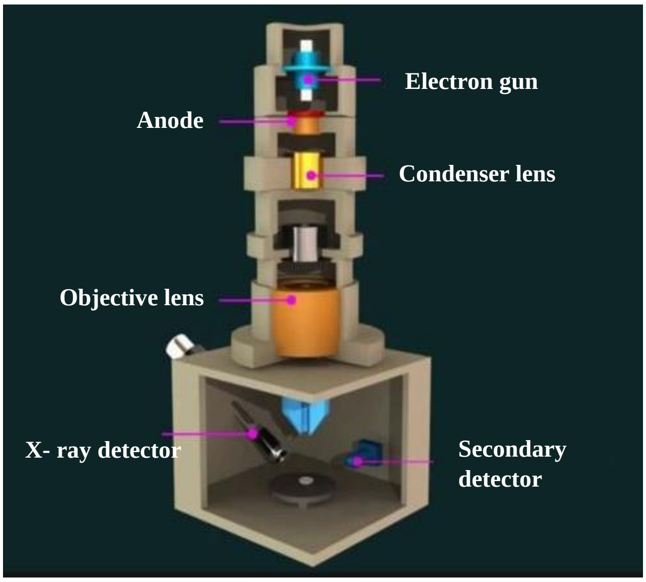

Figure 3.4: Schematic diagram showing a SEM column (reproduced from ref. (Microtech Sciences., 2007)).

3.7 Elemental Composition Analysis Using Energy Dispersive X-Ray Spectroscopy (EDX)

EDX is used to determine the elemental composition of a material, by measuring characteristic X-rays emitted from core electrons that move from higher energy levels to the ground state. It relies on the investigation of an interaction of some source of X-ray excitation and a sample. Its characterization capabilities are due in large part to the fundamental principle that each element has a unique atomic structure allowing unique set of peaks on its X-ray spectrum. By measuring characteristic X-rays that are emitted it is possible to distinguish between the elemental compositions on the sample surface.

To stimulate the emission of these characteristic X-rays, an electron is ejected from a lower energy level. The electrons initially start in the ground state and by ejecting an electron a vacancy is created in one of the electron shells which can then be filled by an electron de-exciting from a higher energy level. In doing so the electron must loose energy, which is emitted in the form of an x-ray energy equivalent to the difference in the initial and final energy levels. Characteristic x-rays are used to identify the elemental composition of the sample.

EDX spectra were recorded at magnifications of 1000x, 1500x and 2000x. An acceleration voltage of 20kV was used. The working distance was set to 7 mm with an acquisition time between 10 and 15 minutes. Figure 3.5 shows EDS microanalysis and SEM images of the reference sample, showing the composition of sample mainly consisted of carbon (C), oxygen(O), silicon (Si), calcium (Ca). Full elemental analysis of cement composites are presented in Chapter 5.

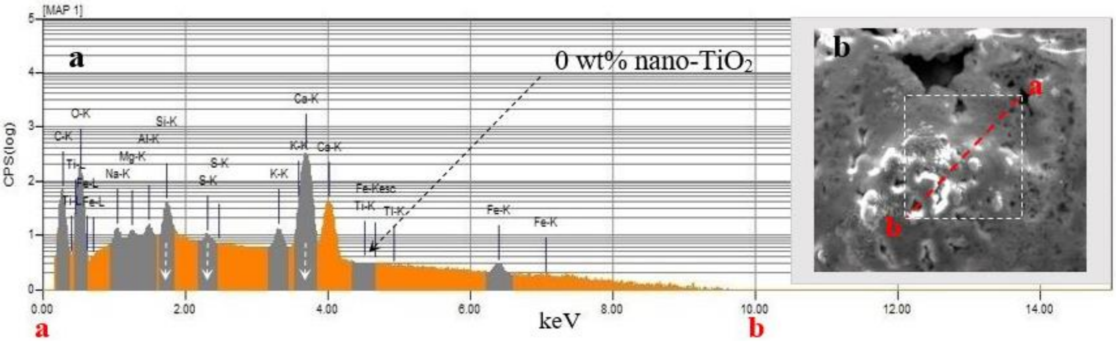

Figure 3.5: Typical EDS analysis (a) and SEM image (b) of the control Mix at 28-day curing

3.8 Identification and Quantification of the Formed Hydrates Using X-Ray Diffraction Analysis (XRD) and Thermo-Gravimetric (TG/DTG)

XRD is a commonly used technique which allows identification of crystalline phases. Each crystalline phase has a unique XRD pattern determined by the spacings of the crystallographic planes described by Bragg's law (Michell, 2004):

$$n\lambda = 2d\sin\theta \tag{3.11}$$

where n is an integer for constructive interference, λ is the X-ray wavelength, d is the interplanar spacing between rows of atoms, and θ is the angle of the X-ray beam with respect to these planes (Figure 3.6). Thus, it is possible to distinguish the phases from their characteristic XRD patterns.

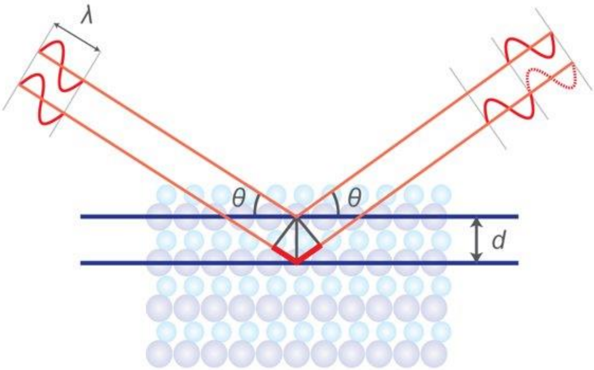

Figure 3.6: Bragg diffraction from a crystalline solid

All patterns for known crystalline phases are combined in the Inorganic Crystal Structure Database (ICSD). Sample type and preparation method used in the XRD analysis depends on the system and required results and can either be powders, solid or hydrated paste. X-ray diffraction analysis was employed to study the effect of different dosages of NT on the formation of various phases in the hydration products of cement mortars.

Powder samples were loaded in an aluminium circular holder with a diameter of 25 mm as illustrated in Figure 3.7. X-ray diffraction analysis was performed using a Bruker D8 Advance, Cu-Kα X-rays of wavelength λ =1.5406 Å =1.5406 Å and the data was taken over the 2θ range of 5° to 70° with a step of 0. 0.02° under an operating voltage of 40 kV and a working current of 40 mA. After identifying the existing phases in the cement using XRD, quantification of the formed hydrates was performed using thermogravimetry analysis in a thermobalance Perkin Elmer TGA7 with a TAC7/DX controller, in a N_2 atmosphere.

The temperature ranged from 20 to 1000 °C at a heating rate of 10 °C a minute. An analytical Gas N_2 5.0 was used to protect the balance (at a flow of 20 mL min^{-1}), and the volatized gases were purged at a rate of 60 mL min^{-1}.

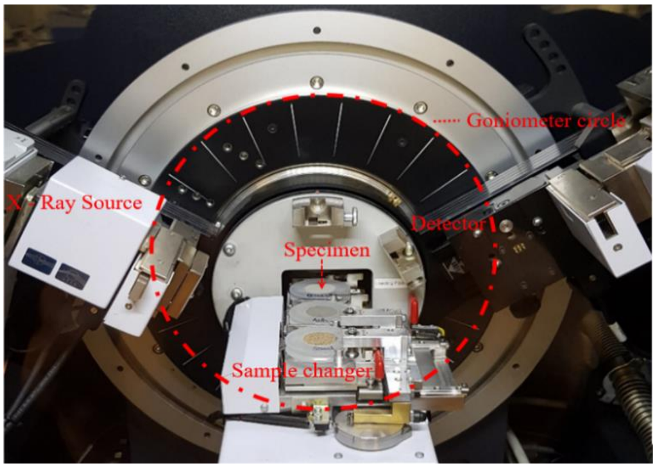

Figure 3.7: Illustration of an X-Ray diffractometer geometry.

TGA is a method for the determination of the composition by detecting the sample's mass loss with the increasing temperature and comparing with the thermal data for pure phases, possibly present in the sample. The obtained mass loss curve is later transformed into derivative form (DTG), where the mass loss effects are more visible. In the cement research TG/DTG is mostly used for hydration reaction, phase identification and studying the effects of pozzolanic additives (Ramachandran et al., 2002). Figures 3.8 and 3.9 illustrate typical TG/DTG analyses of hydrated NT-cement mortars, including the control mix, with different dosages of NT. By analysing these figures, several observations can be made.

The extent of cement hydration was estimated from changes observed by TGA/DTG and considering the mass loss corresponding to each hydrated phase. It has been reported (Taylor, 1990; Hewlett, 2004; Ramachandran et al., 2002) that the mass loss at 100–130 °C corresponds to the evaporation of adsorbed water, at 115–125 °C to C-S-H gel, ettringite at temperatures of 120–130 °C, AFm phases at 180–200 °C, calcium hydroxide (portlandite) in the range of 410–550 °C and calcium carbonate at 680–750

°C. In addition, a presence of a broad initial peak, related to a CO_2 release at 550–680 °C is an indication of a significant fraction of calcium manocarboaluminate (Lothenbach and Wieland, 2006).

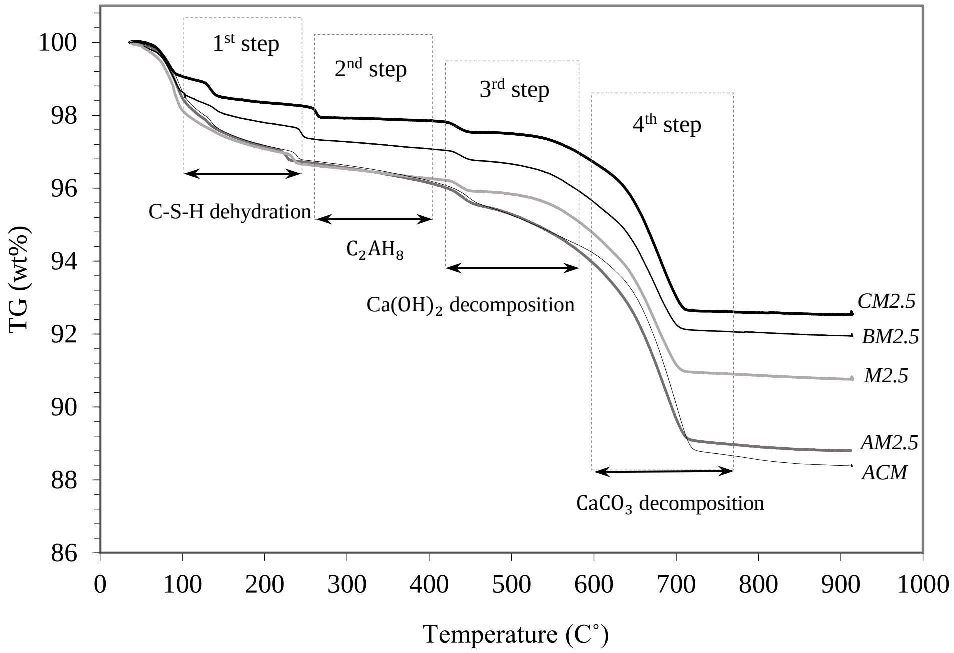

Figure 3.8: TGA curves of the mortar specimens containing different amounts of NT.

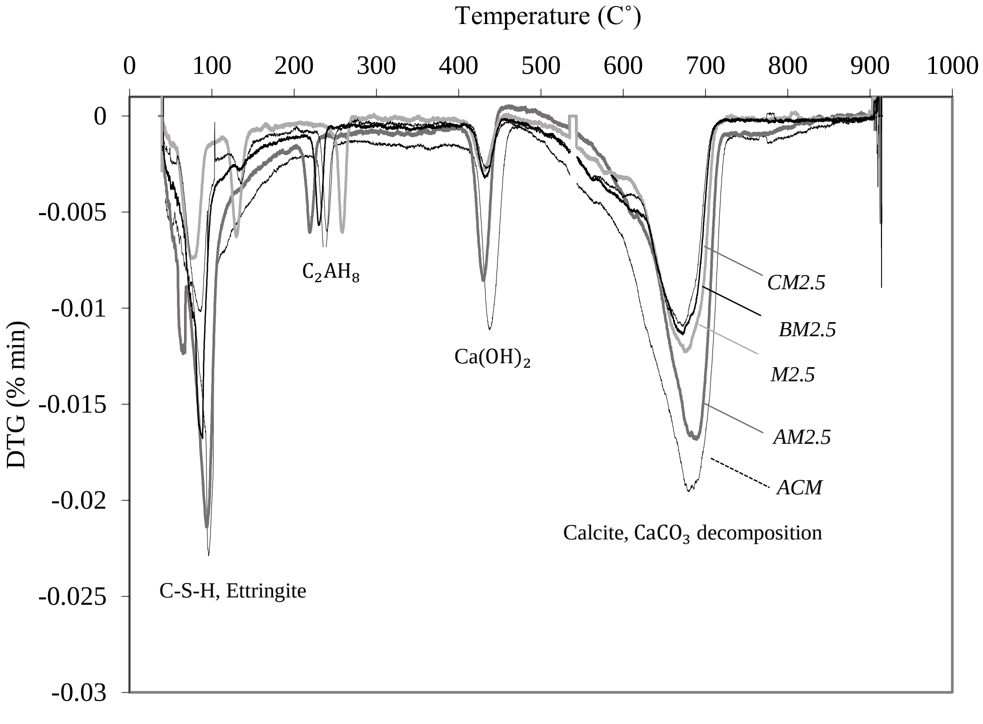

Figure 3.9: DTG curves of the mortar specimens containing different amounts of NT.

3.9 Mechanical Tests Using Instron 5969®

3.9.1 Direct tension test (DTT)

There are no standardized recommendations of direct tension test (DTT) for concrete because it is challenging to ensure that uniaxial stress along the specimen is evenly applied. Various self-designed methods for DTT are commonly used to capture uniaxial tensile behaviour of concrete, which can be distinguished into three catalogues: unnotched prisms or cylinders, notched prisms or cylinders, and dog-bone–shaped specimens. In this PhD thesis, a DTT on notched cylindrical and dog-bone–shaped geometry specimens has been conducted to investigate the tensile behaviour of cement composites. The tension test consists of a tension testing machine (Instron 5969®) with a capacity of 50 kN. The testing arrangement is shown in Figures 3.10(a) and (b). The specimen was notched circumferentially with a depth of 12 mm +/- 1 mm and a width of 2.5 mm. The ends of the steel specimen were gripped within the test frame to eliminate any relative end rotation and ensure that uniaxial stresses were generated in the specimen. In this test, the displacement control at the rate of 0.6 mm / min was applied to the steel rod and the tensile load delivered to the sample to get the accurate readings of the stress-strain curve.

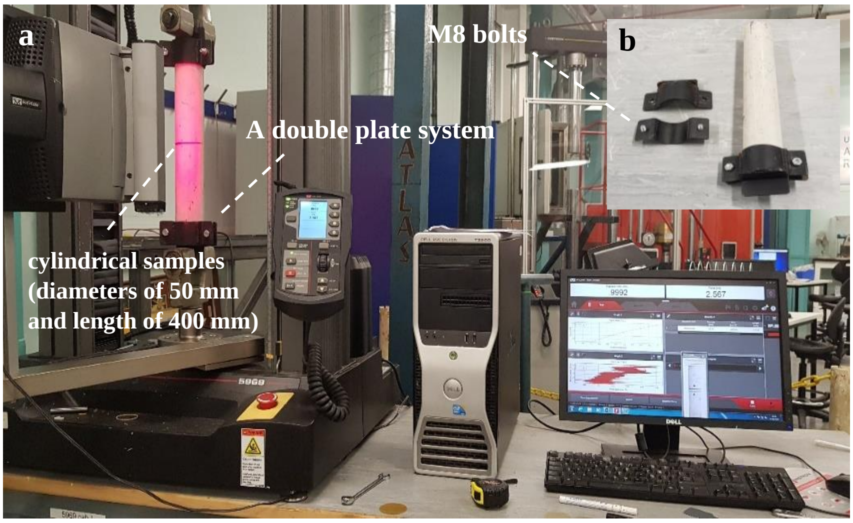

Figure 3.10: a). A general view of the experimental setup for conducting tensile test on the cement mortars using Instron 5969®. b). A double plate system.

3.9.2 Flexural test

Flexural tests were also used to determine the tensile strength of concrete. In this test, notched and unnotched prism specimens were tested under three or four-point bending, and detailed guidances are provided in several standards, i.e. ASTM C 293-94 (ASTM, 1994), BS EN 12390-5 (BSI, 2009) and BS EN 14651 (BSI, 2008). This method of testing is based on simple beam-bending theory and linear elastic stress-strain behaviour up to failure. However, concrete was a non-linear material, and the assumption of a linear stress distribution is not valid. Therefore, the results obtained from this method were always greater than the direct tensile strength. In this PhD thesis, three-point bending beam method was employed to measure the fracture parameters.

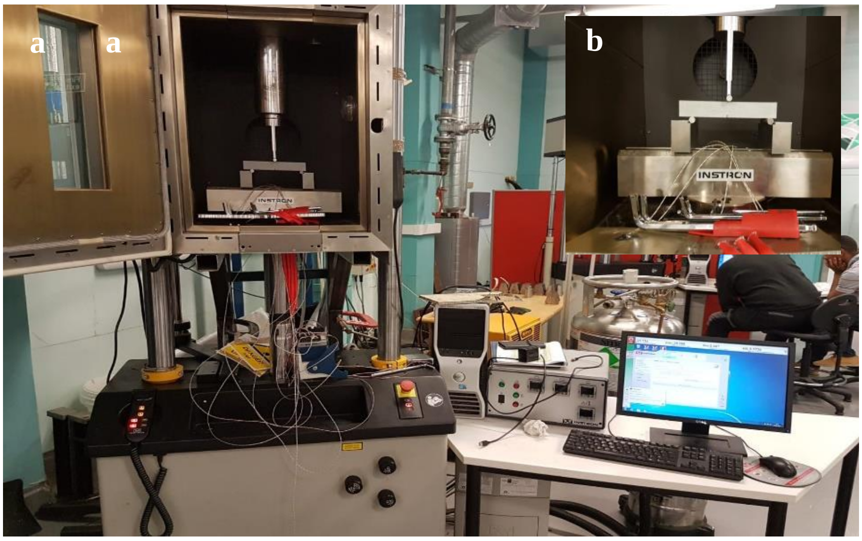

Figure 3.11: a). A general view of the experimental setup for conducting flexural test on the cement mortars using Instron 5969®. b). Three-point bending test setup of a notched concrete beam.

The test was conducted according to the guideline of BS EN 12390-5 (BSI, 2009) Annex A. A series of notched beam specimens with size 100 mm × 25 mm × 25 mm were prepared to determine the fracture properties. The beam specimen was notched from the mid-span of the lower surface to produce a pre-cutting crack, with a depth of 3 mm. Figures 3.11(a) and (b) show the test setup and frames. As shown in Figure 3.11(b), one of the supports was designed to be free to rotate about any axis to minimize the torsional effects on the tested beams. Crack mouth opening displacement (CMOD) and crack tip opening displacement (CTOD) of the notched beam specimens of the composites were measured by clamp type extended instruments. Further discussion regarding the direct tension and flexure tests is to be discussed in Chapter 7.

3.9.3 Compression testing method

The most common test on hardened concrete is the compressive strength test. Many recognised standards, i.e. BS 1881-121 (BSI, 1983) and ASTM C469-94 (ASTM, 1994), have provided detailed guidances for the measurement of the compressive strength and modulus of elasticity for normal strength concrete using cylinder and cube specimens. This study has followed the test configurations described in BS EN12390-3 (BSI, 2009) for the determination of compressive stress-strain relationships and modulus of elasticity. The concrete specimens used in the compression test had the sizes of 100 mm × 100 mm × 100 mm. A general view of the experimental setup for conducting compressive testing is illustrated in Figure 3.12.

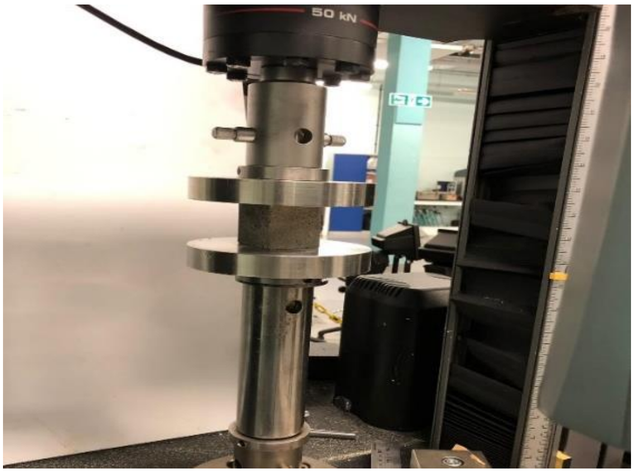

Figure 3.12: Illustration of the experimental setup for conducting compressive testing.

3.9.4 Fracture test

This test method covers the determination of the fracture energy (Gf) of the composites using the disk-shaped compact tension geometry, as outlined in Figure 3.13. The specimen geometry and terminology (disk-shaped compact tension, DC(T)) is modelled after Test Method E399 for Plane-Strain Fracture Toughness of Metallic Materials. The disk-shaped compact tension geometry is a circular specimen with a single edge notch loaded in tension. The fracture energy can be utilized as a parameter to describe the fracture resistance. The fracture energy parameter is particularly useful in the evaluation of mixtures with ductile binders, such as concrete, and has been shown to discriminate between these materials more broadly than the indirect tensile strength parameter. The test method was developed initially for determining the fracture resistance of asphalt-aggregate mixtures. The fracture resistance can help differentiate mixtures whose service life might be compromised by cracking such as concrete. The test method is generally valid for specimens that are tested at temperatures of 10°C (50°F) or below. The specimen geometry was designed to have a diameter of 130 mm and a thickness of 50 mm, as illustrated in Figure 3.13.

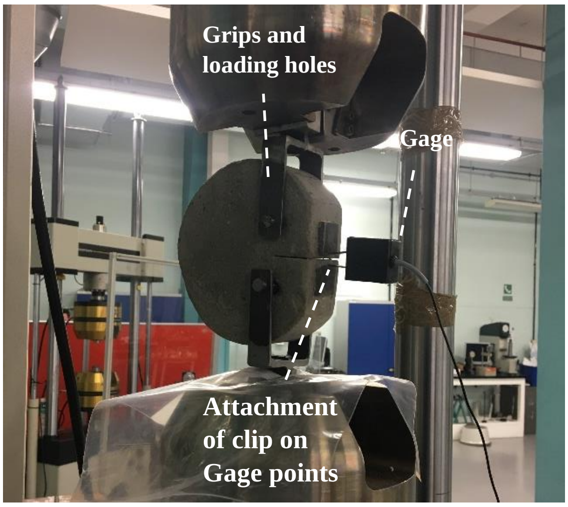

Figure 3.13: Example of the clip-on gage and attachment procedure

3.9.5 Design of moulds using 3D printer

The specimens used to obtain the tensile strength of samples were moulded based on BS EN12390-1 (BSI, 2012). However, in some instances these samples were modified, or new samples were designed to accurately capture the relevant behaviours of the samples. For instance in the case of direct tensile test as the concrete specimens were quite detailed (dog-bone shaped), Ultimaker 2+ plus 3D printer were used in order to print the moulds. Initially the moulds were designed using commercial CAD software Rhino 3D® as shown in Figure 3.14.

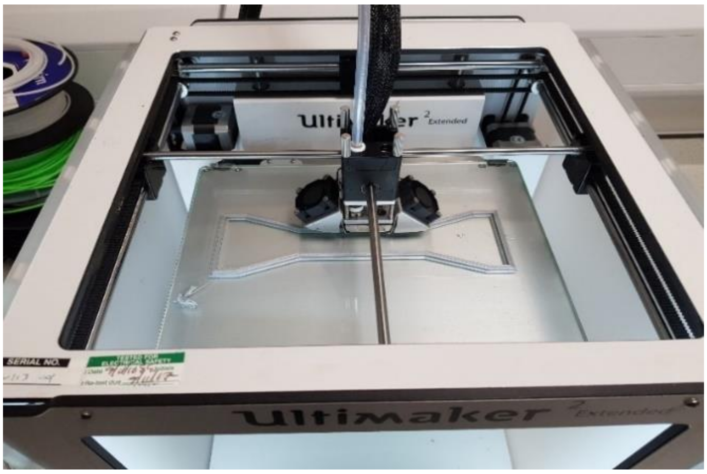

Figure 3.14: Designing and printing the dog-bone shape moulds using Ultimaker 2+ plus 3d for the direct tension test.

3.9.6 Numerical analysis

In this research, manually random sizes of particles were considered to simulate 2D section distribution of NT in the ABAQUS CAE Environment. Figure 3.15(a) shows the geometry of the manual generation of RVE square and the whole model of specimen. Firstly, according to particle volume fractions, the average radius of particles has been assumed and secondly, positions of particles have been posed in ABAQUS sketch. There are some restrictions on particle generation to avoid overlapping: 1. the minimum distance of particle centres is the maximum particle diameter; 2. the minimum distance between the particle centre and specimen boundaries is the maximum particle radius.

The extended finite element method (XFEM, Abaqus 2020 Analysis) is a precise method for fracture and discontinuous problems in mechanics whereby cracks and its growth can be modelled by finite elements. In Figure 3.15(b) the crack tip and the evolution of growth and foreign particles of typical NT cement composite are observable. In this simulation, by extracting properties of the material with different percentages of particles from RVE square and utilizing of it in simulation, we can obtain the behaviour of nano-cement composite. Further discussion regarding the fracture test is to be discussed in Chapter 7.

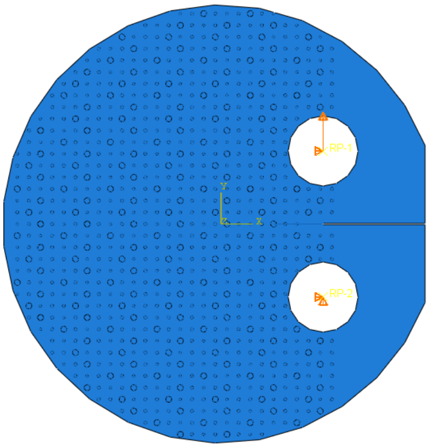

Figure 3.15(a): Schematic of the ABAQUS modelling with boundary conditions and foreign particles

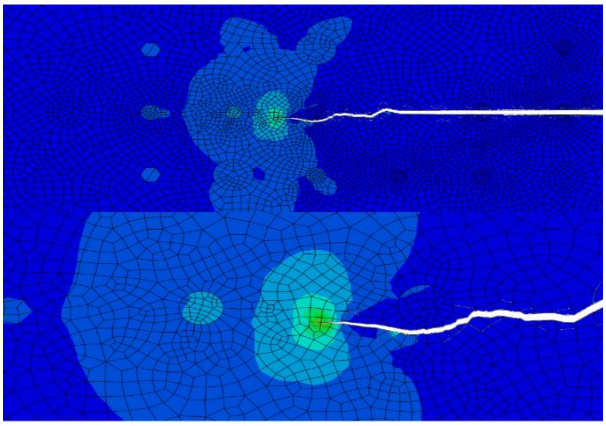

Figure 3.15(b): Initiation and growth of the crack in two views with foreign particles

3.10 Remarks

In this study, a combination of analysing and imaging techniques has been described, such as X-ray computed tomography (XCT), Brunauer-Emmett-Teller (BET), scanning electron microscopy (SEM), X-ray diffraction (XRD), thermogravimetric/derivative thermogravimetric analysis (TG/DTG), and energy-dispersive X-ray spectroscopy (EDAX®) to characterise the microstructure of different cement composites. Furthermore, a novel direct and flexural tensile test has been introduced to quantify and characterise the mechanical properties of the composites. To achieve these aims, the objectives can be summarized as:

1. To apply computed X-ray tomography to provide 3D information of mesoscale pore structures of cement composites.
2. To apply the characterization techniques to determine the nanoscale surface areas, nano pore volume and shapes of the cement composites by Brunauer-Emmett-Teller (BET) and Barrett-Joyner-Halenda (BJH) analyses.
3. To use high-pressure core holder to determine the permeability of the composites.
4. To apply electron microscopy and elemental analysis to obtain information about the different solid phases within the cement mixtures.
5. To use powder X-ray diffraction to explore crystal structure and composition of samples, which allows identification of crystalline phases.
6. To apply the characterization techniques to determine the phase compositions and quantification of the formed hydrates using thermogravimetric/derivative thermogravimetric analysis (TG/DTG).
7. To use direct and flexural tensile tests to quantify and characterise the mechanical properties of the composites.
8. To apply nonlinear finite element analysis of three-dimensional circular specimen using ABAQUS.

Chapter 4

Multiscale Pore Structure Analysis of Nano Titanium Dioxide Cement Composites

4.1 Introduction

The objective of this chapter is to describe and determine the physico-chemical properties of different nano-titanium additives, and to contribute to the understanding of the influences of their main characteristics on the concrete properties. This chapter attempts to determine the pore system of NT cement composites across length scales with different NT dosages. X-ray computed tomography (XCT) was used to analyse the mesoscale pore structures of NT cements with NT percentages of 0 wt%, 2.5 wt%, 3.5 wt%, 5 wt% and 10 wt%.

3D pore structures of the NT mortars were obtained and evaluated. In addition, the scanning electron microscopy (SEM) was used to compare the morphologies of the samples with different NT inclusions. Meanwhile, elementary analysis was performed using an energy-dispersive X-ray spectroscopy (EDAX$^{®}$). Moreover, the nanoscale surface areas and the nano pore volume and shapes of the NT cement samples were obtained by Brunauer-Emmett-Teller (BET) and Barrett-Joyner-Halenda (BJH) analyses. Furthermore, the permeability of the NT cement was measured using a high-pressure core holder with a sensitive and automated measurement capability.

The obtained results from XCT showed that microscale pores (from 20μm to 200μm) of the mortars mixed with 2.5 wt% NT were significantly refined and became smaller in size. When the contents of NT were more than 2.5 wt%, the total pore volume and the number of pores began to increase. However, when the amount of NT exceeded the optimal value, e.g., (2.5 < NT < 5%), the recorded 2D porosity (void area fraction), were still lower than the reference sample. Meanwhile, the SEM results proved that, by adding 2.5 wt% NT, the pores of cement composites were best filled, resulting in a more homogenous morphology.

At the nanoscale, the BET results revealed a clear trend of increasing surface area and pore volume of the NT cement composites, over the entire range of NT percentages, i.e., from 0 wt% to 10 wt%. This could stem from the formation of nanosized needle-shaped products in the presence of the nanoparticles. The nanoparticles would alter the chemistry of the hydration process, increasing the formation of the C-S-H gel. Further, the permeability of NT cement composites was measured using a high-pressure core holder and the results showed that 2.5 wt% NT inclusions could reduce the permeability of the cement mortars by 32%. However, adding more NT (>2.5 wt%) led to higher permeability. This is in line with the microscale pore analysis from XCT. It can be concluded that adding a certain amount of NT (around 2.5 wt%) can modify the pore structure of cement mortars by changing the harmful microscale pores (permeability related) to the nano-sized benign pores, leading to a much stronger durability of cement-based materials.

4.2 Experimental Program

4.2.1 Materials

Different percentages of OPC (Provided by Jewson, which complies with BS EN197-1 (BSI, 2000), with a Grade of 42.5 N/mm^2), were replaced with different amounts of NT, *viz*., (0 wt%, 2.5 wt%, 3.5 wt%, 5 wt% and 10 wt%). Other researchers have also used large NT dosages in their studies (Chen et al., 2012; Lucas et al., 2013; Meng et al., 2012). Lower dosages of NT in the cementitious materials may be insufficient to ensure self-cleaning and air purification over longer periods. Therefore, higher percentages of NT were chosen in this study. Natural river sand, with a minimum particle size of 200 µm served as the fine aggregate. The mineralogical phases and chemical composition of the raw materials used were obtained from the X-ray diffraction (XRD) and X-ray fluorescence (XRF) analyses. The NT particles used in this research were obtained from ALDRICH and had specific surface areas of 35-65 m^2/g. A summary of the physical properties of the sand and cement is given in Table 4.1. Deionised water, with a pH value of 7.5 at 22°C, was used throughout the experimental research. In Figure 4.1, the PSDs of sand and cement used in this chapter are presented considering the sieve sizes (ISO sieves) presented in Chapter 2 (Table 2.1).

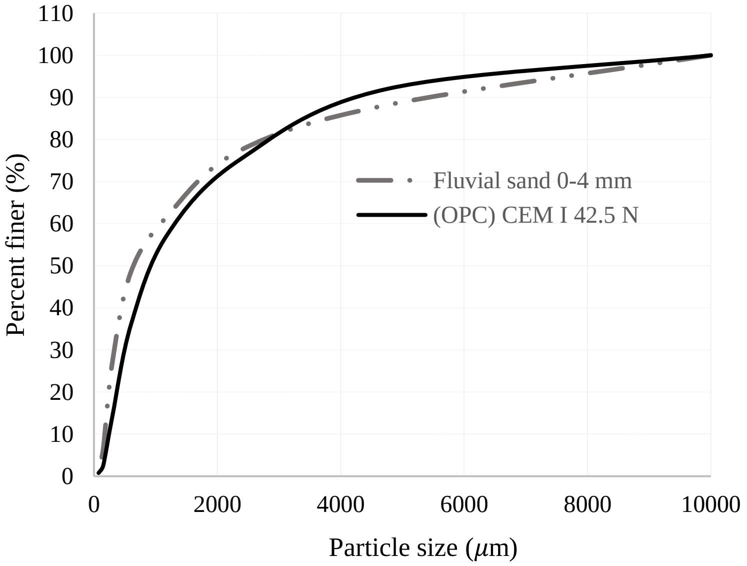

Figure 4.1: Grading curves of the cement and sand determined by sieve analyses.

Table 4.1: Physical properties of the materials used

Properties	Fluvial sand	CEM I 42.5 N
Size	200 µm–4 mm	0.2 µm–200 µm
Specific density (g/cm^3)^2	2.56	3.112
D_{min}(mm, µm)	200 µm	0.23µm
D_{max}(mm, µm)	4.3 mm	160 µm
Shape factor (ξ)^1 (-)	1.10	1.73
Specific surface area (m^2/m^3)	17,568 (BET)	992,145(BET)

1). Referential values taken from ALDRICH
2). Provided by Jewson in Scotland.

4.2.2 Mixing Procedure

The experimental study involved the application of a pan mixer with a 50 kg capacity. The fine aggregate was first poured into the pan-mixer, followed by the OPC CEM I 42.5N, under dry conditions. They were mixed for 45 seconds to ensure homogeneity. The mixing continued for another 2.5 minutes before water, already mixed with nano titanium dioxide, was added and the mixing was allowed to continue for another 7 minutes. As NT particles tend to agglomerate when mixing with water and conventional agitators cannot break down these hard agglomerates, a Silverson high shear mixer was employed to de-agglomerate these particles and return them to the desired particle size. Uniformly distributed nanoparticles play the adhesive role that firmly bonds hydration products and transition zones together and set up a new network in which the nanoparticles are nodes, based on the original network structure of hardened mortars, bonding more nanoscale C-S-H gel and forming a three-dimensional network structure. The recorded mix design code for each sample is presented in Table 4.2.

Slump and slump flow tests were then carried out according to BS EN 12350-2 (BSI, 2009a) and BS EN 12350-5 (BSI, 2009c), respectively. The mix proportion design resulted in a slump ranging from 120 to 240 mm and a slump flow ranging from 180 to 207 mm. Moreover, the vebe time ranged from 9 and 16 seconds which met the required workability based on BS EN 12350-2 (BSI, 2009a). The mix had a constant water/equivalent cement ratio of 0.55.

Table 4.2: Mix proportions of the test specimens

Code number	Cement (kg/m^3)	Water-to-cement ratio	Cement replacement (wt%) NT	Mix proportion (kg/m^3)		Slump	Slump-flow
				Fine aggregate	Water	(mm)	(mm)
ACM	227.3	0.55	0	681.9	125.01	150 ± 1	182 ± 1
AM2.5	221.6	0.55	2.5	681.9	125.01	150 ± 2	180 ± 1
AM3.5	219.3	0.55	3.5	681.9	125.01	170 ± 4	202 ± 1
AM5	215.9	0.55	5	681.9	125.01	190 ± 3	203 ± 1
AM10	204.5	0.55	10	681.9	125.01	230 ± 2	207 ± 1

4.2.3 Specimen preparation

After ascertaining that the mixture met the required workability and cohesion for the specified design mix, moulds for cement mortars with the diameter of 25 mm and the length of 75 mm were designed using commercial CAD software Rhino 3D® and then printed by Ultimaker® 2+ 3D printer. The moulds were then treated with oil to enable later separation from the mortar, which was poured into the mould to create the design suitable for X-ray computed tomography system. Following removal from the moulds, they were covered with polythene sheets and allowed to harden for 36 hours. The specimens were then stored in a water bath at 20 ± 3 °C and 95% relative humidity until the required curing age of 28 days before testing.

In the present research, in order to perform the BET analysis, the samples were dried in the oven at 65°C for 24 hours and then ground to fine powder and passed through a 200 µm sieve. For SEM test, circular samples with a diameter of 12 mm and a thickness of 3 mm were made using a diamond saw and cured for 28 days. The circular samples were dried in a vacuum oven at 45°C until a constant weight was reached.

Samples were then coated with a thin carbon layer to reduce the charging effect on the surface of the samples. This was done by placing the sample in a vacuum chamber below two carbon tips that were brought together to make an electrical connection. A current was passed through the carbon tips to heat them until they glowed red/white. This caused carbon molecules to be emitted and coated the surface of the sample. Images were taken at a range of magnifications, from between 100x magnification to 2600x magnification. The working distance was set to be between 7-10 mm. For permeability test, cement mortar cylinders, with the diameter of 100 mm and the length of 150 mm were cast and vibrated on a table vibrator. The specimens were then demoulded and left to cure for 24 hours and then submerged in water for curing until the time of testing.

Circular sections with the diameter of 35 mm and the thickness of 70 mm were extracted from the samples using a diamond saw. Each sample was prepared by a process of vacuum saturation in which the specimen was placed under vacuum for 4 hours and then submerged in the de-aerated water while it was still under vacuum.

The vacuum was maintained for additional 6 hours and then released. The specimen was then left under water for 10 hours prior to insertion into a permeability cell. An essential requirement of permeability testing is that the pore space must be fully saturated by the permeating fluid. In practice, this implies that for a water-based permeability testing, all air within the communicating pores must be removed and replaced with water.

4.3 Testing Procedure

4.3.1 2D and 3D porosity analysis

The method of porosity analysis from CT data was demonstrated on a simple sample with cylindrical geometry which minimized image artefacts and allowed fast scan times to be possible. The segmentation procedure was followed by 2D or 3D analysis of void area or volume fraction (average porosity) as well as porosity versus distance and volumetric porosity. Scans of 20.0 μm resolution were achieved at an operating voltage of 145 kV and a current of 100 μA, and with 3141 projections recorded during one full rotation of the sample.

The 3141 2D projections were reconstructed into a 3D volume with CT PRO 3-D (Nikon Metrology) as illustrated in Figure 4.2. The data was smoothed using a median filter before any analysis, which removed noise.

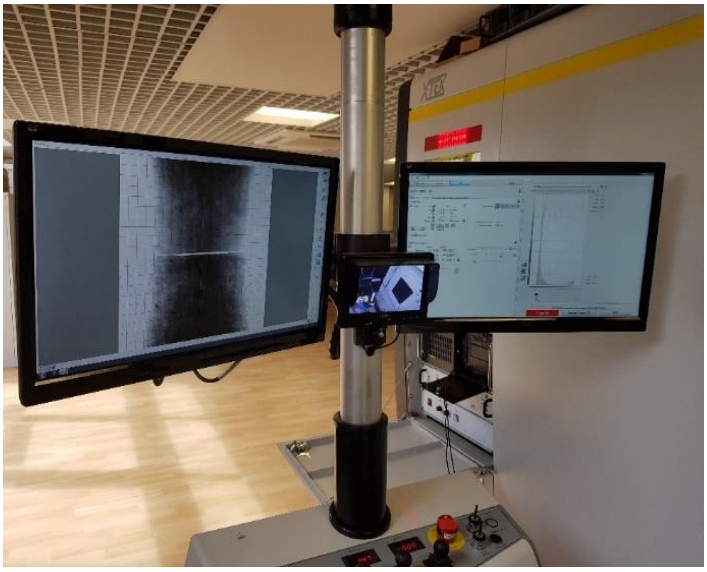

Figure 4.2: X-ray CT scans with Nikon XT H 225/320 LC in the Advanced Materials Research Laboratory (AMRL), the University of Strathclyde CT scanner facility.

Quantitative analysis was carried out using the image analysis software ImageJ and the results were visualised in 3D with ParaView. Low density air filled voids were distinguished from the higher density cement matrix by their relative difference in X-ray attenuation, and then binary segmentation was applied (via a global threshold) so that the volumes of each phase, and hence the porosity, could be calculated. The procedure for calculating the porosity involved selecting the object using an adaptive square around the object, and then removing all air from the 3D data set to calculate the average void fraction using the volume analysis tool.

To increase efficiency in data acquisition, two samples were analysed at the same time which also helped to have more accurate analysis by selecting the same setting for both samples. The experiment setup for micro-XCT analysis and the final 3D visualization of porosity is presented in Figure 4.3.

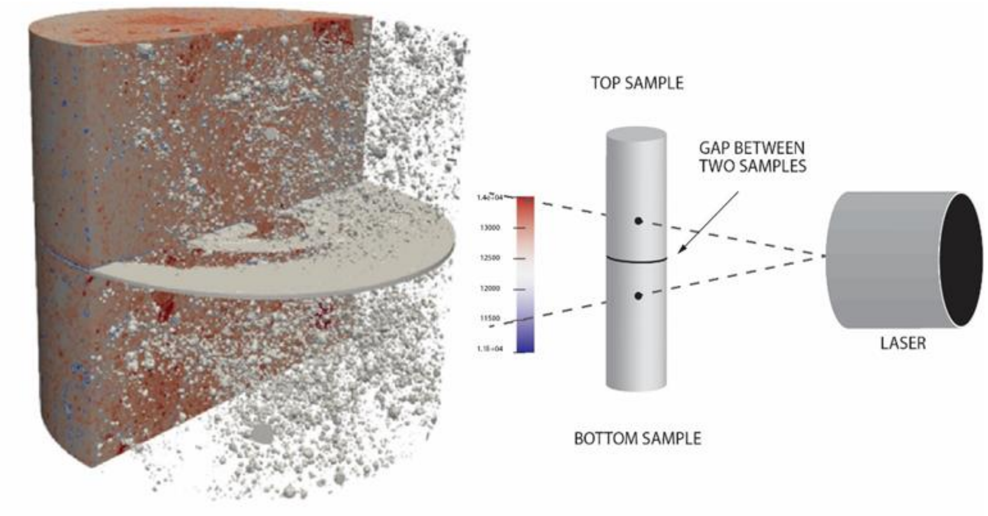

Figure 4.3: Experiment setup for micro-XCT analysis and the final 3D visualization of porosity.

4.3.2 Permeability measurement using high pressure core holder

A general view of the experimental setup for conducting water-permeability measurement using a high-pressure Hassler type core holder is presented in Figure 4.4. Cement mortar samples containing different dosages of NT, i.e. 0 wt%, 2.5 wt%, 3.5 wt%, 5 wt% and 10 wt%, in cylindrical geometry with a diameter of 35 mm and a length of 70 mm were extracted from the samples using a diamond saw. The vacuum saturated core sample was mounted in the core holder and then placed under a confining pressure of 3 MPa to ensure minimal bypass of the injected fluid around the sample.

The water then flowed through the sample under a constant pressure gradient of 2 MPa until steady-state flow was reached. The flow rate and the pressure drop were then recorded. A general view of the data and constants for conducting water-permeability measurement of the composites, sandstone, and steel, is presented in Table 4.3. In order to improve the analysis of the data, the results of permeability measurement of the cement mortars were compared with the results of a low permeability sandstone core and a steel cylinder with zero permeability, each with the same dimensions as the cement mortars. Permeability measurement was performed under steady-state conditions.

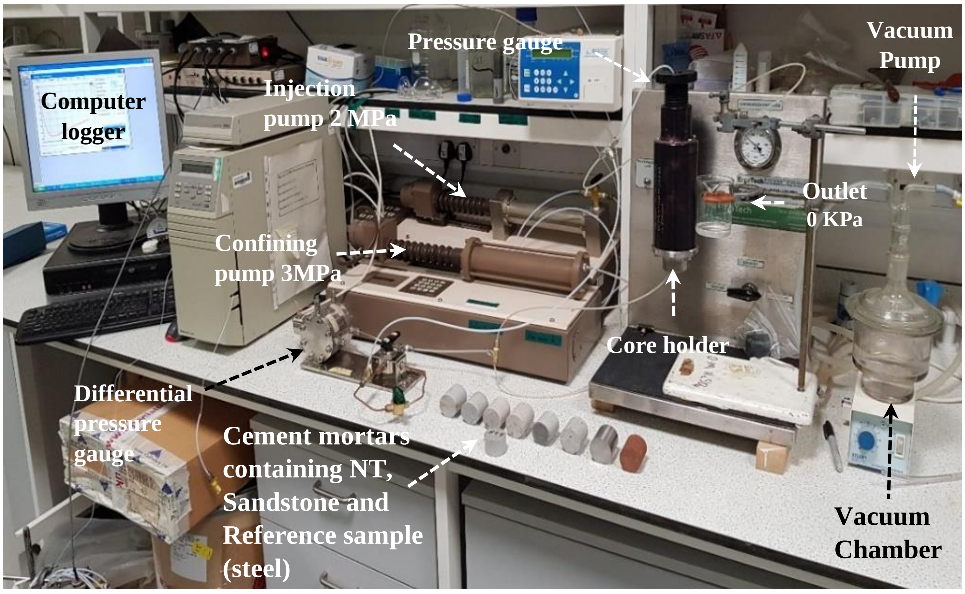

Figure 4.4: A general view of the experimental setup for conducting the water permeability measurement of the cement mortars using high pressure core holder.

Table 4.3: Experiment data and constants used for water-permeability measurement of samples containing different dosages of NT, sandstone, and steel.

Data and constants	Parameters
Sample area (m^2)	0.00385
length [m]	0.07
Injection Pressure offset [MPa]	2
Dynamic viscosity [Pa.s]	0.0009532
Density [kg/m^3]	998.2
Kinematic viscosity [m^2/s]	1.0034E-06
kPa conversion factor	9788.3492
m^2 to Darcy conversion	1.01E+12

The test was repeated at different sets of flow rate and inlet pressure and the data were recorded. Controlling the temperature of the environment surrounding the permeability set-up would contribute to pressure stability, so the test temperature was maintained at 22 ± 2.0 °C. A constant pressure was applied to the inlet of the sample and the pressure drop from inlet to outlet was recorded with a differential pressure transducer. The cumulative volume injected to maintain this constant pressure was recorded at ten second intervals, accurate to ± 0.5 mm^3, and was used to calculate the flow rate. Permeability was calculated by rearranging Darcy's law:

$$Q = -\frac{kA(p_b - p_a)}{\mu L} \tag{4.1}$$

where A is the cross-sectional area of the sample (m^2), Q is the flow rate ($\frac{m^3}{s}$), k is the permeability of the medium (m^2), μ is dynamic viscosity of the fluid, L is the sample length and $(p_b - p_a)$ is the measured pressure drop. The transient tests were conducted for 18 hours, but only the first 2100 seconds of data were used to determine the permeability of the samples. An initial injecting pressure of 2 MPa was adopted and ordinary tap water at room temperature was used as the permeating fluid.

4.3.3 Microstructural analysis using SEM and EDS

SEM analysis was carried out in the secondary electron mode using the field emission scanning electron microscope (FE-SEM). A HITACHI SU-6600, operated with an acceleration voltage of 20 keV, was used. Furthermore, elementary analysis was performed using energy-dispersive X-ray spectroscopy (EDS) with EDS measurements arranged in rectangular grids of 10 × 20 points (vertical and horizontal distances of 5 mm).

4.3.4 Measurement of Nano surface area, Pore size and Pore volume using BET

The specific surface area and pore volume of the composite powders were determined by physical adsorption of a gas on the surface of the solid and by calculating the amount of adsorbate gas corresponding to a monomolecular layer on the surface. Physical adsorption results from relatively weak forces (van der Waals forces) between the adsorbate gas molecules and the adsorbent surface area of the test powder. The determination is usually carried out at the boiling temperature of liquid nitrogen (77 K). The amount of gas adsorbed can be measured by a volumetric or continuous flow method. The surface areas and the pore size diameter were calculated by the Brunauer-Emmett-Teller (BET) and Barrett-Joyner-Halenda (BJH) procedures, respectively, from data obtained using a micromeritics ASAP2020 surface area and porosimetry system. The whole analysis was performed in the range between 0.05 and 0.25 p/p^{o}, where p^{o} is the nitrogen condensation pressure and *p* the pressure used by the equipment in the respective analysis period. A Micromeretics ASAP2020 equipment, using N2 and an evacuation time of 14 h at 130 °C, was used for the gas physisorption analysis.

4.4 RESULTS AND DISCUSSIONS

4.4.1 2D and 3D Porosity obtained from X-ray CT

Figure 4.5 shows the CT images for the sample AM10 (containing 10 wt% NT), located at the bottom of the image, and the sample AM2.5 (containing 2.5 wt% NT) at the top. These two samples (percentages) demonstrated the highest porosity (AM10) and lowest porosity (AM2.5) amongst all specimens tested. For AM2.5, the carbonation of both CH and C-S-H as a result of reactions with CO_2 caused an increase in the volume of products relative to the volume of substrates (see Chapters 5 and 6), which resulted not only in lowering total porosity, but primarily in a change in porosity distribution (Table 6.7). Carbonation caused a significant reduction in the proportion of larger capillary pores (>100 nm) as illustrated in Section 4.4.4.

The 3D volumetric void fraction and 2D area void fraction for sample AM10 and AM2.5 were (7.06%, 7.83%) and (2.42%, 3.26%) respectively. The slightly different volumetric values could be explained by different sub volumes (top and bottom edges were cropped to eliminate the edge artefacts) and other possible causes of the differences could arise from the material segmentation from the background. The recorded average 3D volumetric void fractions and average 2D area void fractions for mortars (three samples of each mix) with different doses of NT at the 28-day curing age are presented in Table 4.4. A refinement of the structure can also be noticed by comparing 3D visualization of the porosities of the samples ACM (bottom) and AM2.5 (top) (as illustrated in Figure 4.6). This could be due to the fact that the NT could provide nucleation sites, which accelerated the precipitation of hydration products, made C-S-

H disperse better, and limited the growth of CH, thus improving the density and homogeneity of cement matrix (Lee and Kurtis, 2010).

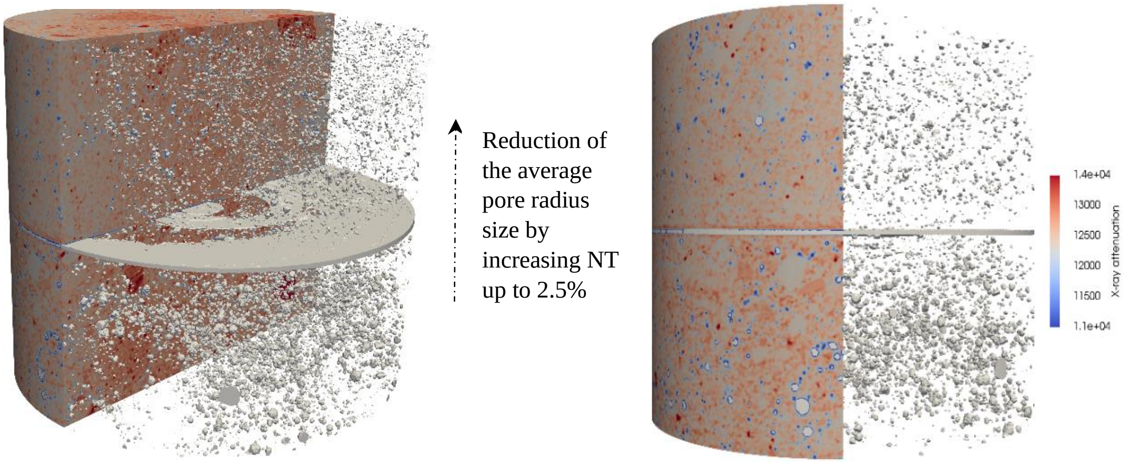

Figure 4.5: 3D visualization porosities of the samples AM10 (bottom) and AM2.5 (top).

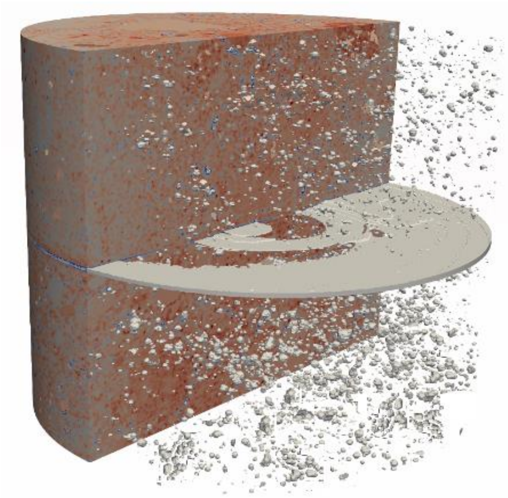

Figure 4.6: 3D visualization of the porosities of the samples ACM (bottom) and AM2.5 (top).

The improvement of the meso-structure of the cement mortars can be clearly noticed. Figure 4.7 presents a comparison of the 2D images for the maximum porosity cross section from the samples AM2.5 and AM10 respectively. These two samples had the least porosity and the largest porosity; to pick up the cross-section images which had the largest porosity from both samples as pointed out in Figure 4.7(b) show remarkably interesting findings.

Table 4.4: Void fractions of the mortars with different dosages of NT at 28 days curing.

Code number of Cement Mortars	Cement replacement (wt%) Nano - TiO_2	3D Volumetric void fractions (%). Sample 1, 2 and 3			Average 3D volumetric void fractions (%)	2D area void fractions (%). Sample 1, 2 and 3			Average 2D area void fractions (%)
		No: 1	No: 2	No: 3		No: 1	No: 2	No: 3	
ACM	0	6.32	6.81	6.88	6.67	7.22	8.11	8.10	7.81
AM2.5	2.5	2.54	2.24	2.48	2.42	2.93	3.33	3.52	3.26
AM3.5	3.5	3.12	2.86	2.96	2.98	3.34	3.91	3.73	3.66
AM5	5	5.73	5.91	5.97	5.87	6.12	5.93	5.80	5.95
AM10	10	6.94	7.13	7.11	7.06	7.33	8.11	8.05	7.83

As shown in Figure 4.7(c), NT particles tended to agglomerate when the optimal value was exceeded, causing internal defects to form in mortars, which would certainly influence the overall voids and the total porosity. Simultaneously, excess NT (*i.e.*, NT ≥5 wt%), is difficult to spread evenly and some internal defects would likely form in NT cement mortars (as illustrated in Figure 4.7(c)). For AM2.5 as shown in Figure 4.7(a), the NT is very much more uniformly distributed, and the pores (in black) were considerably smaller in size and less in number than those in Figure 4.7(c). The difference can be quantitatively calculated from Table 4.4, *i.e.*, the 3D volumetric void fraction of AM10 is about 3 times that of AM2.5. Moreover, the relationships between 3D volumetric void fractions, 2D area void fractions and NT content for the 28-day curing age are presented in Figure 4.8.

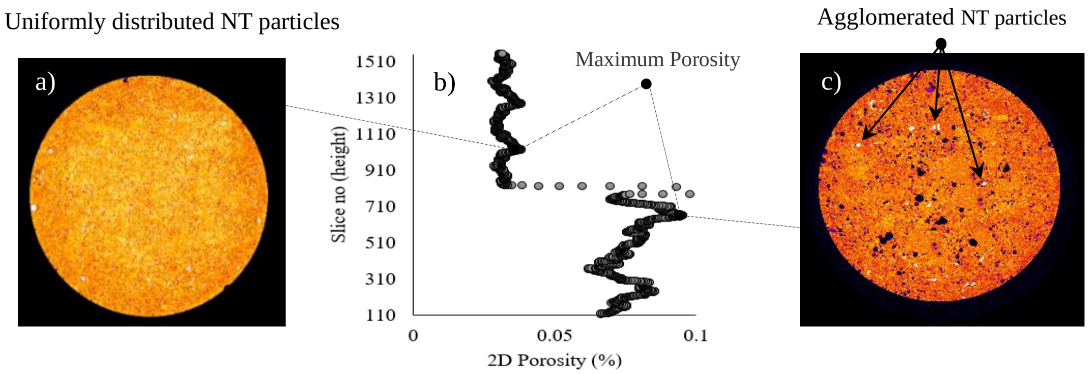

Figure 4.7: a) 2D analysis of porosity of sample AM2.5 (Slice number 1035), b) 2D porosity (void area %) from top to bottom of samples AM10 (bottom) and AM2.5 (top), c) 2D analysis of porosity of sample AM10 (slice number 645).

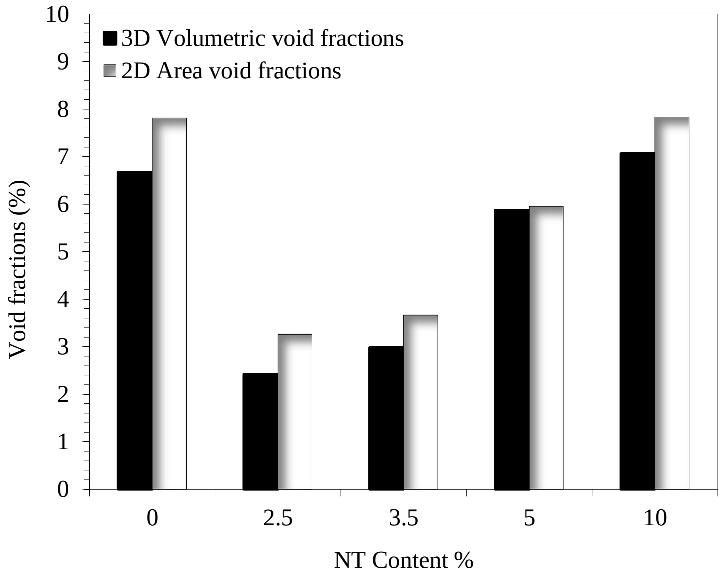

Figure 4.8: Relationships between 3D volumetric void fractions, 2D area void fractions and NT content at the 28-day curing age.

2D analysis of the slices from top to bottom through the sample was performed in order to calculate the actual porosity variation within the sample. XCT scanning porosity profiles of the samples with highest porosity (AM10 at bottom) and lowest porosity (AM2.5 at top) and their corresponding average x-ray attenuation (density) are presented in Figures 4.9 and 4.10. The study has shown that the range 2.5 wt% to 3.5 wt% of NT is the optimal amount for improving the microstructure of the cement mortar (the total average porosity reduced by 60.97 % and 54.22% respectively). When the content of NT was more than 3.5 wt%, the total pore volume and the number of pores began to increase.

This could be due to the fact that the crystallization process of hydration products could be controlled in an appropriate state by restraining the growth of CH crystal when the dosage of nanomaterials and the distance between particles were moderate. When the amount of NT exceeded the optimal value (*i.e.*, NT >2.5 wt%), the recorded 3D volumetric void fractions and 2D area void fractions observed for AM5 (5.87%, 5.95%) were lower than those for the reference sample ACM (6.67%, 7.81 %).

2D XCT scanning porosity profiles of AM2.5 at (bottom) and AM3.5 at (top) and their corresponding average x-ray attenuation (density) are presented in Figures 4.11 and 4.12. The recorded 3D volumetric void fractions indicated that sample AM2.5 contained 3,931 pores with a volume fraction of 2.42% (the lowest volume voids among the samples). Specimens AM5 and AM10 had 6,212 and 6,965 pores with pore volume fractions increasing to 5.87% and 7.06%, respectively (the largest volumes of voids among all samples).

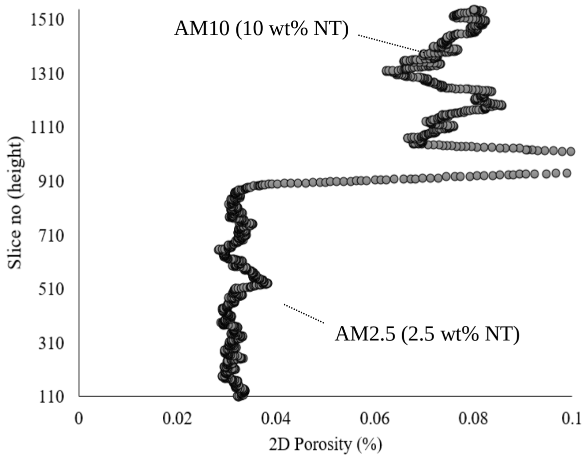

Figure 4.9: 2D porosity (void area %) from top to bottom of the samples AM2.5 (bottom) and AM10 (top).

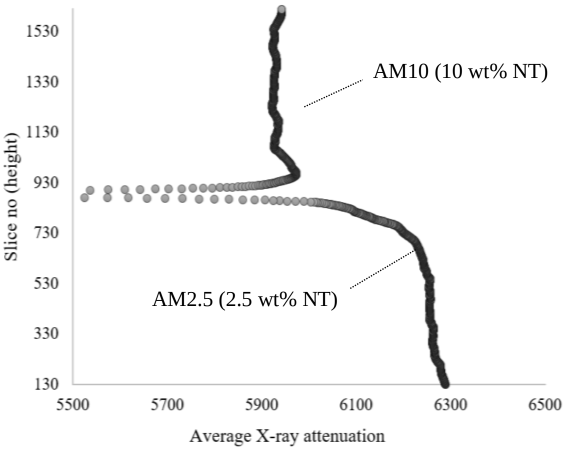

Figure 4.10: Average x-ray attenuation of the samples AM2.5 (bottom) and AM10 (top).

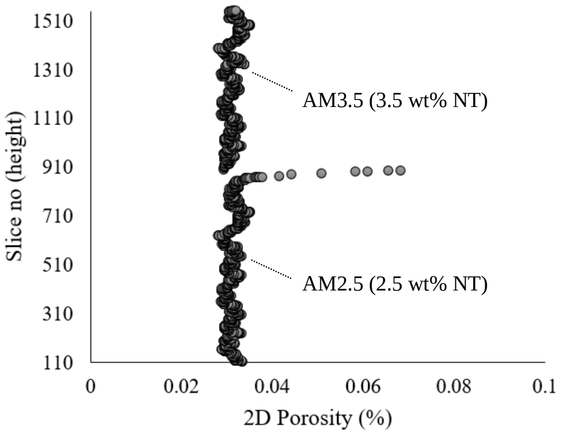

Figure 4.11: 2D porosity (void area %) from top to bottom of the samples AM2.5 (bottom) and AM3.5 (top).

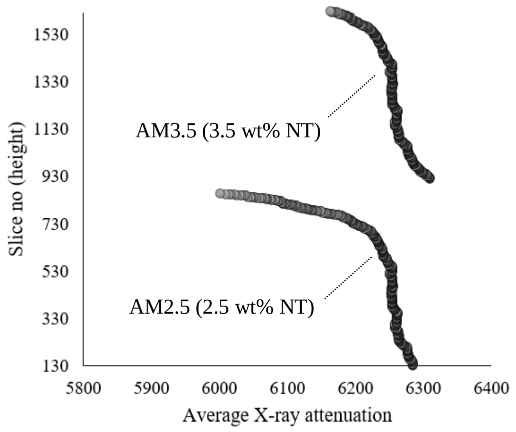

Figure 4.12: Average x-ray attenuation of the samples AM2.5 (bottom) and AM3.5 (top).

Using the volumes calculated for each pore, the pore size distribution (histograms) was plotted. The samples ACM, AM5 and AM10 had similarities in terms of porosity and the number of pores (Figure 4.13). However, this phenomenon was quite different for AM2.5. Specimen with code no AM2.5 (the optimal design) the majority of the pore volume, 43.3%, were contributed by pores ranging in size from 5-50 µm in diameter while for other (larger) pore ranges the percentages were all smaller than the corresponding values. The majority of the pore volume ranging in size from 5-50 µm for the specimens with code no AM10 and AM5, were 46.9% and 47.8% respectively.

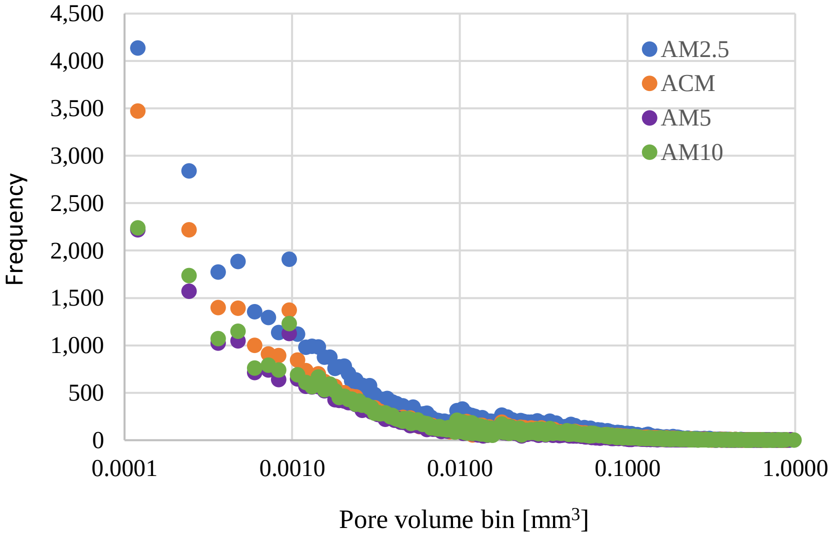

Figure 4.13: Relationships between pore volume and frequency of NT cements.

In order to have more accurate analysis, six sub volumes of 10 mm^3 were extracted (as shown in Figure 4.14) from the outer to the inner part of the samples ACM, AM2.5 AM3.5, AM5 and AM10 and the porosities were measured using an intensity threshold algorithm, and the relative volume percentage was calculated with the volume fraction operator. The results indicate that the average 3D volumetric void fraction of AM2.5 (0.64%) and AM3.5 (0.78%) were the lowest amongst all samples. The results also indicated the increase in porosity from the outer to the inner for sample AM2.5. Such a non-uniform distribution of porosity in the NT cement samples favoured the durability of the composite as surface area of the samples had much lower porosity.

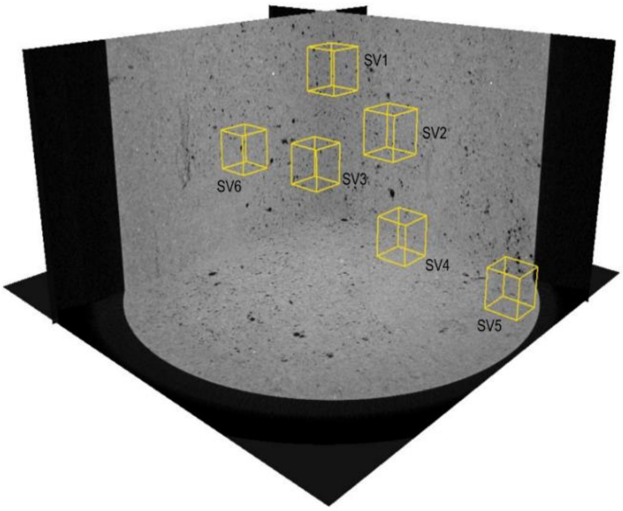

Figure 4.14 : Typical sub volumes analysis of sample AM2.5 showing the Positions of the 6 sub volumes (“Sv1”, “Sv2”, “Sv3”, “Sv4” “Sv5” and “Sv6” used to measure the relative 3D volumetric porosity (yellow squares).

4.4.2 Permeability measurement using high pressure triaxial cell.

The AM2.5 sample has presented the lowest permeability, *i.e.*, 2.59×10^{-16} m^2 amongst all the NT mortar and pure mortar specimens. Comparing with the pure mortar sample, adding 2.5 wt% NT can reduce the permeability by 32.1%. This is a significant improvement in the durability of cement mortars. As the dosage of NT increases, the result shows a clear trend of increasing permeability of the NT cement mortar with NT content, up to 10 wt% (as illustrated in Figure 4.15). I have also tested and benchmarked the permeability of the NT mortar samples against steel and sandstone which are known as two possible extremes of permeability for building materials. Steel should theoretically have a permeability of zero and hence the obtained permeability of $2.82 \times 10^{-20}\ \mathrm{m}^2$ arises from a combination of pressure/volume measurement error, leakage from connections, and bypass of fluid around the sample. This result therefore represents the lower bound of permeability that can be measured with the experimental setup. The sandstone has the highest permeability of $3.50 \times 10^{-15}\ \mathrm{m}^2$ (presented in Table 4.5). It may also be noted that adding NT up to about 5 wt% can reduce the permeability of mortars, and the AM5 and ACM samples had similar permeability values. Higher than 5 wt% dosage of NT will lead to higher permeability of mortars.

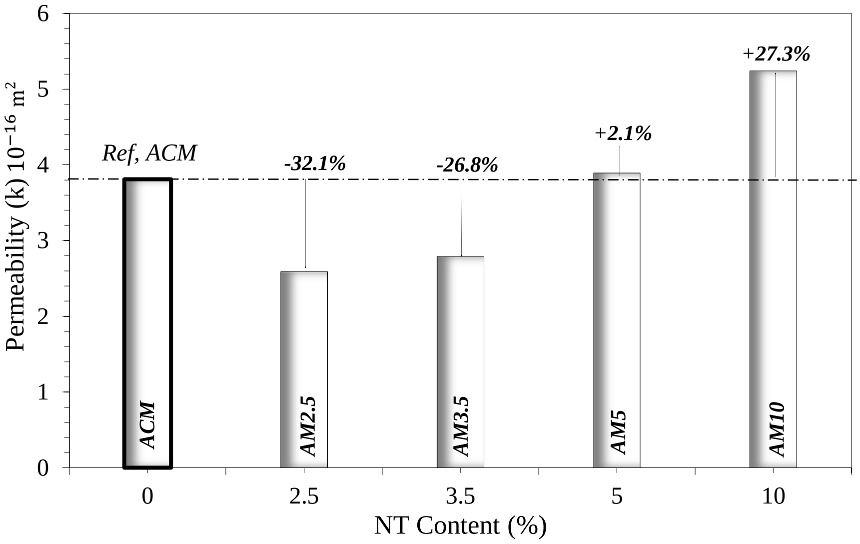

Figure 4.15: Relationships between permeability and NT content in the mortars at 28 days.

This could be caused by the fact that when the amount of NT exceeded the optimal value, (*i.e.*, NT >2.5 wt%), the large specific surface area of the nanoparticles would absorb additional water and make the agglomeration phenomena easily reachable, leading to the formation of undisrupted pockets within the cement paste matrix and resulting in an increase in porosity of mortars. Such a process will certainly influence the permeability. In summary, the resistance to the intrusion of water under pressure in the samples containing NT in the region of 2.5 wt% was improved due to the densification of the microstructure and the high specific surface area of the produced gel.

Table 4.5: Experiment data and results of water-permeability measurement of mortars at 28days.

Types of specimen	Area (m^2) /Length (m)	NT (wt%)	Flow rate = $\frac{\Delta V}{\Delta t}$ (m^3/s)	$(p_b - p_a)$ (kPa)	Permeability (m^2)
Steel (Reference)	0.00385/0.07	0	3.26×10^{-11}	2000.1	2.82×10^{-20}
Sandstone	0.00385/0.07	0	1.74×10^{-8}	86.401	3.50×10^{-15}
ACM	0.00385/0.07	0	1.32×10^{-8}	1424.0	3.81×10^{-16}
AM2.5	0.00385/0.07	2.5	6.45×10^{-10}	1260.4	2.59×10^{-16}
AM3.5	0.00385/0.07	3.5	1.27×10^{-11}	999.50	2.79×10^{-16}
AM5	0.00385/0.07	5	1.21×10^{-10}	1105.8	3.89×10^{-16}
AM10	0.00385/0.07	10	1.40×10^{-8}	1082.8	5.24×10^{-16}

4.4.3 Microstructural morphology

Figures 4.16(a)-4.16(d) show SEM images of the microstructure of the mortars mixed with NT, *i.e*. 0 wt%, 2.5 wt%, 5 wt% and 10 wt%, at 28 days. Clearly different morphologies have been obtained amongst these samples. The reference sample ACM (Figure 4.16(a)) contained a moderate amount of small pores and medium size C-S-H structures. Fewer small needle-like and short columnar crystals were identified and possibly formed of ettringite or other AFt phases. Increasing the NT content up to 2.5 wt% (AM2.5) led to a more homogeneous microstructure compared to the reference mix (ACM). Also, C-S-H gel became larger in size, which indicates a higher degree of hydration. Moreover, the microstructure of AM2.5 contained much smaller air-voids compared to sample ACM (Figure 4.16(b)).

It can be seen from the SEM images that adding NT up to 2.5 wt% resulted in an absence of needle shape structures and produced a homogeneous structure of C-S-H compounds. By comparing with the SEM images of the reference sample in Figure 4.16(a), it is found that some conglobate materials appeared in the NT cement samples. On increasing the NT to 5 wt%, the C-S-H gel remained homogeneous and comparable to the 2.5 wt% NT sample. However, the 5 wt% NT sample now contained larger air-voids compared to the sample AM2.5 (Figure 4.16(c)). Moreover, more agglomerated NT particles were observed. When the added amount of NT reached 10 wt% (AM10), it was still possible to observe some needle-shaped AFt phases in the matrix. However, small size C-S-H gels were formed with larger and more voids produced (Figure 4.16(d)). The microstructure became isolated and defective. Figure 4.17 shows the SEM image and EDS analysis of the cement mortar modified by 2.5 wt% NT. It can be seen from Figure 4.17(a) that the composition of sample AM2.5 mainly consisted of carbon (C), oxygen(O), silicon (Si), calcium (Ca), and Ti. Additionally, with the help of EDS analysis Figures 4.17(a) and (b), a fact that C-S-H was grown on the surface of NT was verified, which shows that NT played a nucleation role in the cement hydration process.

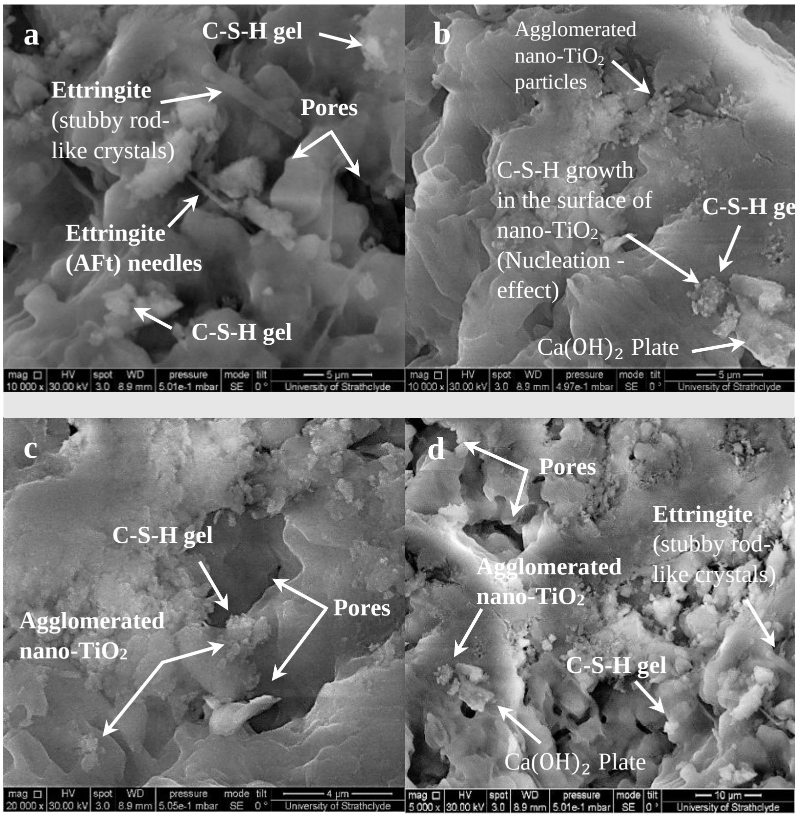

Figure 4.16: Typical SEM image of the specimens with different additions of NT (a) 0%; (b) 2.5%; (c) 5%; (d) 10% at the 28-day curing age.

The EDX analysis indicates that Ca and Si were the main elements of the reference sample (ACM) with relative weight percentages of Ca and Si ratio (Ca: 27.76%, Si: 19.41%, Ca/Si ratio of 1.43). EDS spectra of samples indicate sample AM2.5 had the Ca/Si ratio of 1.18, the lowest among all the samples cured for 28 days. Ca/Si ratios for samples ACM, AM5, AM10 were 1.43, 1.23 and 1.87, respectively. Due to the filler effect of NT substitution and low Ca/Si ratio (Ca: 32.11, Si: 27.21, Ca/Si ratio of 1.18) compared to the other samples a denser cement matrix was formed by adding 2.5 wt% NT. These ratios also indicate the increase in the amount of C–S–H gel formed by adding 2.5 wt% NT.

As to be mentioned in Chapter 5, sample AM2.5 (modified by 2.5 wt% NT) had the highest compressive and tensile strengths compared to the reference sample and other specimens having different NT percentages.

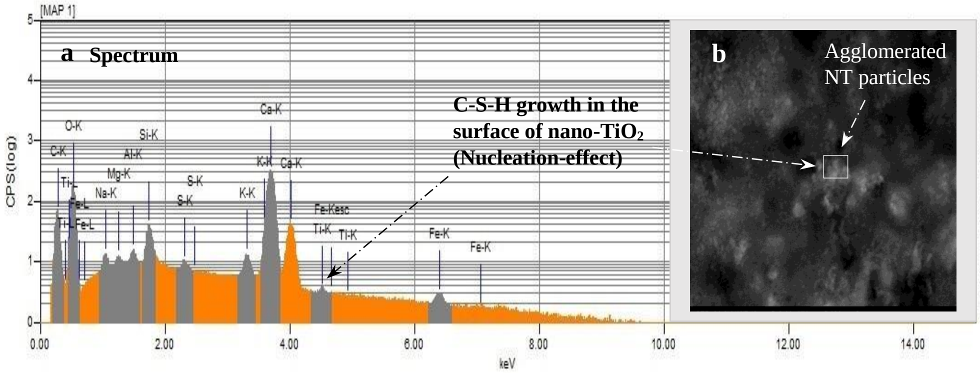

Figure 4.17: (a) Typical EDS analysis and (b) SEM image.

4.4.4 Nanoscale pore system by BET and BJH analyses

The BET data carried out on the powdered samples indicates that the isotherm measured was of Type IV (porous materials) according to the IUPAC nomenclature (IUPAC, 1985), signifying monolayer-multilayer adsorption in the early part of the curve with a type H3 hysteresis loop between adsorption and desorption and capillary condensation in mesopores (2 nm < ϕ < 50 nm) and macropores (ϕ > 50 nm). The presence of a hysteresis loop in the desorption isotherm shows that the samples were mesopores (materials with pores larger than 2 nm and smaller than 50 nm).

The lack of any limiting adsorption at high p/p^o suggests that the sample consists of plate-like particles, giving rise to slit-like pores (Everett et al., 2002). There is a clear trend of increasing surface area and pore volume of the NT cement mortars with NT content, over the range of 0 wt% to10 wt% of the nanoparticles (Figure 4.18). This could stem from the formation of nanosized needle-shaped products in the presence of the nanoparticles. The surface areas and the average pore diameter were calculated by the BET and BJH methods, respectively, and are presented in Table 4.6.

Figures 4.19 to 4.23 represent the pore diameters and pore size distribution of the selected NT cement composites, calculated from the adsorption and desorption branches. The differences between the pore size distributions are related to the shape of the pores. Larger differences mean more bottleneck-type of pores (Gregg and Sing, 1982). The adsorption and desorption isotherms (BET) obtained on NT cement mortars, representing sample ACM (containing 0 wt% NT) which had the lowest pore volume and surface area, and sample AM10 (containing 10 wt% NT) which had the highest pore volume and surface area among the specimens, are presented in Figures 4.19 to 4.23. Another finding is that the pore diameter calculated for the AM10 sample was larger than the size of the primary particles (10 to 20.5 nm). Probably this is due to the fact that the BJH method only considers the pore size distribution between the agglomerates.

Table 4.6: Parameters of pore diameters, pore volumes and surface areas of the cement mortars.

Code number of Cement Mortars	Cement replacement (wt%) Nano - TiO_2	Pore Diameter /nm	Pore Volume /cm^3 g^{-1}	Surface Area /m^2 g^{-1}
ACM	0	19.0	0.015	3.58
AM2.5	2.5	22.5	0.022	4.72
AM3.5	3.5	25.2	0.028	5.53
AM5	5	22.2	0.028	5.33
AM10	10	20.5	0.043	9.98

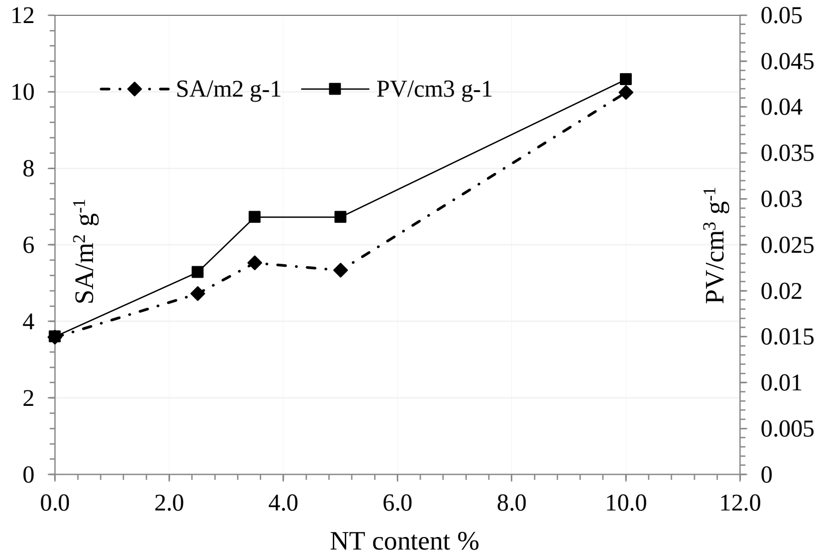

Figure 4.18: Relationships between surface area and pore volume with different dosages of NT.

Additionally, the BJH method employs some approximations that are not valid for very small particles or can only be applied to a given part of the isotherm, as stated by Groen et al. (2003). Another factor that influences the pore structure of NT cement mortars is the drying procedure. As explained in the experimental procedure (Section 2.2.3), the samples were dried at 65 °C for 24 hours prior to the measurements. The drying procedure may affect the micropore structure of AM10, due to coalescence of very small NT particles. The inert TiO_2 nanoparticles, through the increased surface area and provision of heterogeneous nucleation sites, accelerate the hydration reaction and increase the formation of the C-S-H gel at the expense of Portlandite (Jayapalan et al., 2002). It has been mentioned in the literature that beyond 5 wt%, there could be an agglomeration of the nanoparticles so its impact on the properties of the composite would lessen. This is not revealed from the BET measurements which examine the nature of this interaction at the nanoscale level. The pore volumes are evaluated using the BJH method from both nitrogen adsorption and desorption data and the results are presented in Figures 4.24 to 4.28. These figures represent the pore diameters and pore size distributions of the selected NT cement mortars, calculated from the adsorption and desorption branches. It can be clearly seen that the AM10 sample had considerably greater number of pores below 10 nm size than the ACM sample, *i.e.*, pore volume was $0.005/cm^3g^{-1}$ compared to $0.002/cm^3g^{-1}$. For pores between 10 nm and 100 nm in size, the increase of pore volume was even higher when adding 10 wt% NT. This is owing to the fact that NT promotes a higher extent of agglomeration of the NT particles that leads to a larger pore volume, and a considerable amount of water is absorbed in the pores of the agglomerates, resulting in a reduction of water available to lubricate the granular system and for cement hydration, consequently, leading to a lower flowability and a lower extent of hydration. This phenomenon shows that by adding NT in cement mortar, the nano pores (*i.e.*, mainly in the size of 1 nm to 100 nm) are significantly increased.

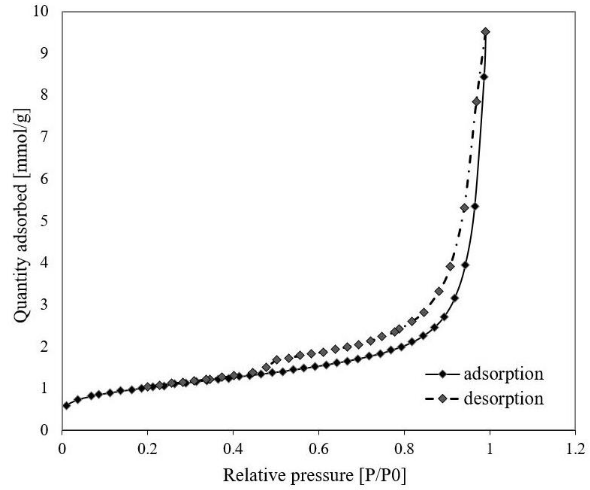

Figure 4.19: N2 Adsorption and Desorption isotherms of the sample with 0% NT (ACM).

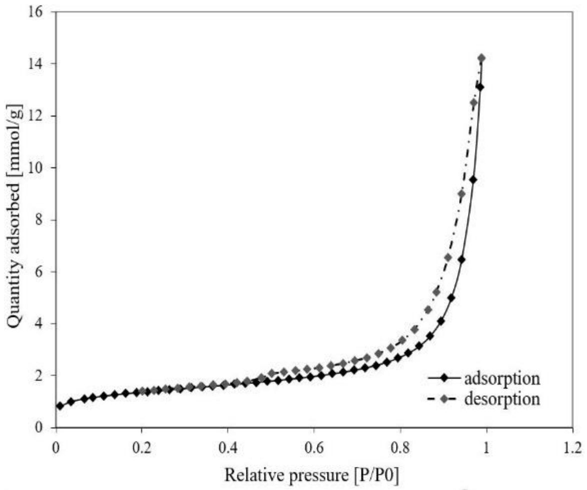

Figure 4.20: N2 Adsorption and Desorption isotherms of the sample with 2.5% NT (AM2.5).

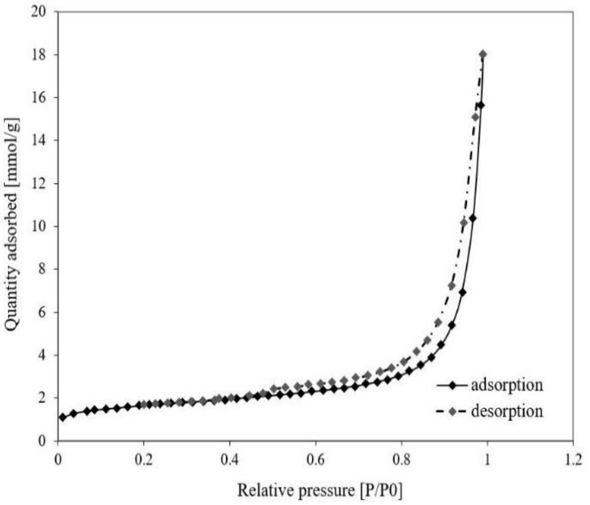

Figure 4.21: N2 Adsorption and Desorption isotherms of the sample with 3.5% NT (AM3.5).

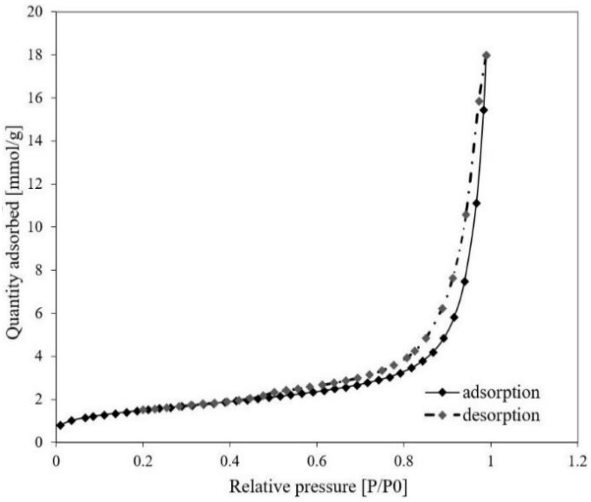

Figure 4.22: N2 Adsorption and Desorption isotherms of the sample with 5% NT (AM5).

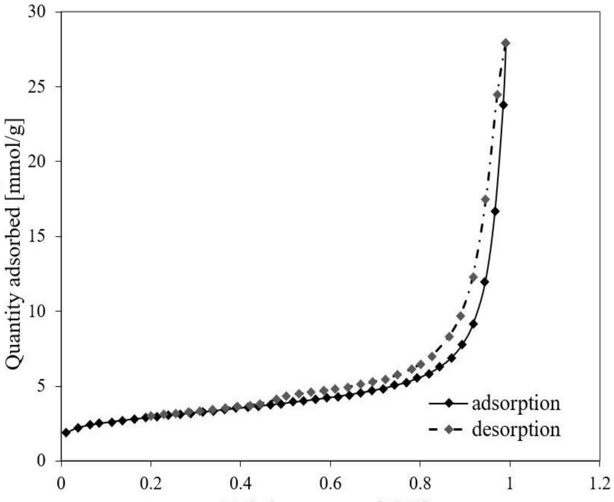

Figure 4.23: N2 Adsorption and Desorption isotherms of the sample with 10% NT (AM10).

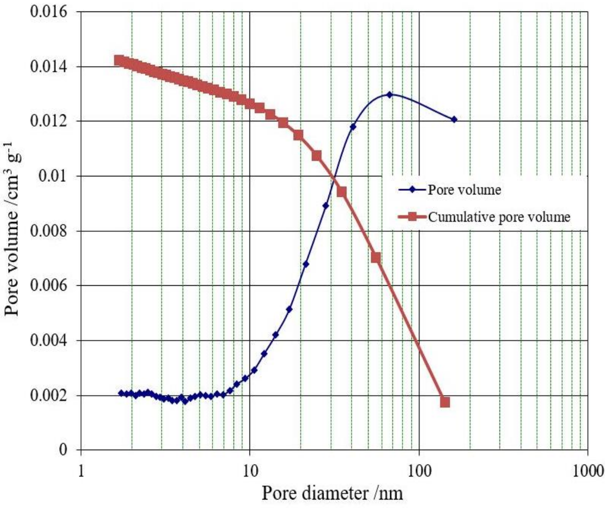

Figure 4.24: BJH adsorption of the sample with 0% NT (ACM).

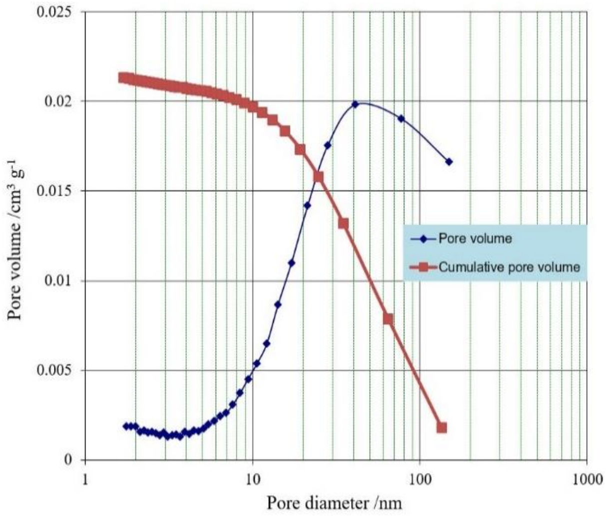

Figure 4.25: BJH adsorption of the sample with 2.5%NT (AM2.5).

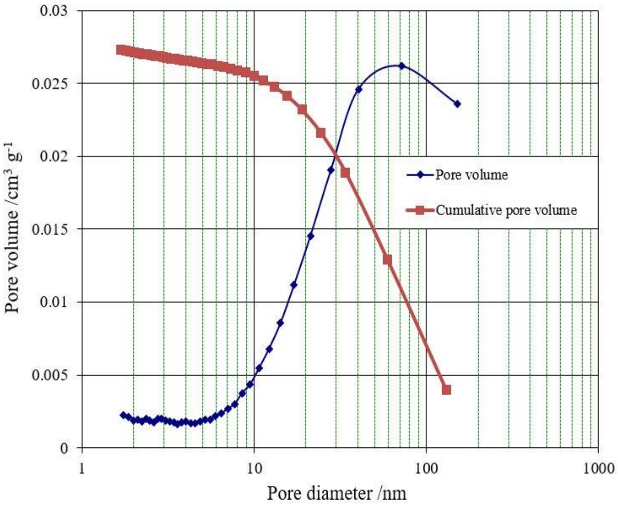

Figure 4.26: BJH adsorption of the sample with 3.5%NT (AM3.5).

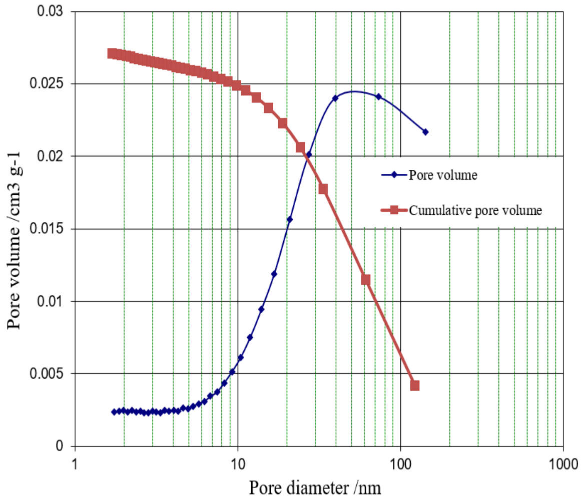

Figure 4.27: BJH adsorption of the sample with 5%NT (AM5).

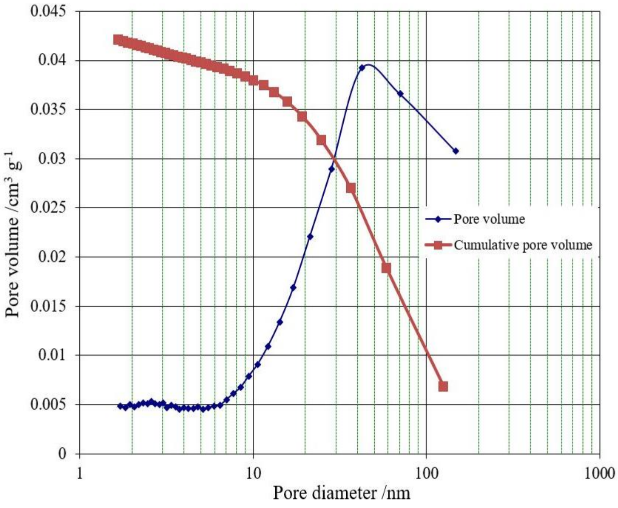

Figure 4.28: BJH adsorption of the sample with 10%NT (AM10).

4.4.5 Hydrophobicity test

To measure the changes in hydrophobicity of the samples from the outer to the inner, wetting angle tests were carried out for the pure mortar sample and the mortars with different NT percentages for three samples of each mix. Figures 4.29(a) and (b) show the water contact angles from the outer to the inner for sample AM2.5 after 24 hours. It is noticeable that addition of 2.5wt% of NT increased the wettability of the sample surface. Contact angle decreased form the outer (82 ± 2°) to the inner (32 ± 2°), as illustrated in Table 4.7. The AM10 sample has presented the highest contact angle at SV3 (92 ± 2°), amongst all the NT mortar and pure mortar specimens. Comparing with the AM2.5 sample, adding 10 wt% NT can increase the hydrophobicity of the sample by 11%. This is a significant improvement in the durability of cement mortars. The results are also in line with the results of 3D volumetric porosity tests performed in Section 4.4.1 as illustrated in Figure 4.29(a). Such a non-uniform distribution of porosity in the NT cement samples favoured the durability of the composite as the surface areas of the samples had much lower porosities. (three samples of each mix).

Table 4.7: Wetting angle tests

Specimens	Contact angle Ø°. Samples 1, 2 and 3.			Average angle Ø° at Sv1	Contact angle Ø°. Sample 1, 2 and 3.			Average angle Ø° at Sv2	Contact angle Ø°. Sample 1, 2 and 3.			Average angle Ø° at Sv3
	No: 1	No: 2	No: 3		No: 1	No:2	No: 3		No: 1	No: 2	No: 3	
ACM	0	0	0	0	0	0	0	0	0	0	0	0
AM2.5	29	33	34	32	43	45	50	46	76	81	89	82
AM5	36	41	34	37	52	46	49	49	92	89	80	87
AM10	49	53	54	52	49	47	57	51	95	97	84	92

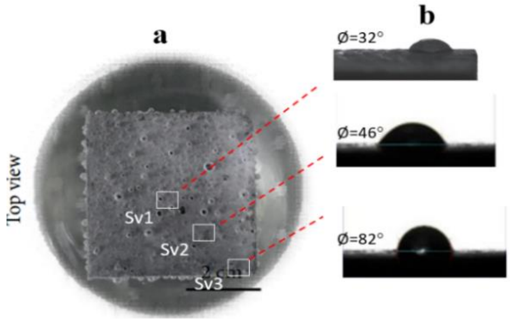

Figure 4.29 (a) and (b): Position of the 3 sub volumes (“Sv1”, “Sv2”, “Sv3”), used to measure hydrophobicity.

4.5 Remarks

In this chapter, multiscale pore structure analyses on cement mortars incorporated with different percentages of NT have been carried out. Novel XCT tests have been conducted to quantify and characterise the pore systems for the NT cement composites. SEM-EDS has been used to evaluate the phases of the microstructures of the composite. In addition, the durability of NT cement mortars was assessed by testing the water permeability using a high-pressure core holder with a sensitive and automated measurement capability. Further, BET analysis was carried out to examine the nanoscale pore systems of the NT mortars, including the pore volume, pore shape and surface area. Specifically, the main findings can be summarised as follows.

(1) The pores of the cement mortars mixed with 2.5 wt% to 3.5 wt% of NT were significantly refined and shifted to nanosized pores with the total average porosities reduced by 60.1 % and 54.2%, respectively.

(2) When the dosage of NT was more than 3.5 wt%, the total pore volume and the number of pores began to increase. However, when the amount of NT exceeded the optimal value with NT >2.5 wt%, the recorded 3D volumetric void fractions and 2D area void fractions observed for AM5 (5.87, 5.95%) were still lower than those for the reference sample ACM (6.67%, 7.81 %). The permeabilities of the cement mortars with 2.5 wt% to 3.5 wt% NT inclusions were significantly decreased by 32.1% and 26.8%, respectively.

(4) The SEM and EDS results indicated that, when NT dosage was in the region of 2.5 wt%, the surface morphology of the cement matrix became denser.

(5) There were clear increasing trends of the surface area and pore volume of the cement mortars with the increasing NT content, over the range 0 wt% to 10 wt% of the nanoparticles.

Chapter 5

Microstructural Characterization of Phases and Interfaces of Cement Mortars Containing Nano Titanium Dioxide

5.1 Introduction

Apart from the photocatalytic and pore structure properties discussed in Chapters 3 and 4, the mechanical properties, microstructures, and hydration of the TiO_2 cement composites have also been studied. Lee and Kurtis (2010) pointed out that NT is chemically inert in the process of cement hydration, but it can provide crystal nuclei to promote the cement hydration process, leading to the increases in the compressive strengths of mortars. Lee et al. (2013) reported that compressive strength increased by 10 wt% NT replacement at a relatively low water-to-cement ratio (0.4). Furthermore, the addition of NT particles has been shown to improve the densification and homogeneity of the microstructure, thereby enhancing the durability of the cementitious materials (Nazari, 2011; Leng et al., 2013).

Compared with the photocatalytic and mechanical properties of the TiO_2 cement, the influence of NT on the genetic defects of cement-based materials, including high brittleness and change in phase composition, has not received attention, which leads to a decline in performance and service life of the building materials. This uncertainty casts doubt on the widespread application of the NT-cement composite. Therefore, this chapter attempts to address this knowledge gap by investigating the phase changes and microstructural characteristics of cement mortars modified with NT particles, cured to the ages of 7 and 28 days.

The effects of NT on the crystalline phases of the cement mortars were investigated. The characterization of the cement hydration process, hydration products and morphology of the cement mortars at 7 and 28 days were conducted by scanning electron microscopy (SEM) and X-ray diffraction (XRD) with different NT inclusions. The changes in calcium silicate hydrates (C-S-H gel) and the other phases of cement mortars (*e.g.*, Ettringite, Portlandite, Alite and Belite), before and after the addition of NT in cement mortar specimens, were detected using thermo-gravimetric method (TG).

Derivative thermogravimetric (DTG) curves were plotted from the TG data to identify the extent of cement hydration and the exact boundaries of various phases or group of phases present in the hydrated samples. Meanwhile, elementary analysis was performed using an energy-dispersive X-ray spectroscopy (EDAX$^{®}$). Finally, mechanical tests were conducted to obtain the changes in compressive and tensile strengths, by adding a broad range of NT dosages. SEM analysis illustrated that the addition of NT content up to 2.5 wt% caused a refinement of the microstructure and probably induced the precipitation of small sized calcium silicate hydrate (C–S–H) gel that has a high stiffness.

Results of XRD analysis showed a large decrease in the intensities of Alite ($\mathrm{C_3}S$) and Belite ($\mathrm{C_2S}$) phases when the amount of NT exceeded the optimal value, NT (> 2.5 wt%), for both curing ages of 7 and 28 days. For hydration at 28 days, compared with the control mix, there is a significant increase in the content of portlandite ($\mathrm{Ca(OH)_2}$) produced from cement hydration, when the added amount of NT increased to 2.5 wt%. Furthermore, DTG results indicated a significant increase in the extent of bond formation between NT and free calcium hydroxide when the amount of NT increased up to 2.5 wt% at 7- and 28-day curing ages. Results show that the tensile and compressive strengths increase with increasing NT content up to 2.5 wt%.

For Further increase in the NT content, the tensile and compressive strengths decreased slightly. However, when the amount of NT exceeded the optimal value, e.g., (2.5 wt% ≤ NT ≤ 5 wt%), the recorded tensile and compressive strengths observed were still higher than the reference sample. These increases in the strengths of the mortars with NT were attributable to the nano sized particles and extensive surface areas of NT. The nano sized particles, as nucleating agents, promoted the hydration process of C_3S, C_2S and the formation of C–S–H phase.

5.2 Experimental

5.2.1 Materials

Different percentages of OPC with the average particle size ranging between 46-153 μm and specific surface of 1.45 m^2/g, were replaced with different amounts of NT, *i.e.*, (0 wt%, 2.5 wt%, 5 wt% and 10 wt%). Natural river sand, with a minimum particle size of 200 μm, a specific gravity of 2.63 and a fineness modulus of 2.89, served as the fine aggregate. The NT used in this experiment had a specific surface area of 55 m^2/g, a specific gravity of 2.1-2.3 at 25 °C, a bulk density of 0.054 $g.mL^{-1}$, and an average particle size of 19 nm. Deionised water, with a pH value of 7.5 at 22°C, was used throughout the experimental research.

5.2.2 Sample preparations

The experimental study involved the application of a pan mixer with a 20 kg capacity. The fine aggregate was first poured into the pan-mixer, followed by the OPC CEM I 42.5N, under dry conditions. They were mixed for 30 seconds to ensure homogeneity. The mixing continued for another 1.5 minutes before the water already mixed with nano titanium dioxide was added and the mixing was allowed to continue for another 5 minutes. The recorded mix design code for each sample is presented in Table 4.3 in Chapter 4. As explained in Section 2.5, slump and slump flow tests were then carried out according to BS EN 12350-2 (BSI, 2009a) and BS EN 12350-5 (BSI, 2009c), respectively. The mix proportion design resulted in a slump ranging from 11 to 21 mm and a slump flow ranging from 170 to 203 mm. Moreover, the vebe time ranged from 8 and 19 seconds which met the required workability based on BS EN 12350-2:2009. The mix had a constant water/equivalent cement ratio of 0.55. Constant quantities of sand (681 $\mathrm{kg/m^3}$) and water (125 $\mathrm{kg/m^3}$) were used in this chapter.

For the XRD and TG-DTG analyses, a sample was taken from the centre of each specimen, then grinded into a powder. In order to stop the hydration of the samples at the ages analysed, the samples were placed in vacuum for 30 minutes and then in acetone for two hours to discontinue the hydration process, following 18 hours in an oven at 45°C. Cement mortar cubes of 50 mm in size for the SEM test were cast and vibrated in a vibrating table. The specimens were then demoulded and cured in tap water for 7 and 28 days. Circular sections with a diameter of 10 mm and a thickness of 5 mm were extracted using a diamond saw from the samples that were moist cured for 7 and 28 days. The samples were then dried overnight in an oven at 55°C until a constant weight was reached.

5.3 Testing Method

X-ray diffraction analysis was employed to study the effect of different dosages of NT on the formation of various phases in the hydration products of cement mortars. The diffraction spectra of the hydrated specimens of cement mortar were acquired after 7- and 28-days curing. Powder samples were loaded in an aluminium circular holder with a diameter of 25 mm. X-ray diffraction analysis was performed using a Bruker D8 Advance, Cu-Kα X-rays of wavelength λ =1.5406 Å and the data was taken over the 2θ ranges of 5° to 70° with a step of 0.02° under an operating voltage of 40 kV and a working current of 100 mA. After identifying the existing phases in the cement using

XRD, quantification of the formed hydrates was performed using thermogravimetry analysis in a thermobalance Perkin Elmer TGA7 with a TAC7/DX controller, in a N_2 atmosphere. The temperature ranged from 20 to 1000 °C at a heating rate of 10 °C/min. An analytical Gas N_2 5.0 was used to protect the balance (at a flow of 20 mL min^{-1}), and the volatized gases were purged at a rate of 60 $mLmin^{-1}$. Direct compression and tension tests were conducted according to BS 1881-121 (BSI, 1983) and ASTM C469-94 (ASTM, 1994), for several NT dosages, to determine the mechanical strengths of the NT cement mortars. The compressive strengths were evaluated from the peak load obtained by crushing the specimen according to BS EN12390-3 (BSI, 2009b). The cement mortars used in the compression test were in the dimensions of 100 mm × 100 mm × 100 mm. The cubes used for the compression tests were cured in tap water for 7 and 28 days and taken out of the water one day prior to the testing. A general view of the experimental setup for obtaining the compressive strengths was illustrated in Figure 3.12.

As demonstrated in Chapter 3, The tension tests consisted of a tension testing machine (Instron 5969®) with a capacity of 50 kN and cylindrical samples with a diameter of 50 mm and a length of 400 mm. The testing arrangement were shown in Figures 3.10(a) and (b). The specimen was prepared with a circumferential notch with a depth of 12 mm +/- 1 mm and a width of 2.5 mm. This set-up made it possible to control the eccentricities of the tensile load during the tests. Furthermore, SEM analysis was carried out in the secondary electron mode using the field emission scanning electron microscope (FE-SEM). A HITACHI SU-6600, operated with an acceleration voltage of 20 keV, was used. Finally, elementary analysis was performed using an energy-dispersive X-ray spectroscopy (EDS) device. The EDS measurements were arranged in rectangular grids of 10 × 20 points (vertical and horizontal spacings of 2.5 mm).

5.4 Results and Discussion

5.4.1. Identification of the formed hydrates using X-Ray diffraction analysis

XRD analyses of NT-cement mortars with different dosages of NT, at the 7- and 28-day curing ages, are shown in Figures 5.1 and 5.2, respectively. Ettringite (3CaO·Al_2O_3.3SO_4 .nH_2O, abbreviated as AFt), alite (Ca_3SiO_5, abbreviated as C_3S), belite (Ca_2SiO_4, abbreviated as C_2S) and portlandite ($Ca(OH)_2$), were found to be the major phases for all the mixes. Figures 5.1(a) to 5.1(d) show the XRD patterns of the microstructure of the mortars mixed with NT, *i.e.* 0 wt%, 2.5 wt%, 5 wt% and 10 wt%, at 7 days. On increasing the NT content up to 2.5 wt% (AM2.5), the increase in the intensities of C_2S and C_3S (2θ values of 32.2°, 32.4°) were observed.

It can be seen from the XRD patterns shown in Figure 5.1 that the intensities of C_3S (2θ values of 29.4°, 38.9°, 45.8°, 51.9°, 56.3°, 60.1°, 63.2°) and C_2S (2θ values of 23.6°, 25.2°) increased when NT ≤ 2.5 wt% and then gradually decreased when the dosage of NT increased beyond 2.5 wt%. This behaviour was attributed to the agglomeration of NT particles when exceeding the optimal value which creates more voids in concrete and decreased the calcium silicate phases (C_3S and C_2S) required for C-S-H gel formation.

AFt generation is related to the concentration of sulfate ions, while the addition of inert nanoparticles can promote the early hydration of the cement (Chen et al., 2013), making mortars more compact with more sulfate ions solvated into C-S-H gel. For hydration at 7 days, the intensities of AFt (Figure 3, 2θ values of 9.1°,15.7°) in mortars with 2.5 wt% NT (Figure 5.1(b)) were significantly greater than those without NT. However, AFt in mortars with 5 wt% NT (Figure 5.1(c)) was about the same as that with 2.5 wt% NT. Further increasing the dosage of NT to 10 wt% (Figure 5.1(d)), the intensity of Aft decreased. It can be seen from the XRD patterns (hydration at 7 days) that, compared with the control mix (ACM), there was not a significant change in the intensity of $Ca(OH)_2$ produced from cement hydration, when the added amount of NT increased to 2.5 wt%.

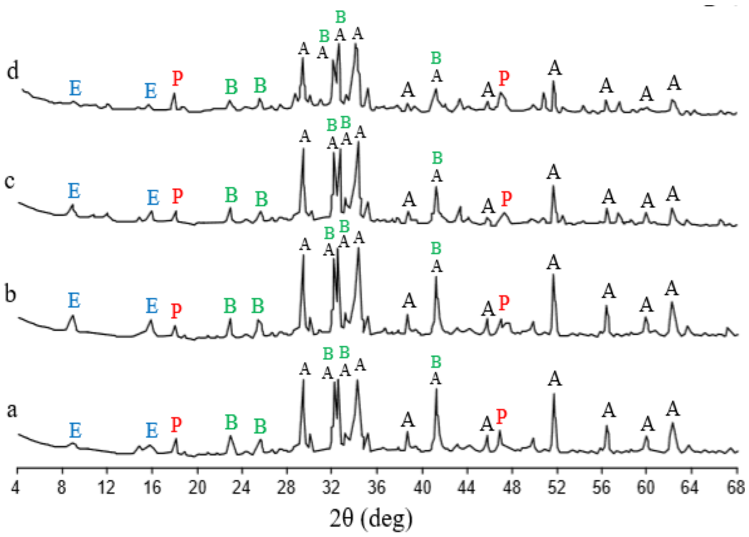

Figure 5.1: XRD analysis of different specimens at the age of 7 days: a) control (ACM), b) AM2.5, c) AM5, d) AM10. A: Alite, B: Belite, P: Portlandite, E: Ettringite

Further increasing the NT content up to 5 wt% (AM5) causes the intensity of $Ca(OH)_2$ to decrease slightly. The peaks at 2θ of 18.4° and 47.2° correspond to calcium hydroxide (JCPDS-International, 2000). Figures 5.2(a) to 5.2(d) show the XRD patterns of the ACM, AM2.5, AM5 and AM10 at the curing age of 28 days. On increasing the NT content up to 2.5 wt% (AM2.5), similar to the 7-day curing, the intensities of C_3S (2θ values of 29.4°, 38.9°, 45.8°, 51.9°, 56.3°, 60.1°, 63.2°) and C_2S (2θ values of 23.6° and 25.2°) increased when NT $\leq$ 2.5 wt% and then gradually decreased when the dosage of NT increased beyond 2.5 wt%.

For hydration at 28 days, the intensities of AFt (Figure 5.2, 2θ values of 9.1° and 15.7°) in mortars with 2.5 wt% NT (Figure 5.2(b)) are significantly greater than those without NT. Further increasing the dosage of NT to 5 wt% and 10 wt% (Figures 5.2(c) and (d)) the intensity of Aft decreased.

It can be seen from the XRD images in Figure 5.2 (hydration at 28 days) that, compared with the control mix (ACM), there was a significant increase in the intensity of $Ca(OH)_2$, when the added amount of NT increased to 2.5 wt% (Figure 4(b), 2θ values of 18.4°). Further increasing the NT to 5 wt%, compared with the control mix (ACM), there was no significant change in the intensity of $Ca(OH)_2$. However, when the added amount of NT increased to 10 wt%, there was a decrease in the intensity of $Ca(OH)_2$ produced from cement hydration (2θ values of 18.4°, 47.2°).

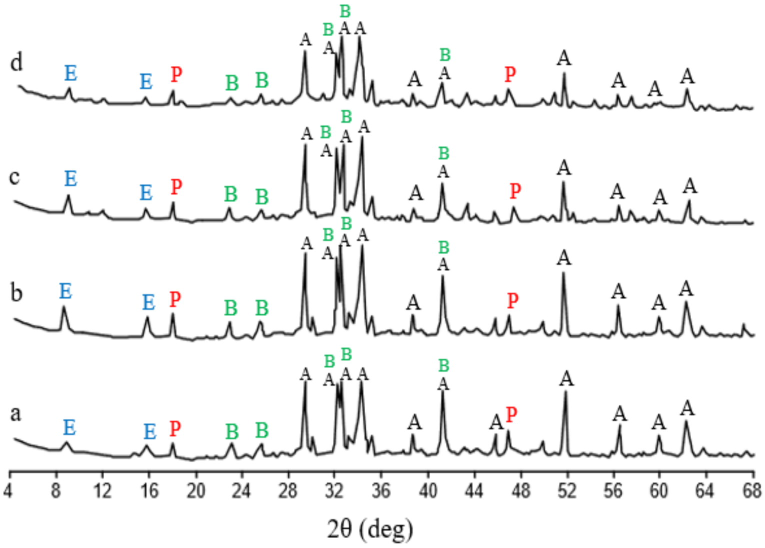

Figure 5.2: XRD analysis of different specimens at the age of 28 days: a) control (ACM), b) AM2.5, c) AM5, d) AM10. A: Alite, B: Belite, P: Portlandite, E: Ettringite.

5.4.2. Quantification of the formed hydrates through thermo-gravimetric analysis (TG/DTG)

Thermogravimetric (TG) curves of hydrated NT-cement mortars, including the control, with different dosages of NT, *i.e.* 0 wt%, 2.5 wt%, 5 wt% and 10 wt%, at 7 and 28 days of curing are shown in Figures 5.3(a) and (b). Derivative thermogravimetric (DTG) curves were plotted from the TG data to identify the extent of cement hydration and the exact boundaries of various phases present in the hydrated samples. The DTG curves of the hydrated cement paste samples are shown in Figures 5.4(a) and (b). The TG-DTG curves showed the typical reactions occurring in the cement mortars when subjected to a progressive temperature increase from room temperature to 1000 °C in 20 mL min^{-1} Nitrogen gas flow. The mass loss in the NT-cement mortars, including the control, during heating in the TG-DTG analyses, occurred in four main steps. The dehydration of water molecules in hydrates such as C–S–H and ettringite took place within the range from room temperature to 200 °C (Tobón et al., 2012; Frias et al., 2001; Ashraf et al., 2009; Aly et al., 2012).

The second reduction at 200–380 °C, caused a loss in mass corresponding to the breakdown of C–A–H phases (Frias et al., 2001; Ashraf et al., 2009; Aly et al., 2012). The third step of thermal degradation occurred at 410-550 °C, and the corresponding mass loss was associated with the dehydroxylation of $Ca(OH)_2$ produced during curing to CaO and H_2O (Tobón et al., 2012; Frias et al., 2001; Ashraf et al., 2009; Aly et al., 2012). When the mortar specimens were cured, calcium hydroxide forming in them gradually combined with carbon dioxide of the air to form calcium carbonate (Chang et al., 2006). Subsequently, the final weight loss area was observed at 550–740 °C occurred due to the decomposition of calcium carbonate and escape of CO_2 from the cement matrix (Frias et al., 2001; Ashraf et al., 2009; Aly et al., 2012; Chang et al., 2006).

Finally, the last difference was observed for the peak at 740-930 °C, the evidence for this was that the peak was higher for the samples with lower surface area and NT content (as illustrated in Table 4.7). Unfortunately, no direct explanation of this extra weight loss was found in the literature. Table 5.1 presents the mass percent of C–S–H, C_2AH_8, $Ca(OH)_2$ and $CaCO_3$ which were calculated by multiplying the mass loss percent of each steps of TG curves, given in Table 5.2, with the stoichiometric molar mass ratios of CSH/H_2O, C_2AH_8/H_2O, $Ca(OH)_2/H_2O$ and $CaCO_3/CO_2$, respectively (Chang et al., 2006; Askarinejad et al., 2012).

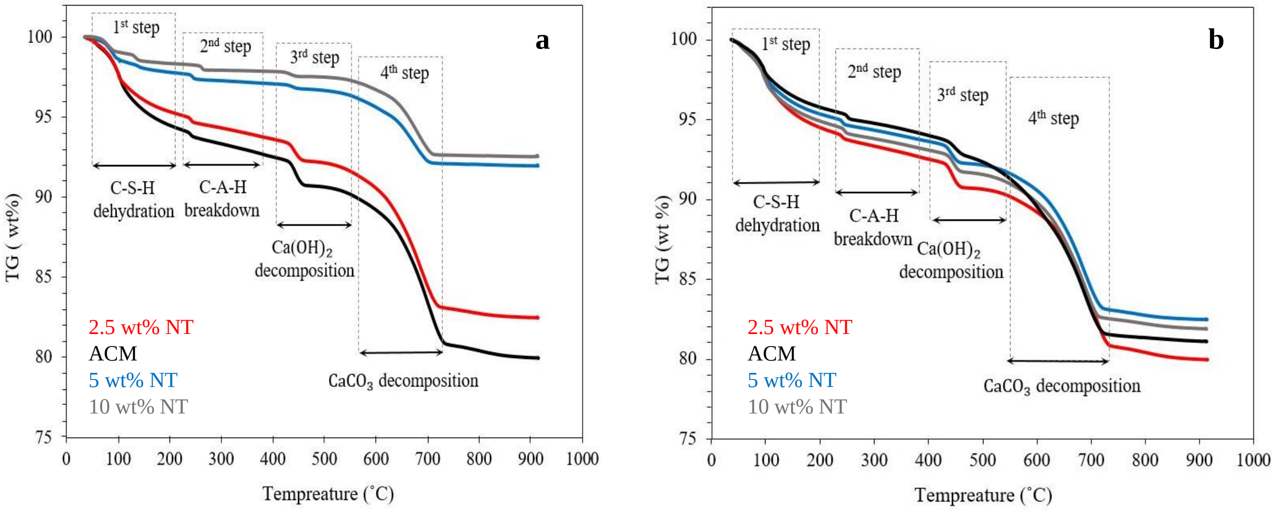

Figure 5.3: TGA curves of hydrated cement paste samples containing different amounts of NT at **a** 7-day, **b** 28 day

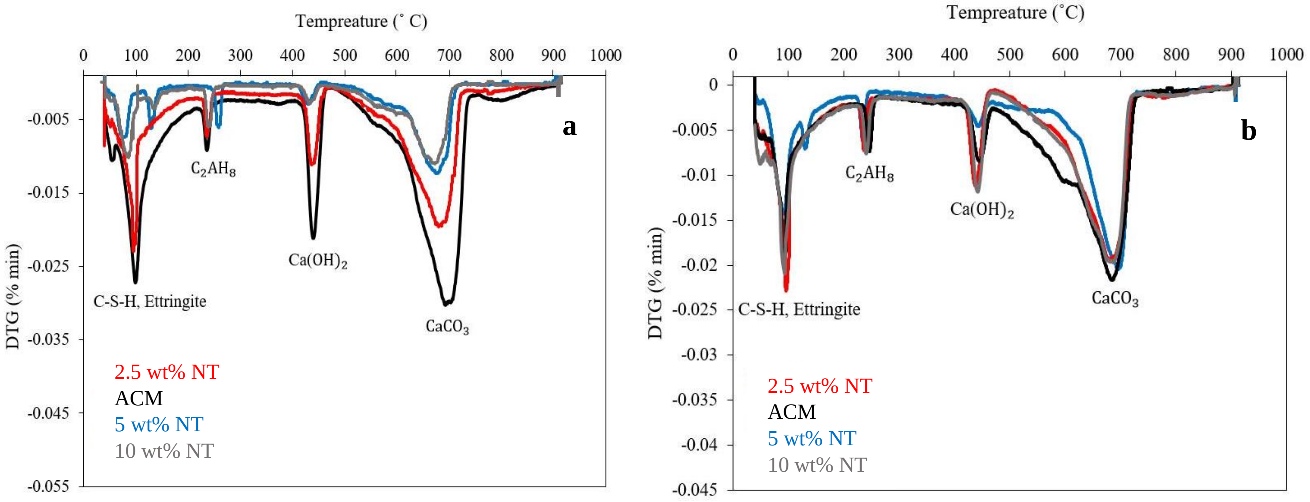

Figure 5.4: DTG curves of hydrated cement paste samples containing different amounts of NT at **a** 7-day, **b** 28 day

The mass percents of C–S–H, C_2AH_8, $Ca(OH)_2$ and $CaCO_3$ in the sample were calculated from the TG curves using the following Eqs. (5.1) to (5.4):

$$CSH\ (\%) = WL\ \%\ (CSH) \times \frac{MW\ (CSH)}{Moles\ of\ water \times MW(H_2O)}$$

$$= WL\ \%\ (CSH) \times \frac{193}{72} \qquad (5.1)$$

$$C_2AH_8\ (\%) = WL\ \%\ (\ C_2AH_8) \times \frac{MW\ (C_2AH_8)}{MW(H_2O)}$$

$$= WL\ \%\ (\ C_2AH_8) \times \frac{134}{18} \qquad (5.2)$$

$$Ca(OH)_2\ (\%) = WL\ \%\ (\ Ca(OH)_2) \times \frac{MW\ (Ca(OH)_2)}{MW(H_2O)}$$

$$= WL\ \%(CH) \times \frac{74}{18} \tag{5.3}$$

$$CaCO_3(\%) = WL\ \%\ (CaCO_3) \times \frac{MW\ (CaCO_3)}{MW\ CO_2}$$

$$= WL\ \%\ (CaCO_3) \times \frac{100}{44} \tag{5.4}$$

where WL % (CSH), WL % (C_2AH_8), WL % ($Ca(OH)_2$) and WL % ($CaCO_3$) corresponded to the mass losses in percentages attributable to C-S-H, C_2AH_8, $Ca(OH)_2$ and $CaCO_3$ dehydration and $MW_{CSH} = 193/g/mol$, $MW_{C_2AH_8} = 134/g/mol$, $MW_{Ca(OH)_2} = 74/g/mol$, $MW_{CaCO_3} = 100/g/mol$, and MW_{H_2O} = $18/g/mol$ are the molecular weights of C-S-H , C_2AH_8, $Ca(OH)_2$, $CaCO_3$ and water, respectively. The composition of C-S-H gel was approximately $1.7Ca.SiO_2.4H_2O$ for saturated C_3S pastes as well as cement, where 4 mol of water including adsorbed water on the surface of hydration products, will be removed at temperature below 115 °C (Taylor., 1997). Therefore, in the present study, the formation of C-S-H with chemical composition of $1.7Ca.SiO_2.2.1H_2O$ was considered (Young et al., 1987).

Table 5.1: Mass losses in TG after 7- and 28-day curing ages.

Mix	Samples 1 and 2 at 7 and 28 days		1st step 20-200˚C C-S-H		Samples 1 and 2 at 7 and 28 days		2nd step 220-38 ˚C C-A-H		Samples 1 and 2 at 7 and 28 days		3rd step 410-550 ˚C $Ca(OH)_2$		Samples 1 and 2 at 7 and 28 days		4th step550-740 ˚C $CaCO_3$	
	7	28	7	28	7	28	7	28	7	28	7	28	7	28	7	28
ACM	6.1, 5.5	4.1, 4.3	5.8	4.2	1.5, 1.9	1.8, 1.4	1.7	1.6	2.7, 2.5	2.1, 2.5	2.6	2.3	9.3, 8.9	10.1, 10.3	9.1	10.2
AM2.5	4.4, 4.8	5.3, 5.9	4.6	5.6	1.2, 1.2	1.3, 1.5	1.2	1.4	2.7, 2.5	1.7, 1.7	2.6	1.7	8.9, 8.5	8.9, 9.3	8.7	9.1
AM5	1.9, 2.3	4.4, 5.2	2.1	4.8	0.8, 0.4	1.1, 1.7	0.6	1.4	0.7, 1.1	2.2, 2.0	0.9	2.1	4.2, 4.2	9.1, 9.3	4.2	9.2
AM10	1.8, 1.4	4.8, 5.0	1.6	4.9	0.5, 0.3	1.3, 1.1	0.4	1.2	0.9, 0.7	2.4, 2.0	0.8	2.2	4.3, 4.5	9.6, 9.6	4.4	9.6

Table 5.2: Masses % of C-S-H, C_2AH_8, $Ca(OH)_2$ and $CaCO_3$ calculated from the 1st to 4th steps of TG analyses for the NT cement mortars including pure cement mortar specimens at the ages of 7 and 28 days.

Mix	1st step		2nd step		3rd step		4th step	
	C-S-H		C-A-H (C_2AH_8)		$Ca(OH)_2$		$CaCO_3$	
	7	28	7	28	7	28	7	28
ACM	15.6	11.3	12.6	11.9	10.7	9.4	20.6	23.1
AM2.5	12.3	15.0	8.9	10.4	10.7	6.9	19.9	20.5
AM5	5.7	12.9	4.5	10.4	3.7	8.6	9.5	20.7
AM10	4.3	13.1	2.9	8.9	3.2	9.1	9.9	22.5

At the age of 7 days, the TG curves of AM2.5, AM5 and AM10 showed similar changes to that of the control mix (ACM), with some changes in mass loss and mass loss rates at each step. The first DTG peaks of ACM after 7 days of curing appeared at 97 °C, corresponding to a 5.8% mass loss in C-S-H and AFt content. Similarly, the first DTG peaks of AM2.5, AM5 and AM10 appeared between 78 °C and 103 °C where the highest C-S-H and AFt mass loss rates were observed for ACM and AM2.5.

The C-S-H and AFt mass losses on the TG curves of AM2.5, AM5 and AM10 occurring in the first step were 4.6%, 2.1% and 1.6% respectively. The second decomposition step of ACM occurred between 220 °C and 380 °C, and reached a maximum rate at 242 °C, resulting in a 1.7% mass loss in C_2AH_8 content. The second thermal decomposition steps of AM2.5, AM5 and AM10 occurred in the same temperature range (∼ 210–390 °C), where the corresponding mass losses were 1.2%, 0.6% and 0.4% respectively.

The third decomposition step of ACM, as well as those of AM2.5, AM5 and AM10, occurred between 410 °C–550 °C. The mass loss rates observed at the third step of DTG showed a decrease in the rate of decomposition of $Ca(OH)_2$ in AM2.5 in comparison to that of ACM. The residues of AM2.5, AM5 and AM10 at 850 °C, as well as the control were about 78-94% at the curing age of 7 days. Finally, the fourth decomposition step occurred between 550 °C and 740 °C.

The mass loss rates observed at the fourth step of DTG showed a significant decrease in the rate of decomposition of calcium carbonate in AM2.5 in comparison to that of ACM. Figures 5.3(b) and 5.4(b) show the TG–DTG behaviour of all the specimens after 28 days of curing. The significant points of the TG–DTG analysis at the age of 28 days can be summarized as follows: the incline of the first step of the TG curve of AM2.5 was very steep, and the corresponding mass loss rate was the maximum (2.1 $\%.\mathrm{min}^{-1}$) and reached 5.6% mass loss at 103 °C, much greater than ACM, AM5 and AM10 due to the higher extent of C–S–H formation in AM2.5 (CEN EN 1015-3, 1999). The second step of decomposition of ACM occurred between 220 °C and 380 °C, and reached a maximum rate at 232 °C, resulting in a 1.6% mass loss in C_2AH_8 content. The mass losses at the third step of TG analyses for CM, AM5 and AM10, related to the decomposition of $Ca(OH)_2$, were 2.3%, 2.1% and 2.2% respectively, which were all lower than 1.7% mass loss of AM2.5.

The third thermal decomposition step of AM2.5 occurred considerably slower than those of ACM, AM5 and AM10 as given in their DTG curves (Figure 5.4(b)). In the fourth decomposition step between 550 °C and 740 °C, the mass loss rate of AM2.5 observed was the smallest among all the samples. Residues of ACM, AM5 and AM10 at 900 °C were 79.6%, 80.2%, 80.3%, respectively, while the residue of AM2.5 was 79.4%. As seen in Table 5.2, at the age of 28 days, the mass percent of free $Ca(OH)_2$, which did not enter the pozzolanic reaction, in AM5, AM10 and CM, were calculated as 8.6%, 9.1% and 9.4%. Alternatively, the amount of free $Ca(OH)_2$ in AM2.5 was found the least among all the samples, i.e., 6.9%.

In addition, the total amount of $Ca(OH)_2$ and $CaCO_3$ for AM2.5 was 27.4%, which was also the smallest among all the samples, indicating the rising extent of bonding between NT and $Ca(OH)_2$ in AM2.5 in comparison to bonding in AM10, AM5 and CM, and also suggesting the difficulty of CO_2 penetration in AM2.5 due to the strength of bond formation and compact structure. These results are in good agreement with the results of the compressive and tensile strengths observed in AM2.5 (as illustrated in Tables 5.4 and 5.5). One further interesting observation is the fact that peaks are shifted to the right for the case of AM2.5 (Figure 5.4).

5.4.3 Specific density by glass and helium pycnometry

The values obtained from the density measurements using the procedure described in Section 2.2.3 are shown in Table 5.3, which also presents a comparison between the density measurement results obtained by the glass and helium pycnometer. The density values are in the expected range for the different NT cement mortars. The specific density of the samples is in the range from 1.1 to 1.4 g/cm^3.

Table 5.3: Computed densities of the NT mortars (helium and gas pycnometry).

Code	Helium pycnometry (g/cm^3)	Gas pycnometry (g/cm^3)	Difference (%)
ACM	1.146 ± 0.016	1.103	3.90
AM2.5	1.346 ± 0.019	1.156	16.4
AM5	1.144 ± 0.013	1.091	4.86
AM10	1.122 ± 0.011	1.021	9.90

Samples with higher contents of NT particles (AM5 and AM10) showed lower specific densities (ranging between 1.09 and 1.02 g/cm^3). This is owing to the fact that NT promoted a higher extent of agglomeration of the NT particles that led to a larger pore volume, and a considerable amount of water was absorbed in the pores of the agglomerates, resulting in a reduction of specific density. Moreover, the helium pycnometer produced more accurate results than the glass pycnometer method. Another difference between both techniques is the required measurement time: 10 measurements in a helium pycnometer take about 45 minutes, while a single measurement using the glass pycnometer takes about 12 hours and requires a controlled room temperature.

5.4.4. Results of the mechanical tests

Results show that the tensile strength increased with the increasing NT content up to 2.5 wt% (Table 5.4). Further increase of the NT content, the tensile strength decreased slightly. However, when the amount of NT exceeded the optimal value (*i.e.*, NT >2.5 wt%), the recorded tensile strengths observed for AM5 at 7 days (1.18 MPa) and 28 days (1.87 MPa) were still higher than the reference sample ACM. The tensile strength of sample with 2.5 wt% NT at the 7- and 28-day curing ages increased by 31.9% and

26.4% respectively which were considerably greater than those without NT. The relationships between the tensile strength and the NT content at 7- and 28-days curing are presented in Figure 5.5.

Table 5.4: Tensile strengths of the mortars with different dosages of NT.

Types of specimens	Cement replacement (wt%)	Direct tensile strength at 7 days curing for samples 1 and 2		Direct tensile strength at 28 days curing for samples 1 and 2		Average direct tensile strength (MPa)/increase rate (%)	
Mix design	Nano - TiO_2	No: 1	No: 2	No:1	No:2	7 days	28 days
ACM	0	1.22	1.00	1.35	1.49	1.11/0.00	1.42/0.00
AM2.5	2.5	1.54	1.72	1.88	1.98	1.63/31.9	1.93/26.4
AM5	5	1.23	1.13	1.76	2.56	1.18/5.09	1.87/24.1
AM10	10	1.11	1.27	1.19	1.25	0.94/-15.3	1.22/-14.1

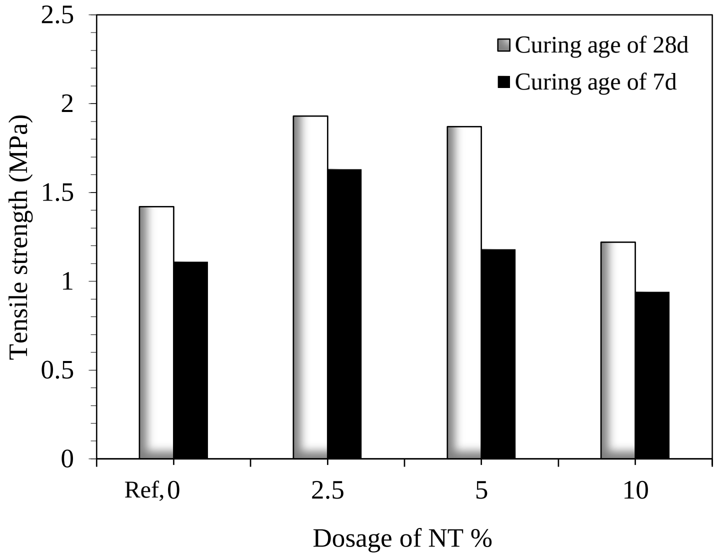

Figure 5.5: Relationships between the average tensile strength and dosage of NT for the curing ages of 7 and 28 days.

Effects of 0 wt%, 2.5 wt%, 5 wt% and 10 wt% contents of NT on the compressive strength of cement mortars are shown in Figure 5.6. The results show that the compressive strength increased with the increasing NT content up to 2.5 wt% (Table 5.5). The compressive strength for 2.5 wt% amount of NT increased by 30.6% and 22.7% at 7 and 28 days respectively, while the compressive strength for 5 wt% only increased by 23.4% and 14.7% respectively. The possible reason for the significant increase in the compressive and tensile strengths at 7 days is the fact that NT promoted the early hydration and acted as an external nucleation to promote the generation of C-S-H gel, which can significantly improve the mechanical properties of cement mortars. Beyond 5 wt%, there could be an agglomeration of the nanoparticles, so its impact on the properties of the composite would lessen. It is important to note that no clear quantitative relations between the mechanical properties and the morphological properties of the NT cement mortars have been obtained. Nevertheless, some observations can be made. The NT cement mortars with the highest specific surface area exhibited the worst performance (Table 4.7). This low performance can be attributed to the particle dispersibility (agglomeration) in cement paste (AM10).

Table 5.5: Compressive strengths of the mortars with different dosages of NT.

Types of specimens	Cement replacement (wt%)	Compressive strength at 7 days curing for samples 1 and 2		Compressive strength at 28 days curing for samples 1 and 2		Average compressive strength (MPa)/increase rate (%) at 7- and 28-days curing	
Mix design	Nano - TiO_2	No: 1	No: 2	No:1	No: 2	7 days	28 days
ACM	0	41.22	38.20	45.80	46.64	39.71/0.00	46.22/0.00
AM2.5	2.5	56.63	57.81	59.60	59.02	57.22/30.60	59.31/22.07
AM5	5	52.40	50.80	55.20	53.20	51.60/23.04	54.20/14.72
AM10	10	38.40	36.08	39.80	40.68	37.24/-6.22	40.24/-12.94

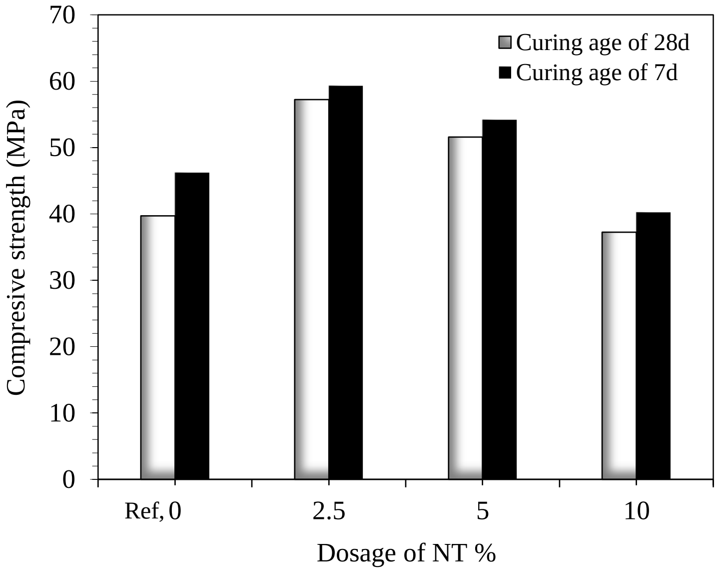

Figure 5.6: Relationships between the average compressive strength and dosage of NT for the curing ages of 7 and 28 days.

The flexural strength of a material is defined as its ability to resist deformation under load. Based on the guidelines of BS EN 12390-5 (BSI, 2009c) Annex A, along with RILEM recommendation, stress is applied on the beam in a continuously increasing manner with a predefined steady rate of about 0.2 mm/min, which is equivalent to 0.0033mm/sec, up to the irredeemable event of failure. The uttermost load is recorded as the flexural strength. Only the maximum load (F) is provided. Therefore, referring to BS EN 12390-5 (BSI, 2009c), the flexural strength is calculated as:

$$f_{cf} = \frac{3FL}{2bh^2} \tag{5.5}$$

where L is the distance between the support rollers, and b and h are the width and height of the beam. There are two forms of flexural strength tests: the four-point bending test and the three-point bending test. For this study, three-point bending method was utilised. The apparatus consisted of two bottom roller supports and a loading roller. One of the support rollers was fixed, while the other supporting roller and loading roller could rotate, as shown in Figure 5.7. Figures 5.8 and 5.9 present the 7 and 28-day flexural properties (load vs deflection curve) of the mortars. The results of the flexural strength show that the best performance was obtained with the AM2.5 and the lowest value was obtained with the AM10 as illustrated in Table 5.6.

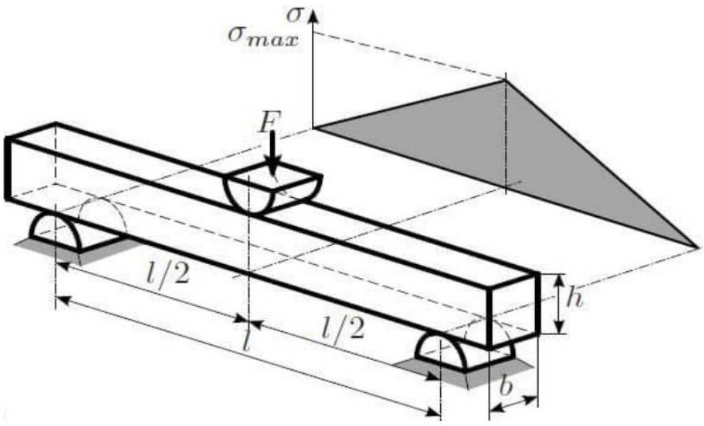

Figure 5.7: Schematic diagrams of three-point bending test.

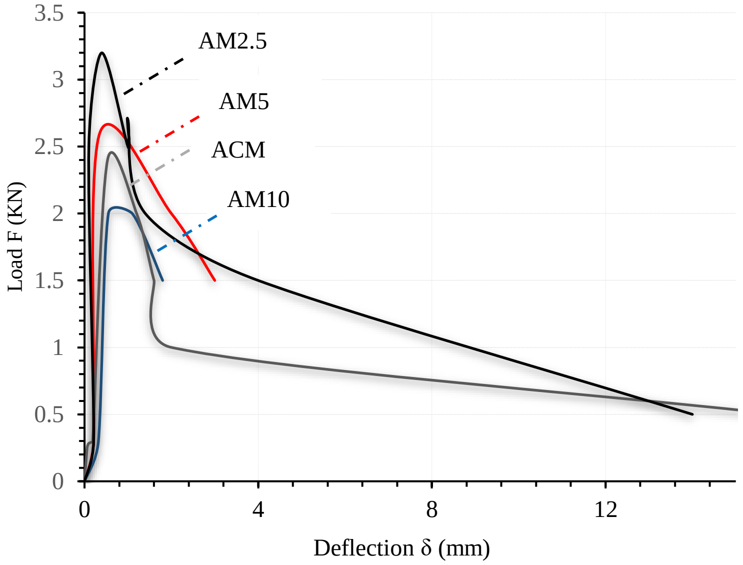

Figure 5.8: Load-deflection curves of the NT mortars at 7 days.

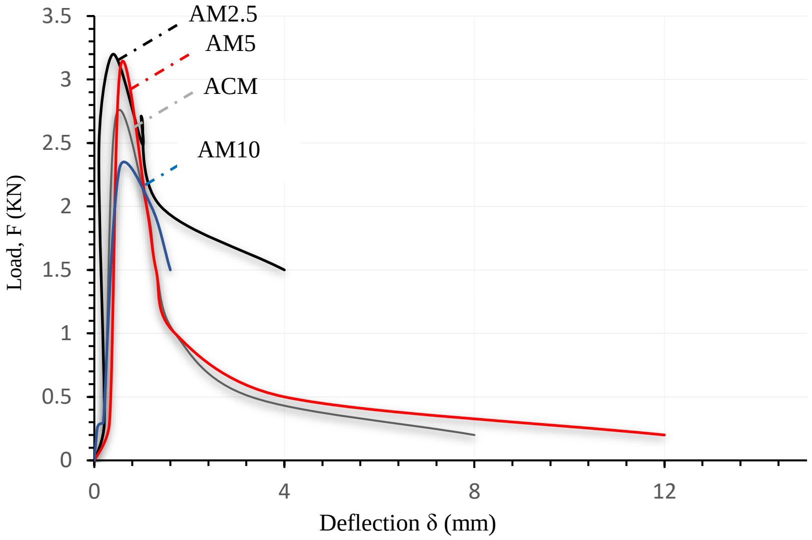

Figure 5.9: Load-deflection curves of the NT mortars at 28 days.

Table 5.6: Maximum forces and flexural strengths at 7- and 28-day curing ages.

Types of specimens	Cement replacement (wt%)	Maximum force at 7 days (MPa)		Maximum force at 28 days (MPa)		Maximum force/ Flexural strength at 7- and 28-days curing	
Mix design	Nano - TiO$_2$	No: 1	No: 2	No:1	No: 2	7 days	28 days
ACM	0	2.2	2.6	2.9	2.5	2.4/3.96	2.7/4.45
AM2.5	2.5	2.9	3.5	3.4	3.0	3.2/5.28	3.2/5.28
AM5	5	2.6	2.6	2.9	3.5	2.6/4.29	3.2/5.28
AM10	10	1.9	2.3	1.9	2.9	2.1/3.46	2.4/3.96

5.4.5 Microstructural analysis

The objective of the microstructural analysis is to support the findings shown in the present research. It is important to notice that the performed microstructural analyses were qualitative, with the objective to give additional information that can explain the obtained results.

In this context, Figures 5.10(a)-5.10(d) represent the SEM images of some selected morphological characteristics of the microstructure of the mortars mixed with NT, *i.e.* 0 wt%, 2.5 wt%, 5 wt% and 10 wt%, at 7 days, showing that samples with different dosages of NT had obvious differences in morphology. The reference sample ACM (Figure 5.10(a)) contained a moderate amount of small pores and medium size C-S-H structures. It had an apparent dense structure and a relatively good ITZ (Figure 5.10(a)).

A good ITZ was defined in the present investigation as the zone (20-30 µm long) in the vicinity of the sand and cement matrix, with a relatively lower amount of gel and air pores. The $\mathrm{Ca(OH)_2}$ crystals were found in the microstructural analysis which was formed in the largest air-voids of the cement matrix.

Fewer ettringites with disordered distribution and a lot of small needle-like crystals were identified and possibly formed with ettringite or other AFt phases. Increasing the NT content up to 2.5 wt% (AM2.5) was linked with a more homogeneous microstructure compared to the reference mix (Figure 5.10(b)).

A homogenous microstructure is defined by a regular morphology and similar size of the hydrates. This microstructure is characterized by apparent compact and small-sized C-S-H gel and the absence of abundant gel porosity. As a consequence, a relatively denser ITZ was also confirmed by SEM (Figure 5.10(b)). On increasing the NT to 5 wt%, the C-S-H gel remained homogeneous and comparable to the 2.5 wt% NT sample.

However, the 5 wt% NT sample now contained larger air-voids compared to the sample AM2.5 (Figure 5.10(c)). Moreover, more agglomerated NT particles were observed. When the added amount of NT reached 10 wt% (AM10), it was still possible to observe some needle-shaped AFt phases and $Ca(OH)_2$ plates in the matrix. However, small size C-S-H gels were formed with larger and more voids produced (Figure 5.10(d)).

The presence of big $Ca(OH)_2$ plates and ettringite at this zone should increases the transport properties and permeability of species through the concrete matrix. This can explain the results obtained for the permeability measurement using high pressure triaxial cell (Section 4.4.2). The microstructure presented high amounts of small pores and medium sized C-S-H gel like structures.

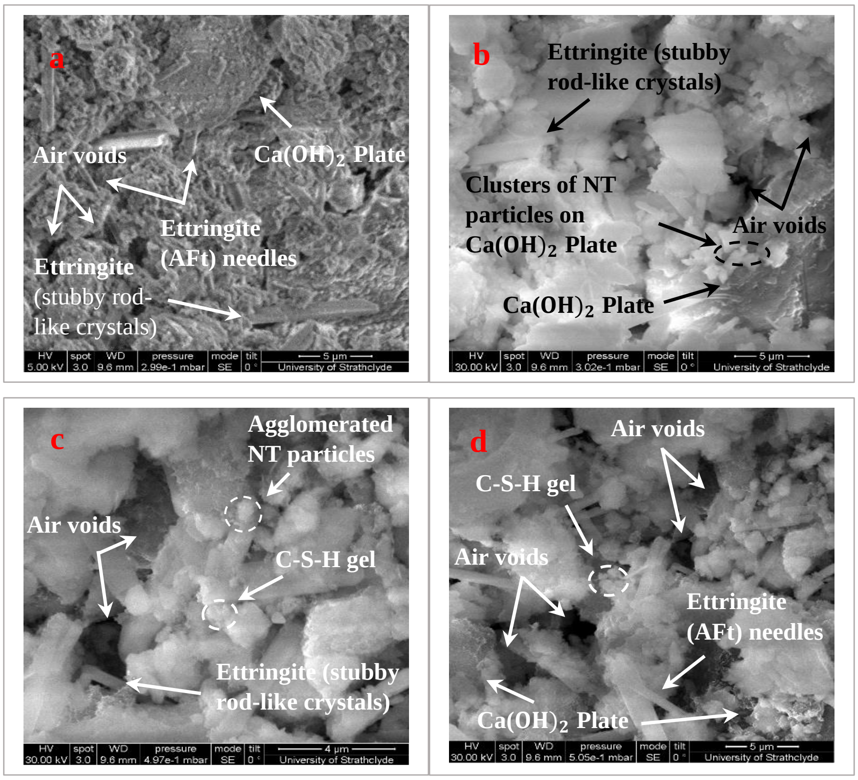

Figure 5.10: Typical SEM images of the specimens with different additions of NT (a) 0%; (b) 2.5%; (c) 5%; (d) 10% at the 7-day curing age.

The microstructure became isolated and defective. The presence of significant amounts of $Ca(OH)_2$ resulted in a lower compressive strength (Gaitero et al., 2008). These findings are in line with the results of the mechanical tests presented in Tables 5.4 and 5.5. The EDS microanalysis in Figures 5.11(a) shows the composition of sample AM2.5 mainly consisted of carbon (C), oxygen(O), silicon (Si), calcium (Ca), and Ti. Additionally, with the help of EDS analysis (Figures 5.11(a) and (b)), a fact that C-S-H grew on the surface of NT particles was verified, which shows that NT played a nucleation role in the cement hydration process.

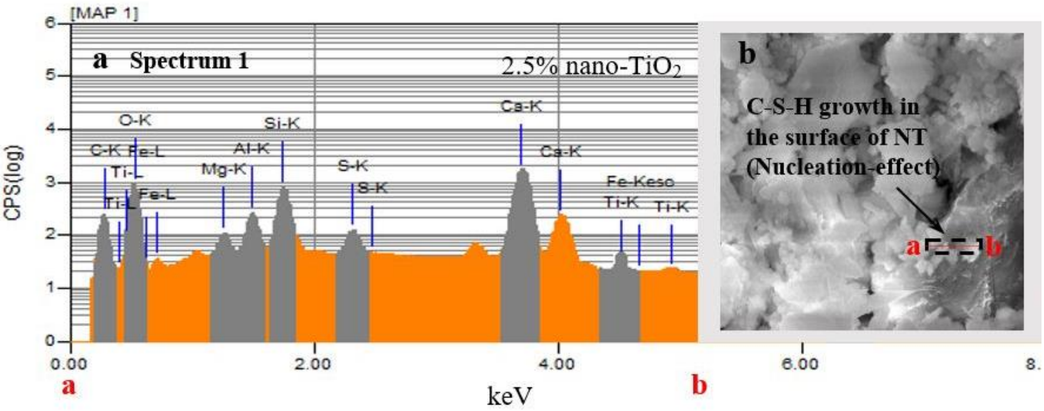

Figure 5.11: Typical SEM image and EDS line analysis of the specimen with 2.5% NT (AM2.5) at the 7-day curing age.

Figures 5.12(a) to 5.12(d) present the SEM images of some selected morphological characteristics of the microstructure of the mortars mixed with NT at 28 days. Figure 5.12(a) shows the microstructure of the reference sample ACM, which presents heterogeneous morphologies, with high number of pores and big sized C-S-H gel. Various micro-cracks were formed on the surface of the reference mix with respect to the axis of specimen, including perpendicular and diagonal as illustrated in Figure 5.13. For hydration at 28 days, increasing the NT content up to 2.5 wt% (AM2.5) was linked with medium sized C-S-H structures and more homogeneous microstructures, compared to the reference mix (ACM). The microstructure of sample AM2.5 contained smaller air-voids compared to sample ACM.

When adding NT to 5 wt%, the C-S-H gel was also homogeneous and comparable to the sample with 2.5 wt% NT inclusion. However, it contained more air-voids compared to the sample AM2.5 (Figure 5.12(c)). Moreover, more agglomerated NT particles were observed. For hydration at 28 days, when the added amount of NT reached 10 wt% (AM10), small - sized C-S-H gel and crystallized $Ca(OH)_2$ plate were formed in the cement matrix (Figure 5.12(d)). The microstructure of sample AM10 contained larger air-voids compare to AM5.

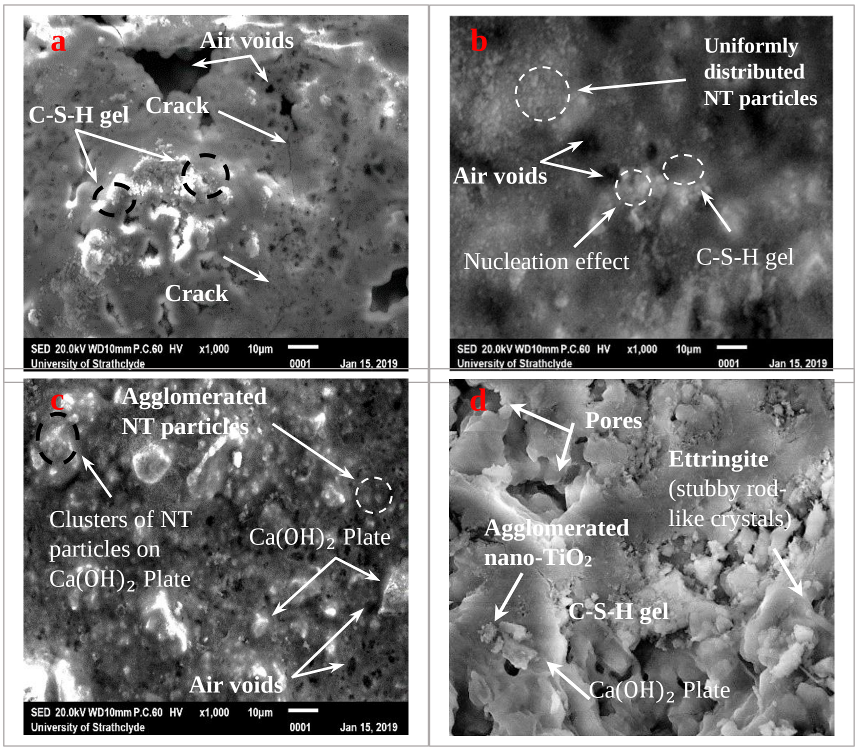

Figure 5.12: Typical SEM image of specimens with different additions of NT (a) 0%; (b) 2.5%; (c) 5%; (d) 10% at 28 days curing.

This could be due to the fact that when the amount of NT exceeds the optimal value, *i.e.* NT > 2.5 wt%, large specific surface area of nanoparticles would absorb additional water and make the agglomeration phenomena easily reachable, leading to the formation of undisrupted pockets within the cement paste matrix and resulting in an increase in porosity of mortars, as the result that the microstructure became isolated and defective. Figures 5.14(a) and (b) and 5.15(a) and (b) show EDS microanalysis and SEM images of the reference sample and cement mortar modified by 2.5 wt% NT, which has demonstrated the highest mechanical properties at the curing time of 28 days than other specimens having different NT percentages (Tables 5.4 and 5.5).

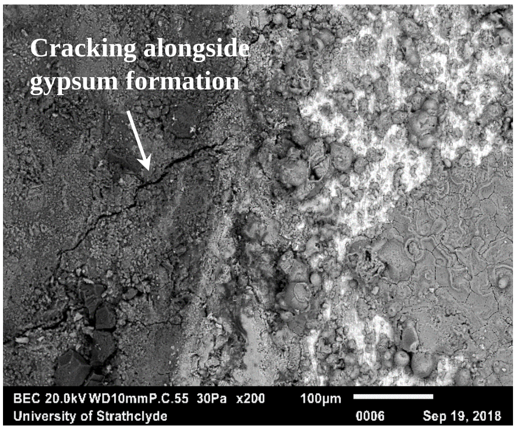

Figure 5.13: Typical SEM image of a specimen with cracking alongside gypsum formation.

By comparing the EDS analysis of sample AM2.5 (Figure 5.15(a)) with ACM (Figure 5.14(a)), it is found that the composition of the sample AM2.5 at 28 days had higher concentrations of calcium (Ca) and oxygen (O) as expected, but also significant amounts of silicon (Si) and sulfur (S) which could yield the conclusion that C-S-H and ettringite were the main hydration products of the specimens with 2.5 wt% NT cured at 28 days.

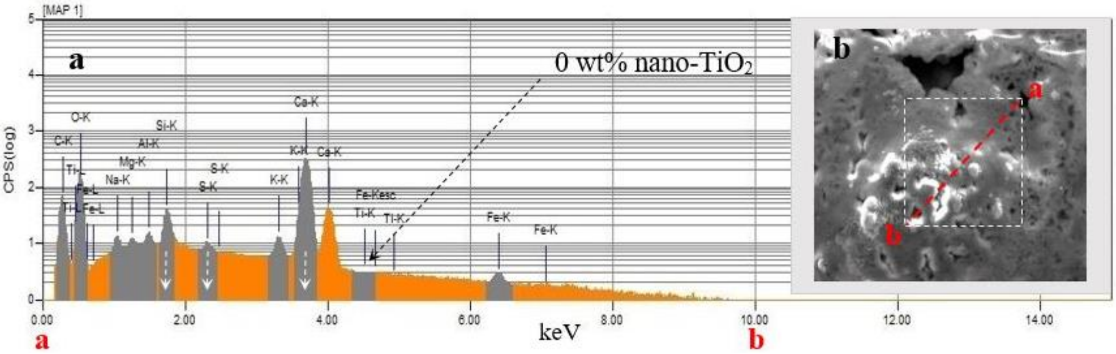

Figure 5.14: Typical EDS analysis (a) and SEM image (b) of the specimen with 0 wt% NT (ACM) at the curing time of 28 days.

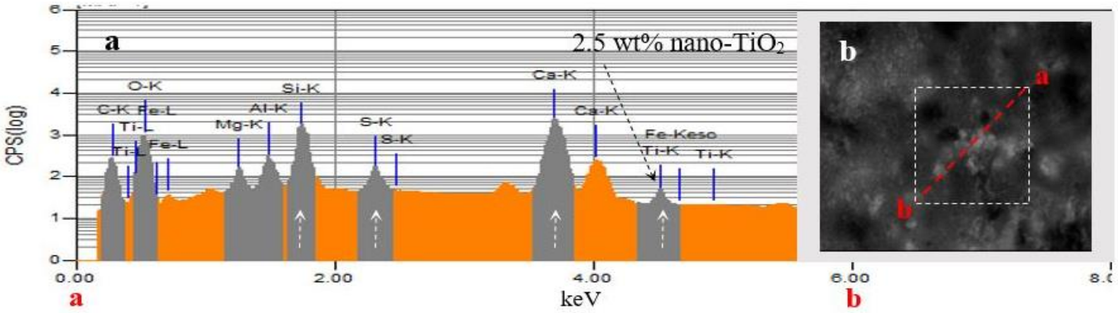

Figure 5.15: Typical EDS analysis (a) and SEM image (b) of the specimen with 2.5 wt% NT (AM2.5) at the curing time of 28 days.

As illustrated in Figure 5.16, the EDX analysis indicates that Ca and Si were the main elements of the reference sample (ACM) with relative weight percentage and Ca/Si ratio as: Ca: 27.76%, Si: 19.41% and Ca/Si ratio of 1.43. The EDS spectra of the samples indicate sample AM2.5 had the Ca/Si ratio of 1.18, the lowest among all the samples cured for 28 days.

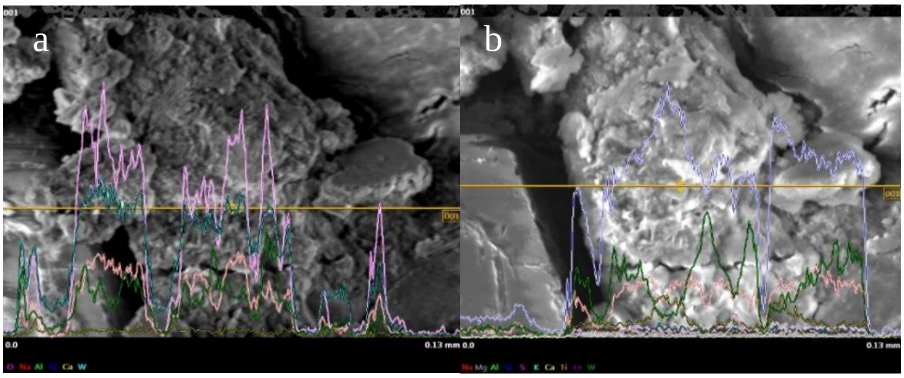

Figure 5.16: Typical EDX-SEM analysis (a) Sample ACM(b) Sample AM2.5 at 28 days

5.5 Remarks

In this chapter, the physical and chemical characteristics of several NT cement mortars including control mix were determined and studied. The change in phase composition and the mechanical evolution of cement mortars incorporated with different percentages of NT were investigated. A novel direct tensile test was conducted to quantify and characterise the mechanical properties of the NT mortar composite. XRD and SEM-EDS were utilised to evaluate the phases of the microstructures. Furthermore, the extent of cement hydration and the exact boundaries of various phases present in the hydrated samples were evaluated by thermogravimetric/derivative thermogravimetric analysis (TG/DTG). Specifically, the main findings can be drawn as follows.

(1) At 28 days, the generation of AFt of each sample reached the maximum compared with that at 7 days, and the mortars with 2.5 wt% NT had the highest amount of AFt phase.

(2) NT is an inert material, it does not react with water, cement. In this study, no other new crystalline phase was found with the addition of NT. The NT particles acted as nuclei for hydration reaction. The hydration products grew around them and filled the voids, thus reducing the porosity.

(3) There was a significant increase in the content of $Ca(OH)_2$ produced from cement hydration when the adding amount of NT increased to 2.5 wt%. With Further increasing the NT (> 2.5 wt%), the intensity of $Ca(OH)_2$ decreased slightly.

(4) The TG-DTG results indicated a significant increase in the extent of bond formation between NT and free calcium hydroxide when the amount of NT increased up to 2.5 wt% at the 7- and 28-day curing ages.

(5) The SEM and EDS results indicated that when the percentage of NT increased to 2.5 wt%, the surface morphology became denser. This is owing to the fact that NT promoted the early hydration and acted as an external nucleation to promote the generation of C-S-H gel, ultimately improving the strength.

(6) The tensile strength of the samples with 2.5 wt% NT at the 7- and 28-day curing ages increased by 31.9% and 26.4% respectively which were considerably greater than those without NT.

(7) With 2.5 wt% amount of NT, the compressive strengths were improved by 30.6% and 22.07% at 7 and 28 days respectively, while the compressive strengths for the of 5 wt% only increased by 23.4% and 14.7% respectively.

Chapter 6

Application of NT Additions in Eco-Cement Composites

6.1 Introduction

The cement industry is considered to be one of the most energy consuming industries, which is also responsible for approximately 8% of the global man-made emissions annually (Bjornstrom et al., 2004; Florence et al., 2010; Shi et al., 2011). In addition, it produces sulfure dioxide (S) and mono-nitrogen oxides (NOx). Hence, to reduce the negative environmental impact, extensive researches have been taking part in developing green cements as replacement materials (Barbhuiya et al., 2009; Ahmaran et al., 2009; Hannesson et al., 2012). Supplementary cementitious materials (SCMs) are widely used in concrete either in blended cements or added separately.

The use of SCMs, such as fly ash (FA), silica fume (SF), hydrated lime (HL) and metakaolin (MK), currently represents a viable solution to partially substitute Portland cement clinker. When these materials are combined with Portland cement through either pozzolanic or hydraulic activity, a contribution towards the properties of hardened concrete is made. As a result, the emission of greenhouse gases are reduced, whilst creating a more economical solution than Portland cement. SCMs are also considered as reactive fines and are added to concrete to improve or influence certain properties, such as workability, strength development or heat release during hydration.

SCMs may be divided into natural materials and artificial ones. The natural materials are true pozzolans and volcanic tuffs. The artificial materials are comprised of siliceous by-products and wastes, such as fly ashes, silica fume and other new waste products such as photovoltaic's waste sludge originating from the manufacturing process of solar panels and electronics. Fly ash is a by-product from thermal power plants, which is widely available in the world. Fly ashes consist mainly of silicate (SiO_2) but can contain also significant quantities of alumina (AL_2O_3). Fly ashes are spherical in nature. Besides the pozzolanic activity, FA plays a role of a micro filler, water reducing agent and prevents the formation of micro-cracks at early ages due to the relatively slow release of the hydration heat (Spiesz, 2013). The amount of CaO in FA is limited for some applications, and it is highly variable depending on the origin. Several standards differentiate and classify fly ashes (BS EN 450-1, ASTM C618, etc) in high calcium (Class C) and low-calcium (Class F) ashes. Class F fly ashes contain between 10 and 35% alumina, so the blending of OPC with such fly ash results in high amounts of Al-rich phases and therefore increased durability of concrete is obtained. Fly ash Superpozz SV80 of class F was utilised in the present research, which complies with BS EN450-1 (BSI, 2002).

In recent years, there has been a growing interest in the use of metakaolin (MK) as a mineral admixture to enhance the strength and durability of concretes. A comprehensive review of the studies on the use of MK as a partial pozzolanic replacement for cement in mortar and concrete has recently been reported by Sabir et al. (2001). It was reported that the concrete incorporating 10% MK had a higher compressive strength than the reference plain concrete (Sabir et al., 1996; Zhang et al., 1995).

With respect to the durability aspects, the resistance of MK concrete to water or chloride ion penetration is significantly higher than the control concrete (Zhang et al., 1995; neyisi et al., 2007; neyisi et al., 2007). Metakaolin has been widely studied for its highly pozzolanic properties, suggesting that metakaolin could be used as an SCM. Unlike other SCMs that are secondary products or by-products, metakaolin is a primary product, obtained by calcining kaolin clay within a temperature range of 650 to 800 C°

(Ramezanianpour et al., 2012; Guneyisi et al., 2012). Metakaolin is increasingly being used to produce materials with higher strength, denser microstructure, lower porosity, higher resistance to ions, and improved durability (Güneyisi et al., 2007). An overview of the physico-chemical properties determined for all SCMs applied in this study have been given in Tables 2.9 and 2.10. Additionally, Figure 6.1 shows their PSDs taking into account the sieve sizes (ISO sieves) presented in Table 2.1.

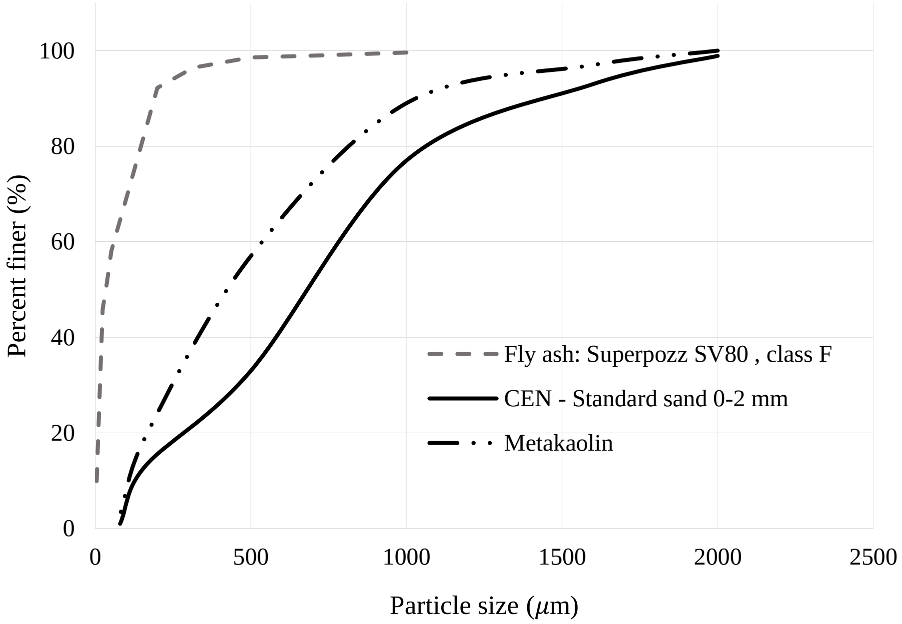

Figure 6.1: Grading curves of the SCMs determined by sieve analysis.

Amongst these various supplementary cementitious materials, FA is the most abundantly available material worldwide (Heidrich et al., 2013). Palomo *et al.* (1999) showed the great potential of FA as an alternative to cement for the future. However, the majority of global FA production falls into the low calcium class F category which has very low reactivity (Wang et al., 2007) and very slow hydration characteristics, thus providing a little contribution to the early age strength (Boukni et al., 2009). Several studies have been performed in the past to address its low reactivity and to improve the mechanical properties of FA cement composites by making use of various materials such as silica fume (Barbhuiya et al., 2009), metakaoline (Güneyisi and Gesoğlu, 2008).

Güneyisi and Gesoğlu (2009) pointed out that the combined use of metakaoline with FA in the ternary blends provided significant reduction in the setting times of the mortars when compared to that containing only FA. Recently, there has been a strong inclination towards the use of nano materials in improving the properties of plain cement and high-volume FA blended mixes because of its highly amorphous nature and nano sized particles. However, most of the researches on nanoparticles were done with nano silica (Zhang et al., 2012; Shaikh et al., 2014; Li, 2004) in cement-based materials. Hou *et al.* (2013) have found that the overall performance of concrete with FA was significantly improved with the addition of variable dosages of nano silica.

In the recent years, a growth in innovative research has been seen on the application of NT in construction materials, due to its safety, chemical stability, self-cleaning and air purifying properties (Zhang et al., 2011; Ma et al., 2015; Nazari., 2011; Leng et al., 2013; Nazari et al., 2010). The addition of NT particles into cement concrete is gaining an attention due to their high surface area and consequently high reactivity. The influence of NT particles on the hydration of cementitious materials was examined by researchers (Lee et al., 2010; Chen et al., 2012) and shown to enhance hydration due to the high specific surface area of NT particles, increasing the nucleation sites for the hydration reaction. Furthermore, the addition of NT particles has been shown to improve the densification of the microstructure, thereby enhancing the durability of the cementitious materials (Nazari., 2011).

Although different aspects of cement-based materials containing FA, MK and NT particles separately have been reported in the literature, to the authors' knowledge, there is no systematic study on the influence of NT in conjunction with FA and MK on the overall performance of cementitious materials. In particular, the effects of FA and MK as by-product materials and NT as a high surface area additive on the permeability, high brittleness, change in phase composition and pore structure properties of cementitious materials which lead to a decline in performance and service life of the building materials need to be studied in detail. This uncertainty casts doubt on the widespread application of the fly ash cement composites modified with NT particles. Therefore, this chapter aims to address this knowledge gap by investigating the permeability, and porosity of FA and MK cement composites modified with NT particles.

In this respect, the pore structures of the composites containing NT, FA and MK were thoroughly analysed. Different percentages of ordinary Portland cement (OPC) were replaced with combined use of NT from 0 wt% to 10wt% and FA and MK within the range of 10 wt% to 30 wt%. The NT-modified FA and MK cement samples were analysed by X-ray computed tomography (XCT) to examine the pore configuration in the matrix. In addition, the samples were analysed by scanning electron microscopy (SEM) and X-ray diffraction (XRD).

Derivative thermogravimetric (DTG) curves were plotted from the TG data to identify the extent of cement hydration and the exact boundaries of various phases or group of phases present in the hydrated samples. 2D and 3D porosity calculations were carried out to find the pores and their exact size, position and distribution from the pore network using a Nikon XT H 225/320 LC X-ray computed tomography system. In addition, reconstructed tomography images were used to extract the main parameters of porosity.

The number of pores in the scanned volume, as well as the volume and shape of individual pores were determined. Moreover, the nanoscale surface areas and nano pore volume and shapes of the NT-modified fly ash composites were measured by Brunauer-Emmett-Teller (BET) and Barrett-Joyner-Halenda (BJH) analyses.

6.2 Experimental

6.2.1 Materials

Different percentages of OPC, Provided by Jewson, which complies with BS EN197 Part 1 (BSI, 2000), with a Grade of 42.5 N/mm^2, was replaced with anatase NT, *viz*. 0 wt%, 2.5 wt%, 3.5 wt%, 5 wt% and 10 wt% and FA/MK within the range of 10 wt% to 30 wt%. Natural river sand, with a minimum particle size of 150 µm served as the fine aggregate. Fly ash, Super-pozz® SV80 of class F, was utilised in the project, which complies with BS EN450 (BSI, 2002). The mineralogical phases and chemical composition of the raw materials used were obtained from the X-ray diffraction (XRD) and X-ray fluorescence (XRF) analyses.

An overview of the chemical composition of cement and FA is given in Tables 6.1. The NT particles used in this research was obtained from ALDRICH and had a specific surface area of 35-65 m^2/g. A summary of the physical properties and of the NT, FA, sand and cement is given in Table 4.1 and Table 6.2. Deionised water, with a pH value of 7.5 at 22°C, was used throughout the experimental research.

Table 6.1: Chemical compositions of the used cement and fly ash.

Composition (wt.%)	SiO_2	Al_2O_3	Fe_2O_3	CaO	MgO	K_2O	Na_2O	SO_3	TiO_2	LOI
CEM I 42.5 N	20.62	3.52	2.98	63.21	1.92	0.74	-	3.12	0.45	3.44
Fly Ash SV80	55.68	19.92	8.65	5.35	1.44	2.13	1.15	0.25	-	5.43
Metakaolin	53.67	37.32	2.11	0.76	0.21	0.65	0.23	2.73	-	3.55

Table 6.2: Physical properties of the materials used.

Properties	Fluvial sand	CEM I 42.5 N	Fly ash (class F)	Metakaolin
Size	150 µm–4	0.2 µm–200 µm	0.15 µm–150 µm	0.17 µm–190 µm
Specific density (g/cm^3)^2	2.56	3.112	2.184	2.728
D_{min}(mm, µm)	150 µm	0.23µm	0.19µm	0.170
D_{max}(mm, µm)	4.3mm	160µm	140µm	18.6
Shape factor (ξ)^1 (-)	1.10	1.73	1.09	1.15
Specific surface area (m^2/m^3)^2	17,568	692,145	989,183	792,145

1). Referential values taken from Hunger (2010).
2). Provided by Jewson, Scotland.

6.2.2 Mixing procedure

The experimental study involved the application of different samples grouped into 7 sets according to their NT, FA, and MK contents. In the first part of the experiment different percentages of OPC were replaced with NT (design set 1). The experimental study involved the application of a pan mixer with a 30 kg capacity. The fine aggregate was first poured into the pan-mixer, followed by the OPC CEM I 42.5N and FA/MK, under dry conditions. They were mixed for 45 seconds to ensure homogeneity. The mixing continued for another 3.5 minutes before water, already mixed with nano titanium dioxide, was added and the mixing was allowed to continue for another 5 minutes. In the second part of the experiment, different percentages of OPC were replaced with combined use of NT, from 0 to 10 wt% in mass of the cement and FA and MK within the range of 10 to 30 wt% based on BS EN197 (BSI, 2000) and then grouped into 6 sets (A, B, C, D, E, and F).

Table 6.3: Mix proportions of the test specimens

Mix design Set 1, A, B and C	(OPC) Cement/Fly ash (kg/m^3)	Cement replacement (wt%) Nano - TiO_2	Mix proportion (kg/m^3)	
			Fine	Water
CM. (W/C: 0.40), (W/B: 0.00)	227.30/0.00	0	318.2	90.92
M2.5 (W/C: 0.40), (W/B: 0.00)	227.30/0.00	2.5	318.2	90.92
M3.5 (W/C: 0.40), (W/B: 0.00)	227.30/0.00	3.5	318.2	90.92
M10 (W/C: 0.40), (W/B: 0.00)	227.30/0.00	10	318.2	90.92
AM3.5. (W/C: 0.44), (W/B: 0.41)	197.37/21.93	3.5	318.2	93.01
AM5. (W/C: 0.44), (W/B: 0.41)	194.31/21.59	5	318.2	93.01
AM10. (W/C: 0.44), (W/B: 0.41)	184.05/20.45	10	318.2	93.01
BCM. (W/C: 0.45), (W/B: 0.39)	181.84/45.46	0	318.2	87.96
BM2.5. (W/C: 0.45), (W/B: 0.39)	177.28/44.32	2.5	318.2	87.96
BM3.5. (W/C: 0.45), (W/B: 0.39)	175.84/43.86	3.5	318.2	87.96
BM5. (W/C: 0.45), (W/B: 0.39)	172.72/43.18	5	318.2	87.96
BM10. (W/C: 0.45), (W/B: 0.39)	163.60/40.90	10	318.2	87.96
CCM. (W/C: 0.47), (W/B: 0.37)	159.11/68.19	0	318.2	84.39
CM2.5. (W/C: 0.47), (W/B: 0.37)	155.12/66.48	2.5	318.2	84.39
CM3.5. (W/C: 0.47), (W/B: 0.37)	153.51/65.79	3.5	318.2	84.39
CM5. (W/C: 0.47), (W/B: 0.37)	151.13/64.77	5	318.2	84.39
CM10. (W/C: 0.47), (W/B: 0.37)	143.15/61.35	10	318.2	84.39

Slump tests were then carried out according to BS EN 12350-2 (BSI, 2009a). The mix proportion design resulted with slumps ranging from 10 to 23 mm and vebe times ranging from 8 and 16 seconds which met the required workability based on BS EN 12350-2 (BSI, 2009). The recorded mix design, water/’equivalent cement’ ratio and water/binder ratio for each set are presented in Table 6.3 and Table 6.4.

Table 6.4: Mix proportions of the test specimens

Mix design Set 1, D, E and F	(OPC) Cement/MK (kg/m^3)	Cement replacement (wt%) Nano - TiO_2	Mix proportion (kg/m^3)	
			Fine	Water
DM2.5. (W/C: 0.44), (W/B: 0.41)	199.44/22.16	2.5	318.2	93.01
DM3.5. (W/C: 0.44), (W/B: 0.41)	197.37/21.93	3.5	318.2	93.01
DM5. (W/C: 0.44), (W/B: 0.41)	194.31/21.59	5	318.2	93.01
DM10. (W/C: 0.44), (W/B: 0.41)	184.05/20.45	10	318.2	93.01
ECM. (W/C: 0.45), (W/B: 0.39)	181.84/45.46	0	318.2	87.96
EM2.5. (W/C: 0.45), (W/B: 0.39)	177.28/44.32	2.5	318.2	87.96
EM3.5. (W/C: 0.45), (W/B: 0.39)	175.84/43.86	3.5	318.2	87.96
EM5. (W/C: 0.45), (W/B: 0.39)	172.72/43.18	5	318.2	87.96
EM10. (W/C: 0.45), (W/B: 0.39)	163.60/40.90	10	318.2	87.96
FCM. (W/C: 0.47), (W/B: 0.37)	159.11/68.19	0	318.2	84.39
FM2.5. (W/C: 0.47), (W/B: 0.37)	155.12/66.48	2.5	318.2	84.39
FM3.5. (W/C: 0.47), (W/B: 0.37)	153.51/65.79	3.5	318.2	84.39
FM5. (W/C: 0.47), (W/B: 0.37)	151.13/64.77	5	318.2	84.39
FM10. (W/C: 0.47), (W/B: 0.37)	143.15/61.35	10	318.2	84.39

6.2.3 Specimen preparation

After ascertaining that the mixture met the required workability and cohesion for the specified design mix, moulds with a diameter of 25 mm and a length of 75 mm were designed using commercial CAD software Rhino 3D® and then printed by Ultimaker® 2+ 3d printer. The moulds were then treated with oil to enable later separation from the mortars, which were poured into the mould to create the design suitable for X-ray computed tomography system. Following removal from the moulds, they were covered with polythene sheets and allowed to harden for 36 hours. The specimens were then stored in a water bath at 20 ± 3 °C and 95% relative humidity until the required curing age of 28 days before testing. In the present research, in order to perform the BET analysis, the samples were dried in the oven at 65°C for 24 hours under 10^{-2} kPa of vacuum and then ground to fine powders and passed through a 100 µm sieve. For SEM test, circular samples with a diameter of 12 mm and a thickness of 3 mm were made using a diamond saw and cured for 28 days. The circular samples were dried in a vacuum oven at 45°C until a constant weight was reached. These specimens were then impregnated with epoxy, polished and sputter coated.

For permeability test, NT-modified fly ash composite cylinders, with the diameter of 100 mm and the length of 150 mm were cast and vibrated on a concrete vibrating table. The specimens were then demoulded and left to cure for 28 days. Circular sections with the diameter of 35 mm and the thickness of 70 mm were extracted from the samples using a diamond precision cutter. Each sample was prepared by a process of vacuum saturation where the specimen was placed under vacuum for about 4 hours and then submerged in the de-aerated water while it was still under vacuum. The vacuum was maintained for an additional 6 hours and then released. The specimen was then left under water for 10 hours prior to insertion into a permeability cell. An essential requirement of permeability testing is that the pore space must be fully saturated by the permeating fluid. In practice, this implies that for a water-based permeability testing, all air within the communicating pores must be removed and replaced with water.

6.3 Testing Procedure

6.3.1. 2D and 3D porosity analysis

In order to investigate the nature of the pore structure configuration of the NT-modified FA and MK composites, XCT tests were carried out. Unlike the more traditional methods for characterization of microstructure, e.g., mercury intrusion porosimetry (MIP) and scanning electron microscope (SEM), XCT could provide a more complete picture of the pore distribution, including interconnected and isolated pores, with 2D and 3D images, with no need of any prior drying preparation.

The NT-modified fly ash samples were subjected to CT scans with a Nikon XT H 225/320 LC in the Advanced Materials Research Laboratory (AMRL) CT scanner facility at the University of Strathclyde as illustrated in Figure 6.2. Scans of 2.5 μm resolution were achieved at an operating voltage of 140 kV, a current of 120 μA, and with 3141 projections recorded during one full rotation of the sample. This operating condition resulted in approximately 40 minutes per scan, excluding sample setup and background detector calibration. The 3141 2D projections were reconstructed into a 3D volume with CT PRO 3-D (Nikon Metrology). Quantitative analysis was carried out using the image analysis software ImageJ and the results visualised in 3D with ParaView. Low-density air-filled voids were distinguished from the higher density cement matrix by their relative difference in X-ray attenuation, and then binary segmentation was applied (via a global threshold) so that the volumes of each phase, and hence the porosity, could be calculated.

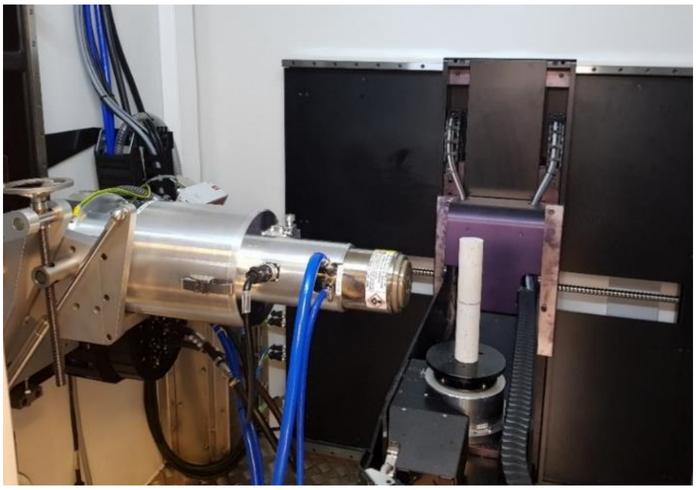

Figure 6.2: Experiment setup of the micro-XCT analysis.

6.3.2. Permeability measurement using high pressure core holder

A general view of the experimental setup for conducting water-permeability measurement using a high-pressure Hassler type core holder was presented in Chapter 3. For the purposes of the experimentation, NT-modified FA and MK composites in cylindrical geometry with a diameter of 35 mm and a thickness of 70 mm were extracted using a diamond saw from the samples. In order to improve the analysis of the data, the permeability measurement results of the specimens were compared with the result of a low permeability sandstone core and a steel cylinder with zero permeability, each with the same dimensions as the geopolymer samples. Similar to the experiment carried out in Chapter 4, the permeability measurement was performed under steady-state conditions.

The vacuum saturated core sample was mounted in the core holder and then placed under a suitable confining pressure of 3 MPa to ensure a tight seal around the sample and minimal bypass of injected fluid around the sample. The water was then flowed through the sample under a constant pressure gradient (max 2.5 MPa) until steady-state flow was reached. The flow rate and the pressure drop were then recorded. The test was repeated at different sets of flow rate and inlet pressure and the data were recorded. Controlling the temperature of the environment surrounding the permeability set-up contributed to pressure stability, so the test temperature was maintained at 22 ± 2.0 °C. A constant pressure was applied to the inlet of the sample and the pressure drop from inlet to outlet was recorded with a differential pressure transducer. The cumulative volume injected to maintain this constant pressure was recorded at fifteen second intervals, accurate to ± 0.5 mm^3, and was used to calculate the flow rate. Permeability was calculated by rearranging Darcy's law (Equation (3.7)).

A general view of the data and constants for conducting water-permeability measurement of the composites, sandstone and steel is presented in Table 4.4. The transient tests were conducted for 18 hours, but only the first 2100 seconds of data were used to determine the permeability of the samples. An initial injecting pressure of 2 MPa was adopted and ordinary tap water at room temperature was used as the permeating fluid.

6.3.3. Microstructural analysis using SEM

SEM analyses were performed using a JEOL JXA840A type SEM instrument. For preparation of the SEM samples, approximately 1 g of a sample taken from the middle of each mortar specimen was placed on a standard mount with 1.5 cm in diameter and 0.2 cm in depth under a vacuum and coated with a 10 nm thick conductive layer of gold to prevent charging prior to imaging. The applied voltage and current values were 20.0 keV and 30.0 mA, respectively.

6.3.4 Measurement of nano surface area, pore size and pore volume using BET

The specific surface area and pore volume of the composite powders were determined by physical adsorption of a gas on the surface of the solid and by calculating the amount of adsorbate gas corresponding to a monomolecular layer on the surface. Physical adsorption resulted from relatively weak forces (van der Waals forces) between the adsorbate gas molecules and the adsorbent surface area of the test powder. The determination is usually carried out at the temperature of liquid nitrogen. The amount of gas adsorbed can be measured by a volumetric or continuous flow method. The surface areas and the pore size diameter were calculated by the Brunauer-Emmett-Teller (BET) and Barrett-Joyner-Halenda (BJH) procedures, respectively, from data obtained using a micromeritics ASAP2020. The whole analysis was performed in the range between 0.05 and 0.25 p/p^o, where p^o is the nitrogen condensation pressure and p the pressure used by the equipment in the respective analysis period.

6.3.5 Identification and quantification of the formed hydrates through x-ray diffraction and thermo-gravimetric analysis

X-ray diffraction analysis was employed to study the effect of different dosages of NT in conjunction with FA and MK on the formation of various phases in the hydration products of cement mortars. The diffraction spectra of the hydrated specimens were acquired after curing for 7 and 28 days.

Powder samples were loaded on the aluminium sample holder having dimensions of 2 cm × 1·5 cm × 0·2 cm (vol. 0·6cm^3). X-ray diffraction analysis was performed using a Bruker D8 Advance with Cu-Kα x-rays with a wavelength λ=1.5406 Å, and the data was taken over the 2θ range of 5° to 70° with a step of 0.02° under an operating voltage of 30 kV and a working current of 120 mA. After identifying the existing phases in the cement using XRD, quantification of the formed hydrates was performed using thermogravimetry analysis in a thermobalance Perkin Elmer TGA7 with a TAC7/DX controller, in a N_2 atmosphere. The temperature ranged from 22 to 1000 °C at a heating rate of 10 °C/min. An analytical Gas N_2 5.0 was used to protect the balance at a flow of 20 mL min^{-1}, and the volatized gases were purged at a rate of 60 mL min^{-1}.

6.3.6 Mechanical tests

Direct compression and tension tests were conducted, for several NT, FA, and MK dosages. To determine the mechanical strengths of the samples, the compressive strengths were evaluated from the peak load obtained by crushing the specimens according to BS EN12390-3 (BSI, 2009). The specimens used in the compression tests were in the dimensions of 100 mm × 100 mm × 100 mm. The cubes used for the compression test were cured in tap water for 7 and 28 days and taken out of the water one day prior to the testing.

The tension tests consisted of a tension testing machine (Instron 5969®) with a loading capacity of 50 kN and dog-bone shaped samples with dimensions began with the cross section of 10 mm × 40 mm and changed to 20 mm × 40 mm in prismatic shape after 10 mm away from each ends of the samples with the length of the cross section as 70 mm as shown in Figure 6.3. The dog-bone specimens were glued to steel supporting plates and final fin plates would be fixed at each end through an epoxy resin-based bicomponent as shown in Figures 6.4(a) and (b). The specimens were notched with a circumferential notch with a depth of 5 mm +/- 1 mm and a width of 2.5 mm. This set-up made it possible to control the eccentricities of the tensile load during the tests.

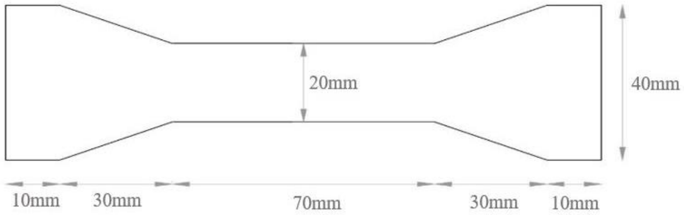

Figure 6.3: Detailed geometry of the dog bone shaped specimen.

The ends of the steel specimen were gripped within the test frame to eliminate any relative end rotation and ensure that uniaxial stresses were generated in the specimen. In this test, the displacement control at the rate of 0.6 mm/min was applied to the steel rod and the tensile load delivered to the sample to get the accurate readings for the stress-strain curve.

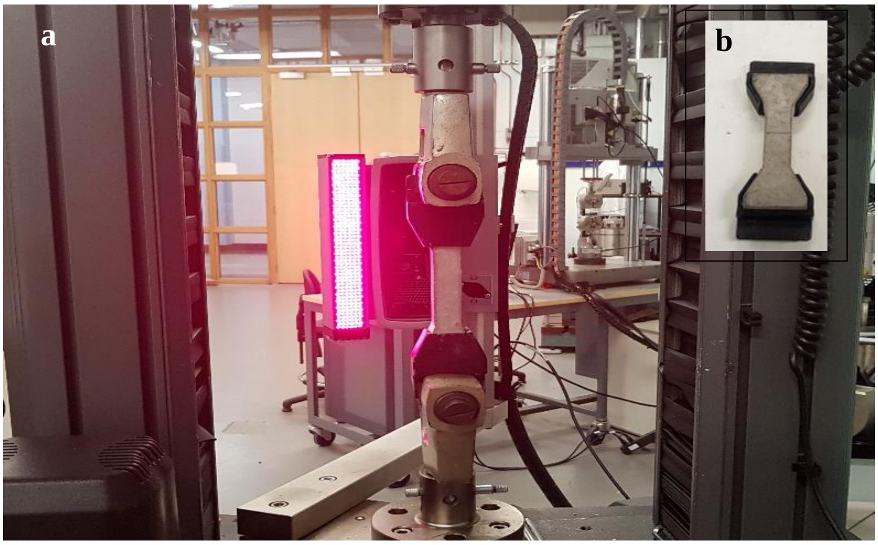

Figure 6.4: a). A general view of the experimental setup for conducting tensile tests on dog boned shaped samples. b). Steel supporting plates gripped within the test frame.

This set-up made it possible to control the eccentricities of the tensile load during the tests. The specimens used to test the tensile strengths of the NT-modified fly ash samples were moulded based on BS EN12390-1 (BSI, 2012). However, in some instances these samples were modified, or new samples were designed to accurately capture the relevant behaviours of the samples. For instance, in the case of direct tensile test, as the concrete specimens were quite detailed (dog-bone shaped), and Ultimaker 2 + plus 3D printer was used in order to print the moulds. Initially the moulds were designed using commercial CAD software Rhino 3D® as shown in Figures 6.5 and 6.6.

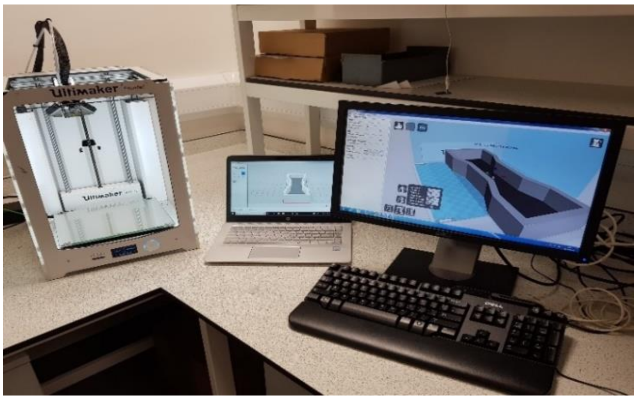

Figure 6.5: Design of the moulds using Rhino 3D®.

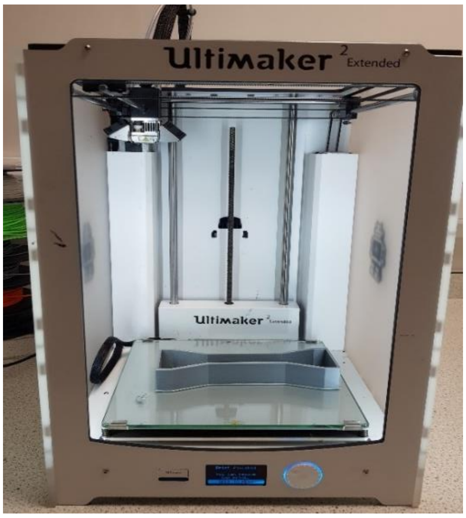

Figure 6.6: Design and printing of the dog-bone shape moulds using Ultimaker 2+ plus 3d for direct tension tests.

6.4 Results and Discussion

6.4.1 2D and 3D porosity obtained from X-ray CT

The recorded 3D volumetric void fractions and 2D area void fractions for the samples in mix design set 1, with different doses of NT, at the 28-day curing age are presented in Table 6.5. In order to have more accurate analysis, three samples of each mix were analysed in this section. To increase the efficiency in data acquisition, two samples were analysed at the same time which also helped to have more accurate analysis by selecting the same setting for both samples. The experiment setup for micro-XCT analysis and the final 3D visualization of porosity are presented in Figures 6.7 and 6.8.

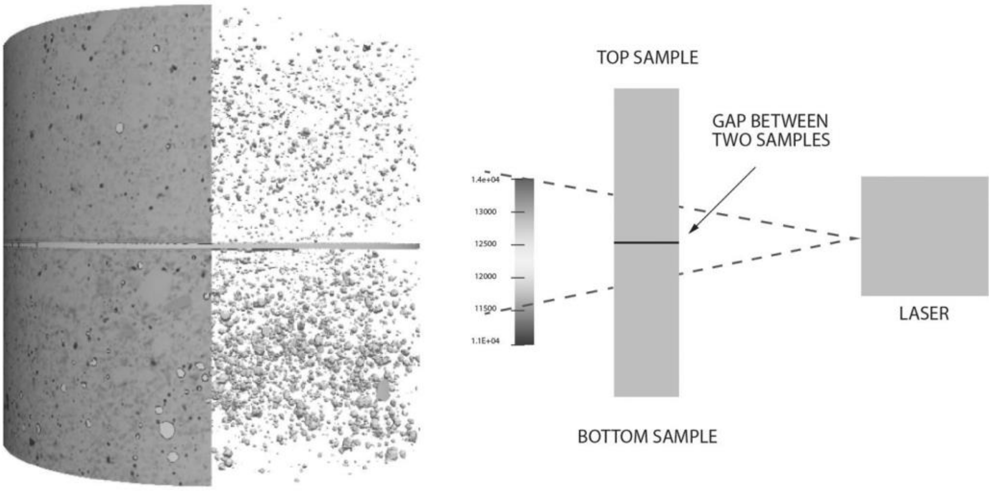

Figure 6.7: Experiment setup for the micro-XCT analysis and final 3D visualization of porosity.

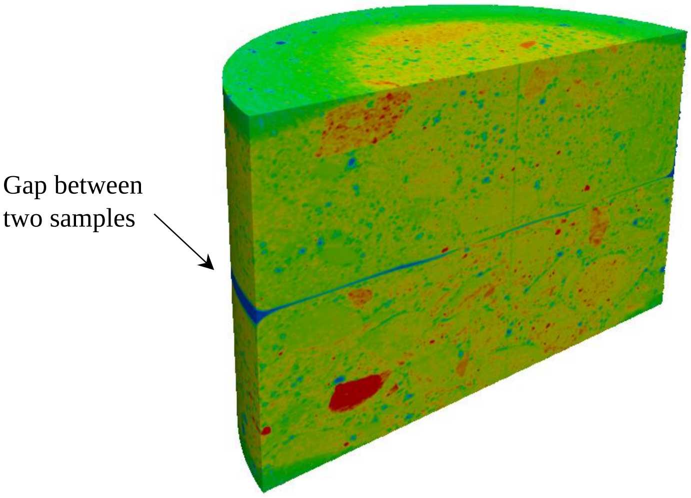

Figure 6.8: Final 3D visualization of porosity.

An example of such a scan is shown in Figure 6.9. This shows the data for sample CM (control mix without NT), located at bottom, and sample M2.5 (contain 2.5 wt% NT) at the top which had the lowest porosity amongst all specimens tested in mix design Set 1, with the voids removed and visualized in 3D with a grey colour. The 3D volumetric void fraction and 2D area void fraction for sample CM and M2.5 were (7.13% and

8.20%) and (2.42% and 3.26%) respectively. The slightly different volumetric values can be explained by slightly different sub volumes (top and bottom edges were cropped to eliminate edge artefacts). As shown in Table 6.5 the improvement of the microstructure of the samples due to the fact that the presence of the NT was observed with increasing its content up to 2.5 wt%. With further increasing the NT content, the average porosity of the samples increased slightly. A refinement of the structure can also be noticed by comparing 3D visualization of porosity of sample CM (bottom) and M2.5 (top), as illustrated in Figure 6.5.

Table 6.5: The recorded 3D volumetric void fractions and 2D area void fractions for the samples in Mix 1.

Code number of Cement Mortars	Cement replacement (wt%) Nano - TiO_2	3D Volumetric void fractions (%). Sample 1, 2 and 3			Average 3D volumetric void fractions (%)	2D area void fractions (%). Sample 1, 2 and 3			Average 2D area void fractions (%)
		No: 1	No: 2	No: 3		No: 1	No: 2	No: 3	
ACM	0	7.22	8.11	6.06	7.13	8.33	7.96	8.31	8.20
AM2.5	2.5	2.12	2.96	2.18	2.42	3.12	3.44	3.22	3.26
AM3.5	3.5	2.42	2.78	2.63	2.61	3.33	3.56	3.37	3.42
AM5	5	3.98	4.44	4.24	4.22	6.11	6.42	5.83	6.12
AM10	10	5.98	6.12	4.91	5.67	7.22	6.94	7.56	7.24

Figure 6.9: 3D visualization of the porosities of the samples CM (bottom) and M2.5 (top)

In the second part of the experiment, different percentages of OPC were replaced by combined use of NT, *i.e.* 0 wt%, 2.5 wt%, 5 wt% and 10 wt% and FA within the range of 10 wt% to 30 wt%. The samples in mix 2 were grouped into 3 sets (A, B, C). Set A contained 10 wt% FA, Set B contained 20 wt% FA, and Set C contained 30 wt% FA.

The recorded 3D volumetric void fractions and 2D area void fractions for the Mix 2 samples are presented in Table 6.6. An example of such a scan is shown in Figure 6.10(a), representing sample CCM with the highest average porosity, and 6.10(b), representing sample AM2.5 with the lowest porosity amongst all specimens tested. The 3D volumetric void fraction and 2D area void fraction for sample CCM and AM2.5 were (13.02% and 12.12%) and (2.56% and 3.20%) respectively.

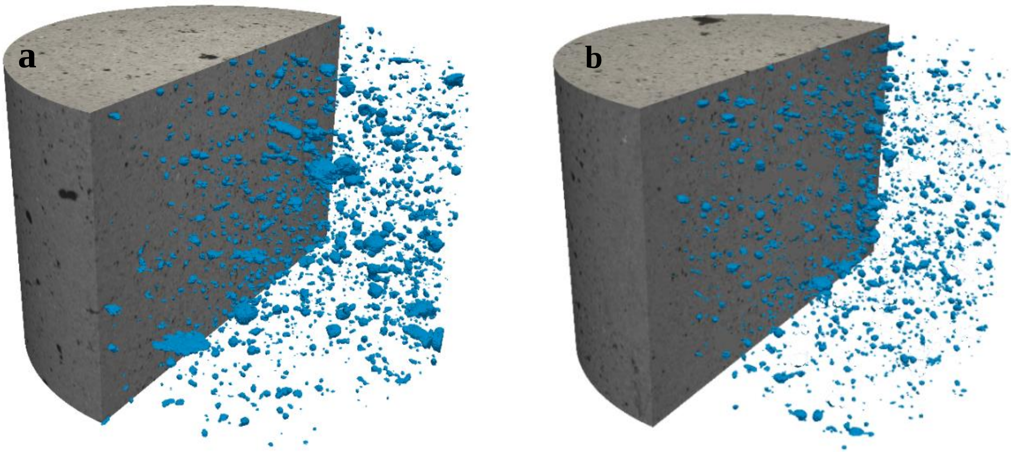

Figure 6.10: a) 3D visualization of porosity of sample CCM, b) 3D visualization of porosity of sample AM2.5.

The difference can also be quantitatively calculated from Table 6.6, *i.e.*, the 3D volumetric void fraction of CCM was about 5 times that of AM2.5. Moreover, the relationships between 3D volumetric void fractions, 2D Area void fractions and NT content for the 28-day curing age are presented in Figures 6.11 and 6.12.

In order to have more accurate analysis, five subvolumes of 5 mm^3 were extracted (as shown in Figure 6.13) from the outer part to the inner part of the sample CCM and AM2.5. Porosity was measured using an intensity threshold algorithm, and the relative volume percentage was calculated with the volume fraction operator. The results indicate that the average 3D volumetric void fraction of CCM (2.64%), in subvolumes of 5 mm^3, was about 4.1 times of AM2.5 (0.65%). The results also showed the increase in porosity from the outer to the inner for sample AM2.5, showing relative values of

0.13% and 2.14% as illustrated in Figure 6.14. The difference in the spatial distributions of porosity in this case became up to 16 times. Such a non-uniform distribution of porosity in the NT fly ash cement samples favoured the durability of the composite as surface area of the samples had much lower porosity.

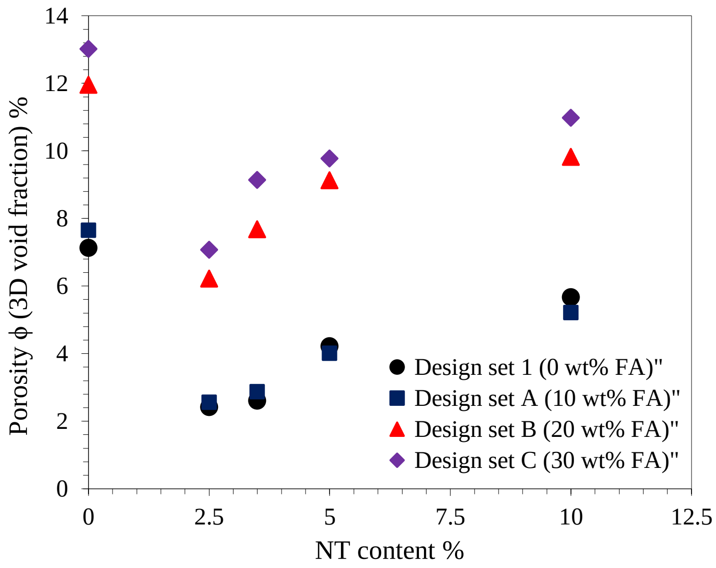

Figure 6.11: Relationships between 3D volumetric void fractions and NT content at 28 days.

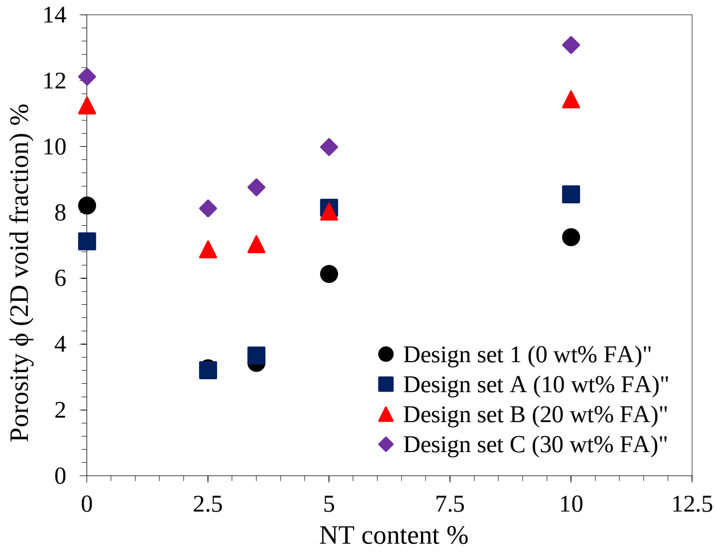

Figure 6.12: Relationships between 2D area void fractions and NT content at 28 days.

2D analysis of porosity of sample AM2.5 (Slice number 1035) and 2D porosity (void area %) from top to bottom of sample CM10 (Slice number 925) are shown in Figure 6.15. 2D XCT scanning porosity profiles of samples with lowest porosity at each group and their corresponding average x-ray attenuation (density) are presented in Figure 6.16. It can be seen from Figures 6.16 (a) and (c) that increasing the NT content up to 2.5

wt% and FA to 10 wt% (AM2.5) led to a more homogeneous microstructure compared to the BM2.5 and CM2.5. The study has shown that replacing cement by combination of 2.5 wt% NT and 10 wt% FA was the optimal amount for improving the microstructure of the NT-modified fly ash composite samples, with 3D volumetric void fraction and 2D area void fraction reduced by 64.09% and 60.97%, respectively.

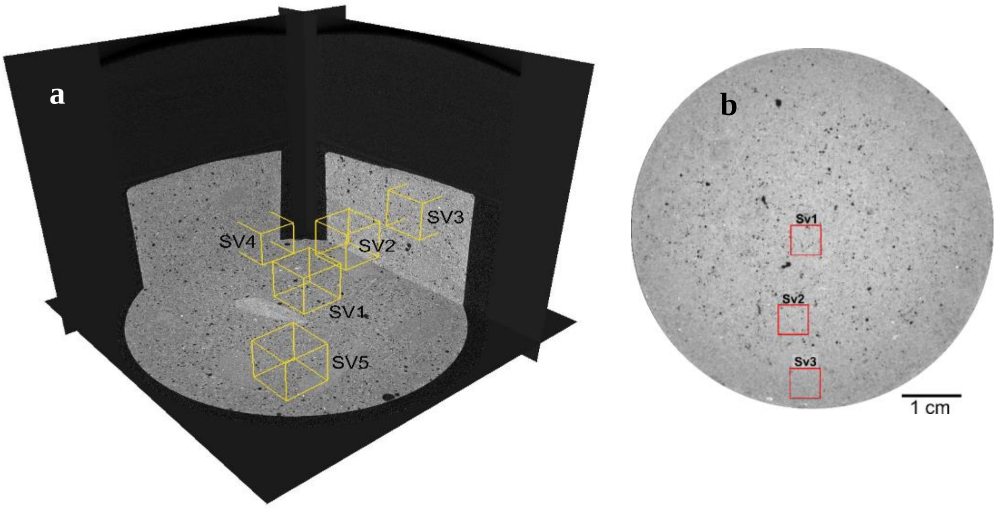

Figure 6.13 (a) and (b): Positions of the 5 subvolumes “Sv1”, “Sv2”, “Sv3”, “Sv4” and “Sv5” used to measure the relative 3D volumetric porosity (yellow squares).

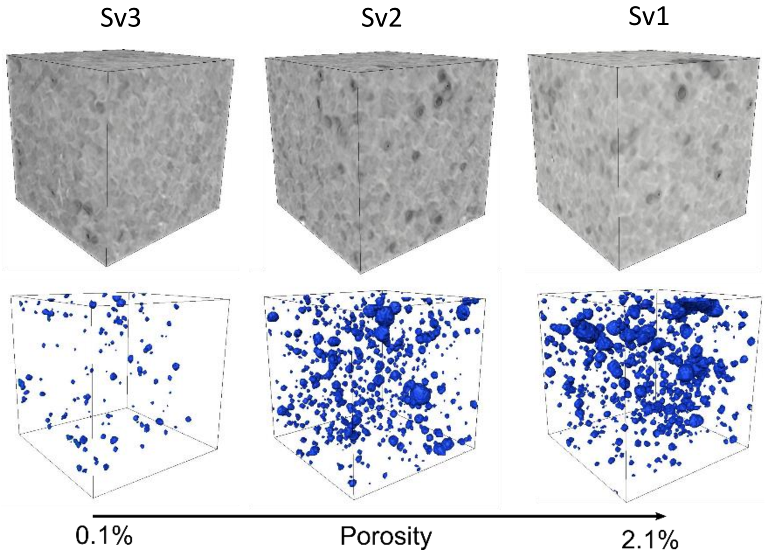

Figure 6.14: Top: 3D renderings of subvolumes of sample AM2.5. Bottom: 3D renderings of the pores in blue colour. Porosity increased from the outer edge to the inner core of the sample.

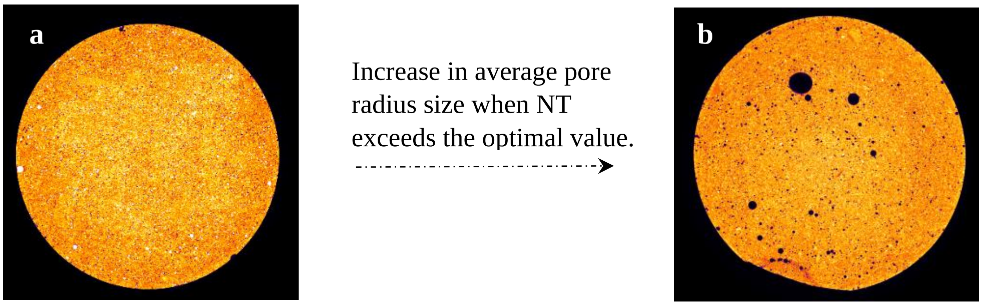

Figure 6.15: a) 2D analysis of porosity of sample AM2.5 (Slice number 1035), b) 2D porosity (void area %) from top to bottom of sample CM10 (Slice number 925).

Reconstructed tomography images were used to extract the main parameters of porosity. The number of pores in the scanned volume, as well as the volume and shape of individual pores were determined (Table 6.7).

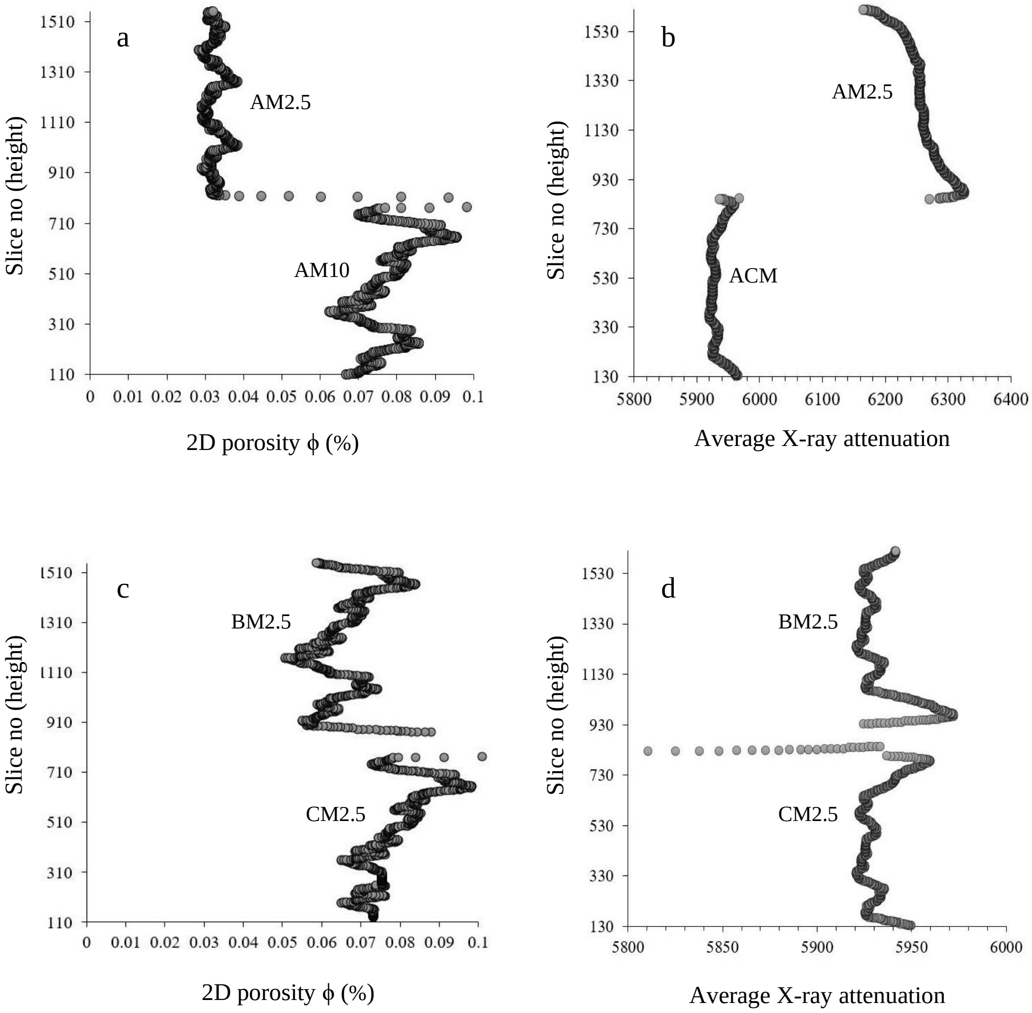

Figure 6.16: 2D porosities (void area %) and average X-ray attenuations from top to bottom of different specimens at 28 days: a. (AM2.5, ACM), b. (AM2.5, ACM), c. (BM2.5, CM2.5), d. (BM2.5, CM2.5).

The recorded 3D volumetric void fractions indicate that sample AM2.5 contained 3,233 pores with a volume fraction of 2.56%, the lowest volume voids among the samples in mix design 2. Specimens CCM and CM10 had 8,212 and 7,965 pores with pore volume fractions increasing to 13.02% and 10.98%, respectively, the largest volumes of voids among all samples.

As shown in Table 6.7, pores between 5-50 μm in diameter were found to make up the majority of the pore population among all samples. It was found that in specimen with code nos M2.5 and AM2.5 as the optimal designs, the majority of the pore volume, 48.3% and 42.6% respectively, were contributed by pores ranging in size from 5-50 µm in diameter while for other (larger) pore ranges the percentages were all smaller than the corresponding values. The majority of the pore volume ranging in size from 5-50 µm for the specimens with code nos CCM and CM10, were 52.2% and 53.0% respectively. The relationships between the average volumetric porosity and internal pore distributions of the specimens at 28 days are illustrated in Table 6.7.

Table 6.6: The recorded 3D volumetric void fractions and 2D area void fractions for the Mix 2.

Mix no /Mix design Set (A, B, C)	Cement replacement (wt%) FA	Cement replacement (wt%) NT	3D Volumetric void fractions (%)	2D Area void fractions (%)
ACM	10	0	7.65	7.12
AM2.5	10	2.5	2.56	3.20
AM3.5	10	3.5	2.87	3.65
AM5	10	5	4.01	8.13
AM10	10	10	5.22	8.54
BCM	20	0	11.96	11.24
BM2.5	20	2.5	6.22	6.87
BM3.5	20	3.5	7.68	7.03
BM5	20	5	9.13	8.02
BM10	20	10	9.82	11.43
CCM	30	0	13.02	12.12
CM2.5	30	2.5	7.07	8.12
CM3.5	30	3.5	9.14	8.76
CM5	30	5	9.78	9.98
CM10	30	10	10.98	13.08

It can be concluded that adding a certain amount of NT, *i.e.* NT $\leq$ 2.5 wt%, and FA *i.e.* FA $\leq$ 10 wt%, could modify the pore structure of cement mortars by changing the harmful microscale pores (permeability related) to the nano-sized benign pores (see BET analysis), leading to a much stronger durability of cement-based materials.

Table 6.7: Internal pore distributions of TiO_2-modified fly ash geopolymer samples

Code no	Pore size distribution % (5μm < D < 200μm)			Average volumetric Porosity
Size	5μm	5 μm -50 μm	D >50 μm	(%)
CM	0.89	4.18	2.06	7.13
M2.5	0.36	1.17	0.89	2.42
M3.5	0.36	1.07	1.18	2.61
M5	0.62	2.14	1.46	4.22
M10	0.74	2.07	2.86	5.67
ACM	1.16	3.18	3.31	7.65
AM2.5	0.91	1.09	0.56	2.56
AM3.5	0.87	1.13	0.87	2.87
AM5	1.12	1.81	1.08	4.01
AM10	1.76	2.43	1.03	5.22
BCM	3.44	5.45	3.07	11.96
BM2.5	1.76	3.87	0.59	6.22
BM3.5	2.04	4.12	1.52	7.68
BM5	2.43	4.69	2.01	9.13
BM10	3.47	5.12	1.23	9.82
CCM	4.23	6.22	2.47	13.02
CM2.5	2.97	3.16	0.94	7.07
CM3.5	2.88	3.88	2.38	9.14
CM5	3.77	4.33	1.68	9.78
CM10	4.11	5.16	1.71	10.98

In the third part of the experiment, different percentages of OPC were replaced by combined use of NT, *i.e.* 0 wt%, 2.5 wt%, 5 wt% and 10 wt%, and MK within the range of 10 wt% to 30 wt%. The samples in mix 3 were grouped into 3 sets (D, E, F). Set D contained 10 wt% MK, Set E contained 20 wt% MK, and Set MK contained 30 wt% MK.

The recorded 3D volumetric void fractions and 2D area void fractions for the Mix 3 samples are presented in Table 6.8. An example of such a scan is shown in Figures 6.17(a) and (b), representing sample FM10 with the highest average porosity (6.17(a)), and sample DM2.5 with the lowest porosity amongst all specimens tested (6.17(b)). The 3D volumetric void fraction and 2D area void fraction for sample FM10 and DM2.5

were (11.9%, 12.1%) and (3.45%, 2.40%) respectively. Similar to the mix 2 design, 2D XCT scanning porosity profiles of samples with lowest porosity at each group and their corresponding average x-ray attenuation (density) are presented in Figure 6.18.

Table 6.8: The recorded 3D volumetric void fractions and 2D area void fractions for the Mix 3.

Mix no /Mix design Set (A, B, C)	Cement replacement (wt%) MK	Cement replacement (wt%) NT	3D Volumetric void fractions (%)	2D Area void fractions (%)
DCM	10	0	6.54	6.12
DM2.5	10	2.5	3.45	2.40
DM3.5	10	3.5	2.65	3.15
DM5	10	5	3.13	7.11
DM10	10	10	5.33	7.44
ECM	20	0	9.2	9.4
EM2.5	20	2.5	5.13	5.87
EM3.5	20	3.5	6.56	6.33
EM5	20	5	9.56	8.02
EM10	20	10	10.7	11.3
FCM	30	0	12.1	11.2
FM2.5	30	2.5	7.02	7.12
FM3.5	30	3.5	8.73	9.76
FM5	30	5	10.4	10.9
FM10	30	10	11.9	12.1

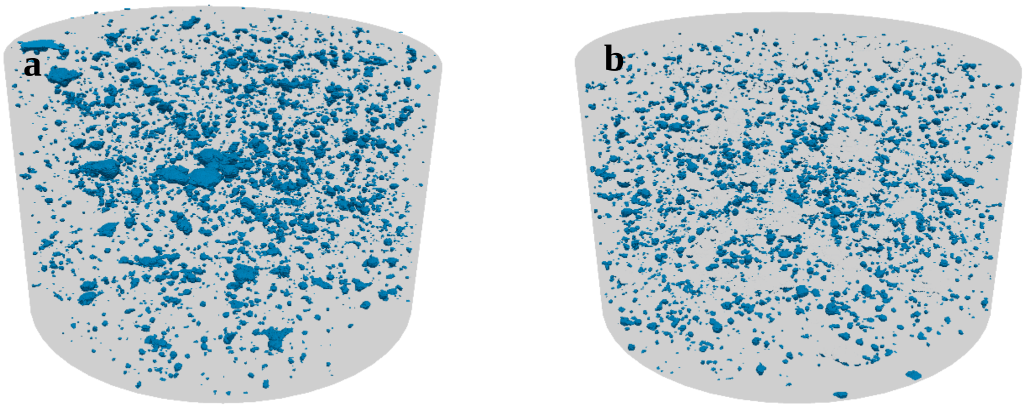

Figure 6.17: 3D visualizations of the porosities of the samples FM10 (left) and DM2.5 (right).

It can be seen from Figure 6.18 that increasing the NT content up to 2.5 wt% and MK to 10 wt% (DM2.5) led to a more homogeneous microstructure compared to the EM2.5 and FM2.5. The study has shown that replacing cement by combination of 2.5 wt% NT and 10 wt% MK was the optimal amount for improving the microstructure of the NT-modified MK geopolymer samples with 3D volumetric void fraction and 2D area void fraction reduced by 54.9% and 66.3%, respectively. Using the volumes calculated for each pore, the pore size distribution (histograms) was plotted. The results show that the samples CM, EM2.5 and FM2.5 had similarities in terms of porosity and the number of pores (Figure 6.19). However, this phenomenon was quite different for DM2.5.

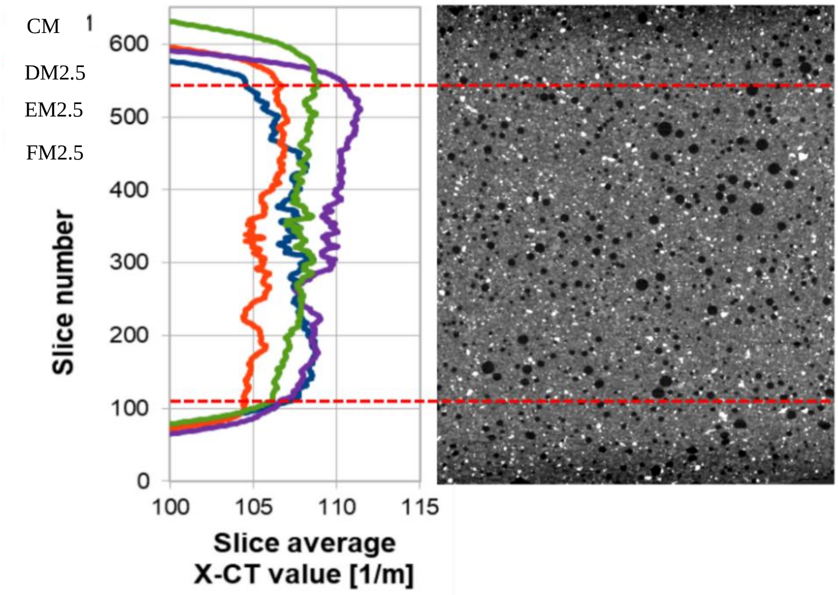

Figure 6.18: 2D porosities (void area %) and average X-ray attenuations from top to bottom of different specimens at 28 days.

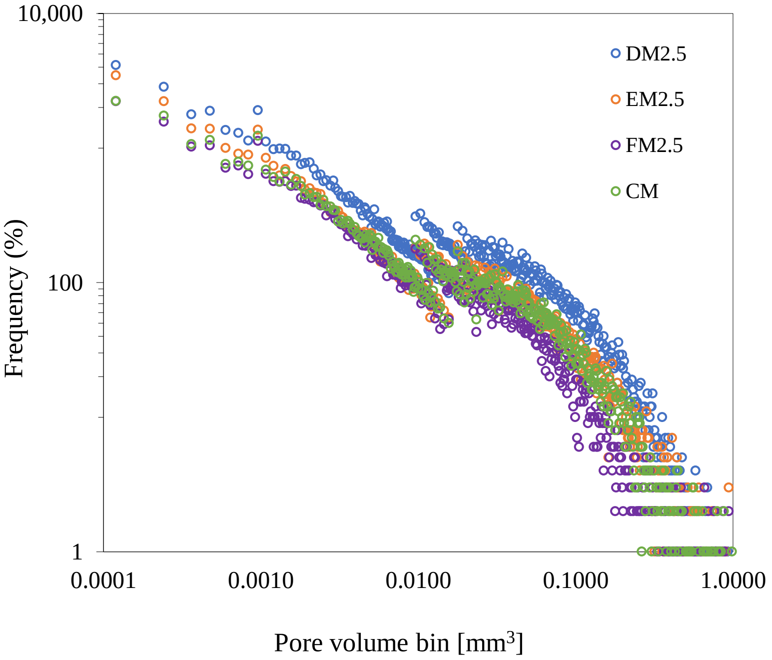

Figure 6.19: Relationships between pore volume and frequency for the NT cements.

Reconstructed tomography images were used to extract the main parameters of porosity. The number of pores in the scanned volume, as well as the volume and the shape of individual pores were determined (Table 6.9). The recorded 3D volumetric void fractions indicated that sample DM2.5 contained 4,166 pores with a volume fraction of 3.45%, i.e. the lowest volume voids among the samples in mix design 3. Specimens DM2.5, EM2.5 and FM2.5 had 2,116, 5133 and 6,164 pores with pore volume fractions increasing to 5.13% and 7.02%, respectively.

As shown in Table 6.9, samples in mix design 3, similar to mix design 2, had pores between 5-50 μm in diameter. It was found that in specimen with code no DM2.5 (the optimal design), the majority of the pore volumes (66%) were contributed by pores ranging in size from 5-50 µm in diameter while for other (larger) pore ranges the percentages were all smaller than the corresponding values.

Table 6.9: Internal pore distributions of TiO_2-modified MK composite samples

Code no	Pore size distribution % (5μm < D < 200μm)			Average volumetric Porosity
Size	5μm	5 μm -50 μm	D >50 μm	(%)
CM	0.89	4.18	2.06	7.13
M2.5	0.36	1.17	0.89	2.42
M3.5	0.36	1.07	1.18	2.61
M5	0.62	2.14	1.46	4.22
M10	0.74	2.07	2.86	5.67
DCM	0.25	2.37	3.92	6.54
DM2.5	1.81	2.31	0.67	3.45
DM3.5	0.66	2.23	0.24	2.65
DM5	2.23	2.12	1.22	3.13
DM10	2.55	2.24	0.54	5.33
ECM	1.33	4.36	3.51	9.2
EM2.5	1.65	4.38	0.90	5.13
EM3.5	2.13	5.41	0.98	6.56
EM5	2.51	5.44	1.61	9.56
EM10	4.54	5.54	0.62	10.7
FCM	4.51	5.53	2.06	12.1
FM2.5	1.83	4.25	0.94	7.02
FM3.5	2.53	4.15	2.05	8.73
FM5	4.62	5.26	0.52	10.4
FM10	4.80	5.29	1.81	11.9

In order to have more accurate analysis, The XCT data was split into two categories based on X-ray attenuations: low attenuation pore space, and high attenuation cement matrix. The segmentation algorithm used was Trainable Weka Segmentation which used machine learning to identify feature structures within the data. Weka segmentation was applied in 3D and trained on dataset 1-1 with a minimum of 30 pore regions and 30 matrix regions manually identified in the first, mid, and last slice of the dataset. Training features used were mean, variance, maximum and minimum greyscale values of each pixel and its neighbours, and all other training parameters were left at their default values (Figure 6.20(a)).

The Weka segmentation took approximately 62 minutes to segment each dataset subvolume. Connected pores were separated from each other using a disconnection algorithm applied in 3D. Each disconnected pore was labelled. Labelled pore regions were analysed for volume, surface area, sphericity, and max inscribed ball. The results were used to create a particle size distribution for each sample. 3D images were created using ParaView, where spherical balls are shown. An example of such a scan is shown in Figures 6.20(b), (A), (B) and (C), representing sample CM.

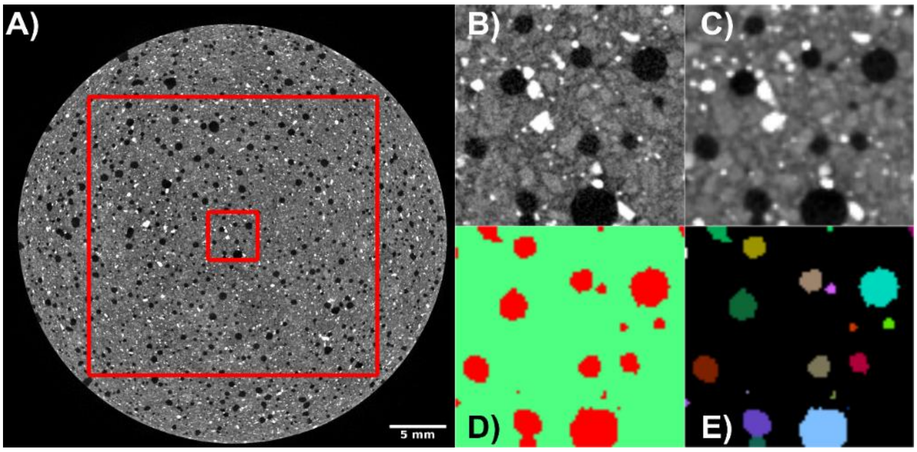

Figure 6.20 (a). A) Raw XCT data with 25 mm × 25 mm subvolume used for further processing analysis (outer red square) and close-up view (inner red square). B) Close-up view of raw XCT data in a 4 mm × 4 mm region. C) After 2x2x2 coarsening. D) After binary segmentation with Trainable Weka 3D. E) Disconnected and labelled pore regions.

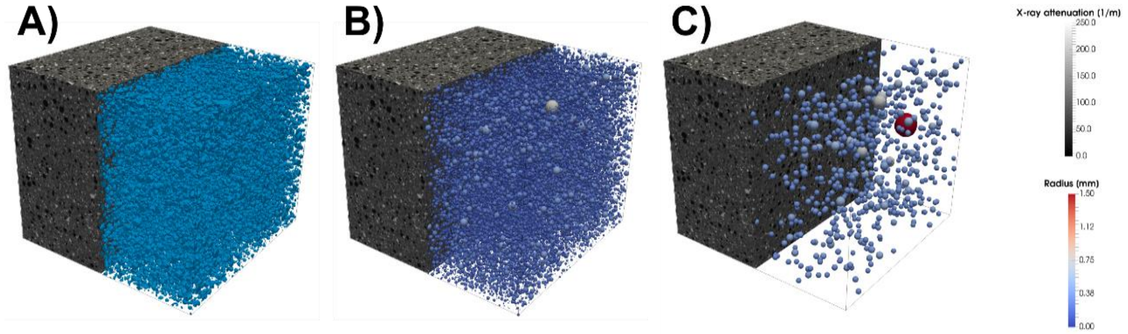

Figure 6.20 (b): Sample CM showing A) XCT greyscale data and segmented pore regions. B) Pore regions replaced with their maximum inscribed balls. C) Only balls greater than 3µm radius shown.

A refinement of the structure can also be noticed by comparing 3D porosity visualizations of samples CM (top left), EM2.5 (top right), DM2.5 (bottom left) and FM2.5 (bottom right), as illustrated in Figure 6.21.

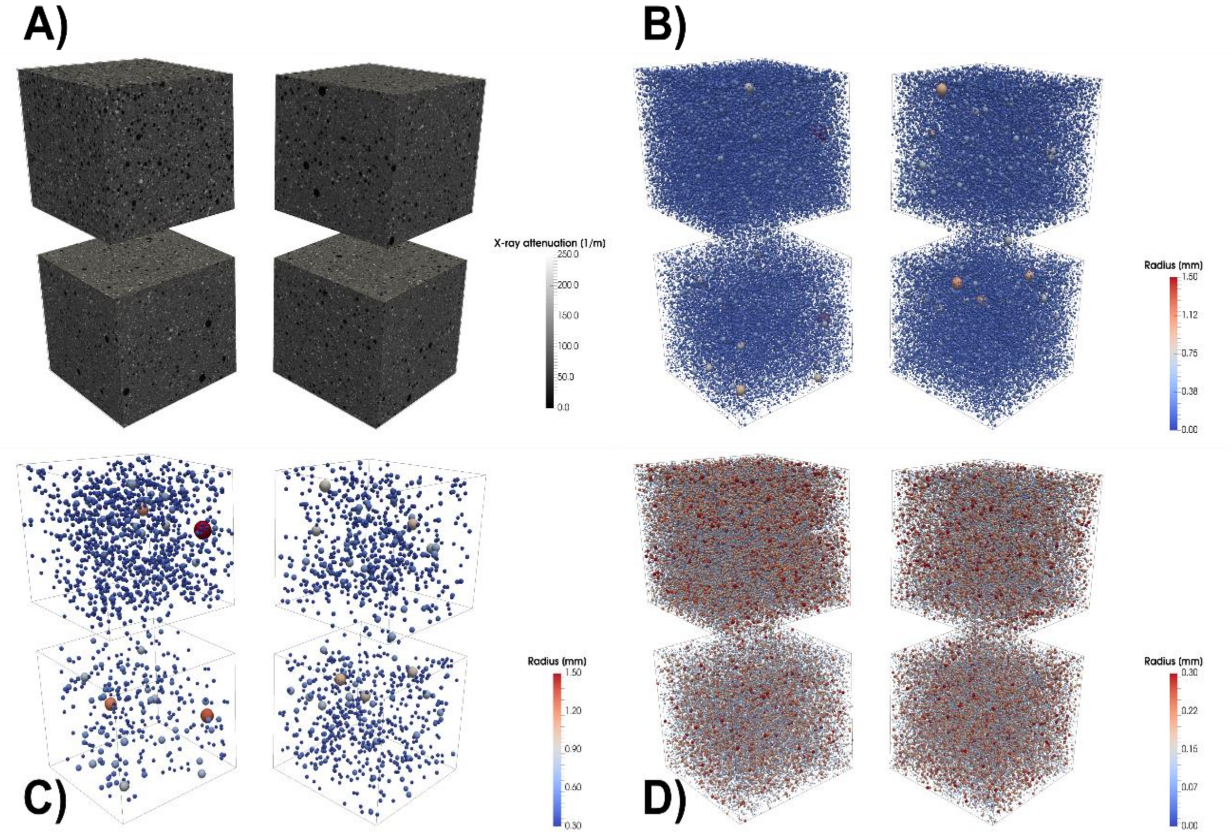

Figure 6.21: A) Samples CM (top left), EM2.5 (top right), DM2.5 (bottom left), FM2.5 (bottom right). B) All maximum inscribed balls. C) Only balls greater than 2.5µm radius shown. D) Only balls less than 0.3µm radius shown.

The difference could also be quantitatively calculated from Table 6.9, *i.e.*, the 3D volumetric void fraction of CM was about 2 times that of DM2.5.

Moreover, the relationships between 3D volumetric void fractions, 2D area void fractions and NT content for the 28-day curing age presented in Figures 6.22 and 6.23.

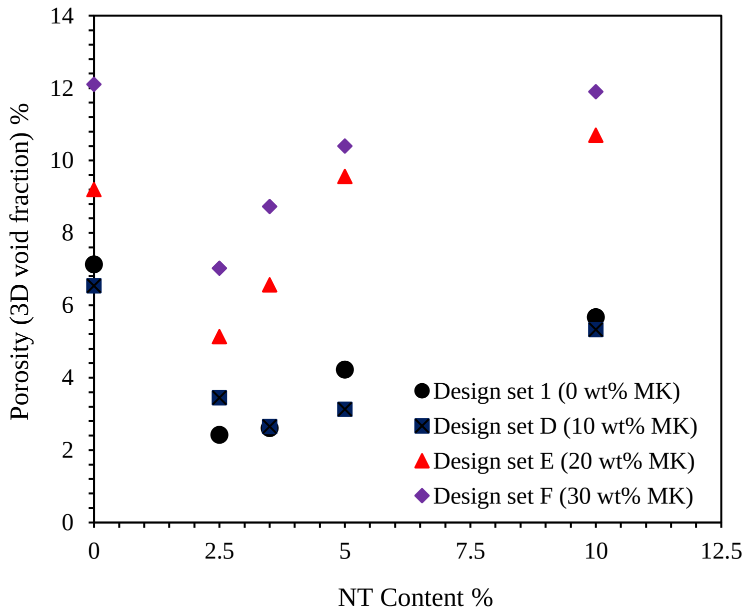

Figure 6.22: Relationships between 3D volumetric void fractions and NT content at 28 days.

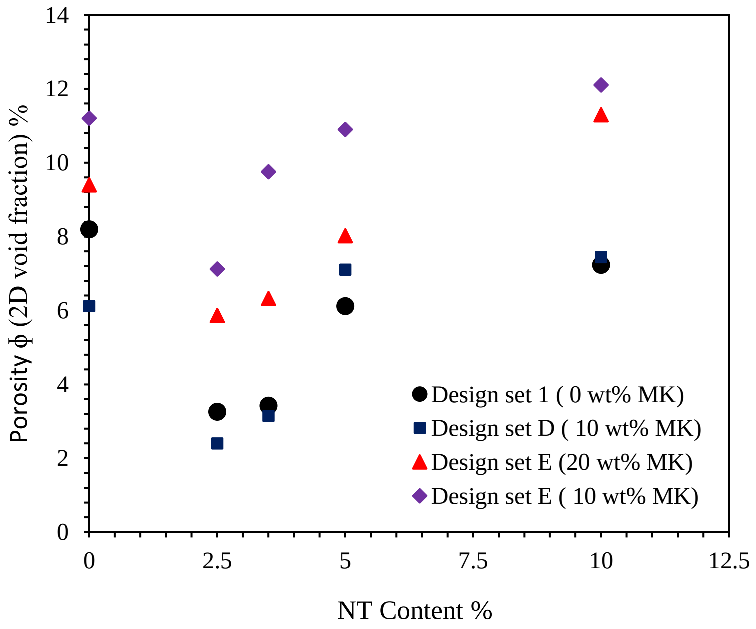

Figure 6.23: Relationships between 2D area void fractions and NT content at 28 days.

6.4.2. Permeability

The M2.5 sample presented the lowest permeability, *i.e.*, 2.59×10^{-16} m^2 amongst all the NT mortar and pure mortar specimens. Comparing with the pure mortar sample, adding 2.5 wt% NT could reduce the permeability by 46.1%. This is a significant improvement in the durability of cement mortars. Increasing the NT content up to 2.5 wt% and FA to 10 wt% (AM2.5) led to a more reduction in permeability of the NT-modified fly ash composite compared with control mix (CM), with the permeability reduced by 44.1%.

It has been suggested that the presence of FA, *i.e.* FA $\leq$ 10 wt%, led to a more preponderant precipitation of cement gel products in comparison to the CM. This resulted in an efficacious blocking of pores and, thus, availed in reducing permeability. In addition, pozzolanic reaction of FA engendered supplemental cementitious compounds that blocked channels, and filled pore space and, thus further reducing the permeability of the hardened pastes. When the amount of NT and FA exceeded the optimal value, *i.e.* NT > 2.5 wt% and FA >10 wt%, the result showed clear trends of increasing permeability and porosity of specimens (as illustrated in Figures 6.24, 6.25 and 6.26).

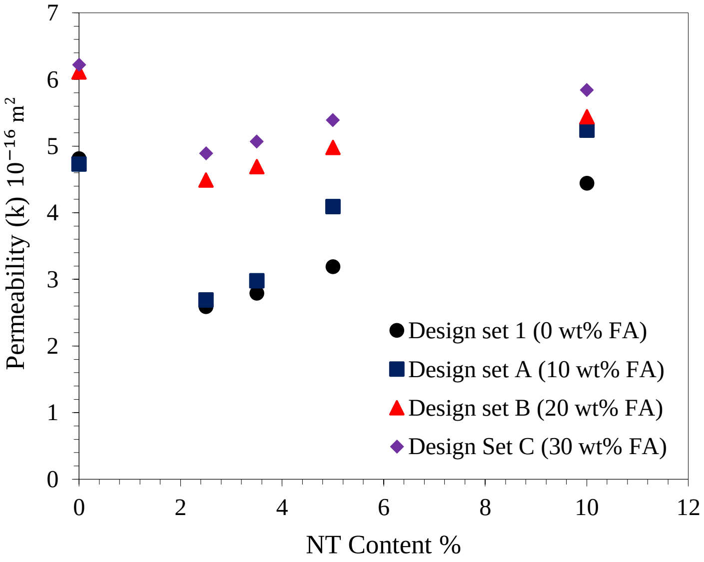

Figure 6.24: Relationships between permeability, NT, and FA content at the 28-day age.

I also tested and benchmarked the permeability of the NT mortar samples against steel and sandstone which are known as two possible extremes of permeability for building materials. Steel should theoretically have a permeability of zero and hence the obtained permeability of $2.82 \times 10^{-20}\ \mathrm{m}^2$ arose from a combination of pressure/volume measurement error, leakage from connections, and bypass of fluid around the sample.

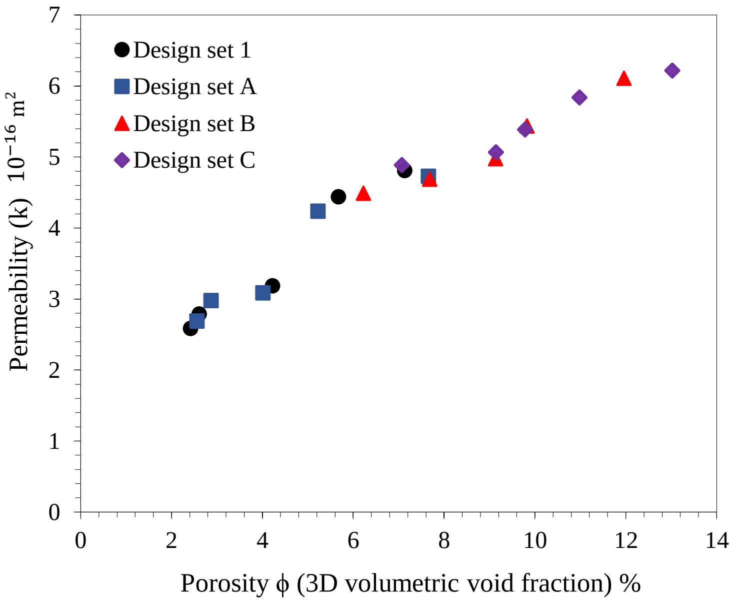

Figure 6.25: Relationships between 3D volumetric void fraction and porosity of the specimens at the 28-day curing age.

This result therefore represents the lower bound of permeability that can be measured with the experimental setup. The sandstone had the highest permeability of $3.50 \times 10^{-15}\ \mathrm{m}^2$, as presented in Table 6.10.

In the third part of the experiment, different percentages of OPC were replaced by combined use of NT, *i.e.* 0 wt%, 2.5 wt%, 5 wt% and 10 wt%, and MK within the range of 10 wt% to 30 wt%. The samples in mix 3 were grouped into 3 sets (D, E, F). Set D contained 10 wt% MK, Set E contained 20 wt% MK and Set MK contained 30 wt% MK. The recorded permeability for the Mix 3 samples are presented in Table 6.11.

Table 6.10: Experiment data and results of water- permeability measurement.

Types of specimen	Area (m^2) /Length (m)	NT (wt%)	FA (wt%)	Flow rate = $\frac{\Delta V}{\Delta t}$ $(\mathrm{m}^3/\mathrm{s})$	$(p_b - p_a)$(kPa)	Permeability(m^2)
Steel (Reference)	0.00385/0.07	0	0	3.26×10^{-11}	2000.1	2.82×10^{-20}
Sandstone	0.00385/0.07	0	0	1.74×10^{-8}	86.40	3.50×10^{-15}
CM	0.00385/0.07	0	0	1.32×10^{-8}	1424.0	4.81×10^{-16}
M2.5	0.00385/0.07	2.5	0	6.45×10^{-10}	1260.4	2.59×10^{-16}
M3.5	0.00385/0.07	3.5	0	1.27×10^{-11}	999.50	2.79×10^{-16}
M5	0.00385/0.07	5	0	1.21×10^{-10}	1105.8	3.19×10^{-16}
M10	0.00385/0.07	10	0	1.40×10^{-8}	1082.8	4.44×10^{-16}
ACM	0.00385/0.07	0	10	2.26×10^{-11}	1314.0	4.73×10^{-16}
AM2.5	0.00385/0.07	2.5	10	1.34×10^{-8}	1160.2	2.69×10^{-16}
AM3.5	0.00385/0.07	3.5	10	1.12×10^{-8}	960.50	2.98×10^{-16}
AM5	0.00385/0.07	5	10	5.35×10^{-10}	1115.3	3.09×10^{-16}
AM10	0.00385/0.07	10	10	1.17×10^{-11}	1012.4	4.24×10^{-16}
BCM	0.00385/0.07	0	20	1.11×10^{-10}	1224.0	6.11×10^{-16}
BM2.5	0.00385/0.07	2.5	20	1.49×10^{-8}	1110.8	4.49×10^{-16}
BM3.5	0.00385/0.07	3.5	20	2.23×10^{-11}	895.50	4.69×10^{-16}
BM5	0.00385/0.07	5	20	3.16×10^{-11}	1335.7	4.98×10^{-16}
BM10	0.00385/0.07	10	20	1.14×10^{-8}	1112.1	5.44×10^{-16}
CCM	0.00385/0.07	0	30	2.32×10^{-8}	1344.0	6.22×10^{-16}
CM2.5	0.00385/0.07	2.5	30	5.45×10^{-10}	1120.4	4.89×10^{-16}
CM3.5	0.00385/0.07	3.5	30	1.17×10^{-11}	932.50	5.07×10^{-16}
CM5	0.00385/0.07	5	30	1.11×10^{-10}	1095.3	5.39×10^{-16}
CM10	0.00385/0.07	10	30	1.33×10^{-8}	1044.3	5.84×10^{-16}

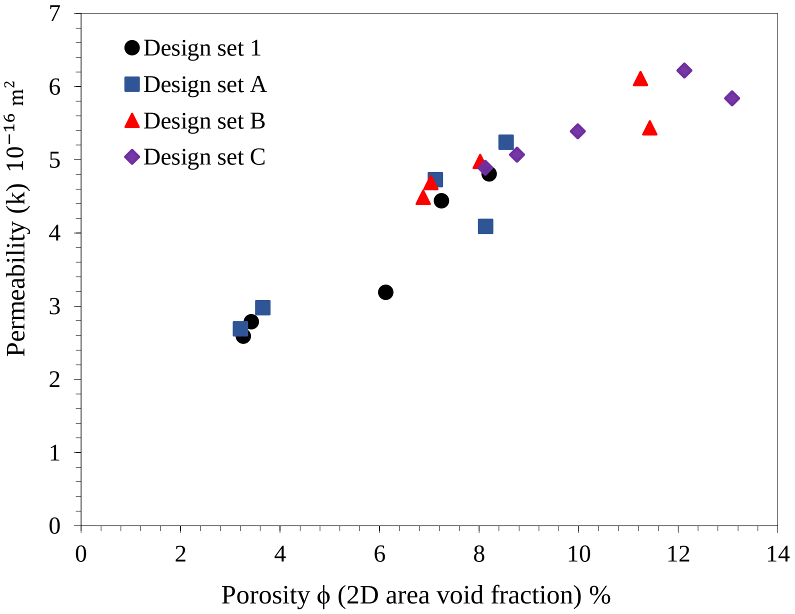

Figure 6.26: Relationships between 2D area void fraction and porosity of the specimens at the 28-day curing age.

Table 6.11: Experiment data and results of water- permeability measurement.

Types of specimen	Area (m^2) /Length (m)	NT (wt%)	MK (wt%)	Flow rate = $\frac{\Delta V}{\Delta t}$ (m^3/s)	$(p_b - p_a)$(kPa)	Permeability(m^2)
DCM	0.00385/0.07	0	10	3.17×10^{-11}	1402.0	4.73×10^{-16}
DM2.5	0.00385/0.07	2.5	10	2.18×10^{-9}	1415.2	3.19×10^{-16}
DM3.5	0.00385/0.07	3.5	10	2.01×10^{-8}	1125.5	3.29×10^{-16}
DM5	0.00385/0.07	5	10	6.24×10^{-8}	1026.3	3.61×10^{-16}
DM10	0.00385/0.07	10	10	2.04×10^{-11}	1007.4	3.97×10^{-16}
ECM	0.00385/0.07	0	20	2.23×10^{-11}	1118.0	5.41×10^{-16}
EM2.5	0.00385/0.07	2.5	20	2.36×10^{-9}	1233.8	4.34×10^{-16}
EM3.5	0.00385/0.07	3.5	20	3.51×10^{-10}	963.20	4.81×10^{-16}
EM5	0.00385/0.07	5	20	4.67×10^{-10}	1202.7	5.12×10^{-16}
EM10	0.00385/0.07	10	20	2.63×10^{-9}	1241.1	5.31×10^{-16}
FCM	0.00385/0.07	0	30	3.53×10^{-9}	1435.0	6.44×10^{-16}
FM2.5	0.00385/0.07	2.5	30	5.22×10^{-10}	1536.4	5.11×10^{-16}
FM3.5	0.00385/0.07	3.5	30	2.41×10^{-10}	1113.5	5.31×10^{-16}
FM5	0.00385/0.07	5	30	2.31×10^{-10}	1221.3	6.19×10^{-16}
FM10	0.00385/0.07	10	30	2.53×10^{-9}	1222.3	6.73×10^{-16}

As shown in Table 6.11, the DM2.5 sample presented the lowest permeability, *i.e.* 3.19×10^{-16} m^2, amongst all the samples in mix design 3. Comparing with the pure mortar sample, adding 2.5 wt% NT and 10 wt% MK reduced the permeability by 33.7%. This is a significant improvement in the durability of cement mortars. Increasing the NT content up to 2.5 wt% and MK to 20 wt% (EM2.5) led to a more reduction in permeability of the NT- modified MK composite compared with control mix (CM) having the permeability reduced by 10.4%. When the amount of NT and MK exceeded the optimal value, *i.e.* NT > 2.5 wt% and MK > 10/20 wt%, the results showed clear trends of increasing permeability and porosity of specimens, as illustrated in Figures 6.27, 6.28 and 6.29. In addition, when the amount of FA and MK exceeded the optimal value, *i.e.* FA > 10 wt%, the unreacted or partially reacted particles create porosity in the matrix dispersed in small sized pores, so cavities were formed from the spaces left after the dissolve of the FA and MK particles.

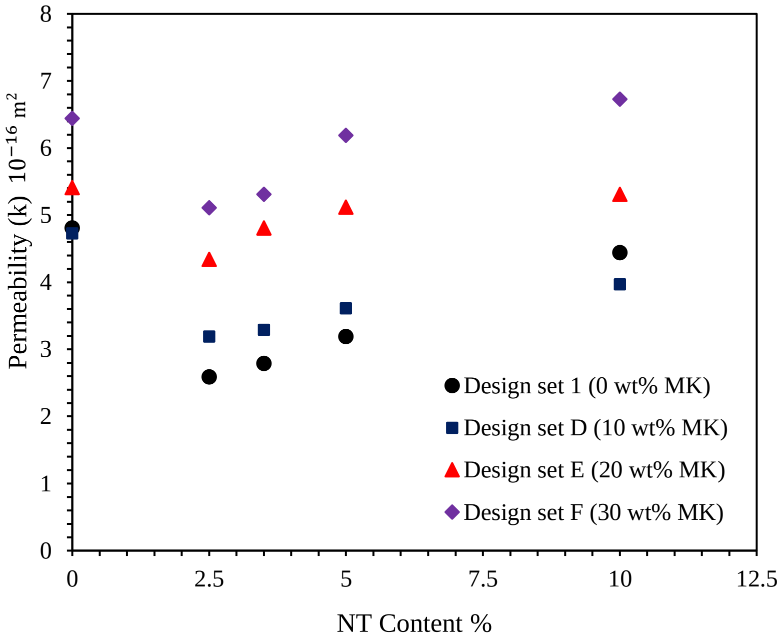

Figure 6.27: Relationships between permeability, NT, and FA content at the-28 day curing age.

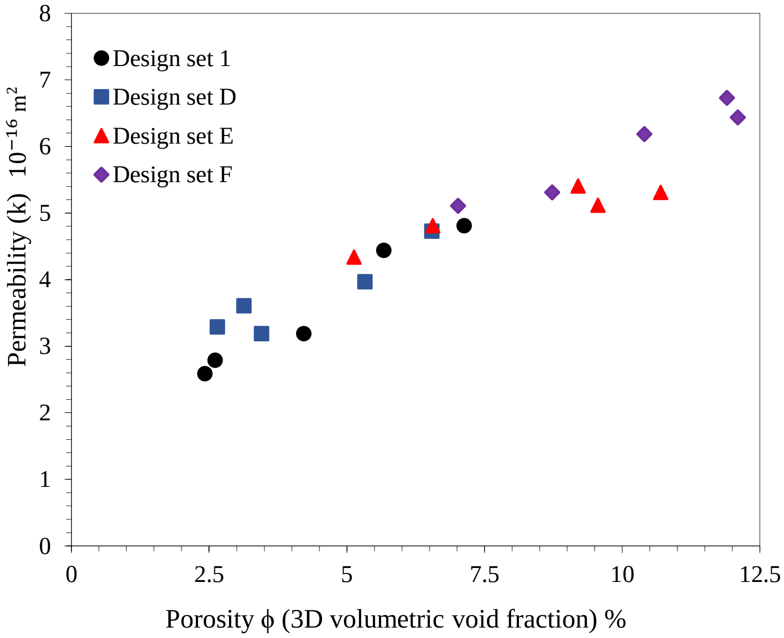

Figure 6.28: Relationships between 3D volumetric void fraction and porosity of the specimens at the 28-day curing age.

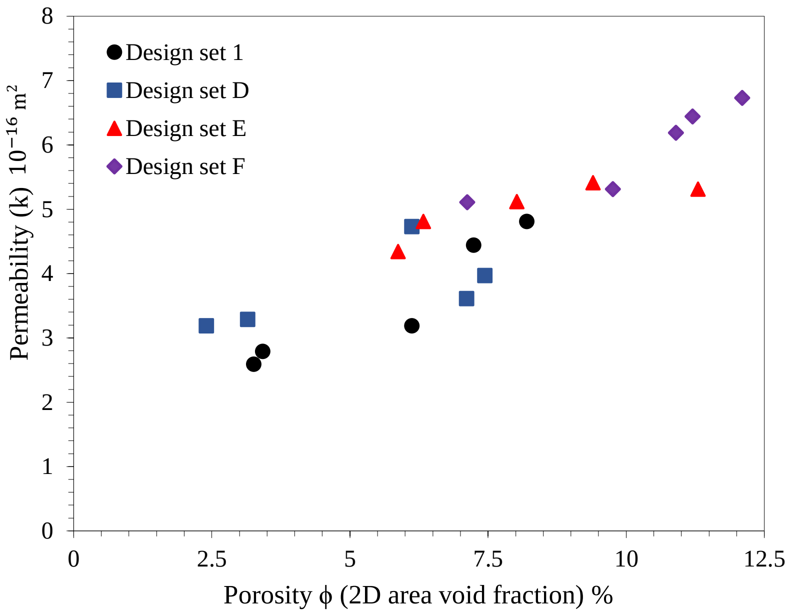

Figure 6.29: Relationships between 2D area void fraction and porosity of the specimens at the 28-day curing age.

6.4.3. Microstructural morphology

The objective of the microstructural analysis is to support the findings shown in the present research. It is important to notice that the performed microstructural analyses were qualitative, with the objective to give additional information that can explain the obtained results. In this context, SEM analyses were used to study the influence of NT and FA on the microstructure of the OPC mortar. Figures 6.30(a) to 6.30(f) show the SEM images of the surfaces of samples CM, M2.5, ACM, AM2.5, BM2.5 and CM2.5 at the 7-day curing age.

Figure 6.30(a) illustrates the microstructure of the reference sample CM, and the microstructure appeared as obvious acicular crystals, with high number of small pores and big sized C-S-H gel. The $Ca(OH)_2$ crystals were found in the microstructural analysis which was formed in the largest air-voids of the cement matrix. Fewer ettringites with messy distribution and a lot of small needle-like crystals were identified and possibly formed as ettringite or other AFt phases. Increasing the NT content up to 2.5 wt% (M2.5) was linked with a more homogeneous microstructure compared to the reference mix. Thick short columnar crystals were equally distributed to form a net (Figure 6.30(b)). Ettringite also grew from small needle-like crystals to stubby rod-like crystals, which had positive implications for improving the mechanical properties. On increasing the FA content to 10 wt% (ACM), the C-S-H gel remained homogeneous and comparable to the 2.5 wt% NT sample. However, the 10 wt% FA sample contained larger air-voids compared to the sample M2.5 (Figure 6.30(c)).

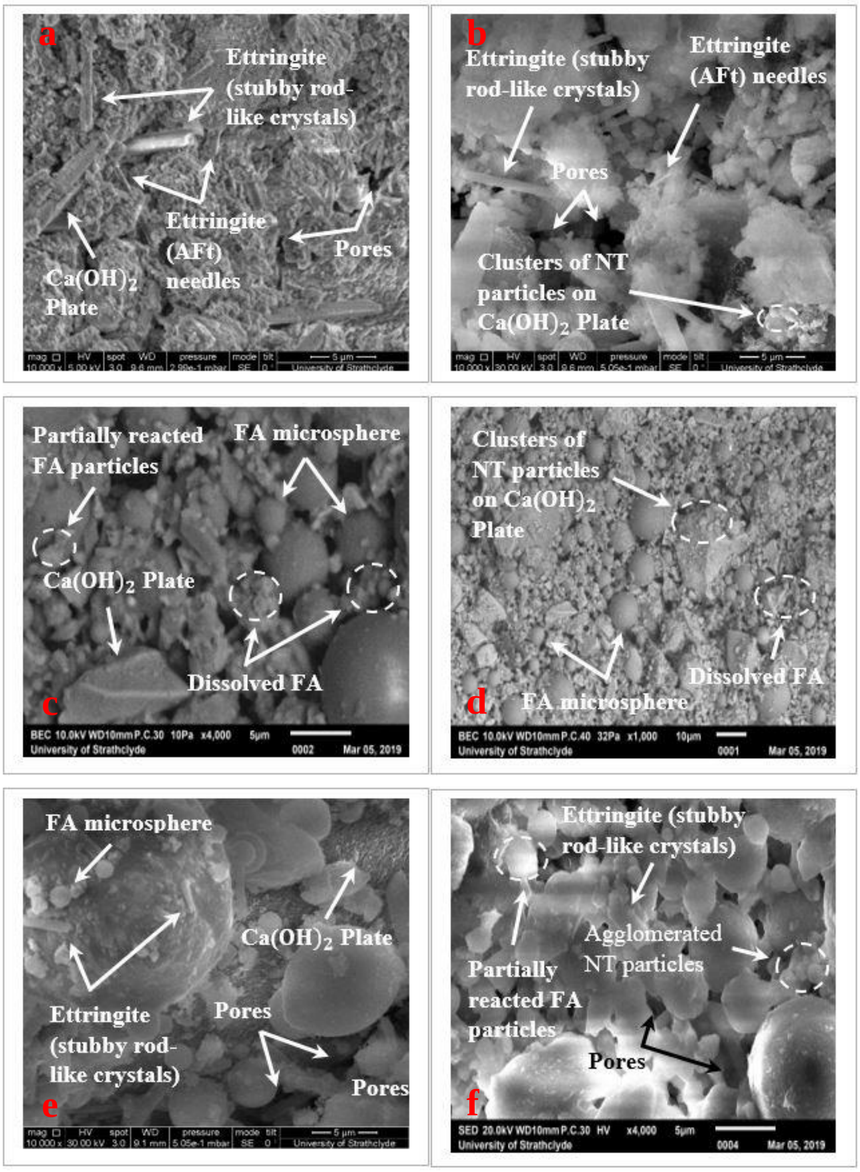

Figure 6.30: SEM images of the mortar specimens containing NT/MK after 7 days of curing: a) CM (control), b) M2.5, c) ACM, d) AM2.5, e) BM2.5 and f) CM2.5.

Increasing the NT content up to 2.5 wt% and FA to 10 wt% (AM2.5) led to a well compacted, uniform, denser pore structure with the least amount of unreacted fly ash grains compare to sample ACM. This would explain the high compressive strength observed in AM2.5. The SEM images of BM2.5 and CM2.5 after 7 days of curing were similar and showed condensed packing of cement hydration products. Both samples showed that microstructures were heterogeneous, with more partially reacted and unreacted fly ashes existing in the matrix geopolymer. However, the 20 wt% FA and 30 wt% FA samples now contained larger air-voids compared to the sample AM2.5, see Figures 6.30(e) and (f).

SEM analyses were used to study the influence of NT and FA on the microstructure of the OPC mortar. Figures 6.31(a)-6.31(f) show the SEM images of the surfaces of samples CM, M2.5, ACM, AM2.5, BM2.5 and CM2.5 at 28 days of curing. Clearly different morphologies were obtained amongst these samples. FA spheres shown in Figures 6.31(c)-6.31(f) clearly exhibited different levels of dissolution. Some spheres were partially dissolved, some collapsed, whereas some were only at the onset of dissolution. The reference sample CM (Figure 6.31(a)) contained a moderate amount of small pores and medium size C-S-H structures. Fewer small needle-like and short columnar crystals are identified and possibly formed as ettringite or other AFt phases.

Increasing the NT content up to 2.5 wt% (M2.5) led to a more homogeneous microstructure compared to the reference mix (CM). Also, C-S-H gel became larger in size, which indicated a higher degree of hydration. Moreover, the microstructure of M2.5 contained much smaller air-voids compared to sample CM (Figure 6.31(b)). It can be seen from the SEM images that adding NT up to 2.5 wt% resulted in an absence of needle shape structures and produced a homogeneous structure of C-S-H compounds. By comparing with the SEM images of the reference sample in Figure 6.31(a), it is found that some conglobate materials appeared in NT mortar samples. On increasing the FA content to 10 wt% (ACM), the C-S-H gel remained homogeneous and comparable to the 2.5 wt% NT sample. However, the 10 wt% FA sample now contained larger air-voids compared to the sample M2.5 (Figure 6.31(c)).

The large $Ca(OH)_2$ crystals were found in the microstructural analysis of ACM which was formed in the largest air-voids of the cement matrix. In addition, the unreacted or partially reacted FA particles were visible within the structure. Increasing the NT content up to 2.5 wt% and FA to 10 wt% (AM2.5) led to a more homogeneous microstructure compared to the ACM. The SEM image of the AM2.5 illustrates a very condensed mortar structure and a good dispersion of NT clusters throughout the entire surface of hydrated cement products. The possible reason is that NT could provide nucleation sites, which accelerated the precipitation of hydration products, made C-S-H disperse better, and limited the growth of $Ca(OH)_2$, thus improving the density and homogeneity of cement matrix.

Another reason is that NT had a high surface area to volume ratio, provided high reactivity, facilitated the fly ash hydration and modified the structure of hydration products at molecular level, which in turn improved the mechanical performance of fly ash geopolymer. The $Ca(OH)_2$ grains of AM2.5 were less visible than those of CM, M2.5 and ACM. The absence of large crystallized $Ca(OH)_2$ confirms that the addition of 2.5 wt% NT and 10 wt% FA caused a refinement of the microstructure (AM2.5 contained smaller air-voids) and probably induced the precipitation of medium sized C-S-H gel that normally had a high stiffness. This was due to interaction among the particles of FA with the calcium hydroxide, which resulted “in the formation of re-crystallized calcium carbonate in the cementitious matrix causing the reduction in porosity of the matrix and the transition zone”. The SEM images of BM2.5 and CM2.5

after 28 days of curing were similar and showed condensed packing of cement hydration products. The mineral particles of FA were arbitrarily dispersed throughout the hydrated cement products. However, the 20 wt% FA and 30 wt% FA samples contained larger air-voids compared to the sample AM2.5, see Figures 6.31(e) and (f).

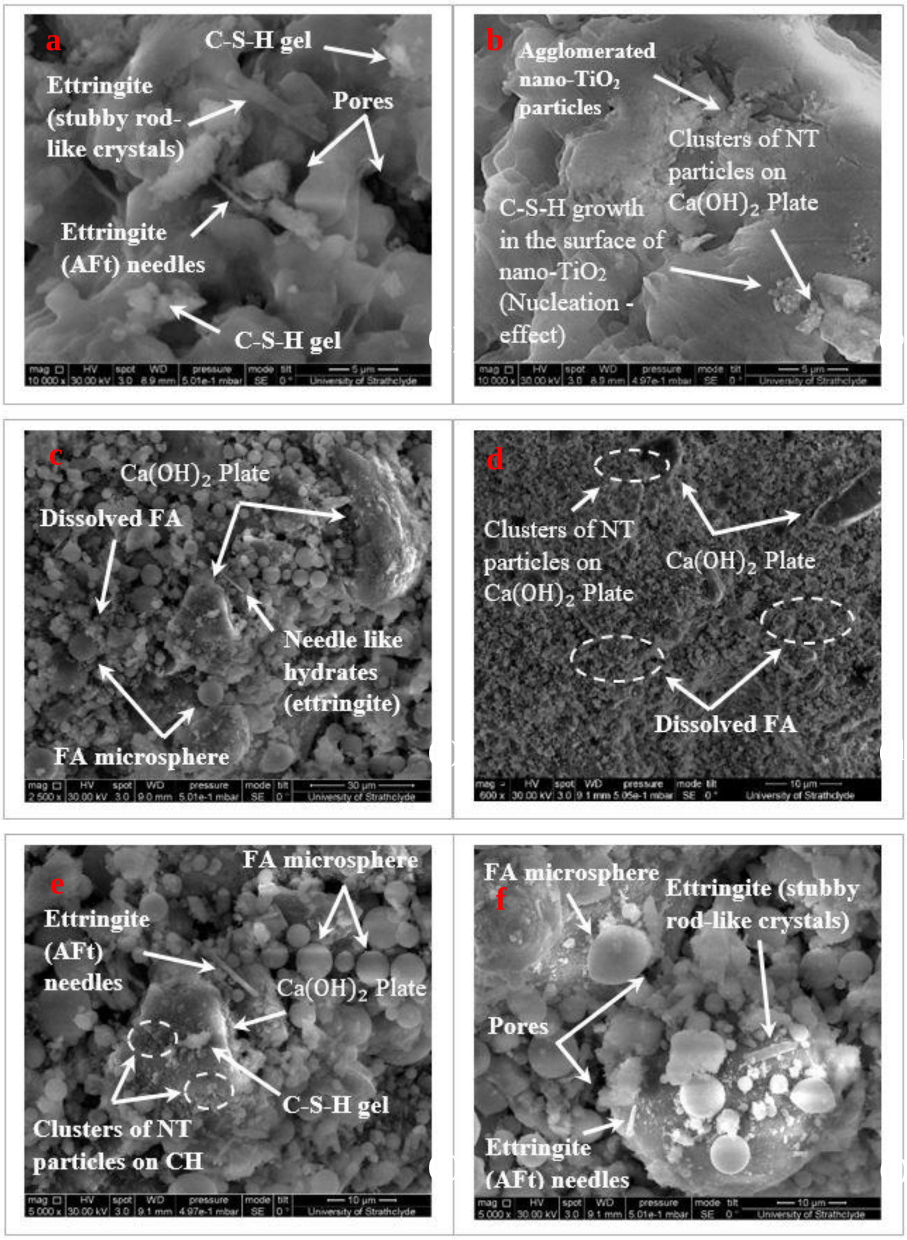

Figure 6.31: SEM images of the mortar specimens containing NT/FA after 28 days of curing: a) CM (control), b) M2.5, c) ACM, d) AM2.5, e) BM2.5 and f) CM2.5.

It is important to notice that well grown Portlandite $Ca(OH)_2$ crystals were not found in the microstructural analysis of sample CM2.5. If the dosage of fly ash is too high, *i.e.* FA > 20 wt%, drying shrinkage distortions of mortars are enlarged, leading to increase in average pore radius size and causing internal defects to form in mortars, which will certainly influence the overall voids and the total porosity, as the result that the microstructure became isolated and defective (Figure 6.31(e)). In addition, when the amount of FA exceeded the optimal value, *i.e.* FA > 10 wt%, the unreacted or partially reacted FA particles created porosity in the matrix dispersed in small sized pores so cavities were found from the spaces left after the dissolve of the FA particles.

SEM analyses were used to study the influence of NT and MK on the microstructure of the OPC mortar. Figures 6.32(a)-6.32(d) show the SEM images of the surfaces of samples DCM, DM2.5, EM2.5, and FM2.5 at 7 days of curing. The reference DCM had an apparent dense structure and a relatively good ITZ (Figure 6.32(a)). A good ITZ is defined in the present investigation as the zone (10-20 µm long) in the vicinity of the sand and gravel aggregates, with a relatively lower amount of gel and air pores. The microstructure presented heterogeneous morphologies, with high amount of small pores and big sized CS-H gel. Additionally, acicular (needle-shaped) structures (Figure 6.32(a)) were identified. As it can be observed in Figure 6.32(b), the DM2.5 showed a more homogeneous microstructure compared to the reference mix.

A homogenous microstructure is defined by a regular morphology and similar size of the hydrates. This microstructure is characterized by apparent compact and small-sized C-S-H gel. The $Ca(OH)_2$ crystals were found in the microstructural analysis which were formed in the largest air-voids of the cement matrix. Fewer ettringites with messy distribution and a lot of small needle-like crystals were identified and possibly formed as ettringite or other AFt phases. By comparing with the SEM images of the reference sample in Figure 6.32(a), it is found that some conglobate materials appeared in DM2.5. This microstructure was characterized by apparent compact and small-sized C-S-H gel and the absence of abundant gel porosity. Consequently, a relatively denser ITZ was also confirmed by SEM (Figure 6.32b). Despite the presence of large agglomerates, the hardened matrix appeared denser, probably due to a higher degree of hydration caused by the presence of MK particles with high specific surface area. The SEM images of EM2.5 and FM2.5 were similar and showed condensed packing of cement hydration products. The mineral particles of MK were randomly dispersed throughout the hydrated cement products. However, the 20 wt% MK and 30 wt% MK samples contained larger air-voids compared to the sample DM2.5 (Figures 6.32(c) and (d)).

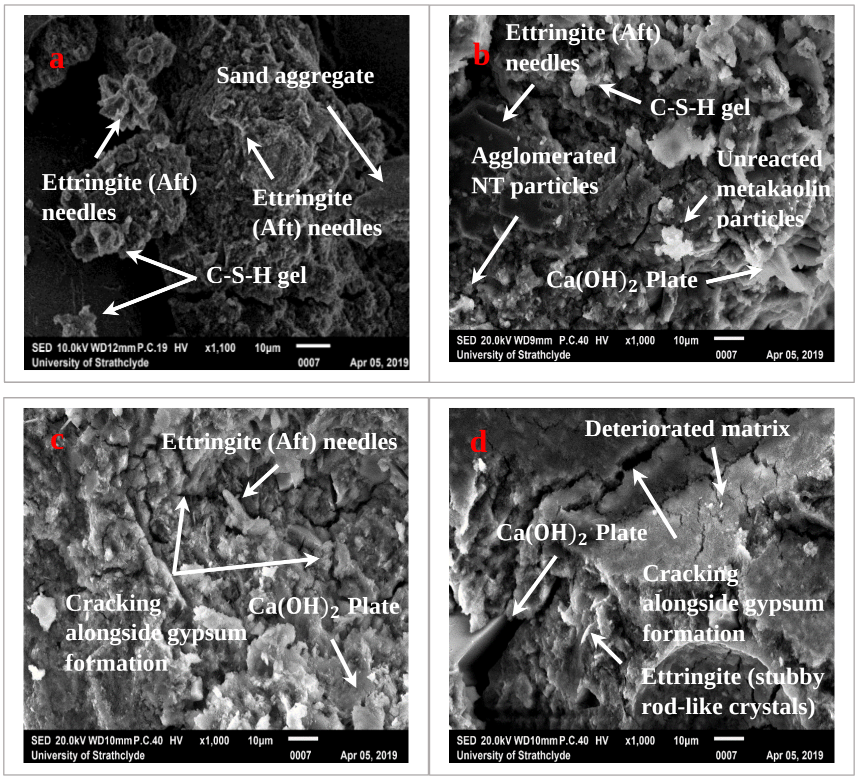

Figure 6.32: SEM images of the mortar specimens containing NT/ MK after 7 days of curing: a) DCM (control), b) DM2.5, c) EM2.5 and FM2.5(d).

It is important to notice that well grown Portlandite $Ca(OH)_2$ crystals were not found in the microstructural analysis of sample EM2.5. Various micro-cracks were formed on the surface of the EM2.5 and FM2.5 with respect to the axis of the specimen, including perpendicular and diagonal. The microstructure became isolated and defective. The presence of significant amounts of $Ca(OH)_2$ resulted in a lower compressive strength as illustrated in Figures 6.47 and 6.49. Finally, Figure 6.33 shows some selected morphological characteristics of the microstructure of the OPC mortar containing NT and MK at the 28-day curing age. On increasing the MK content to 10 wt% (DCM), the C-S-H gel remained homogeneous and comparable to the 2.5 wt% NT sample. However, the 10 wt% MK sample now contained smaller air-voids compared to the sample DCM (Figure 6.33(c)). The smaller $Ca(OH)_2$ crystals were found in the microstructural analysis of DCM which were formed in the largest air-voids of the cement matrix.

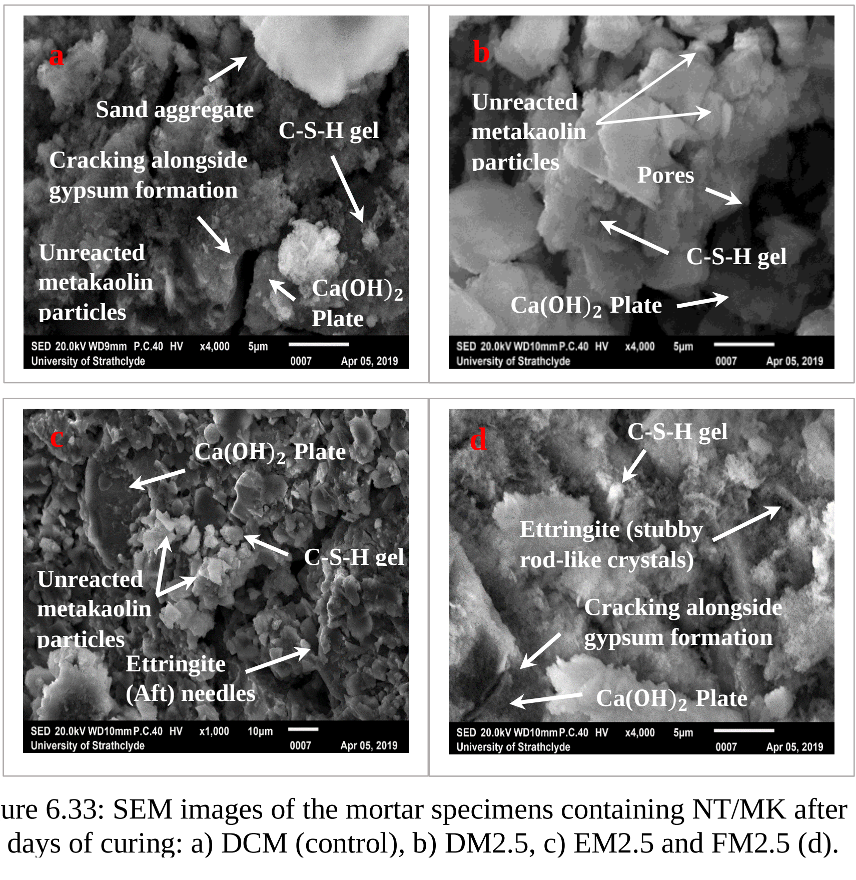

Figure 6.33: SEM images of the mortar specimens containing NT/MK after 28 days of curing: a) DCM (control), b) DM2.5, c) EM2.5 and FM2.5 (d).

In addition, the unreacted or partially reacted MK particles were visible within the structure. Increasing the NT content up to 2.5 wt% and MK to 20 wt% (EM2.5) led to development of cracks alongside gypsum formation. Additionally, acicular (needle-shaped) structures (Figure 6.33(c)) were identified and possibly formed as ettringite or other AFt phases that were rich in $CO3^{-2}$ (verified by EDS) as illustrated in Figure 6.34. On increasing the MK content to 30 wt% (FM2.5), the $Ca(OH)_2$ grains were more visible than those of DCM, DM2.5 and EM2.5 (Figure 6.33(d)). As explained before, the presence of significant amounts of $Ca(OH)_2$ resulted in a higher permeability and lower compressive strength. These findings were in line with the results of the mechanical and durability test discussed previously. The C-S-H gel became larger in size which indicated a higher degree of hydration. Moreover, the microstructure of FM2.5 contained much larger air-voids compared to sample EM2.5 (Figure 6.33(d)).

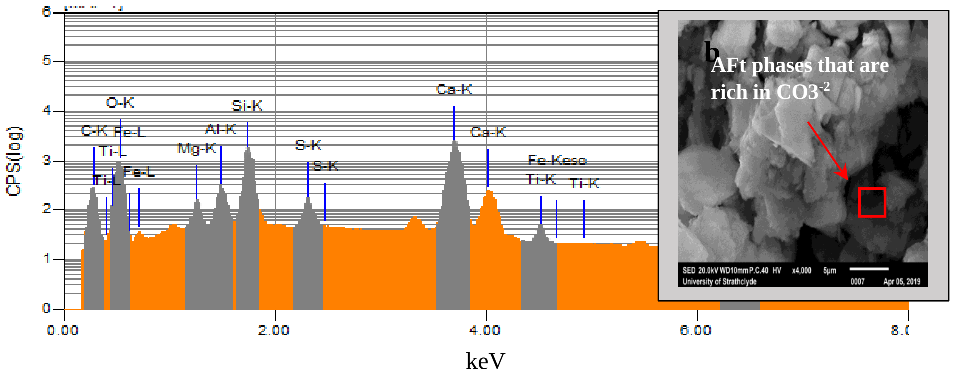

Figure 6.34: Typical SEM image and EDS analysis of the specimen with 2.5% nano-TiO_2 and 20 wt% MK at the curing time of 28 days.

6.4.4. Nanoscale pore system by BET and BJH analyses

Figures 6.35-6.38 present the pore diameters and pore size distributions of the selected NT cement mortars with FA and MK inclusions, calculated from the adsorption and desorption branches. The BET data carried out on the powdered samples indicated that the isotherm measured was of Type IV (porous materials), signifying monolayer-multilayer adsorption in the early part of the curve with a type H3 hysteresis loop between adsorption and desorption and capillary condensation in mesopores (2 nm < ϕ

< 50 nm) and macropores ($\phi > 50$ nm). In general, a larger content of NT in the samples gave a larger specific surface area. The lack of any limiting adsorption at high p/p^o suggested that the sample consisted of plate-like particles giving rise to slit-like pores (Everett et al.,1985). The surface areas and the average pore diameter were calculated by the BET and BJH methods, respectively and are presented in Table 6.12.

The adsorption and desorption isotherms (BET) obtained on specimens, representing sample CM (containing 0 wt% NT and 0 wt% FA) which had the lowest pore volume and surface area, and sample ACM (containing 0 wt% NT and 10 wt% FA) which had the highest pore volume and surface area among the specimens are presented in Figures 6.35 and 6.36. This sample also had a type IV (H3) isotherm, mainly exhibited by highly agglomerated and exceedingly small primary particles (18.2 nm). The pore volumes were evaluated using the BJH method from both nitrogen adsorption and desorption data and the results are presented in Figures 6.37 and 6.38 for the cement mortars with the highest pore volume (ACM) and the lowest pore volume (CM).

The maximum volume of the adsorbed nitrogen was related to the pore volume of the samples. In general, a smaller particle size led to a larger pore volume, as shown for the sample ACM (Table 6.12). It can be clearly seen that the ACM sample had considerably greater number of pores below 10 nm size than the CM sample, *i.e.* pore volume was $0.01/\text{cm}^3\text{g}^{-1}$ compared to $0.002/\text{cm}^3\text{g}^{-1}$ (as illustrated in Figures 6.37 and 6.38). For pores between 10 nm and 200 nm in size, the increase of pore volume was even higher for sample ACM. From the pore size distributions of the samples studied (Table 6.12), it can be concluded that adding a certain amount of NT (*i.e.*, NT $\leq$ 2.5 wt%), FA (*i.e.*, FA $\leq$ 10 wt%) and MK (*i.e.*, MK $\leq$ 10 wt%) could modify the pore structure of cement mortars by changing the harmful microscale pores, permeability related (see XCT analysis) to the nano-sized benign pores (see BET analysis), leading to a much stronger durability of cement-based materials.

Table 6.12: Parameters of pore diameter, pore volume and surface area of the cement mortars by the BET and BJH methods.

Code number of Cement Mortars	Cement replacement (wt%) NT	Cement replacement (wt%) MK	Cement replacement (wt%) FA	Average pore Diameter /nm	Pore Volume /cm^3 g^{-1}	Surface Area /m^2 g^{-1}
CM	0	0	0	19	0.015	3.58
M2.5	2.5	0	0	22.5	0.022	4.72
M10	10	0	0	20.5	0.043	9.98
ACM	0	0	10	18.2	0.065	13.7
AM2.5	2.5	0	10	16.6	0.044	9.72
AM10	10	0	10	16.3	0.053	12.3
BM2.5	2.5	0	20	22.4	0.023	12.5
CM2.5	2.5	0	30	22.6	0.064	13.1
DM2.5	2.5	10	0	21.4	0.042	5.32
EM2.5	2.5	20	0	22.7	0.032	6.12
FM2.5	2.5	30	0	23.6	0.062	6.34

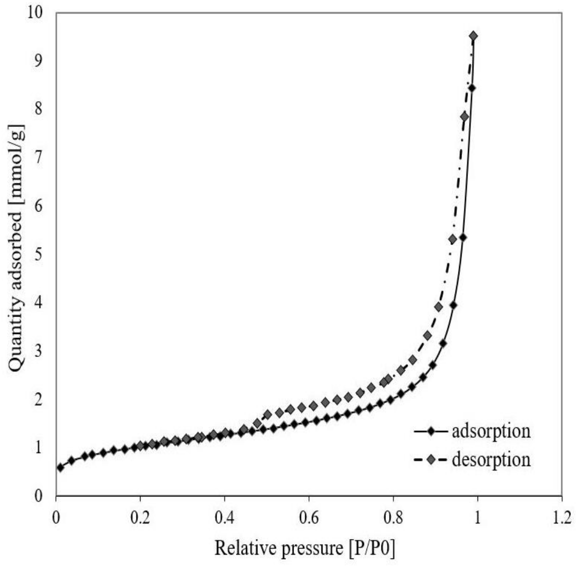

Figure 6.35: N2 adsorption and desorption isotherms of sample CM

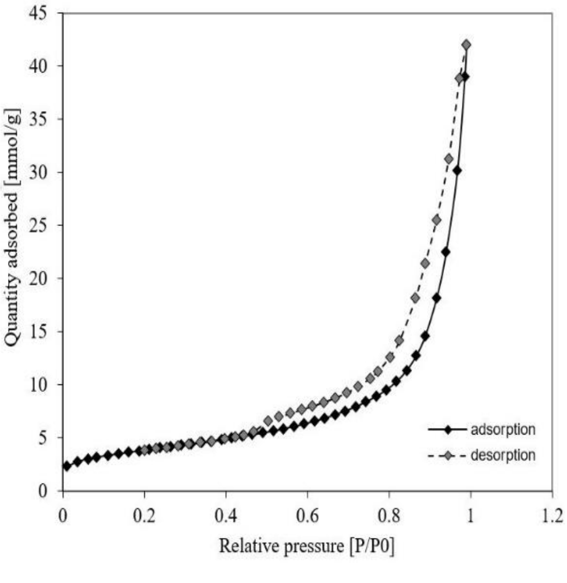

Figure 6.36: N2 adsorption and desorption isotherms of sample ACM

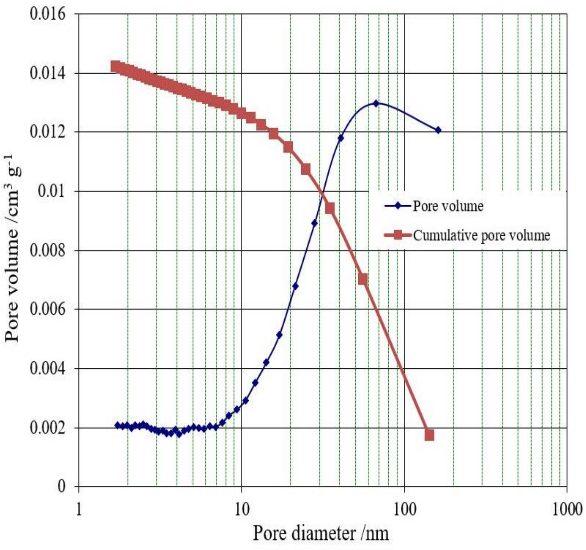

Figure 6.37: BJH adsorption of sample CM

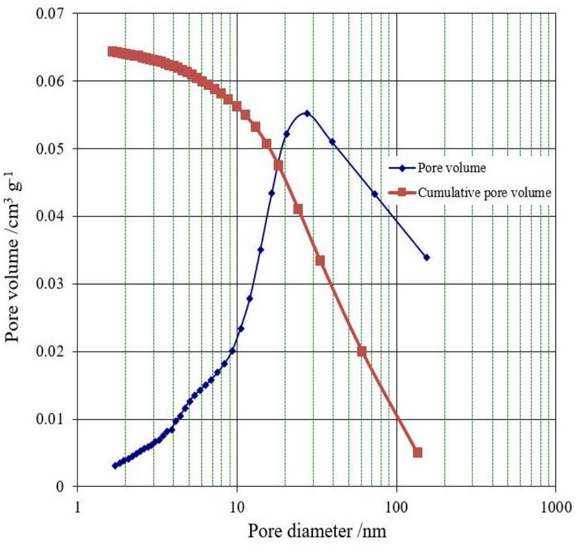

Figure 6.38: BJH adsorption of sample ACM

6.4.5 Identification of the formed hydrates using X-Ray diffraction analysis

XRD analysis of NT-modified fly ash and NT-modified metakaolin samples with different dosages, at 28 days of curing are shown in Figures 6.39 and 6.40, respectively. Ettringite, Portlandite, Alite and Belite were found to be major phases for the specimens. Other phases could not be identified in the XRD analysis as many peaks overlapped or were poorly crystalline.

On increasing the NT to 2.5 wt%, the intensities of Alite $(\mathrm{C_3S})$ and Belite $(\mathrm{C_2}S\ )$ increased (2θvalues of 23.6°, 25.7°, 29.6°, 34.6°, 41.6°, 46.3°,46.2° and 51.9°) for both samples. However, no other new crystalline phase was found.

It can be seen from the XRD images in Figures 6.39(b) and 6.40(b) that, compared with the control mix (ACM), there was not a significant increase in the intensity of Ca$(\mathrm{OH})_2$ produced from cement hydration, when the added amount of NT increased to 2.5 wt% (2θvalues of 18°, 50.81°) (JCPDS-International, 2000). For NT-modified MK samples, the generation amounts of AFt of each sample reached the maximum compared with the NT-modified fly ash (2θvalues of 9.1°,16.1°).

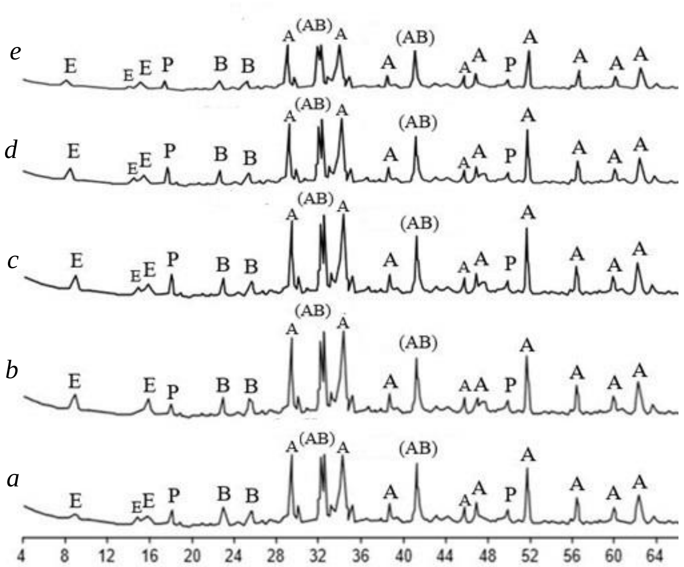

Figure 6.39: XRD analysis of different specimens at the 28-day curing age: a) control (ACM), b) M2.5, c) AM2.5, d) BM2.5, e) CM2.5. A: Alite, B: Belite, P: Portlandite, E: Ettringite.

On increasing the NT to 2.5 wt%, and MK to 10 wt%, the intensities of C_3S and C_2S further increased for 2θ values of 29.6°, 34.6°, 41.6°, 46.3°,47.2° and 51.9°, and reached the peak for hydration at 28 days. It should be noted that $Ca(OH)_2$ and Aft peak intensities increased for the samples containing FA (2θ values of 18°, 50.21° and 9.1°,16.1°) and slightly decreased for the samples containing MK. FA lengthened the induction period of the hydration process (Figure 6.39(c)).

The increased degree of hydration was presumably due to the enhanced dissolution and precipitation of hydration products upon FA, MK and NT incorporation. When the added amount of FA and MK reached 20 wt% and 30 wt% (Figures 6.39(d) and (e) and Figures 6.40(d) and (e)), the intensities of C_3S and C_2S for 2θ values of 29.6°, 34.6°, 41.6°, 46.3°,46.2°, and 51.9° decreased, suggesting increased consumption of C_3S and C_2S phases and also increased formation of C-S-H phase compared with the control mix (ACM).

Also, the decrease in the intensities of AFt (2θ values of 9.1°,16.1°) were observed for both samples. It can be seen from the XRD images that, compared with the control mix (ACM), there was not a significant change in the intensity of $Ca(OH)_2$ produced from cement hydration, when the added amount of FA and MK increased to 20 wt%. However, when the amount of FA and MK reached 30 wt%, there was a significant decrease in the intensity of $Ca(OH)_2$ (2θ values of 18°, 50.21°).

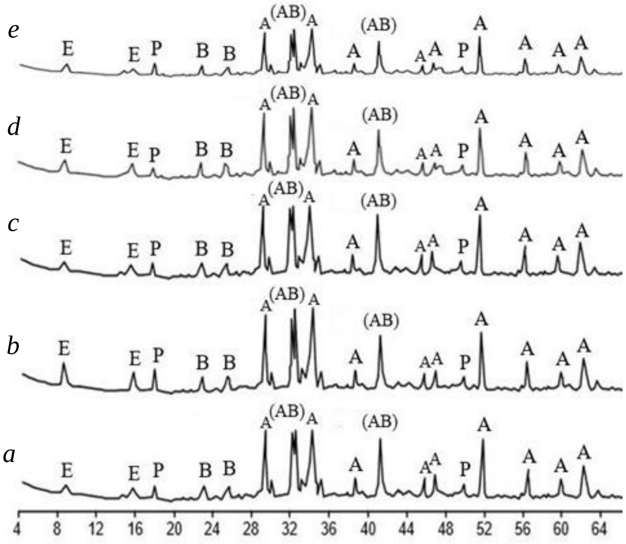

Figure 6.40: XRD analysis of different specimens at the 28-day curing age: a) control (CM), b) AM2.5, c) DM2.5, d) EM2.5, e) FM2.5. A: Alite, B: Belite, P: Portlandite, E: Ettringite.

6.4.6. Quantification of the formed hydrates through thermo-gravimetric analysis (TG/DTG).

Thermogravimetric (TG) curves of the hydrated NT-modified FA and MK samples, including the control, at 28 days of curing are shown in Figures 6.41 and 6.43. Derivative thermogravimetric (DTG) curves were plotted from the TG data to identify the extent of cement hydration and the exact boundaries of various phases present in the hydrated samples. DTG curves of the hydrated cement paste samples are shown in Figures 6.42 and 6.44. The TG-DTG curves showed the typical reactions occurring in the cement mortars when subjected to a progressive temperature increase from room temperature to 1000 °C in 20 mL min^{-1} Nitrogen gas flow. The mass loss in the NT-cement mortars, NT-modified FA and MK geopolymer, including the control, during heating in the TG-DTG analyses occurred in four main steps. As explained in Chapter 5, the dehydration of water molecules in hydrates such as C-S-H and ettringite took place within the range from room temperature to 200 °C (Toon et al., 2012; Frias et al., 2001; Ashraf et al., 2009; Aly et al., 2012). The second reduction at 200-380 °C, caused a loss in mass corresponding to the breakdown of C-A-H phases (Frias et al., 2001; Ashraf et al., 2009; Aly et al., 2012). The third step of thermal degradation occurred between 410-550 °C, and the corresponding mass loss was associated with the dehydroxylation of $\mathrm{Ca(OH)_2}$ produced during curing to CaO and $\mathrm{H_2O}$ (Tobón et al., 2012; Frias et al., 2001; Ashraf et al., 2009; Aly et al., 2012).

When the mortar specimens were cured, calcium hydroxide forming in them gradually combined with carbon dioxide of the air to form calcium carbonate (Chang et al., 2006). Subsequently, the final weight loss area was observed at 550–740 °C, occurred due to the decomposition of calcium carbonate and escape of $\mathrm{CO_2}$ from the cement matrix (Frias et al., 2001; Ashraf et al., 2009; Aly et al., 2012; Chang et al., 2006).

Table 6.14 presents the mass percent of C–S–H, $\mathrm{C_2AH_8}$, $\mathrm{Ca(OH)_2}$ and $\mathrm{CaCO_3}$ which were calculated by multiplying the mass loss percent of each steps of TG curves, given in Table 6.13, with the stoichiometric molar mass ratios of $\mathrm{CSH/H_2O}$, $\mathrm{C_2AH_8/H_2O}$, $\mathrm{Ca(OH)_2/H_2O}$ and $\mathrm{CaCO_3/CO_2}$, respectively. The mass percents of C-S-H, $\mathrm{C_2AH_8}$, $\mathrm{Ca(OH)_2}$ and $\mathrm{CaCO_3}$ in the sample were calculated from the TG curves using the following Eqs. (5.1)-(5.4) as described in Chapter 5. The TG curves of samples M2.5, AM2.5, BM2.5, CM2.5 showed similar changes to that of control mix (ACM), with some changes in mass loss and mass loss rates at each step. The first DTG peaks of ACM appeared at 94°C, corresponding to a 2.6% mass loss in C-S-H and AFt content.

Similarly, the first DTG peaks of samples M2.5, AM2.5, BM2.5 and CM10 appeared between 64 °C and 107 °C where the highest C-S-H and AFt mass loss rate was observed for AM2.5. The second decomposition step of ACM occurred between 215 °C and 376 °C, and reached a maximum rate at 232 °C, resulting in a 0.31% mass loss in C_2AH_8 content. The second thermal decomposition steps of sample M2.5, AM2.5, BM2.5 and CM2.5 occurred in the same temperature range of 210–390 °C, where the corresponding mass losses were 0.35%, 0.31%, 0.91% and 0.82, respectively.

The third decomposition step of ACM, as well as those of M2.5, AM2.5, BM2.5 and CM2.5, occurred between 410 °C–550 °C. The mass loss rates observed at the third step of DTG showed decreases in the rates of decomposition of $Ca(OH)_2$ in ACM and AM2.5 in comparison to those of M2.5, BM2.5 and CM2.5. The residues of M2.5, AM2.5, BM2.5 and CM10 at 850 °C, as well as the control were about 87-92% at 28 days of curing. Finally, the fourth decomposition step occurred between 550 °C and 740 °C. The mass loss rates observed at the fourth step of DTG showed a significant decrease in the rate of decomposition of calcium carbonate in M2.5 in comparison to that of ACM.

Figures 6.43 and 6.44 show the TG-DTG behaviour of specimens containing different dosages of NT and MK at 28 days of curing. The significant points of the TG–DTG analysis for the NT modified MK geopolymer samples can be summarized as follows: the incline of the first step of the TG curve of DM2.5 was very steep, and the corresponding mass loss rate was the maximum (2.6 % min^{-1}) and reached 5.2% mass loss at 109 °C, much greater than EM2.5 and FM2.5 due to the higher extent of C-S-H formation in DM2.5. The second step of decomposition of DM2.5 occurred between 220 °C and 380 °C, and reached a maximum rate at 242 °C, resulting in a 1.31% mass loss in C_2AH_8 content. The mass losses at the third step of TG analyses for DM2.5, EM2.5 and FM2.5, related to the decomposition of $Ca(OH)_2$, were 2.4%, 1.2% and 1.2 respectively, which were all relatively higher than NT cement mortars containing FA. The third thermal decomposition step of DM2.5 occurred considerably faster than those of ACM, M2.5, BM2.5, CM2.5, EM2.5 and FM2.5 as given in their DTG curves (Figure 6.44). In the fourth decomposition step between 550 °C and 740 °C, the mass loss rate of FM2.5 observed was the smallest among all the samples. Residues of DM2.5, EM2.5 and FM2.5 at 900 °C were 79.8, 85.3. and 87.6%. In addition, the total amount of $Ca(OH)_2$ and $CaCO_3$ for M2.5 was 7.65%, which was also the smallest among all the samples, indicating the rising extent of bonding between NT and $Ca(OH)_2$ in M2.5 in comparison to bonding in other samples suggesting the difficulty of CO_2 penetration in M2.5 due to the strength of bond formation and compact structure.

Table 6.13: Mass losses in TG after 28 days curing (%).

Mix	1st step	2nd step	3rd step	4th step	Residue (%)
	20-200˚C	220-380 ˚C	410-550 ˚C	550-740 ˚C	850 ˚C
ACM	2.6	0.31	1.21	5.2	87.6
M2.5	2.7	0.35	0.70	2.1	91.1
AM2.5	2.8	0.31	1.41	4.8	88.7
BM2.5	2.1	0.41	0.61	4.4	90.5
CM2.5	1.6	0.42	0.60	5.2	90.2
DM2.5	5.2	1.31	2.4	9.1	79.8
EM2.5	3.2	0.91	1.2	6.8	85.3
FM2.5	3.1	0.82	1.2	5.8	87.6

Table 6.14: Masses % of C-S-H, C_2AH_8, $Ca(OH)_2$ and $CaCO_3$ calculated from the 1st to 4th steps of TG analyses for the NT cement mortars containing different dosages of the FA and MK and pure cement mortar specimens at the age 28 days.

Mix	1st step	2nd step	3rd step	4th step
	C-S-H	C-A-H (C_2AH_8)	$Ca(OH)_2$	$CaCO_3$
ACM	6.97	2.30	4.97	11.8
M2.5	7.23	2.60	2.88	4.77
AM2.5	7.50	2.30	5.79	10.9
BM2.5	5.60	3.05	2.41	9.98
CM2.5	4.30	3.12	2.47	11.8
DM2.5	13.9	9.75	9.86	20.6
EM2.5	8.58	6.77	4.93	18.4
FM2.5	8.31	6.10	4.93	13.2

These results are in good agreement with the result of compressive and tensile strengths observed in M2.5 (Figures 6.47-6.50). As seen in Table 6.14, the mass percent of free $Ca(OH)_2$, which did not enter the pozzolanic reaction, in samples containing FA is lower than those containing MK. Alternatively, the amount of free $Ca(OH)_2$ in BM2.5 was found the least among all the samples, i.e., 2.41%. These findings indicated the noticeable increase in the extent of bond formation between NT and free calcium hydroxide when the amount of NT is 2.5 wt.% and FA 20 wt% at 28 days curing.

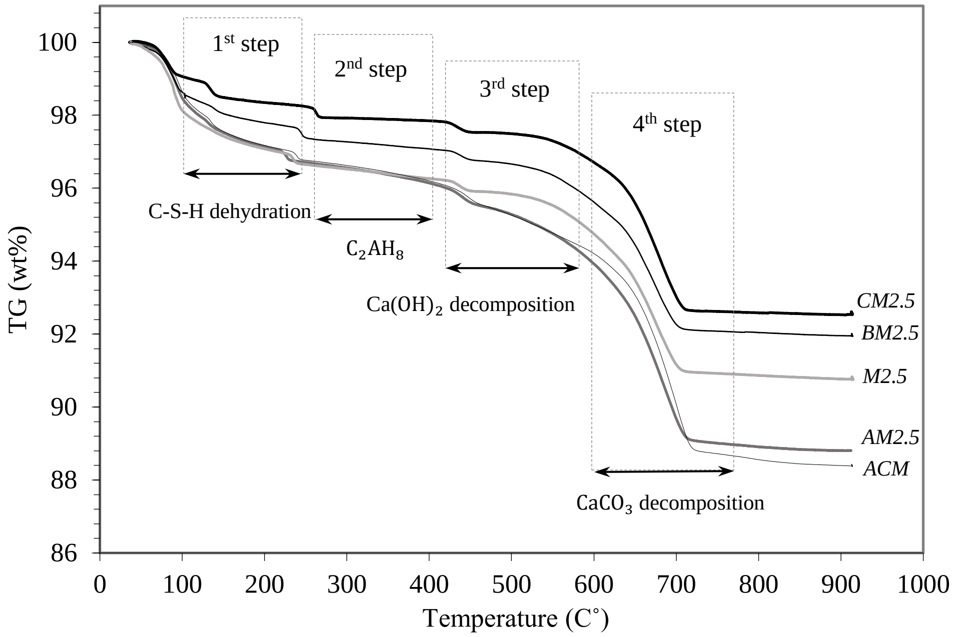

Figure 6.41: TGA curves of the mortar specimens containing different amount of NT at the age of 28 days.

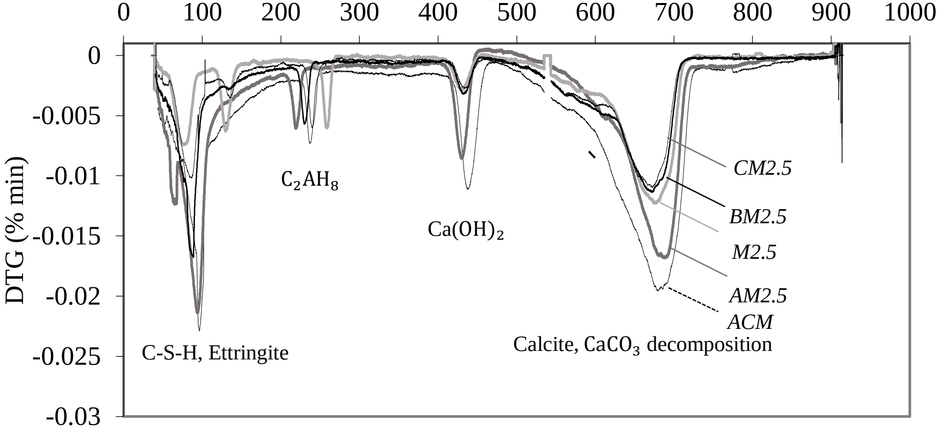

Figure 6.42: DTG curves of the mortar specimens containing different amount of NT at the age of 28 days.

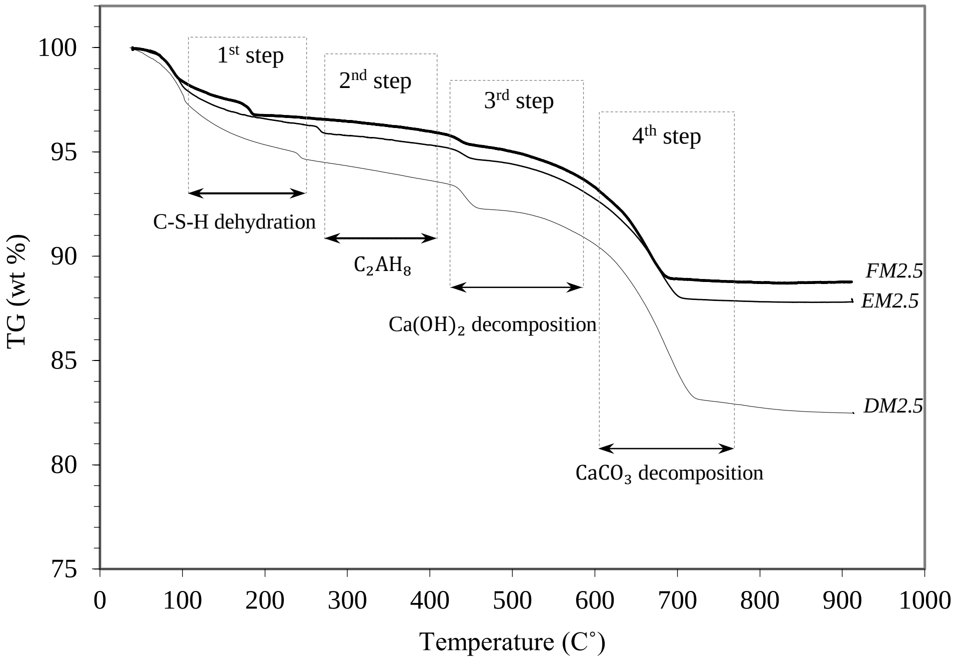

Figure 6.43: TGA curves of the mortar specimens containing different amounts of NT at the curing age of 28 days.

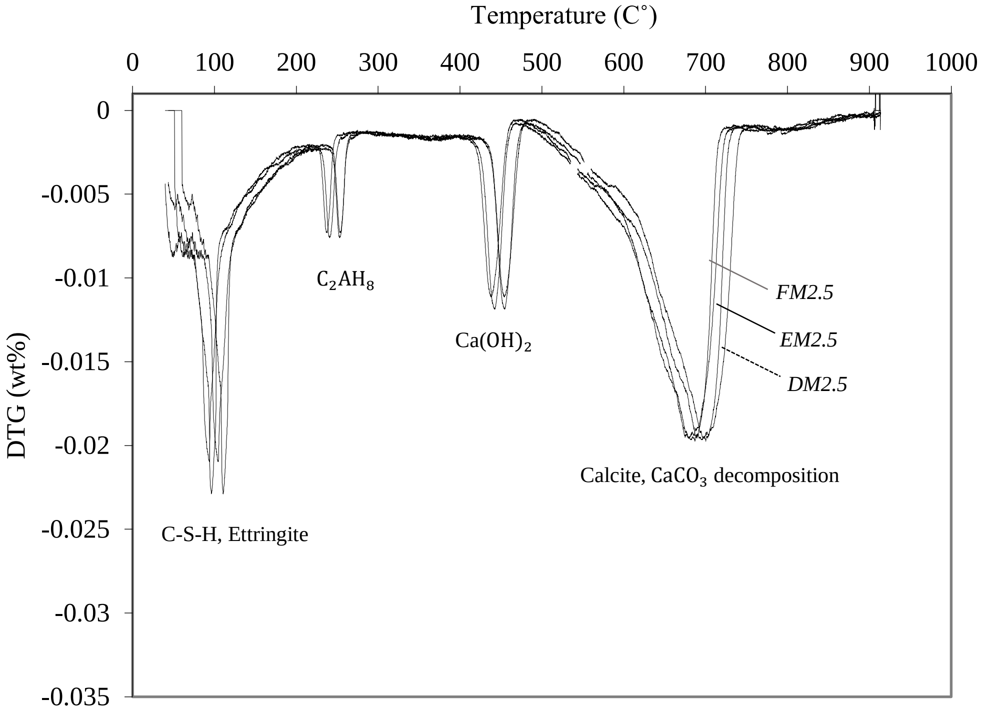

Figure 6.44: DTG curves of the mortar specimens containing different amounts of NT at the curing age of 28 days.

6.4.7 Results of the direct tension and compression tests using Instron 5969®.

Direct compression and tension tests were conducted, on a number of NT-cement samples with different dosages of FA and MK, to determine the mechanical strengths. The compressive strengths were evaluated from the peak load obtained by crushing the specimens according to BS EN12390-3 (BSI, 2009b). The concrete specimens used in the compression test were in the size of 100mm × 100mm × 100mm. The cubes used for the compression test were cured in tap water for 28 days and taken out of the water one day prior to the testing.

A general view of the experimental setup for conducting compressive strength is illustrated in Figure 6.45(a). The tension tests consisted of a tension testing machine (Instron 5969®) with a capacity of 50 kN and cylindrical samples with a diameter of 50 mm and a length of 400 mm. The testing arrangement is shown in Figure 6.45(b). The specimens were prepared with a circumferential notch with a depth of 10 mm +/- 1 mm and a width of 2.5 mm. This set-up made it possible to control the eccentricities of the tensile load during the tests. A double plate system with an M8 bolt connection for each side of the sample was designed and is illustrated in Figure 6.46.

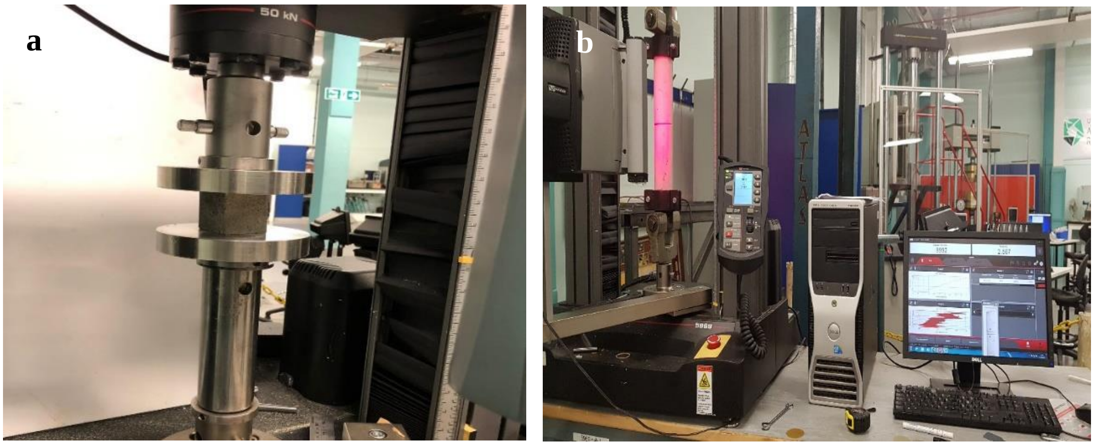

Figure 6.45: a). Illustration of the experimental setup for conducting compressive strength. b). A general view of the experimental setup for conducting tensile test on the cement mortars using Instron 5969®.

In this experiment different percentages of OPC were replaced with combined use of NT, from 0 to 10 wt% in mass of the cement and FA and MK within the range of 10 to 30 wt% based on BS EN197(BSI, 2000) and then grouped into 6 sets (A, B, C, D, E, and F) as illustrated in Figures 6.38-6.41. Slump tests were then carried out according to in BS EN 12350-2 (BSI, 2009a). The mix proportion design resulted with slumps ranging from 100 to 230 mm and vebe times ranging from 8 and 16 seconds, which met the required workability based on BS EN 12350-2 (BSI, 2009).

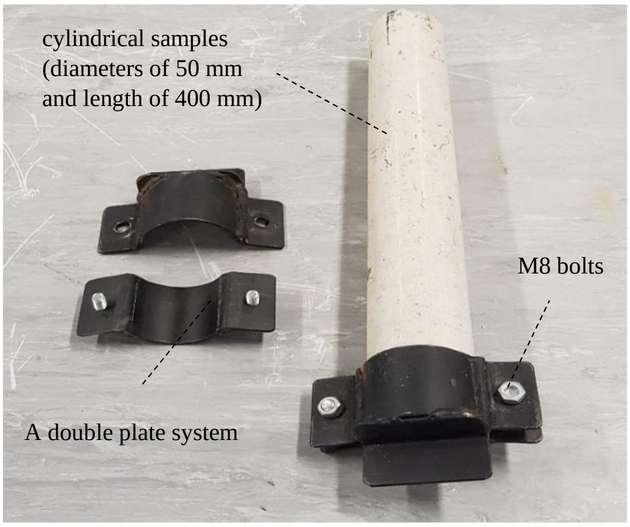

Figure 6.46: A double plate system with an M8 bolt connection for each side of the sample.

As it is shown in Figure 6.47-6.50, the compressive and tensile strengths of the NT cement mortars were significantly improved by using FA and MK as cementitious material replacements. Results show that the compressive strength increased with the increasing NT content up to 2.5 wt%. The compressive strength of 2.5 wt% amount of NT increased by 30.6% at 28 days, while the compressive strength of 5 wt% only increased by 23.4%. On increasing the NT (>2.5 wt%) and FA (>10 wt%) the tensile strength increased by 56.3%. The changes in the microstructure of the AM2.5 were also in line for the slightly increase in the compressive strength. However, the compressive strength only improved by 1.4%.

When the dosage of fly ash exceeded the optimal value, *i.e.* FA > 10 wt%, drying shrinkage distortions of mortars were enlarged, leading to the increase in the average pore radius size and causing internal defects to form in mortars. This would certainly influence the overall voids and the total porosity, as the result the microstructure became isolated and defective (Figure 6.31(e)). This is due to the fact that the unreacted or partially reacted FA particles created porosity in the matrix dispersed in small sized pores, so cavities were found from the spaces left after the dissolve of the FA particles. The lowest compressive and tensile strengths were obtained by CM10 containing 2.5 wt% NT and 30 wt% FA as illustrated in Figures 6.47 and 6.48. An important factor that should be considered is that the compressive strength was statistically close between the mixes but that was not the case for the tensile strength. The study has shown that replacing cement by combination of 2.5 wt% NT and 10 wt% FA was the optimal amount for improving the microstructure of the NT-modified FA composites. As it is shown in Figures 6.49, 6.50 and 6.52, the compressive and tensile strengths of the NT cement mortars were significantly improved by using MK as a cementitious material replacement.

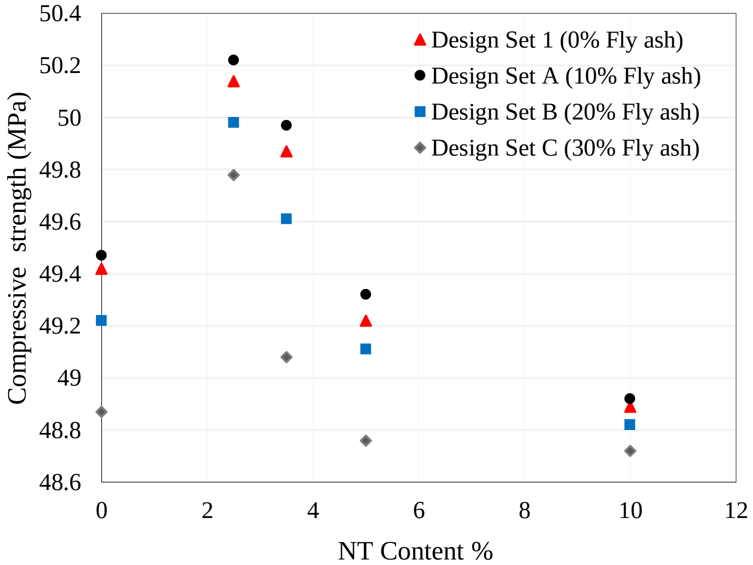

Figure 6.47: Relationships between compressive strength and dosage of NT for the NT-modified FA samples.

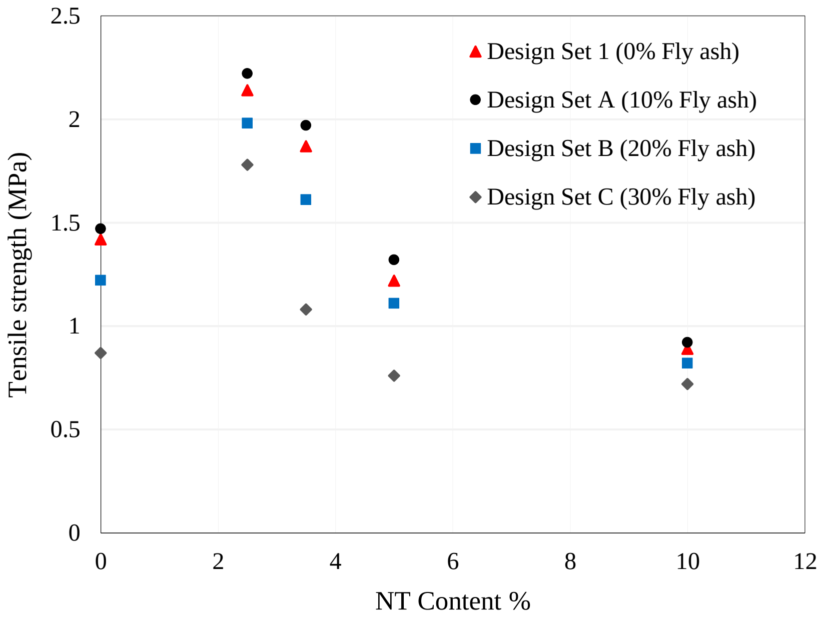

Figure 6.48: Relationships between tensile strength and dosage of NT for the NT-modified FA samples.

On increasing the NT (> 2.5 wt%) and MK (> 10 wt%) the tensile strength increased by 50.0%. However, the increase in the compressive strength was heightened as much as 1.0 % to that of the control specimen. Similar to the NT-modified FA composites, when the amounts of NT and MK exceeded the optimal values, *i.e.* NT > 2.5 wt% and FA > 10 wt%, the results showed clear trends of the decreasing compressive and tensile strengths of the specimens, as illustrated in Figures 6.49 and 6.50. These results were in good agreement with the results of 2D and 3D Porosity analyses observed in DM2.5, with 3D volumetric void fraction and 2D area void fraction reduced by 54.9% and 66.3%, respectively. The porosity as well as the tortuosity of the pores in the hardened cement paste were normally reduced when pozzolanic materials were added, which influenced many properties such as the compressive and tensile strengths. This might be caused by the interactions among the particles of MK with the portlandite ($Ca(OH)_2$), and resulted in the formation of re-crystallized calcium carbonate in the cementitious matrix causing the reduction in porosity, thus improving the density and tensile strength of concrete. I have also tested and benchmarked the tensile strengths of the composites with dog-bone shaped geometry. The tension tests consisted of a tension testing machine

(Instron 5969®) with a capacity of 50 kN and dog-bone shaped samples with dimensions beginning with the cross section of 10 mm × 40 mm and later changing to 20 mm × 40 mm in prismatic shape after 10 mm away from each ends of the samples with a length of 70 mm for the cross section as described and shown in Section 6.3.6.

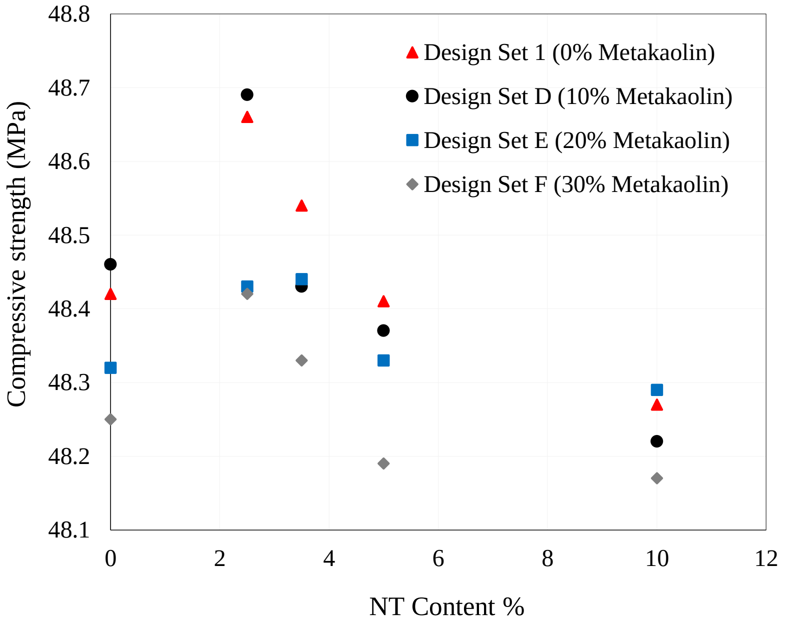

Figure 6.49: Relationships between compressive strength and dosage of NT for the NT-modified MK samples.

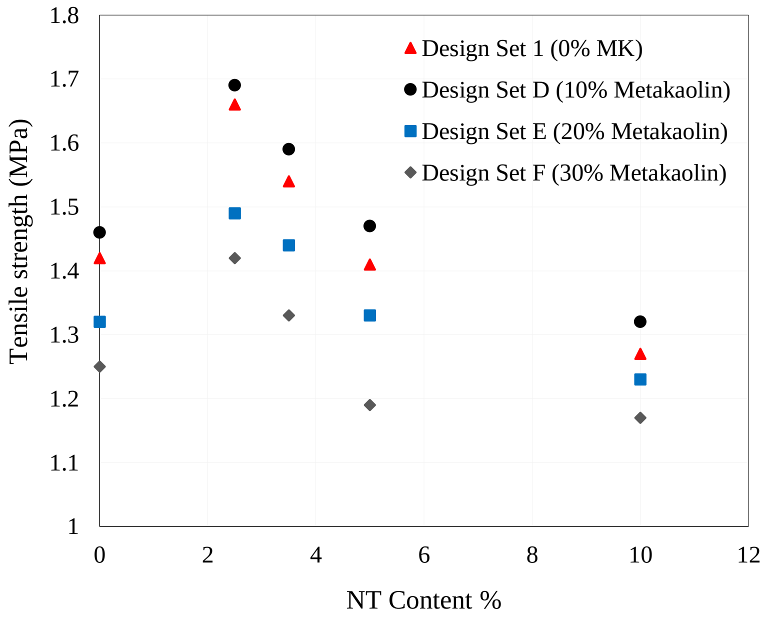

Figure 6.50: Relationships between tensile strength and dosage of NT for the MK-modified samples.

The dog-bone specimens were glued to steel supporting plates and final fin plates would be fixed at each end through an epoxy resin-based bicomponent as shown in Section 6.3.6. In this test, the displacement control at the rate of 0.7 mm/min was applied to the steel rod and the tensile load delivered to the sample to get the accurate readings of the stress-strain curves. As it is shown in Figure 6.51, the tensile strength of NT composites was significantly improved by using MK and FA as cementitious material replacements.

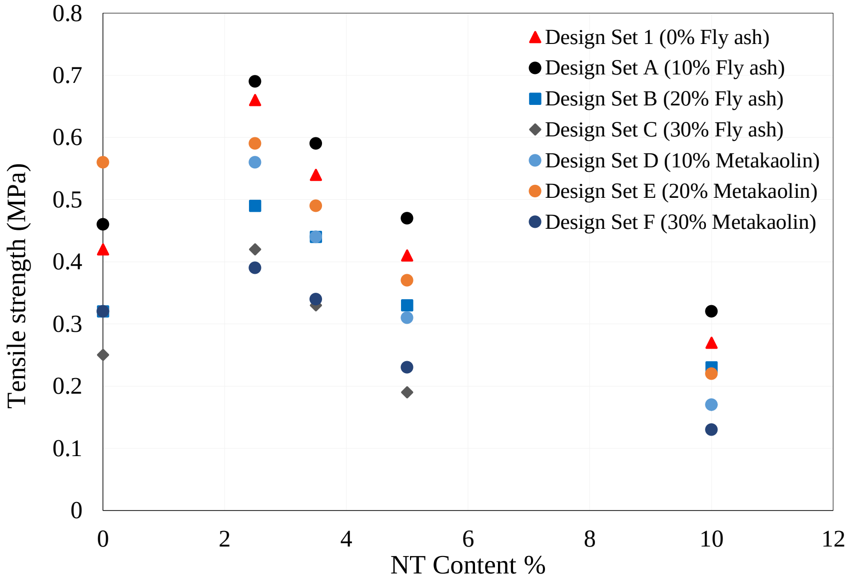

Figure 6.51: Relationships between tensile strength and dosage of NT for the FA and MK-modified dog bone samples.

6.5 Remarks

In this chapter, multiscale pore structure analyses on the NT-modified FA and MK composite samples incorporated with different percentages of NT and FA were carried out. Novel XCT tests were conducted to quantify and characterise the pore system for the NT cement composite. SEM-EDS was been used to evaluate the phases of the microstructures of the composite. Direct tension and compressive tests were conducted to quantify and characterise the mechanical properties of the NT mortar composite. XRD and SEM-EDS were utilised to evaluate the phases of the microstructures. The extent of cement hydration and the exact boundaries of various phases present in the hydrated samples were evaluated by thermogravimetric/derivative thermogravimetric analysis (TG/DTG). In addition, the durability was assessed by testing the water permeability using a high-pressure core holder with a sensitive and automated measurement capability. Further, BET analysis was carried out to examine the nanoscale pore system of the NT cement samples, including the pore volume, pore shape and surface area. The findings of this study were expected to contribute to the better and broader utilization of NT in FA and MK composites. Based on the experimental results, the following findings were obtained.

(1) The study showed that replacing cement by combination of 2.5 wt% NT and 10 wt% FA was the optimal amount for improving the microstructure of the NT-modified fly ash composites, with 3D volumetric void fraction and 2D area void fraction reduced by 64.09% and 60.97%, respectively.

(2) Increasing the NT content up to 2.5 wt% and FA to 10 wt% led to a more reduction in permeability of the NT-modified fly ash composites compared with the control mix (CM), with the permeability reduced by 44.1%. When the amount of NT and FA exceeded the optimal value, *i.e.*, NT > 2.5 wt% and FA > 10 wt%, the result showed clear trends of the increased permeability and porosity of specimens. Significant increases in the contents were found of portlandite $Ca(OH)_2$ and C-S-H phases and the pores of cement mortars were best filled, resulting in a more homogenous morphology.

(3) The study showed that replacing cement by combination of 2.5 wt% NT and 10 wt% MK was the optimal amount for improving the microstructure of the NT-modified MK composites, with 3D volumetric void fraction and 2D area void fraction reduced by 54.9% and 66.3%, respectively.

(4) For the NT-modified MK samples, the generation amounts of AFt of each sample reached the maximum compared with the NT-modified fly ash (2θ values of 9.1°,16.1°).

(5) The results showed that the increased degree of hydration was presumably due to the enhanced dissolution and precipitation of hydration products upon FA, MK and NT incorporation. When the added amount of FA and MK reached 20 wt% and 30 wt%, the intensities of C_3S and C_2S decreased, suggesting increased consumption of C_3S and C_2S phases and also increased formation of C-S-H phase compared with the control mix.

(6) DTG results indicated a significant increase in the extent of bond formation between NT and free calcium hydroxide when the amount of NT was 2.5 wt% and the amount of FA was 20 wt% at 28 days of curing.

(7) SEM results indicate that by adding 2.5 wt% NT and 10 wt% FA, the pores of cement mortars were best filled, resulting in a more homogenous morphology.

(8) At the nanoscale, the BET results revealed a clear increasing trend of the surface area of the NT-modified fly ash composites due to the combined presence of the NT (up to 2.5 wt%) and FA (up to 10 wt%).

(9) The compressive and tensile strengths of the NT cement composites were significantly improved by using FA and MK as cementitious materials.

In summary, it can be concluded that adding a certain amount of NT (around 2.5 wt%) and FA/MK (10 wt%) could modify the pore structure of cement mortars by changing the harmful microscale pores to the nano-sized benign pores, leading to a much stronger durability of cement-based materials. The results demonstrated that the photovoltaic waste could be used as a potential NT-SCM composite to partly replace cement in concrete, thereby decreasing the CO_2 footprint of concrete and the environmental impact associated with landfill.

Chapter 7

Effect of Nano-Titanium Dioxide on Fracture Properties of Concrete

7.1 Introduction

Fracture mechanics involves the study of cracks propagation in materials. Gdoutos (1993) in his publication described “Fracture mechanics” as the fracture procedure in solids as “new material surfaces are formed in the medium in a thermodynamically irreversible manner”. Fractures may be distinguished between the ones characterised as brittle, ductile and quasi-brittle. The main difference between the three groups is the velocity of the fracture. The first category is described as having a low energy and high fracture velocity for unstable loading condition. The second category is related to large deformation and has a slow rate of fracture and a high energy dissipation. However, the third category has a steady rate of fracture beyond the ultimate stress.

Considering stress as a base point, brittle fractures result in a sudden drop in stress to “zero”, whereas in ductile fractures, the stress remains constant as the material yields. For quasi-brittle fracture, the stress decreases gradually once it exceeds the highest stress. When tensile loading cracks are formed and separate the cement particles which hold the aggregates together. This separation of cement particles causes the entire structure to fail as crack propagates. While the shape of the crack is likely to be highly irregular, it is expected that the irregularities will cause the cracks to grow in a slow manner to simple shapes along which the stress intensity factor (SIF) is nearly uniform. For an ideally brittle material, the stress–strain curve is linearly elastic up to the maximum stress, at which an initial flaw catastrophically propagates, leading to failure. For a quasi-brittle material like concrete, a substantial non-linearity exists before the maximum stress. The mechanisms of deformation beyond the proportional limit are not clearly understood. Initially, randomly distributed micro-cracks are formed. At some point before the peak stress, micro-cracks begin to localize into a macro-crack that critically propagates at the peak stress. Strain softening is observed under steady-state propagation of this crack.

Under a closed loop displacement-controlled testing condition, it is observed that the displacement during the post-peak stage consists of opening of the major crack accompanied by unloading of the rest of the specimen. This region is defined as the Fracture Process Zone (FPZ). The FPZ consists of micro cracks which are situated nearer to the crack tip. As the crack propagates these micro cracks merge and becomes a single structure to give continuity to the already existing crack. Therefore, the FPZ acts as a bridging zone between the cracked and uncracked regions. Analysis of this zone needs a careful consideration because it can help to predict the propagation of a crack and ultimate failure in concrete. This problem in concrete is resolved by the introduction of reinforcing components such as metallic bars, fibres, etc.

Another approach to reduce the amount of the steel reinforcement in order for the concrete to have high strength, lighter weight and good durability includes the use of nano particles which are capable of holding aggregates under tensile loading. For heterogenous composites such as concrete composites, addition of nanoparticles makes them an ideal candidate for the application of nanotechnology. To improve the pore structure of concrete, NT can be applied and this causes densification of paste-aggregate transition zone, which in turn affects the fracture properties. The main functions of the nano particles in structural members subjected to tension are to resist the opening of cracks due to micro-cracking, to increase the ability of the composite to withstand loads, and to allow large strains.

Although most nano-materials show various positive effects on the properties of concrete, they have limited application due to their toxicity. NT particles have attracted extensive interest due to their safety, chemical stability and their potential applications in many fields. NT particles have an enormous potential in crack arresting and therefore can be used in liquid storage structures and nuclear power plants where cracking must be avoided.

Due to the lack of quantitative research conducted towards the effects of nano-titanium on characteristics of concrete such as fracture behaviour, there is an effort in the industry to carry out studies that focus on inspecting these properties by using and comparing different dosages of nano titanium to maintain a durable structure, which is also the main topic of this chapter. As part of the recent developments in concrete engineering, some industrial by-products are used as important additives in partial replacement of cement.

Among these, silica fume, ground granulated blast furnace slag, fly ash and metakaolin are the most widely used ones in producing high-strength and high-performance concrete, mostly because they have favourable engineering performances. When these materials are combined with Portland cement through either pozzolanic or hydraulic activity, a contribution towards the properties of hardened concrete is made. Fly ash is a by-product from the thermal power plants, which is widely available in the world. Fly ashes consist mainly of silicate ($\mathrm{SiO_2}$) but can contain also significant quantities of alumina ($\mathrm{AL_2O_3}$).

Fly ashes are spherical in nature. Besides the pozzolanic activity, FA plays roles of a micro filler and water reducing agent, and prevents the formation of micro-cracks at early ages due to the relatively slow release of the hydration heat (Spiesz, 2013). Zhang, et al. (2011) concluded from their experimental study that fly ash cement replacement of 10% to 20% increases the fracture properties of the concrete. However, once the percentage increases beyond those values, the fracture energy decreases gradually. According to Lam et al. (1998) experimental investigation, replacing OPC with 45% and 55% fly ash resulted with low bearing capacity load. However, it resulted with "greater crack tip opening displacement and final deflection at mid-span". As per the fracture energy and toughness, it resulted with equal or greater values in comparison to 100% OPC concrete.

A comprehensive review of the studies on the use of MK as a partial pozzolanic replacement for cement in mortar and concrete has recently been reported by Sabir et al. (2001). It was reported that the concrete incorporating 10% MK had a higher compressive strength than the reference plain concrete (Sabir et al., 1996; Zhang et al., 1995).

Qian and Li (2001) found that tensile and bending strengths increased with the amount of metakaolin in concretes containing 5, 10 and 15% metakaolin. Concrete in which 15% cement was replaced by metakaolin had 28% higher tensile strength than the reference concrete which contained no metakaolin. With respect to the durability aspects, the resistance of MK concrete to water or chloride ion penetration was significantly higher than the control concrete (Zhang et al., 1995; neyisi et al., 2007). Metakaolin has been widely studied for its highly pozzolanic properties, suggesting that metakaolin could be used as an SCM. Unlike other SCMs that are secondary products or by-products, metakaolin is a primary product, obtained by calcining kaolin clay within a temperature range of 650 to 800 C° (Guneyisi et al., 2008).

Metakaolin is increasingly being used to produce materials with higher strength, denser microstructure, lower porosity, higher resistance to ions, and improved durability (Güneyisi et al., 2007).

An overview of the physico-chemical properties determined for all SCMs applied in this chapter was given in Tables 2.9 and 2.10. Additionally, Figure 6.1 showed their PSDs considering the sieve sizes (ISO sieves) presented in Table 2.1. Although, different aspects of cement-based materials containing FA and MK particles separately have been reported in the literature, to my knowledge, there is no systematic study on the influence of NT in conjunction with FA and MK on the overall performance of cementitious materials. In particular, the effects of FA and MK as by-product materials and NT as a high surface area additive on the fracture properties of cementitious materials need to be studied in detail.

The experimental study in this chapter involved the application of different samples grouped into 4 sets according to their NT, FA and MK presence in order to determine their toughening mechanism, by means direct tension tests, and the fracture toughness, fracture energy and crack mouth opening displacement (CMOD) of the notched specimens of mortar composite were measured. For these purposes, such possible effects were explored on samples with different weight fractions of MK and FA replacement (10%, 20% and 30%) and a range of w/b ratios (0.42, 0.38 and 0.32).

The results revealed that the addition of lower NT content (< 2.5%) nanoparticles may help improve the fracture properties of mortar composite containing FA and MK. In addition, the fracture parameters increased gradually, and the fracture relational curves became thicker as the NT content increased from 0 wt% to 2.5 wt%. However, the fracture parameters began to decrease, and the curves became thinner when the NT content exceeded 5wt%. These variation phenomena of the fracture parameters and fracture relational curves indicated that NT contributed significantly to the improvement of fracture properties of mortar composite containing FA and MK only when its content did not exceed 2.5 wt%.

7.2 Experimental

7.2.1 Materials

Different percentages of OPC, Provided by Jewson, which complies with BS EN197 Part 1 (BSI, 2000), with a grade of 42.5 N/mm^2, was replaced with anatase NT, *viz*. 0 wt%, 2.5 wt%, 3.5 wt%, 5 wt% and 10 wt% and FA/MK within the range of 10 wt% to 30 wt%, Natural river sand, with a minimum particle size of 150 μm, served as the fine aggregate. Fly ash, Super-pozz® SV80 of class F, was utilised in the project, which complies with BS EN450 (BSI, 2002). The mineralogical phases and chemical composition of the raw materials used were obtained from the X-ray diffraction (XRD) and X-ray fluorescence (XRF) analyses. An overview of the chemical composition of cement and FA was given in Tables 6.1. The NT particles used in this research were obtained from ALDRICH and had a specific surface area of 35-65 m^2/g. A summary of the physical properties of the NT, FA, sand and cement were given in Table 4.1 and Table 6.2. Deionised water, with a pH value of 7.5 at 22°C, was used throughout the experimental research.

7.2.2 Mixing procedure

The experimental study involved the application of different samples grouped into 7 sets according to their NT, FA and MK contents. In the first part of the experiment different percentages of OPC were replaced with NT (design set 1). The experimental study involved the application of a pan mixer with a 30 kg capacity. The fine aggregate was first poured into the pan-mixer, followed by the OPC CEM I 42.5N and FA/MK, under dry conditions. They were mixed for 45 seconds to ensure homogeneity. The mixing continued for another 3.5 minutes before water, already mixed with nano titanium dioxide, was added and the mixing was allowed to continue for another 10 minutes. In the second part of the experiment different percentages of OPC were replaced with combined use of NT, from 0 to 10 wt% in mass of the cement and FA and

MK within the range of 10 to 30 wt% based on BS EN197 (BSI, 2000) and then grouped into 6 sets (A, B, C, D, E, and F) as described in Chapter 6. Slump tests were then carried out according to in BS EN 12350-2 (BSI, 2009a). The mix proportion design resulted with the slump ranging from 90 to 260 mm and the vebe time ranging from 6 and 14 seconds, which met the required workability based on BS EN 12350-2 (BSI, 2009a). The recorded mix design, water/'equivalent cement' ratios and water/binder ratios for individual sets were presented in Chapter 6.

7.2.3 Test procedure

In the 1920s, Griffith developed a hypothesis based on glass experiments that led towards the establishment of the size effect concept, which contributed to the development of fracture mechanics (Gdoutos, 1993). However, Griffth and Irwin law cannot be used for concrete (Karihaloo, 2010). In 1961, Kaplan evolved the hypothesis of analysing the fracture mechanics of concrete based on linear elastic fracture mechanics 'LEFM' (Bažant, 2002). Since concrete counts as quasi-brittle material, LEFM method is not valid.

The LEFM method failed to examine the fracture properties of concrete, due to misunderstanding of the cement-based material. Cement deforms gradually, in association with a decrease in tension carrying capacity once the ultimate load is exceeded. The latter action is known as tension softening. In the applied method, the concrete behaves in a deviated manner, due to the development of the fracture process zone (FPZ) preceding the pre-existing notch. Since the material gradually softens at the FPZ, a non-linear fracture mechanics (NLFM) method is to be adapted for quasi-brittle materials. It is worth noting that structures of quasi-brittle failures are attributed with size and scale effects (Karihaloo, 2010). Hillerborg developed a fictitious crack model to assess the fracture of concrete by utilising fracture energy concept.

It assumes that the crack initiates once tensile strength is attained. Enhancement was adapted on the latter method by Bažant and Oh known as the crack band model. It assumes that cracks take place over a specific band width (Østergaard, 2003). There are methods that focus on FEA analyses of fracture, but this chapter will focus only on experimental methods. This test method covered the determination of fracture energy (G_f) of composites using the disk-shaped compact tension geometry, as outlined in Figure 7.1. The specimen geometry and terminology for the disk-shaped compact tension, DC(T)), was modelled for plane-strain fracture toughness of metallic materials. The disk-shaped compact tension geometry was a circular specimen with a single edge notch loaded in tension. The fracture energy can be utilized as a parameter to describe the fracture resistance. The fracture energy parameter is particularly useful in the evaluation of mixtures with ductile binders, such as concrete, and has been shown to discriminate between these materials more broadly than the indirect tensile strength parameter.

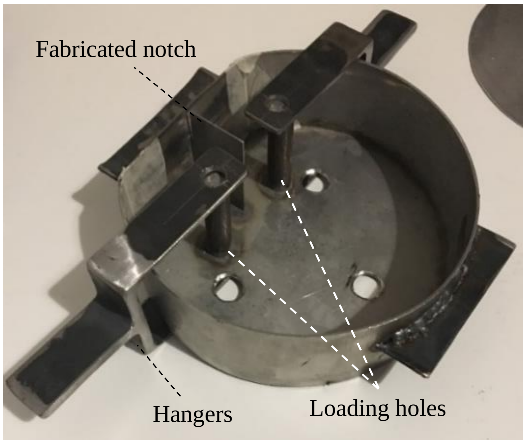

Figure 7.1: Disk-shaped mould geometry.

The test method was developed initially for determining the fracture resistance of asphalt-aggregate mixtures. The fracture resistance can help differentiate mixtures whose service life might be compromised by cracking such as concrete. The test method is generally valid for specimens that are tested at temperatures of 10°C (50°F) or below.

The specimen geometry in this study was designed to have a diameter of 130 mm and a thickness of 50 mm, as illustrated in Figure 7.2. The specimen geometry can also be adapted for forensic investigations using field cores of pavements where thin lifts are present.

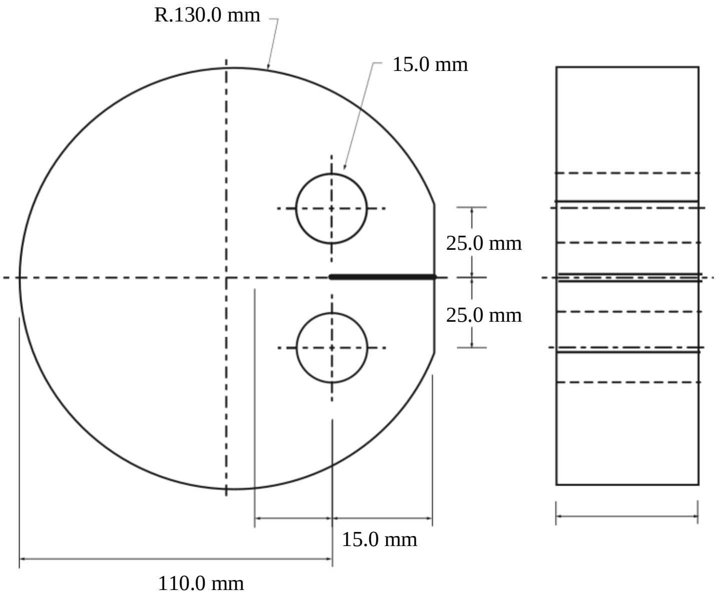

Figure 7.2: Specimen dimensions.

Specimens were tested in a loading machine 8801 servo hydraulic capable of delivering a maximum of 100 kN in tension as illustrated in Figure 7.3. The load apparatus could maintain a constant crack mouth opening displacement within 2% of the target value throughout the test.

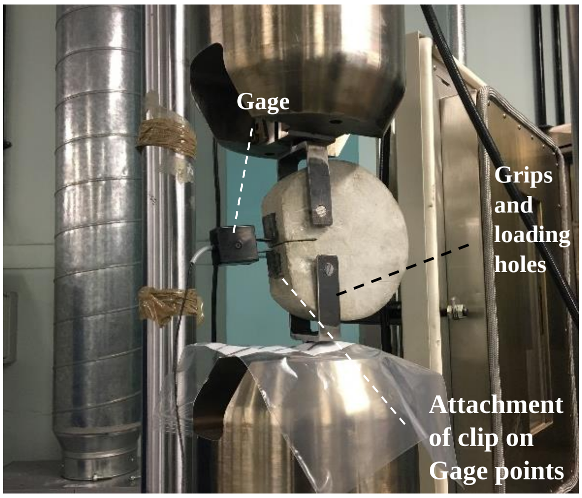

Figure 7.3:Setup of the clip-on gauge on the specimen in the testing machine.

The specimen was loaded through the pins which were allowed to roll freely on the flat surfaces of the loading clevis. A clip-on gauge was used to measure the relative displacement of the crack mouth across two points, initially 5 mm apart. The gauge was attached securely to gage points yet had the ability to be released without damage if the specimen broke.

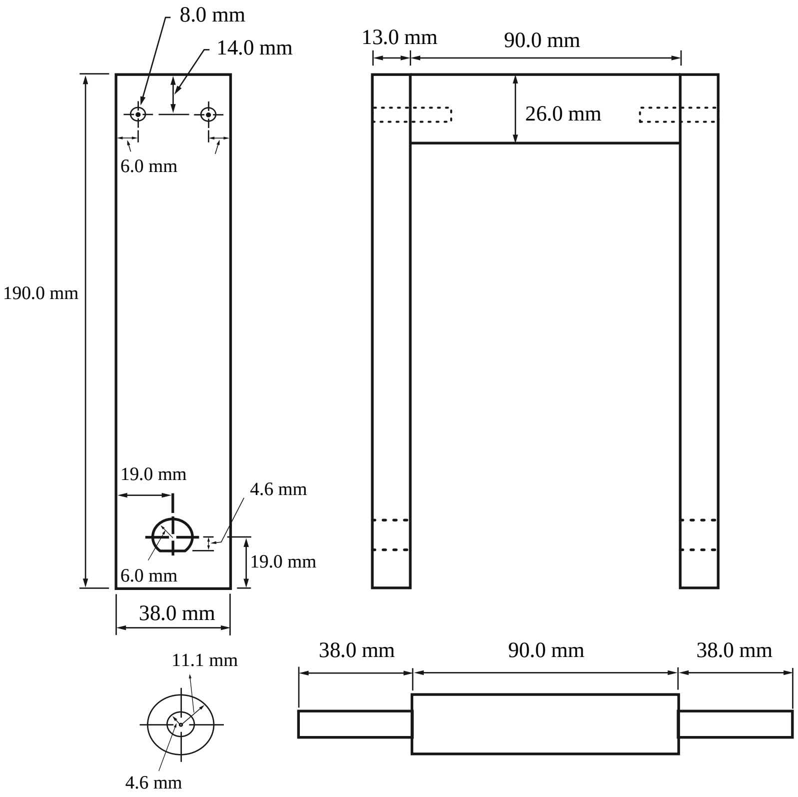

Figure 7.4: Schematic of the loading clevis.

A clip-on gauge was attached to the gauge points via knife edges. The gauge points were then glued to the specimen so that the clip-on gauge was set to the proper gauge length, which was typically 5 mm. Schematic drawings of the loading clevis and gauge points are shown in Figures 7.4 and 7.5. At the beginning of the test, the displacement gauge had a minimum displacement of 6.00 mm. Two channels of data acquisition were required: load and CMOD. The acquisition system was designed to have the ability to acquire the data at a minimum of 25 sets of data points per second.

The notch was fabricated along the diameter of the specimen as illustrated in Figure 7.2. which was perpendicular to the faces within. It should be noted that the fabrication of the notch was a critical step in providing a valid fracture energy value. If the notch varies significantly between replicates, then the value of the fracture energy will be influenced. The notch length is also critical since providing a fatigue crack of a known length. The flat surface at the crack mouth was at 90.2° to the notch.

The loading holes were fabricated at 90.1° to the faces of the specimen. The test was performed a constant crack mouth opening displacement rate of 0.017 mm/s. The test is complete when the post-peak load level had reduced to 0.1 kN. The validity of the test was a function of the ability to reach the specified load level.

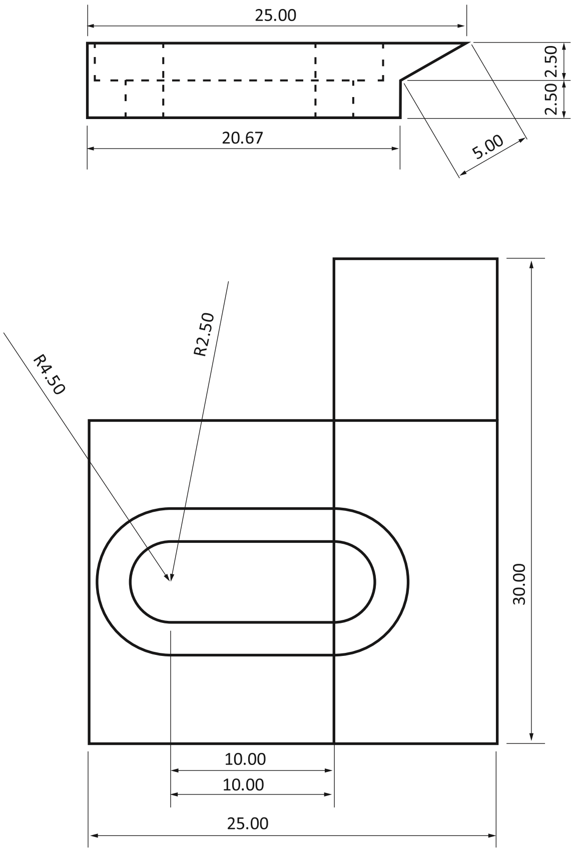

Figure 7.5: Schematic of the gauge points.

7.3 Experimental Results and Discussion

7.3.1 Mechanical and fracture properties

Direct tension tests were conducted, for several NT-cement samples with different dosages of FA and MK, to determine the mechanical strengths. In this experiment different percentages of OPC were replaced with combined use of NT at 2.5 wt% in mass of the cement and with FA and MK within the range of 10 to 30 wt% based on BS EN197 (BSI, 2000). As illustrated in Figures 6.47 and 6.48, the tensile strength of NT cement mortars was significantly improved by using FA and MK as cementitious material replacements. Results show that the tensile strength increased with the increasing NT content up to 2.5 wt%. On increasing the NT at > 2.5 wt% and FA at > 10 wt%, the tensile strength increased by 57%.

When the dosage of fly ash exceeded the optimal value, *i.e.* FA >20 wt%, drying shrinkage distortions of mortars were enlarged, leading to the increase in the average pore radius size and causing internal defects to form in mortars, which would certainly influence the overall voids and the total porosity, as the result the microstructure became isolated and defective. On increasing the NT (>2 .5 wt%) and MK (> 10 wt%) the tensile strength increased by 50.0%. Similar to the NT-modified FA geopolymer samples, when the amount of NT and MK exceeded the optimal values, *i.e.* NT > 2.5 wt% and FA > 10 wt%, the result shows a clear trend of decreasing the tensile strength of specimens, as illustrated in Figure 6.50.

These results were in good agreement with the results of the 2D and 3D porosity analysis observed in Chapters 4 and 6. The mechanical properties and some of the fracture parameters of the tested NT cement composites with different dosages of FA and MK, are listed in Table 7.1. The fracture energy of each beam specimen for each mix, was done through identifying the energy absorption capacity (D_{BZ}).

The results of fracture energy calculated from the area under the curve are shown in Figure 7.6. The recorded deflections at the limit of proportionality load (δ_{Fu}) can be obtained from Figures 7.6(a) to 7.6(d). Based on the resulted deflections using the following equations "$\delta_1 = \delta_{\mathrm{Fu}} + 0.3$" and "$\delta_2 = \delta_{\mathrm{Fu}} + 0.65$", which assess towards attaining the energy absorption capacity for each mix. The figures below demonstrate the concluded energy absorption capacity for some of the selected samples.

The aforementioned parameters represent the outcome of the shaded area, which represents the fracture energy. Table 7.1 summarises the output of the fracture energy for each mix. It also includes the distances δ_1 and δ_2, which were utilised in the abovementioned graphs to attain the energy areas. δ_1 and δ_2 represent the distances 0.3 and 0.35, respectively.

Increasing the NT content up to 2.5 wt% (AM2.5) led to a slightly higher GF compared to the reference mix (CM). However, once the percentage of NT increased to 5 wt% the fracture energy slightly dropped compared to sample AM2.5. The BM2.5 sample presented the highest GF, *i.e.*, 1654 N/mm amongst all the samples. Comparing with the pure mortar sample, adding 2.5 wt% NT and 10 wt% FA can increase GF by 47%.

On increasing the NT (> 2.5 wt%) and MK (> 10 wt%) GF increased by 30.2%. However, once the percentage of MK increased to 20 wt% and 30 wt%, the fracture energy dramatically dropped. It can be concluded that adding a certain amount of NT (*i.e.*, NT $\leq$ 2.5 wt%), FA (i.e. FA $\leq$ 10 wt%) and MK (i.e. MK $\leq$ 10 wt%) can significantly increase GF, leading the sample to endure a greater load without exceeding the elastic limit. The effect of NT addition on the load-CMOD curves of FA/MK cement composites incorporated with different percentages of NT, FA and MK has been plotted and shown in Figure 7.7.

Table 7.1: Energy absorption capacity (fracture energy) of the NT-cement mortars.

Types of specimen	Code no	CMOD (mm)	$\delta_1\ (mm)$	$\delta_2\ (mm)$	$D^{f}_{BZ,2,I}$ N/mm	$D^{f}_{BZ,2,II}$ N/mm	Average Fracture Energy ($D^{f}_{BZ,2}$) N/mm
0% NT	CM	0.25	0.55	0.9	60	1170	1230
3.5w% NT	AM3.5	0.27	0.57	0.92	103.5	1500	1603.5
2.5 wt% NT	AM2.5	0.2	0.5	0.85	460	1350	1810
5w% NT	AM5	0.2	0.5	0.85	585	1050	1605
Control Mix + 10% Fly Ash	BM	0.2	0.5	0.85	112	1040	1152
2.5% NT + 10% Fly Ash	BM2.5	0.25	0.55	0.9	600	1054	1654
2.5% NT + 20% Fly Ash	CM2.5	0.25	0.55	0.9	112	1012	1124
2.5% NT + 30% Fly Ash	DM2.5	0.28	0.58	0.93	156	1243	1399
Control Mix + 10% Metakaolin	EM	0.24	0.54	0.84	128	1060	1188
2.5% NT + 10% Metakaolin	EM2.5	0.24	0.54	0.84	401	1200	1601
2.5% NT + 20% Metakaolin	F2.5	0.2	0.5	0.8	440	903	1343
2.5% NT + 30% Metakaolin	G2.5	0.25	0.55	0.85	390	880	1270

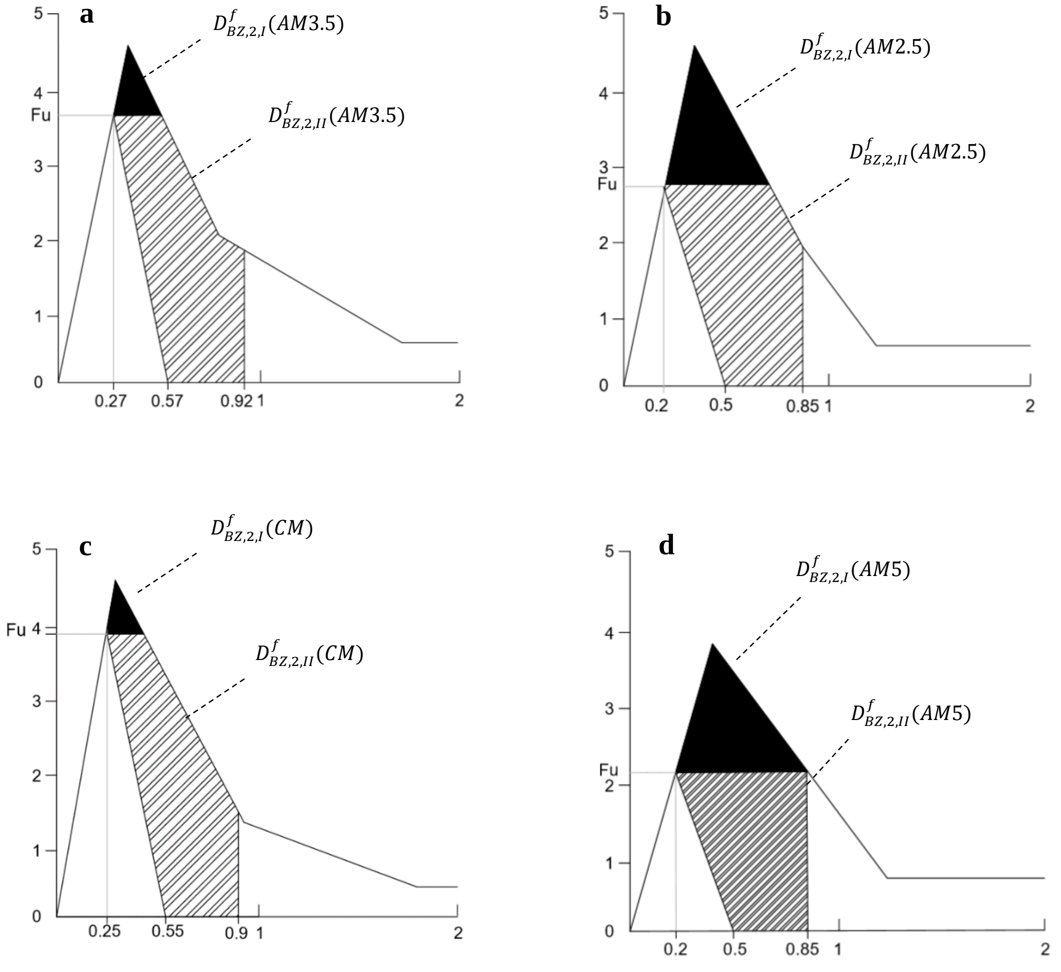

Figure 7.6: Energy absorption capacities of the samples a) AM3.5, b) AM2.5, c) CM, d) AM5.

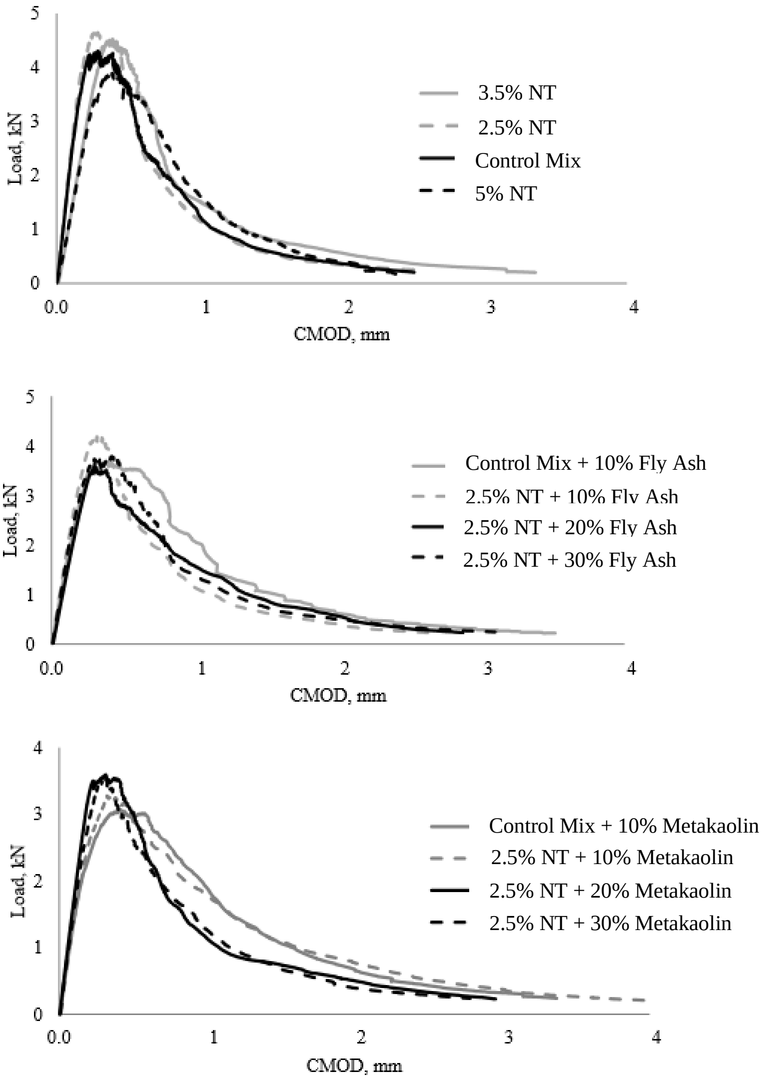

Figure 7.7 Load-CMOD curves of the NT-cement mortars with the added FA/MK.

It can be seen that peak load increased with the increasing NT content up to 2.5 wt%, while this effect was diminished with increasing the amount of NT, i.e. NT (> 2.5 wt%). On increasing the NT (>2.5 wt%) and FA (>10 wt%) the peak load decreased by 36.4%. However, on increasing the NT (>2.5 wt%) and MK (>10 wt%) the peak load decreased by 39.2%. With the increasing amounts of FA and MK, due possibly to the rapid localization of micro-cracks (Figure 7.8), the material became more brittle, which led to an increase in both width and number of cracks, hence decreasing CMOD or the ability of deflection. On the other hand, the use of higher amounts of FA and MK reduced the density of toughening mechanisms that are operational at the descending branch of the curve after the peak load.

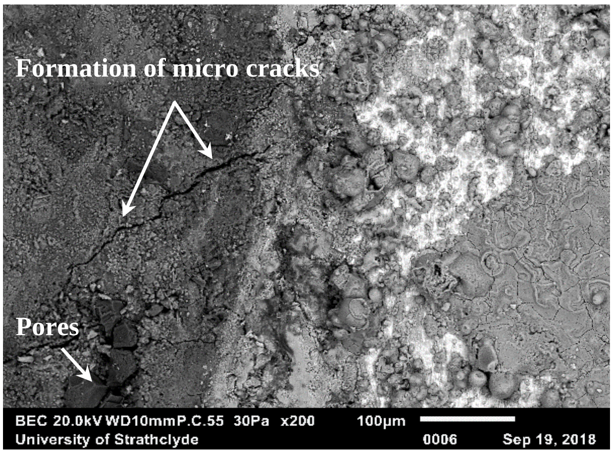

Figure 7.8: Typical SEM image of the specimen with rapid localization of micro-cracks

7.3.2 Numerical analysis

Assuming that nanoparticles cannot be uniformly scattered in the material. Therefore, the random size and location of nanoparticles should be considered in this simulation. As this is a 2D analysis here, the distribution of particles can be selected from the cutting plane (Figure 7.9) of the three-dimensional model. Thus, considering that the size of particles and the position of cutting section, these vary from zero to full particle size. Halphin and tsai, (2009) found that the elastic modulus of particulate composites can be predicted by the semiempirical relationship. Guth (1945) added a particle interaction term in the Einstein equation which becomes:

$$\frac{E_c}{E_m} = 1 + 2.5V_P + 14.1V_P^2 \tag{7.1}$$

where the linear term is the stiffening effect of individual particles, and the second power term is the contribution of particle interaction.

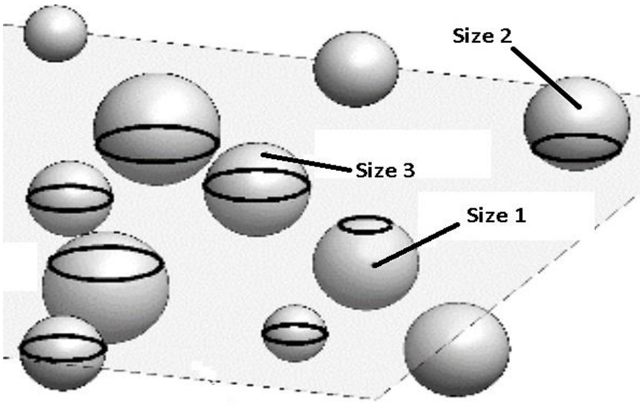

Figure 7.9: Random sizes of particles in the cutting section.

Counto (1964) suggested a simple model for particulate cement by assuming bonding effects between particles and matrix. By these assumptions, the agreement between experimental and numerical with bonding effects was in a good shape.

There are errors which may be caused by some aggregations of nanoparticles, due to volume fraction. In the present research, manually random sizes of particles are considered to simulate 2D section distribution of NT with FA and MK particles in the ABAQUS CAE Environment.

Figure 7.10 shows the geometry of the manual generation of RVE square and the whole model of the specimen. In order to generate particle distribution manually, firstly, a regular RVE should be presented in this method. Corresponding parameters such as side length, particle volume fraction and radius should be considered before running. Secondly, nanoparticle centres and their dimensions inside RVE will manually be generated according to particle volume fractions in the ABAQUS sketch.

In this simulation, by extracting properties of materials with different percentages of particles from RVE square and utilizing it in simulation, the behaviour of nano-cement could be obtained. The size of the representative volume element square (RVE) selected in ABAQUS for modelling was 400 nm × 400 nm. There were some restrictions on particle generation in RVE to avoid overlapping: (i) The minimum distance of particle centres is the maximum particle diameter, (ii) the minimum distance between the particle centre and specimen boundaries is the maximum particle radius.

The extended finite element method (XFEM, Abaqus 2020 Analysis) is a precise method for fracture and discontinuous problems in mechanics whereby cracks and their growth can be modelled by finite element method. Figure 7.10 illustrates the specimen and foreign particles spread into the RVE and also the loads and BCs applied in their positions.

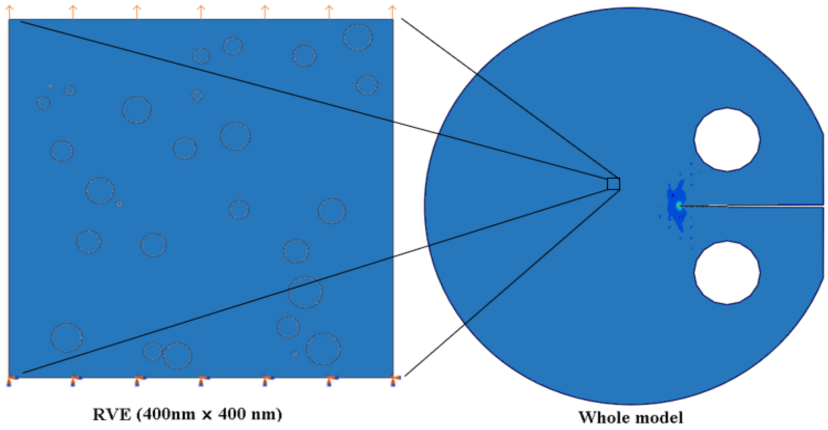

re: 7.10: Schematic of ABAQUS modelling with the whole model and RVE with boundary conditions and foreign particles.

7.3.3 Simulation results and discussion

In this simulation, the numerical results of NT with various percents of FA and MK were considered according to Table 7.2. The material properties were extracted (Pascoe., 1978), for RVE modelling. The tensile strengths of the nano titanium dioxide composites with different percentages of FA was derived by using ABAQUS. Many scholars utilized XFEM for simulating the failure process of nanocomposites, which is adopted in this paper, so the failure process here was simulated by matrix crack failure (XFEM). The initiation and evolution of matrix failure used the maximum principal stress criterion and the energy criterion, respectively.

The max average load values for different nanocomposites in the simulation are shown in Table 7.2. Figures 7.11 to 7.13 give the NT composite load values for different FA and MK particle contents in terms of the crack mouth opening displacement (CMOD). From the load curves, we can see that particle debonding and crack growth, which absorb energy during simulation, may play a substantial role in strengthening. For investigating the interaction between NT particles with FA and cement under the tensile load, the nanoscale model is needed in this simulation, while the experimental data came from the macro specimen. Cross-scale models may create a minor difference between macro mechanics and micromechanics results, which may be acceptable.

Table 7.2: Numerical and experimental results for the specimens with different particle percentages.

Types of specimens	Code no	Maximum force (kN)-Experimental	CMOD (mm)-Experimental	Maximum force (kN)-Numerical	CMOD (mm)-Numerical
0% NT	CM	3.65	0.3	3.3	0.33
3.5w% NT	AM3.5	4.48	0.37	3.5	0.38
2.5 wt% NT	AM2.5	4.61	0.27	3.61	0.32
5w% NT	AM5	3.85	0.36	3.36	0.4
Control Mix + 10% Fly Ash	BM	3.6	0.32	3.33	0.33
2.5% NT + 10% Fly Ash	BM2.5	4.1	0.25	3.4	0.3
2.5% NT + 20% Fly Ash	CM2.5	3.5	0.3	3.09	0.31
2.5% NT + 30% Fly Ash	DM2.5	3.6	0.3	3.02	0.29
Control Mix + 10% Metakaolin	EM	3.55	0.3	3.01	0.34
2.5% NT + 10% Metakaolin	EM2.5	0.34	3	0.35	3.3
2.5% NT + 20% Metakaolin	F2.5	0.35	3.29	0.3	3.4
2.5% NT + 30% Metakaolin	G2.5	0.28	2.94	0.3	3.3

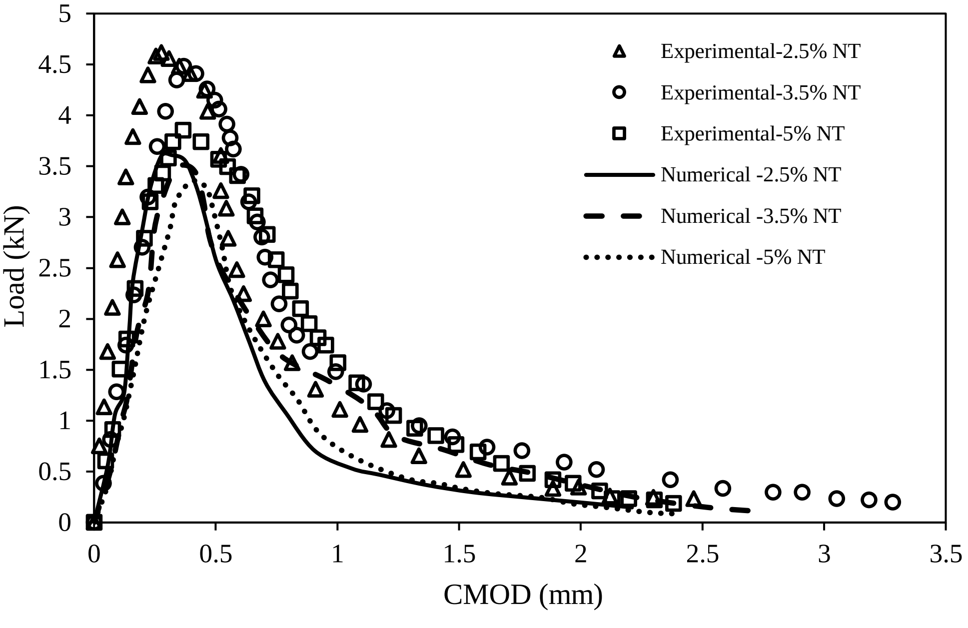

gure 7.11 Comparison of the numerical and experimental results for different NT particles.

Increasing the NT content up to 2.5 wt% (AM2.5) led to a slightly higher GF and tensile strength compared to the reference mix (CM). However, once the percentage of NT increased to the tensile strength slightly dropped compared to sample AM2.5. The lowest tensile strengths were obtained by DM2.5 and G2.5 containing 2.5 wt% NT and

30 wt% FA and 2.5 wt% NT and 30 wt% MK as illustrated in Figures 7.12 and 7.13. This is due to interaction among the particles of FA and MK with the calcium hydroxide, which resulted "in the formation of re-crystallized calcium carbonate in the cementitious matrix causing the reduction in porosity of the matrix and the transition zone" (Huang, et al., 2013). In addition, when the amount of FA and MK exceeded the optimal values, i.e. FA > 10 wt% and MK > 10 wt%, the unreacted or partially reacted FA and MK particles created porosity in the matrix dispersed in small sized pores so cavities were found from the spaces left after the dissolve of the particles.

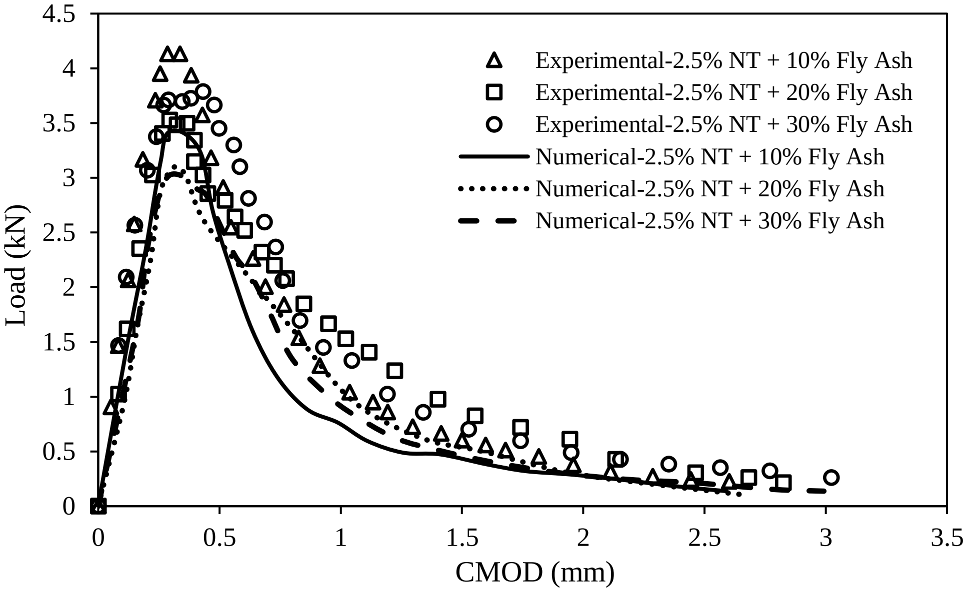

Figure 7.12 Comparison of the numerical and experimental results for the specimens with different FA particles

It can be also seen from Figures 7.11 to 7.13 that numerical and experimental results showed good agreement with each other and they had similar trends with the maximum 21% error between the experimental and numerical results. Figure 7.14 shows that the crack tip and the evolution of growth and foreign particles also were observable. This indicated the strengthening mechanism of NT composites by the method of simulation and XFEM and this is effective ways to simulate the mechanical behaviours of the NT with FA and MK contents.

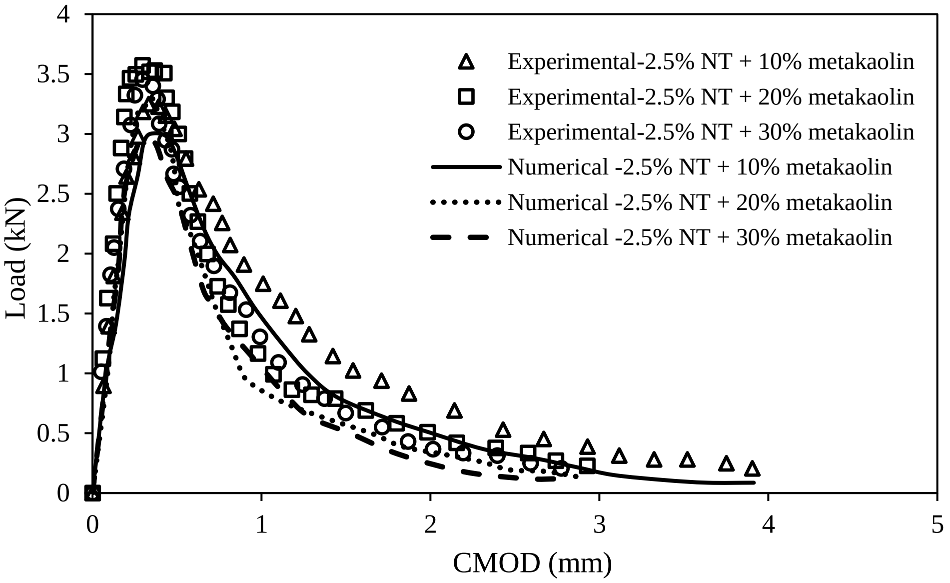

Figure 7.13 Comparison of the numerical and experimental results for the specimens with different MK particles

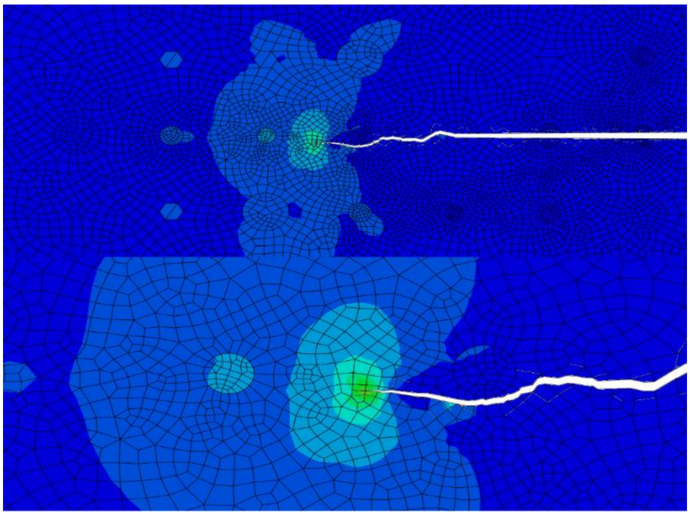

igure 7.14: Initiation and growth of the crack in two views with foreign particles

7.4 Remarks

In this chapter, load amounts in terms of CMOD with different percents of FA and MK particles in NT cement were studied. In addition, manually random sizes of particles were considered to simulate 2D section distribution of the NT composites with FA and MK particles in the ABAQUS CAE Environment. In this simulation, by extracting properties of materials with different percentages of particles from the RVE square and utilizing it in simulation, the behaviours of nano-cement containing different dosages of FA and MK were obtained. The results showed that the numerical and experimental results had similar trends, i.e. the bearing load increased at first and decreased after that. In addition, the strengthening mechanism of NT cement with FA and MK was confirmed by the numerical simulation (XFEM). Thus, the results from the simulation may reflect macroscopic mechanical properties and numerical simulation can become an effective way to predict the mechanical properties of nano-cement composites. The maximum error between the numerical and experimental data was recorded at 21%. Based on the experimental and numerical results, the following findings can be summarised as follows.

(1) The Results show that the tensile strength increases with increasing NT content up to 2.5 wt%. On increasing the NT (>2.5 wt%) and FA (>10 wt%) the tensile strengths increased by 56.3%. When the dosage of fly ash exceeded the optimal value, i.e. FA > 20 wt%, drying shrinkage distortions of mortars were enlarged, leading to the increase in the average pore radius size and causing internal defects to form in mortars, which would certainly influence the overall voids and the total porosity, as the result the microstructure became isolated and defective.

(2) The study showed that by increasing the NT (> 2.5 wt%) and MK (> 10 wt%), the tensile strength increased by 50.0%. Similar to NT- modified FA samples, when the

amounts of NT and MK exceeded the optimal values, i.e. NT > 2.5 wt% and FA > 10 wt%, the results showed a clear decreasing trend of the tensile strength of specimens. These results were in good agreement with the result of 2D and 3D Porosity analysis observed in Chapters 4 and 6.

(3) On increasing the NT (> 2.5 wt%) and MK (> 10 wt%) GF increased by 30.2%. However, once the percentage of MK increased to 20 wt% and 30 wt%, the fracture energy dramatically dropped. This indicated that adding a certain amount of NT (*i.e.*, NT ≤ 2.5 wt%), FA (*i.e.*, FA ≤ 10 wt%) and MK (*i.e.*, MK ≤ 10 wt%) can significantly increase GF, leading the samples to endure a greater load without exceeding the elastic limit.

(4) With increasing the amounts of FA and MK, due possibly to the rapid localization of micro-cracks, the material became more brittle, which led to an increase in both width and number of cracks, hence decreasing CMOD or the ability of making deflection. On the other hand, the use of higher amounts of FA and MK reduced the density of toughening mechanisms that are operational at the descending branch of the curve after the peak load.

In summary, it can be concluded that adding a certain amount of NT, i.e. NT ≤ 5 wt%, may help improve the fracture properties of concrete composites containing FA and MK. The fracture parameters increased gradually, and the fracture relational curves became thicker as the NT content increased from 0% to 5%. However, the fracture parameters began to decrease, and the curves became thinner when the NT content exceeded 5%. These variation phenomena of the fracture parameters and fracture relational curves indicate that NT could contribute significantly to the improvement of the fracture properties of the concrete composites containing FA and MK only when its content did not exceed 5%.

Chapter 8

Evaluating the Effects of Titanium Dioxide on the Resistance of Cement Composites Exposed to Sodium Sulfate Solution

8.1 Introduction

The objective of this chapter is to enhance the durability of cement composite mixtures against sulfate deterioration by replacing a certain amount of cement with nano titanium dioxide (TiO_2). Marine environments contain high concentrations of sulfates. To improve the concrete durability within such conditions, it is important to control the concentration of this ion. There are also other sources of sulfate, such as sewage, industrial waste, and fertilizers. The industrial development generated an increase in the cases of structures damaged by sulfate attacks. One of the extremely costly factors in the construction field is the reduction of material lifetime. Because this type of deterioration process is complex, it has raised many controversial theories in order to understand its mechanism (Santhanam et al, 2001; Neville, 2004).

There are numerous factors that influence the severity of the process. These factors can be related to the material's nature (w/c ratio, cure process, clinker constitution, additions and so on) and to the surrounding environmental circumstances (temperature, pH, external sulfate concentration, cyclic exposure and so on). Concrete with a higher w/c ratio leads to high permeability that facilitates the ingress of hazardous chemical ions into the inner material. Moreover, it is known that Portlandite reacts with sulfate to form gypsum, causing a decalcification of the cement matrix and, consequently, loss of strength (Santhanam et al, 2002). Hence, the clicker composition plays an important role, since tricalcium silicate (C_3 S) hydration produces 2.5 times more CH (Calcium Hydroxide) than the dicalcium silicate (C_2 S) hydration, and therefore the silica ratio is also significant for material durability (Irassar, 2000). Furthermore, the tricalcium aluminate (C_3A) reacts with sulfate to form ettringite (Aft), and thus, decreasing its content is crucial to increase the concrete sulfate resistance. Meanwhile, the environment is crucial when it comes to sulfate attack. The type of cation associated with SO_4^{2-} modifies the mechanisms and the consequences of the attack (Neville, 2004). Additionally, a higher sulfate external concentration leads to a faster diffusion generating a more severe attack. Sulfate attack is one of the most aggressive environmental conditions to address for concrete. Sulfate ions present in the soil, run-off water, seawater, groundwater, and sewer lines can move to the interior of the concrete through pores and react with unhydrated and hydrated alumina phases, portlandite (CH), calcium silicate hydrate (C-S-H) to produce ettringite and gypsum. Incoming $SO4^{2-}$ ions react with calcium alumino monosulfate phases and produce ettringite ($3CaO \cdot AL_2O_3 \cdot 3CaSO_4 . 32H_2O$) according to Equation (8.1) (Yu et al, 2000):

$$SO_4^{-2} + 4CaO \cdot AL_2O_3 \cdot SO_3 \cdot 12H_2O + 2Ca^{2+} + 20H_2O \rightarrow 3CaO \cdot AL_2O_3 \cdot 3CaSO_4 . 32H_2O \quad (8.1)$$

Sodium sulfate reacts with portlandite to produce gypsum and sodium hydroxide according to Equation (8.2):

$$Na_2SO_4 + Ca(OH)_2 \rightarrow CaSO_4 .2H_2O + NaOH \quad (8.2)$$

Gypsum reacts with hydrated products such as calcium aluminates, calcium sulfoaluminate (monosulfate-C_4ASH_{12-18}) or tricalcium aluminate, (unhydrated phase in cement clinker) to produce ettringite, as given in the Equations (8.3)–(8.5):

$$4CaO. AL_2O_3 . 13H_2O + 3(CaSO_4 .2H_2O) + 13H_2O \rightarrow 3CaO. AL_2O_3 .3\ CaSO_4 . 32H_2O + Ca(OH)_2 \quad (8.3)$$

$$4CaO. AL_2O_3 . SO_3 . 12H_2O + 2(CaSO_4 . 2H_2O) + (10\text{-}16)\ H_2O \rightarrow 3CaO. AL_2O_3 . 3CaSO_4 . 32H_2O \quad (8.4)$$

$$3CaO.\,AL_2\,O_3 + 3(CaSO_4\,.\,2H_2\,O) + 26H_2\,O \longrightarrow 3CaO.\,AL_2\,O_3\,.3\,CaSO_4\,.\,32H_2\,O \qquad (8.5)$$

Ettringite is an expansive product and causes expansion in the hardened cement paste. Expansion due to gypsum is disputed (Gruyaert et al, 2012), and researchers agree that gypsum softens mortar and reduces its strength (Santhanam et al, 2001). If the expansive stresses from the formation of new products exceed the tensile strength of the hardened concrete, then microcracks are formed. These microcracks causes greater transport of sulfate ions from the external environment to the interior of the concrete and accelerate the sulfate attack. Sulfate attack increases porosity, reduces strength, softens concrete, changes mass, and causes expansion, cracking and spalling. The severity and nature of these defects are dependent on factors such as cement type and composition, water/binder ratio, presence and amount of supplementary cementitious materials, porosity, permeability, ambient temperature, the concentration of sulfate ions and types of cations, such as sodium or magnesium, etc.

Corrosion of reinforcing steel is a critical factor for the durability of concrete structures in marine environments (Alsulaimani et al, 2013; Chen et al 1990). It results in cracking of concrete cover, loss of steel section or even failure of structures (Aldea et al, 2013; Apostolopoulos et al 1990). Natural corrosion is a slow and complex process. In the corrosion laboratory researches, to control corrosion effectively, researchers have developed different methods to accelerate the corrosion of reinforcing steel as well as to simulate the mechanism of corrosion degradation process (Dong et al, 2013; Wong et al, 1990), and among them, the impressed current method is widely used in the durability related research of reinforced concrete structures. It is commonly awarded that impressed current technique does not provide any mechanistic information, as the dissolution process is forced to be far higher than any transport process in mortar. This might lead to erroneous results and conclusions with regard e.g., to cracking, but this method has an advantage that it could control the degree of corrosion by tuning both current intensity and power-on time. In the impressed current technique, Faraday's law is generally employed to theoretically estimate the mass loss of reinforcing steel (Dong et al, 2013).

$$\Delta \mathrm{m} = M \times I \times \mathrm{t} / (n \times F), \tag{8.6}$$

where Δm is the mass loss of steel during corrosion, M signifies the atomic mass of metal, I denotes current, t is time, n represents valency, and F is Faraday's constant. During the theoretical calculation of corrosion mass loss using Faraday's law, it was assumed that impressed current participated in the corrosion reaction and produced all ferrous ions on the anode.

Nossoni et al. defined the current efficiency as the percentage of impressed charge that participated in the corrosion reaction of steel, and estimated the bulk current efficiencies for different based on gravimetric method (Nossoni et al., 2009). It was figured out that the mass loss of steel does not always follow Faraday's law and under critical conditions, only a part of the impressed current oxidizes the anode to create corrosion products while the remaining current is consumed in competing reactions.

In this chapter, different amounts of nano-TiO_2 on the sulfate attack resistance of pure Portland cement pastes were investigated. The mortars were immersed in 5% sodium sulfate solution at 25°C, and expansion, the characterization of the cement hydration process, and morphology of the cement mortars were conducted by scanning electron microscopy (SEM) and energy-dispersive X-ray spectroscopy (EDAX®). Furthermore, the corrosion progression of a steel bar in concrete was investigated by X-ray computed tomography (i.e. XCT). Finally, accelerated corrosion process of reinforcing steel with impressed current was traced by X-ray micro-computed tomography (µCT) with high accuracy and the mass losses of steel over different accelerated corrosion periods were analysed.

8.2 Experimental Program

8.2.1 Materials and mix proportion

Different percentages of OPC, provided by Jewson, which complies with BS EN197 Part 1 (BSI, 2000), with a Grade of 42.5 N/mm², were replaced with anatase different amounts of NT, viz. 0 wt%, 2.5 wt%, 3.5 wt%, 5 wt% and 10 wt%. Lower dosages of NT in the cementitious materials may be insufficient to ensure self-cleaning and air purification over longer periods. Therefore, higher percentages of NT were chosen in this study. Natural river sand, with a minimum particle size of 200 µm served as the fine aggregate. The mineralogical phases and chemical composition of the raw materials used were obtained from the X-ray diffraction (XRD) and X-ray fluorescence (XRF) analyses. The NT particles used in this research were obtained from ALDRICH and had a specific surface area of 35-65 m^2/g. Deionised water, with a pH value of 7.5 at 22°C, was used throughout the experimental research. The recorded mix design code for each sample is presented in Table 8.1. Slump tests were then carried out according to BS EN 12350-2:2009. The mix proportion design resulted in the slump ranging from 100 to 230 mm and the vebe time ranging from 9 and 17 seconds, which met the required workability based on BS EN 12350-2:2009. The mix had a constant water/equivalent cement ratio of 0.55.

Table 8.1: Mix proportions of the test specimens.

Code number	Cement (kg/m^3)	Water-to-cement ratio	Cement replacement (wt%) Nano - TiO_2	Mix proportion (kg/m^3)	
				Fine aggregate	Water
ACM	227.3	0.55	0	681.9	125.01
AM2.5	221.6	0.55	2.5	681.9	125.01
AM5	215.9	0.55	5	681.9	125.01
AM10	204.5	0.55	10	681.9	125.01

8.2.2 Specimen preparation

ASTM C 1012 (ASTM, 2018) is one of the test methods used to evaluate the sulfate resistance. According to this method, mortar prisms with dimensions of 25 mm × 25 mm × 280 mm with pins at both ends are prepared and stored in limewater until reaching a strength of 20 MPa. They are then stored in 10% sodium sulfate (Na_2SO_4) solution and any expansion is measured. The ASTM C 1012 process takes several months to complete; however, many accelerated tests have been proposed using small specimen sizes and higher concentrations of sulfate solution. A summary of these tests can be found in the work Van Tittelboom et al. (2013).

Ferraris developed a new accelerated test technique for measuring the sulfate resistance of mortar. Here, their test method was used in this study with some modifications. They had immersed 10 mm × 10 mm × 40 mm rectangular prism specimens in 5% Na_2SO_4 solution. In this study, cylindrical mortar specimens with a diameter of 20 mm and a length 40 mm were immersed in 10% Na_2SO_4 solution. After 48h of casting, the mortar specimens were removed from the moulds and placed in the saturated limewater for 28 days. Four specimens of each mix proportion were left immersed in saturated limewater while other specimens were selected for immersion in Na_2SO_4 solution.

The studs were firmly fixed on the ends of these mortar specimens with epoxy. To allow sulfate ions to attack only from the sides, the epoxy was applied to both end faces of the specimens. Then they were immersed in 10% Na_2SO4 solution which was renewed every 7 days. The volumetric ratio of the solution to the test specimens was 20:1. The specimens were stored at a temperature of 25 ± 1 °C. Water absorption was measured at the age of 28 days. For the corrosion test, fresh mortar was cast into a mould and placed into a curing chamber for 1 day. The specimens were then demoulded and placed into a standard curing chamber for 28 days.

The sample was immersed in 3.5 wt% NaCl solution for 6 h before the experiment. To achieve better resolution from μCT images, specimen sizes were kept small in this research. Schematic diagram and photograph of a reinforced mortar specimen is presented in Figure 8.1.

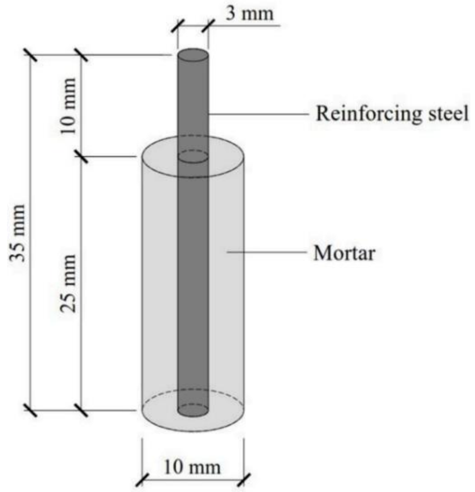

Figure 8.1: Schematic diagram and photograph of the reinforced mortar specimen.

As nano-TiO_2 particles tend to agglomerate when mixing with water and conventional agitators cannot break down these hard agglomerates due to the strong van der Waals forces, ultrasonication was performed using a horn ultrasonicator (UP400st) as illustrated in Figure 8.2. The rotor disperses the nano-TiO_2 particles into the water, leading to a more uniform liquid and shorter processing times. Insufficient dispersion of NT has been viewed as a key detrimental factor for the mechanical properties of NT–OPC composites. Four series of NT suspensions were prepared with time-controlled and power-controlled ultrasonication respectively. NT cement composites with various proportions, i.e. 0 wt%, 2.5 wt%, 5 wt%, and 10 wt%, were investigated at different solid loadings and viscosities of continuous phase (1–100 mPa.s). The ultrasonic time was set at 60 min and the amplitude was fixed at 94 W. De-agglomerations of different concentrations of NT particles over a periodic time interval of 60 minutes are shown in

Figure 8.3, which shows monomodal distribution based on the frequency of fines generated in all the cases.

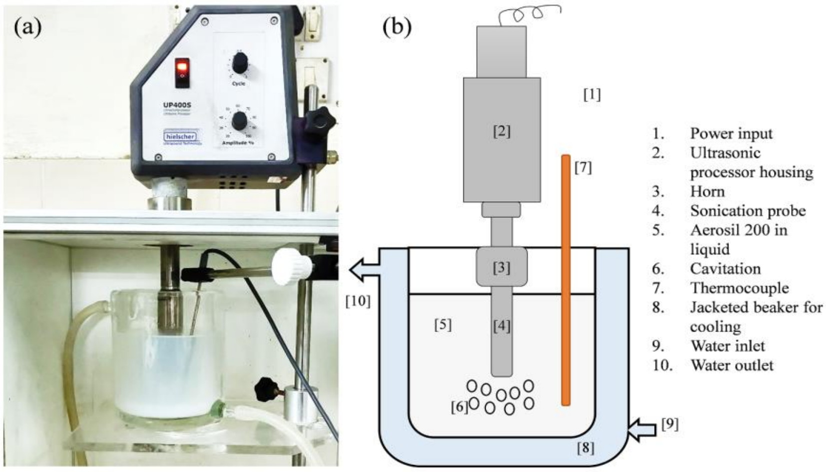

Figure 8.2: a) Experimental setup, and b) Schematic configuration

From Figure 8.3, it can be found that the particle size distribution became narrow as the concertation of NT particles increased from 2.5 wt% to 10 wt%. Therefore, the frequency of fines generation increased with the increase in the solid loading of NT particles. Average particle size of the fine generated was found constant (< 20 nm size difference) throughout the de-agglomeration process in water-based dispersion, i.e., independency of size on the operating conditions.

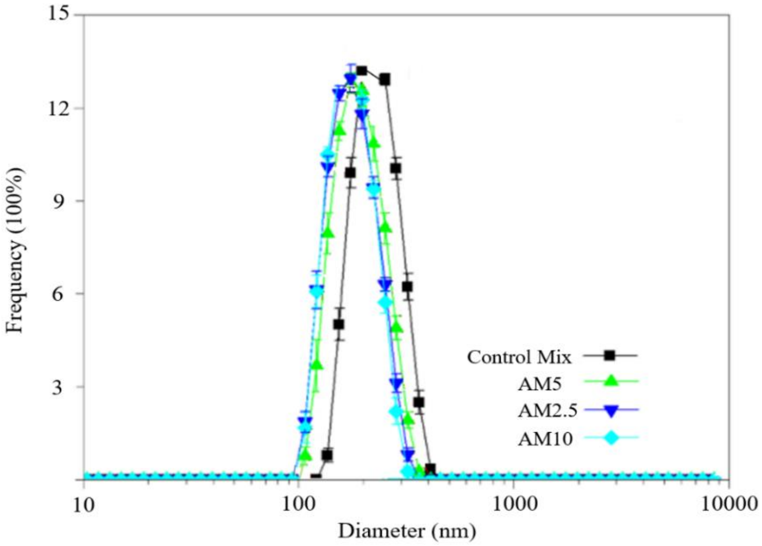

Figure 8.3: Particle size distribution of the NT-cement at 60 min time interval.

In the present study the Z-average size of the fine particles was measured from 105 nm to 130 nm for dispersion in water. Agglomerates were still present in the final solution as the primary size of the solid particle was 22 nm. Also, the stability of nanoparticle dispersion was investigated over 30 hours as illustrated in Figure 8.4. Dispersion was found to be very stable, and insignificant change was found for 2.5 wt% NT. Hence, no agglomeration was seen after 20 hours. However, slight change in the Z average over 30 hours for 10 wt% NT was seen, and hence further aggregation started after longer duration storage.

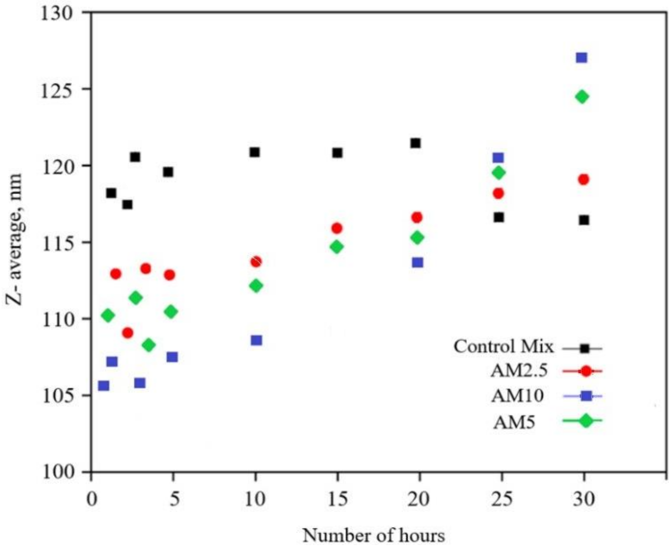

Figure 8.4: . Z-average as a function of time in hours for NT particles in water

8.3 Test Procedure

8.3.1 Expansion and mass variations

The length and mass of the specimens were measured every seventh day during the immersion period using Equations (8.7) and (8.8):

$$t = \frac{L_t - L_i}{L_i \times 100} \tag{8.7}$$

$$t = \frac{M_t - M_i}{M_i \times 100} \tag{8.8}$$

where L is the length, t is the time, i is the initial and M is the mass. The test was stopped after 84 days of immersion.

8.3.2 Accelerated corrosion with impressed current

To simulate corrosion, in this study, the accelerated corrosion test was carried out in 3.5 wt% NaCl, and the temperature was set to 25 °C (Nossoni, et al., 2012; Dong et al., 2017). The experimental setup consisted of five different components: specimen, silver sheet, cotton, wire, D.C and power supply. The reinforcing steel was connected to the positive pole of D.C. power supply as anode to induce corrosion, and the silver piece was connected to the negative pole of D.C. power supply as cathode. Moreover, to ensure an effective contact between silver sheet and test specimen, a layer of cotton (pre-wetted with 3.5 wt% NaCl) was placed between them. A programmable D.C. power supply with an accuracy of 0.001 mA was used in the accelerated corrosion experiment. The accelerated corrosion was conducted at the impressed current intensity of 305 $\mu A/cm^2$ and the impressed current was calculated using Eq. (8.9).

$$I = i_c \times (\pi \times d \times h) \tag{8.9}$$

where I is the signified output current, i_c is current intensity (the current value per unit area), d is reinforcing steel diameter, and h is the height of reinforcing steel embedded in the mortar. Hence, the output current of the D.C. power supply was set as 0.715 mA.

8.3.3 Potential testing

The potential testing was conducted to obtain the potential of anode (reinforcing steel) during the accelerated corrosion at 25 °C (Figures 8.5(a) and (b)). The saturated calomel electrode (SCE) was selected as the reference electrode and immersed in the 3.5 wt% NaCl solution. To avoid any leakage, which could cause changes in the original state inside the specimen during potential testing, the bottom of the specimen was covered with a layer of plastic wrap and the lap joint of silver sheet was coated with Vaseline. The potential of silver sheet (relative to SCE) was measured with a voltmeter (accuracy of 0.001 mV), and the potential difference between the reinforcing steel and silver sheet was recorded by the D.C. power supply. The standard potential of the anode (relative to standard hydrogen electrode (SHE)) was calculated from the cathode potential using Eq. (8.10) as:

$$E_{a(vs\ SHE)}= U_{a/c} + E_{a(vs\ SCE)} \ + E_{SCE(VS\ SHE)}, \tag{8.10}$$

where $E_{a(\text{vs SHE})}$ is the anode potential relative to the SHE, $U_{a/c}$ is the voltage difference between the anode (reinforcing steel) and cathode (silver sheet), $E_{c(\text{vs SCE})}$ is the cathode potential relative to SCE, and $E_{SCE(\text{vs SHE})}$ is the potential of the SCE relative to the SHE (ESCE(vs SHE) = 0.24 V).

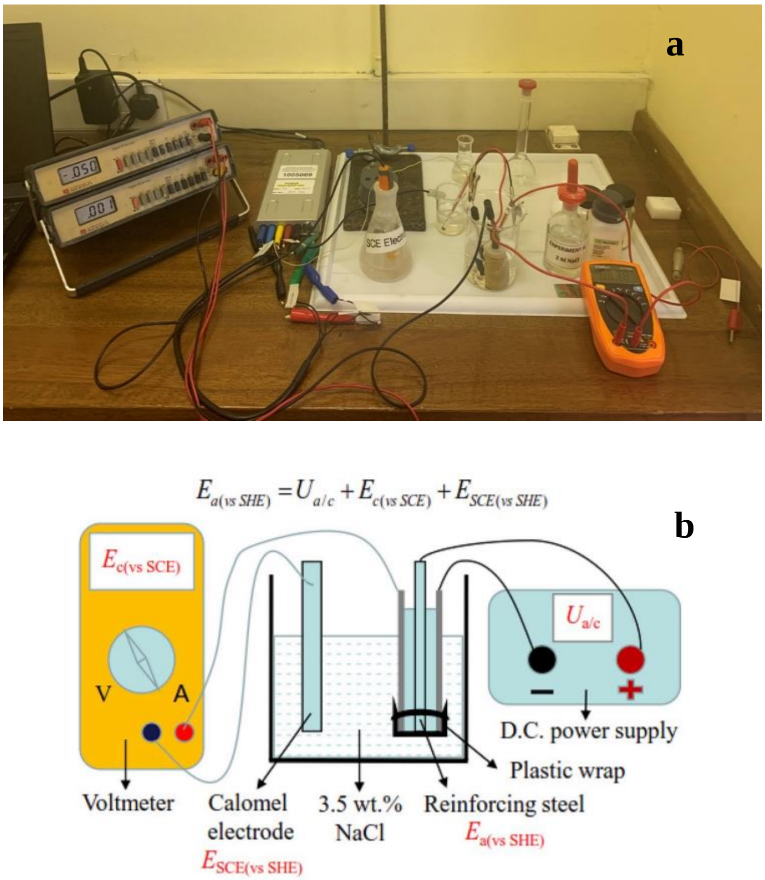

Figure 8.5 (a)/(b) Schematic views of the potential test setup.

8.3.4 X-ray computed tomography testing

In this research, the μCT technique was applied to trace the entire steel corrosion process. In μCT, the level of linear attenuation is not the same when X-ray penetrates different materials. The obtained μCT 3D images were displayed with different gray-values as illustrated in Figure 8.6, which reflected absorption levels of different materials. Based on the disparities in linear attenuation levels of different substances, reinforcing steel, corrosion products, mortar, and cracks were distinguished by threshold division. The test parameters for μCT were set as follows: voltage = 70 kV, Power = 8 W, Magnification = x 0.4, Distance between the emitter and specimen = 70 mm, Distance between the detector and specimen = 200 mm, and Exposure time = 10 s.

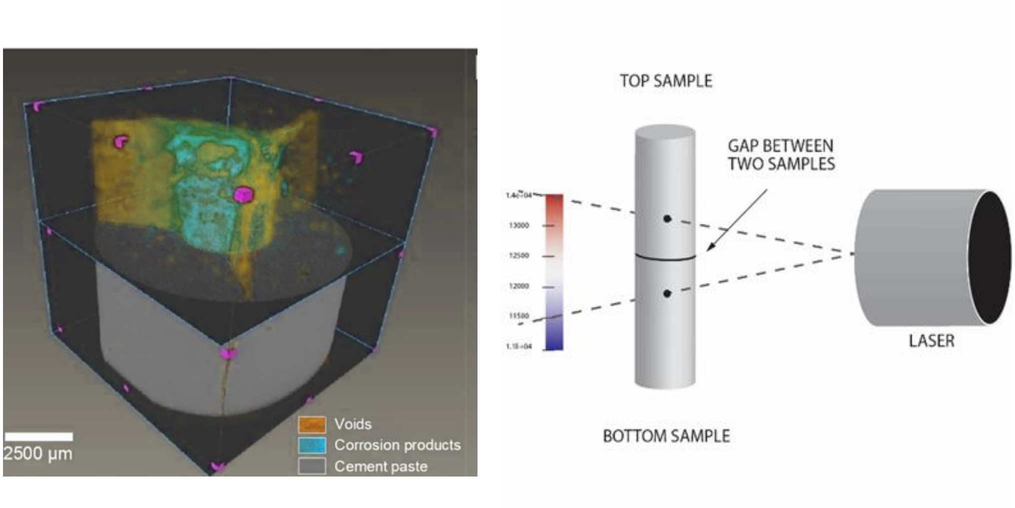

Figure 8.6: Experiment setup for micro-XCT analysis and the final 3D visualization of voids, corrosion products and cement paste

8.3.5 Microstructural analysis

SEM analyses were performed using a JEOL JXA840A type SEM instrument. For preparation, the samples were placed on the standard mounts (1.5 cm in diameter and 0.2 cm in depth) under a vacuum and coated with a 10 nm thick conductive layer of gold to prevent charging prior to imaging. The applied voltage and current values were 20.0 keV and 30.0 mA, respectively.

8.3.6 Mercury intrusion porosimetry (MIP)

To investigate the nature of the pore structure configurations of the NT cement mortar composites, mercury intrusion porosimetry (MIP Quantachrome Ltd., PM-60- GT) tests were carried out. Unlike the more traditional methods for characterization of microstructure, e.g., XCT and scanning electron microscope (SEM), MIP provides a more complete picture of the pore distribution including interconnected and isolated pores, volume of pores and surface area.

8.4 Results and Discussion

8.4.1 Expansion and mass variations

Figure 8.7 shows the expansion of the NT cement mortars including control mix immersed in $\mathrm{Na_2SO_4}$ solution at 25 ˚C and 28 days of curing. The AM2.5 sample has presented the lowest expansion rate, *i.e.*, 0.31%, while the expansions in OPC, 5 wt% and 10 wt% NT mortars were 0.38%, 0.43% and 0.57%, respectively, after 28 days. Comparing with the pure mortar sample, adding 2.5 wt% NT could reduce the expansion rate by 18.4%, therefore leading to higher resistant to expansion. As the dosage of NT increased, the results showed a clear trend of increasing the expansion rate of the NT cement mortars with NT contents up to 10 wt%, as illustrated in Figure 8.7. Figure 8.8 shows the mass variations of the NT cement mortars including the control mix immersed in $\mathrm{Na_2SO_4}$ solution at 25 ˚C. Comparing with the pure mortar sample, adding 2.5 wt% NT resulted in less mass gains, i.e. 18.5%. When the amount of NT exceeded the optimal value, i.e. NT > 2.5 wt%, the recorded masses gained observed for AM3.5, AM5 and AM10 were 4.4%, 5.7% and 6.3% of the original masses, respectively. In order to have more accurate results spontaneous imbibition was used as a proxy measurement for how the addition of NT would affect the liquid flow through the samples. The samples were placed in a beaker and partially submerged in $\mathrm{Na_2SO_4}$ to the depth of 5mm and left for 28 days.

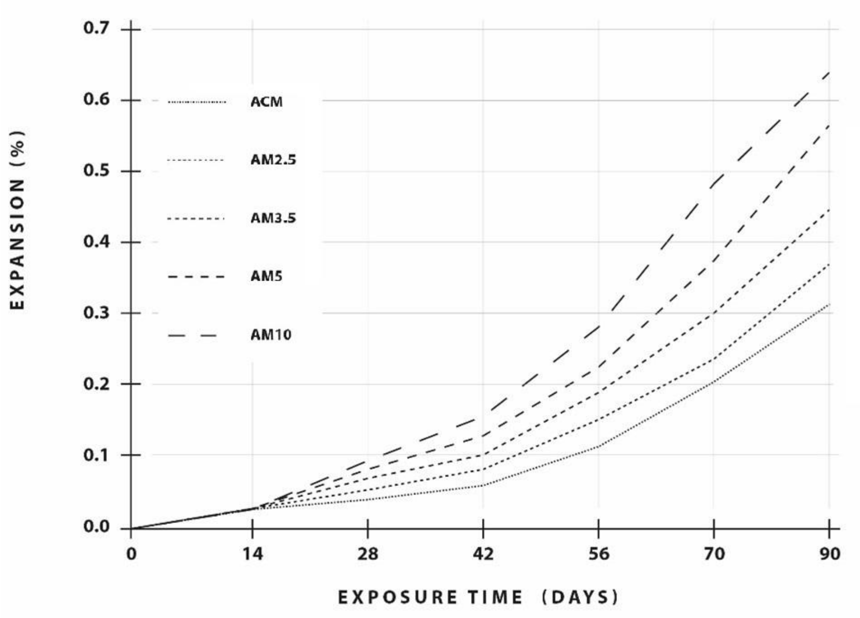

Figure 8.7. Expansion of the NT cement mortars including the control mix immersed in Na_2SO_4 solution at 25 °C and 28 days of curing.

Over this time the lower parts of the samples became darker, indicating that Na_2SO_4 was drawn up into the samples. The samples were placed in XCT scanner and 2d radiography scan was made. This scan revealed the average density and hence the degree of saturation as air pockets in the cement were replaced with Na_2SO_4. Based on the grey scale image of the sample density, a line was determined as the upper extent of water saturation. The elevation of this line was related to the sample's capacity for spontaneous imbibition. The addition of 2.5 wt% NT refined pores and reduced capillary pores and their connectivity, hence reducing the absorption of sodium sulfate solution. Therefore, mortars containing NT, i.e. NT ≤ 2.5 wt%, were less vulnerable to the formation of gypsum and ettringite and exhibited less expansion materials and variation in mass. The increases in the masses of mortars may be due to absorption of sodium sulfate solution and precipitation of gypsum and ettringite in pores and cracks as illustrated in Figure 8.9. Just to be noted that the effects of NT addition on the rate of mass increases were negligible in the first few weeks but prominent at later stages.

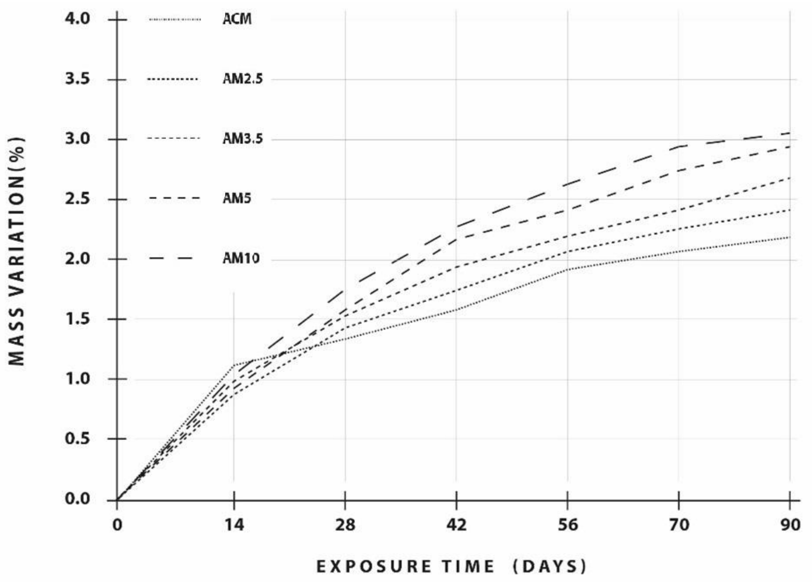

Figure 8.8 Mass variations of the NT cement mortars including the control mix immersed in Na_2SO_4 solution at 25 °C and 28 days curing.

.

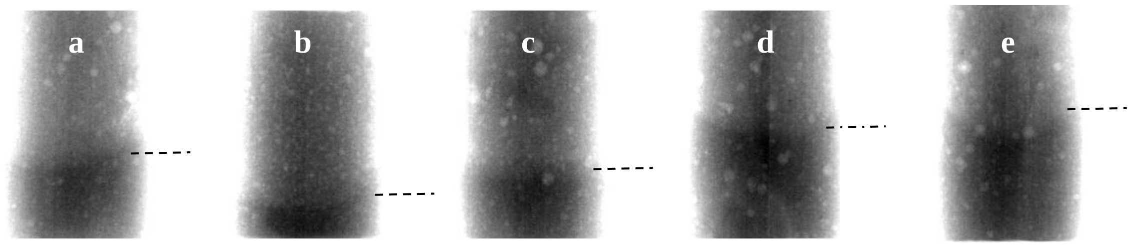

Figure 8.9. Spontaneous imbibitions of the samples with different dosages of NT, a) ACM, b) AM2.5, c) AM3.5, d) AM5 and e) AM10.

8.4.2 Image analysis of X-ray µCT measurements

Images obtained by X-ray µCT method were analysed to separate the steel phase from the cement-based material phase and to quantify the change taking place in the steel phase after different corrosion procedures. The data obtained from X-ray µCT were treated mathematically as a three-dimensional set, including the density and corresponding coordinates (X, Y and Z). Figures 8.10(a) and (b) show a typical cross-sectional image, from which the material could be initially identified. Each raw image contained pixels consisting of 256 possible levels (0–255) of grey intensity. The grey level of each pixel represents a density value that corresponds to the linear attenuation coefficient of the element contained in that pixel. These raw images generally contain two phases: (1) a gas phase including cracks and pores and (2) a solid phase including steel and cement paste. Within the solid phase, steel has a higher density than cement-based material, and thus steel absorbs most of the X-ray and appears as brighter pixels in the images.

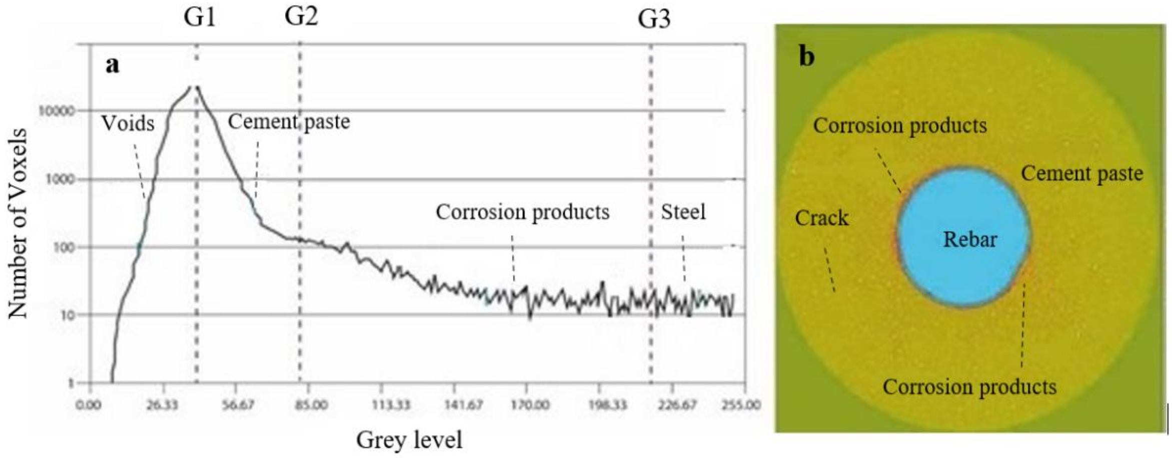

Figure 8.10. Reconstructed 2D X-ray µCT image.

Based on the different grey scale values (GSV), the materials were identified and extracted from the whole data set, in which G_1 separated the gas phase from the solid phase, while G_2 divided the solid phase by separating the cement paste from the steel and G_3 further divided the steel area by separating the corrosion products from the steel. Therefore, a polychromatic greyscale was applied, as shown in Figures 8.10(a) and (b). In this way, different materials are labelled in different colours, for instance, the voids in orange, the cement paste in yellow and the steel in blue. Since corrosion products are a kind of combined material that consists of different chemical compounds (e.g., FeO, Fe_3O_4, $FeOH_2$ and $FeOH_3 \cdot 3H_2O$, etc.), such products represent a relatively wide interzone. Hence, different materials can be easily detected and analysed based on different colours.

As shown in Figures 8.11(a)-(d), steel, corrosion products and voids are reconstructed respectively, in which the morphology of rust pits, corrosion products and voids (including cracks and pores) are clearly distinguishable.

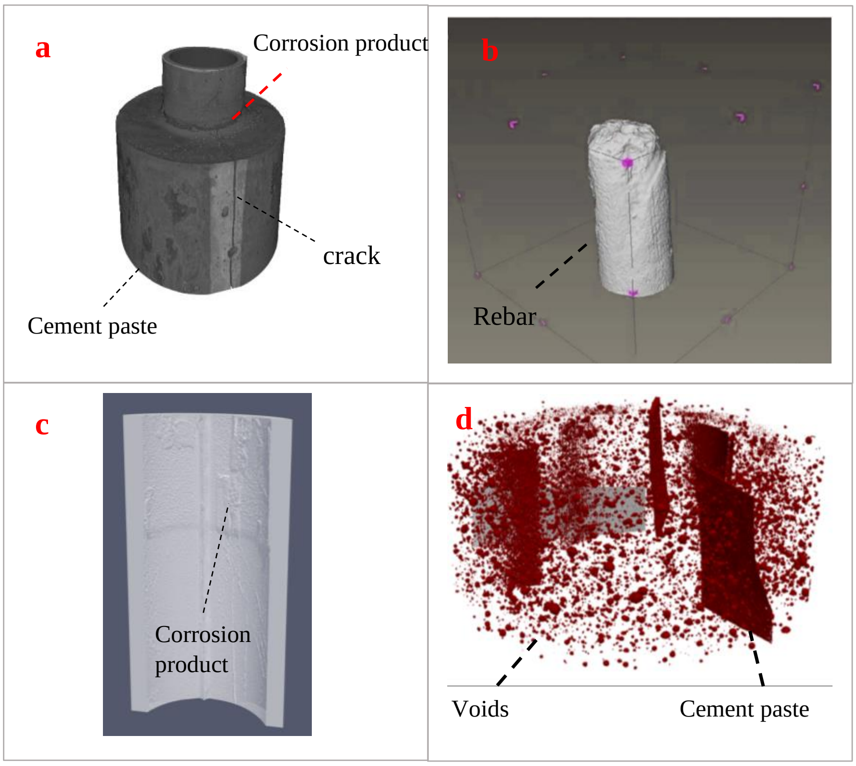

Figure 8.11. Reconstruction of 3D X-ray µCT

Figure 8.12 illustrates the grey values along a probing line which pass through mortar, voids, steel, and the corrosion products. Depending on the densities of the materials, the XCT pictures show different grey value for each of the material phases, and the denser material shows the brighter in the XCT image and has the higher grey value. In Figure 8.12(b), the grey values are plotted along the probing line passing all phases, i.e., steel, corrosion products, mortar and voids or cracks. It should be noted that corrosion products are mixed materials consisting of FeO, Fe_2O_3 and Fe_3O_4, respectively, in terms of oxides, of which the densities vary between 3.3-5.2 g/cm^3.

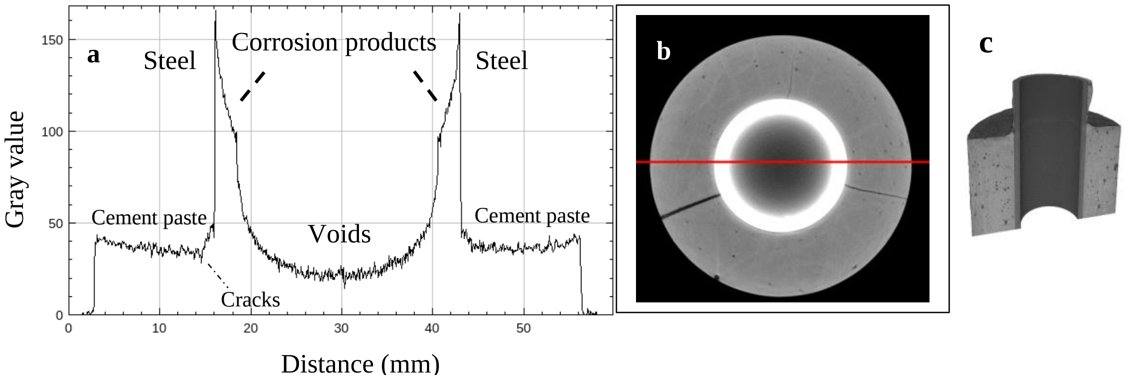

Figure 8.12. Phase recognition in the XCT image a) Gray values along the probing line, b) A typical probing line, c) Image analysed.

To complete a quantitative analysis of target materials (e.g., steel), image binarization is applied to extract the target object, which is based on the greyscale and morphological analysis. The binarization is to transform a greyscale image into a binary image (i.e., a label image with only interior and exterior materials), where the threshold is determined by relevant information in the greyscale image that corresponds to a certain grey level interval. In the output binary image, all pixels with an initial grey level value lying inside the threshold interval are set to 1, and all the other pixels are set to 0. A binary image pixel can either have a value of “1” when it is included in target pixels, or “0” when it is part of other pixels. Thus, the feature of the identified space can be extracted from the whole data set. Based on the different greyscale values the target objects (including steel, corrosion products and cracks) can be separately extracted, as shown in Figure 8.12. Moreover, as the X-ray μCT image is composed of pixels in 2D (voxels in 3D), the volume of the target object can be calculated using Eq. (8.11).

$$V_{XCT} = N_{vox} = Z_{vox} \tag{8.11}$$

where, V_{XCT} is the label space volume (mm^3), N_{vox} is the number of label space voxels (−), and Z_{vox} is the spatial voxel size (mm^3) of the image. Thus, the mass loss of the steel during different corrosion stages can be calculated by Eq. (8.12) as:

$$\Delta m_{XCT} = (V_{0,XCT} - V_{i,XCT}) \times P_{steel} \quad (8.12)$$

where, Δm_{XCT} is the mass loss determined by the data obtained from Xray µCT (mg), $V_{0,XCT}$ is the resulting steel volume calculated by data obtained from X-ray µCT before corrosion (mm^3), $V_{i,XCT}$ is the resulting steel volume after corrosion (mm^3), and P_{steel} is the density of steel (3 mg/mm^3). The corrosion results measured for mortars mixed with NT, *i.e.* 0 wt%, 2.5 wt%, 5 wt% and 10 wt%, are shown in Table 8.2. In most studies on steel corrosion, the mass loss is measured using the gravimetric method, in which the mass of the steel cylinder is compared by weighing before embedding and after destroying the concrete cylinder. Here, the steel is first pickled with the help of hydrochloric acid (15 wt% HCl), and then the pickled steel is cleaned with pure water and neutralized in limewater. After neutralization, the steel is cleaned again with pure water. In addition, the cleaned steel is dried in an oven for at least 4 h. Finally, an electronic balance is employed to weigh the steel (accurate to 0.001 g). To further improve the accuracy of the gravimetric method, three specimens for each case were tested to measure the average mass loss. Based on the data measured by weighing, the mass loss of steel can be calculated according to Eq. (8.13).

$$\Delta \mathrm{m}_{\mathrm{grav}} = \mathrm{m}_{0,\mathrm{grav}} - \mathrm{m}_{\mathrm{i,grav}} \quad (8.13)$$

where, $\Delta \mathrm{m}_{\mathrm{grav}}$ is the gravimetric mass loss (mg), $\mathrm{m}_{0,\mathrm{grav}}$ is the mass of specimen before corrosion (mg), and $\mathrm{m}_{\mathrm{i,grav}}$ is the mass of specimen after corrosion (mg). Table 8.3 details the mass loss results as measured by gravimetry.

Note that the mass loss can be also determined by theoretical calculations based on Faraday's law Eq. (8.14). As shown in Eq. (8.14), the time factors and electrochemical parameters are considered when calculating the actual mass loss.

$$\Delta \mathrm{m}_{\mathrm{EC}} = \frac{M}{zF} \mathrm{I}_{corr} t \quad (8.14)$$

where Δm_{EC} is the mass loss determined by electrochemical data (g), M is the molar mass (g/mol), I_{corr} is the current (A), t is the pre-damaging time (s), z is the number of valence electrons (−), and F is the Faraday's constant (1F = 9.6432 × 10,000C/mol).

Table 8.2: The corrosion results measured by means of X-ray CT.

Specimens	Steel volume voxel count (x10^7)	Label volume (mm^3)	Volume loss (mm^3)	Mass loss (mg)	Corrosion products volume voxel count (x10^6)	Corrosion induced crack volume voxel count (x10^6)
	0, 460, 920, 1380	0, 460, 920, 1380	0, 460, 920, 1380	0, 460, 920, 1380	0, 460, 920, 1380	0, 460, 920, 1380
ACM	7.27, 7.11, 6.97, 6.84	28.2, 25.4, 24.9, 23.2	2.3, 3.6, 5.3, 6.3	4.9, 8.7, 9.8, 13.2	5.1, 5.8, 7.9, 9.7	9.2, 9.5, 13.3, 17.2
AM2.5	7.33, 7.22, 7.01, 6.92	28.4, 25.9, 23.8, 22.9	2.2, 3.5, 4.9, 5.6	4.8, 8.3, 9.3, 12.4	4.9, 5.7, 7.9, 9.6	9.2, 9.3, 13.1, 16.4
AM3.5	7.44, 7.32, 7.11, 7.02	28.9, 26.1, 24.7, 23.9	2.3,3.6, 5.2, 6.3	4.9, 8.6, 9.8, 13.1	5.2, 6.2, 8.3, 10.3	9.6, 9.9, 13.8, 17.2
AM5	7.48, 7.33, 7.12.7.06	29.3, 27.4, 25.2, 24.3	2.6, 3.9, 5.6, 6.9	5.3, 9.2, 10.6,14.8	5.4, 6.4, 8.3, 10.2	9.8, 10.2, 14.1, 17.8
AM10	7.48, 7.36, 7.22, 7.12	29.7, 27.6, 25.8, 24.9	2.6, 3.8, 5.7, 6.9	5.6, 9.7, 10.8,15.2	5.4, 6.6, 8.9, 11.3	9.8, 10.3, 14.2, 17.8

Table 8.3: The corrosion results measured by means of weighing.

Specimens	Initial mass	Post mass	Maa loss (mg)
	460, 920, 1380	460, 920, 1380	460, 920, 1380
ACM	0.069, 0.072, 0.105	0.067, 0.066, 0.095	0.002, 0.006, 0.010
AM2.5	0.070, 0.074, 0.107	0.069, 0.071, 0.095	0.001, 0.003, 0.012
AM3.5	0.072, 0.076, 0.109	0.067, 0.070, 0.095	0.005, 0.006, 0.014
AM5	0.072, 0.077, 0.11	0.065, 0.070, 0.094	0.007, 0.007, 0.016
AM10	0.076, 0.079, 0.113	0.069, 0.069. 0.093	0.007, 0.01, 0.020

8.4.3 Reinforcement corrosion

The recorded 2D and 3D tomographies of sample AM2.5, which has the lowest volume loss of steel amongst all specimens tested (Table 8.1), at different times are shown in Figure 8.13. The recorded 2D tomography shows after the first 460 s, corrosion initiated from the interface between the steel and cement paste, with a corrosion pit on the steel surface. From 460 s to 920 s of corrosion, the pit grew deeper and wider, while two more corrosion pits formed on the other sides. After the third 460 s, the corrosion situation was clearly represented by the loss of the steel cross-sectional area. In the reconstructed 3D tomography of steel under corrosion attack, the steel showed an overall smooth initial surface, with some homogeneously scattered small pits due to the resolution limit of the instrument.

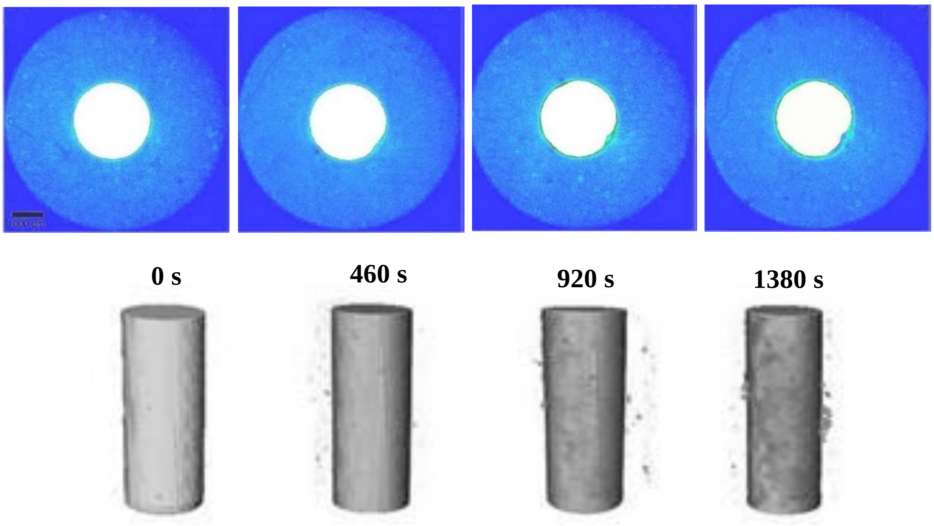

Figure 8.13: Corrosion behaviour of the reinforcing steel for sample AM2.5 at different

After performing galvanostatic corrosion during the first 460 s, some were about to corrode on the surface of the steel. Corrosion propagated greatly during the second and third accelerated corrosion sessions, with deeper and wider hollow pits forming along the entire steel surface. As shown in Figure 8.13, corrosion products were clearly detected at the concrete-steel interface after accelerated corrosion testing. Initially, the steel was protected by a hard-passive layer. After the first accelerated corrosion session, corrosion products began to form on the lateral surface of the steel. At the same time, corrosion products protruded into the entrapped void near the steel face and penetrated corrosion induced cracks. In addition, corrosion products penetrated much deeper into the cement pastes and cracks due to the accelerated corrosion testing.

After the third 460-s period, some corrosion products penetrated outward from the steel bar along the cracks. As shown in the reconstructed 3D tomography of corrosion products, the coverage area of corrosion products became wider and deeper under continued corrosion. In the end, the steel was almost covered by corrosion products. The concentration of corrosion products was also identified based on variations in grey levels.

The experimental results illustrate that the concentration of corrosion products was high near the steel surface but decreased with the distance from the steel surface. Figures 8.14(a)-8.14(d) represent the SEM images of some selected morphological characteristics of the microstructure of the mortars in the naturally corroded sample, mixed with NT, i.e. 0 wt%, 2.5 wt%, 5 wt% and 10 wt%, at 28 days showing that samples with different dosages of NT had obvious differences in morphology.

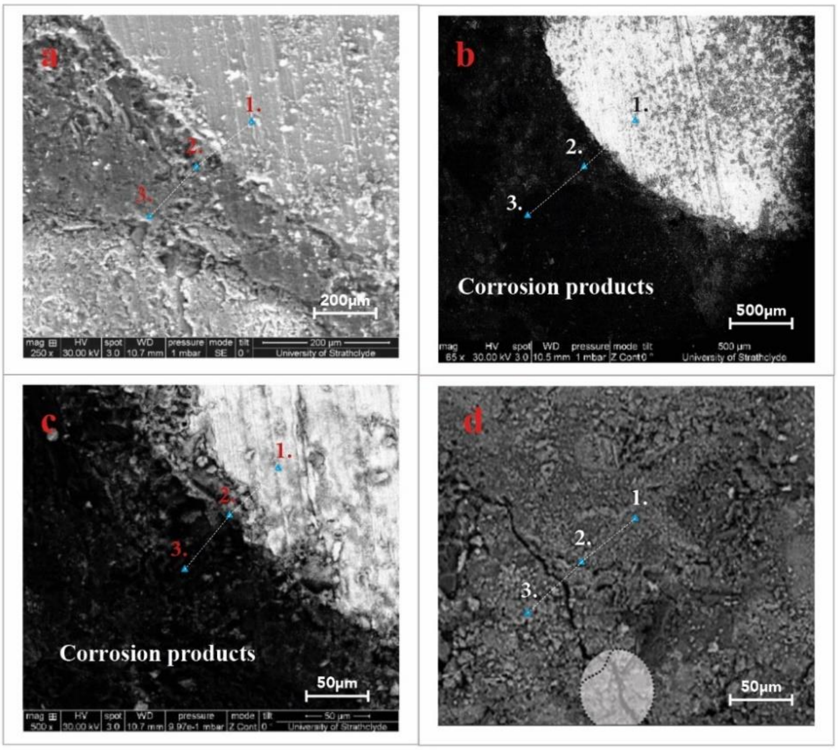

Figure 8.14: Typical SEM images of the specimens with different additions of NT (a) 0%; (b) 2.5%; (c) 5%; (d) 10% at 7 days of curing.

The surfaces of the corroded samples were examined by scanning electron microscopy (SEM) and the scanned surface areas were analysed by EDS to detect the observable chemical elements in the close to surface zones in the depth of 1 µm. Corrosion products are represented in white, corresponding to higher neutron attenuation. In contrast, voids, having low attenuation coefficients, are shown as dark features in the image. Various micro-cracks were formed on the surface of the mix with respect to the axes of specimen, including perpendicular and diagonal as illustrated in Figures 8.14(a)-(d).

The presence of corrosion products was clearly linked to the presence of a macro-pore adjacent to the bar. As shown in Figure 8.14(a), the corrosion products were observed to partially occupy the pore, growing directly from the corresponding corrosion pits in the reinforcing bar. The reference sample ACM (Figure 8.14(a)) contained a moderate number of small pores and medium size C-S-H structures. It had minor cracking on the surface, but nothing close to the reinforcement. Sample AM2.5 did not contain significant cracks. It has an apparent dense structure and a relatively good ITZ (Figure 8.14(b)). Samples AM5 and AM10 had cracks going from the surface until reinforcement with the average sizes of 0.2 mm and 0.1 mm, respectively.

SEM-EDS surface analyses were performed on intersection between rebar and cement matrix for all samples. The oxide was identified as some kind of mill-scale with an average chemical composition close to that of FeO as illustrated in Figure 8.15.

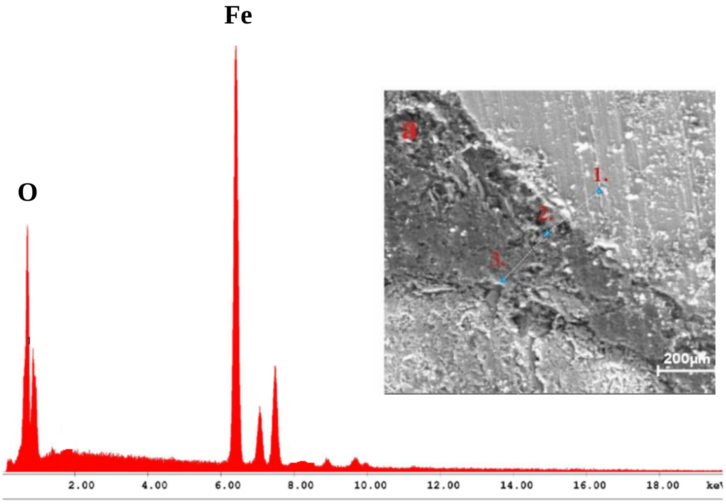

Figure 8.15: Typical SEM image and EDS analysis of ACM at the curing time of 28 days.

An example of such analysis is presented in Figure 8.15 for sample ACM at point 2. EDS spot analysis showed approximate Fe and O atomic percentages at Point 1: Fe at ~87%, O at ~11%, at Point 2: Fe at ~38%, O at ~60%, and at Point 3: Fe at ~19%, O at ~78%, as illustrated in Table 8.4 (other minor detected elements are not listed.). However, by adding 2.5wt% NT approximate Fe concentration detected at point 2 decreased by 50%. Further increasing the amount of NT, i.e. 5 wt% and 10 wt%, the amounts of Fe concentration detected at point 2 increased by 48.6% and 51%.

Table 8.4: Approximate Fe and O atomic percentages.

Specimens	Fe (at%)			O (at%)		
	1	2	3	1	2	3
ACM	87	38	19	11	60	78
AM2.5	89	19	11	8	78	87
AM5	89	37	22	8	60	75
AM10	89	39	26	9	57	71

8.4.4 Quantitative analysis of corrosion process

In order to further investigate the corrosion process, the amounts of focus objects, e.g. the loss of steel, corrosion products and corrosion induced cracks, were quantified for NT cement composites with respect to the distance from the bottom surface to the top surface. In this case, all the corrosion process can be clearly quantified. Figure 8.16 displays an example of obtained cross-sectional area with respect to the loss of steel, used to evaluate the corrosion dynamics for AM2.5.

From the bottom surface to about 6900 μm in depth, the loss of steel cross-sectional area remained stable at around 0.25 mm^2. Strong corrosion development was found from 6900 μm–7800 μm above the bottom. The loss of steel cross-sectional area increased dramatically, from about 0.25 to 0.35 mm^2 , and then dropped sharply over the remaining course to the top. As the monitoring of time-dependent corrosion processes was very important to corrosion study, the volume of steel loss, corrosion products and concrete cracks were calculated over the accelerated corrosion time as illustrated in Table 8.2. In Table 8.2, the deviation from the volume loss of steel for NT cements is given. During the accelerated corrosion, the targets including volume loss, mass loss, and corrosion products showed similar increasing trends with the increase of time for all samples.

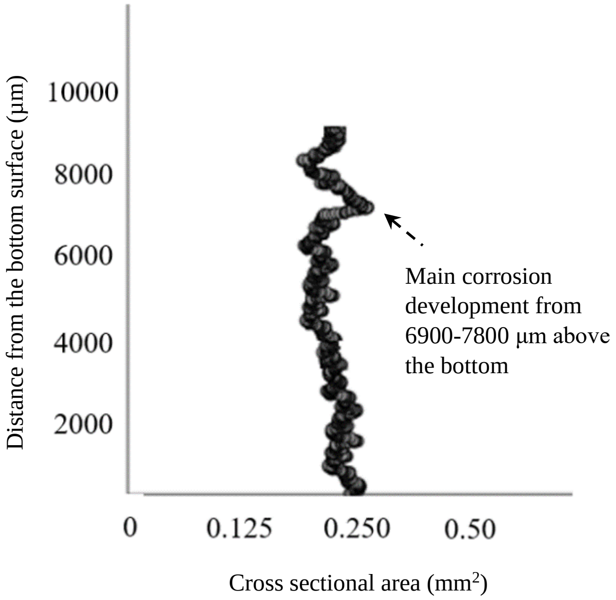

Main corrosion development from 6900-7800 μm above the bottom

Figure 8.16: Cross-sectional area across the sample from bottom surface to top surface after the fourth accelerated corrosion for AM2.5.

For ACM the initial volume loss was 3.6 mm^3 after the first accelerated corrosion (460s) slightly higher than AM2.5. For AM2.5, the initial volume loss was 3.5 mm^3 after the first accelerated corrosion (460s). After that, it steadily increased and reached its final value of 5.6 mm^3 after the third accelerated corrosion. For the volume of corrosion products, the initial volume increased to 4.7 mm^3 for AM2.5 which was slightly higher than the volume loss of steel with the deviation of 25.4%. After the second accelerated corrosion, it increased slowly to 5.9 mm^3 which was lower than the volume loss of steel with the deviation of 20.2%. Furthermore, the volume of corrosion products increased slowly and reached the final volume of 6.12 mm^3. However, the deviation also increased from 20.2% to 34.1%. For the volume of corrosion-induced cracks, the initial volume was 3.98 mm^3 which was almost three times the volume loss of steel (deviation of 201%). After the second accelerated corrosion, it increased slightly to 4.34 mm^3 while the deviation dropped significantly to 58.7%. However, after that, it increased dramatically and reached the final value at 8.39 mm^3. When the dosage of NT was more than 2.5 wt%, the total volume loss of steel and corrosion products would begin to increase.

8.4.5 Mercury intrusion porosimetry (MIP)

Table 8.5 shows the distributions of the internal pore structures of the hardened mortars at 28 days, which were measured by MIP method. As shown, pores between 10-50 nm in diameter were found to make up the majority of the pore population among all samples. It was found that in the specimens with code nos AM2.5 and AM3.5 as the optimal designs, the majority of the pore volumes at 30.2% and 32.6%, respectively, were contributed by pores ranging in size from 10-50 nm in diameter while for other (larger) pore ranges the percentages were all smaller than the corresponding values. The majority of the pore volumes ranging in size from 10-50 nm for the specimens with code nos AM5 and AM10 were 26.9% and 27.2%, respectively.

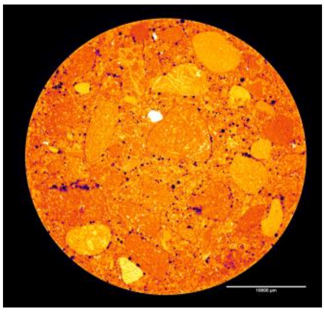

Increase in average pore radius size when the NT content exceeds the optimal value.

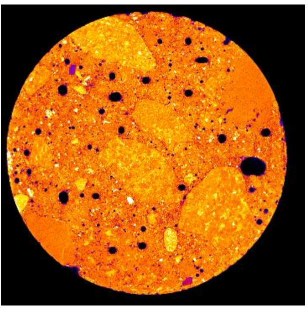

Figure 8.17: 2D porosity analysis of sample AM2.5 (Slice number 1035).

Figure 8.18: 2D porosity analysis of sample AM5 (Slice number 645)

As can be seen from the table the total pore volume initially decreased but turned to increase after reaching a minimum with 2.5 wt% NT, where the total pore volume reduced by 19.4%, harmless pores ($d < 10$ nm) increased by 6.4%, and harmful pores ($d \geq 50$ nm) decreased by 64.6% compared with the blank sample, indicating that the pores of mortars mixed with 2.5% NT were significantly refined by changing harmful pores to the nano-sized benign pores, leading to a much stronger durability of cement-based materials. When the content of NT was more than 2.5 wt%, the total pore volume and the number of harmful pores began to increase as illustrated in Figures 8.17 and 8.18. This could be due to the fact that the crystallization process of hydration products could be controlled in an appropriate state by restraining the growth of CH crystal when the dosage of nanomaterials and the distance between particles were moderate. When the addition of NT was excessive, huge specific surface area of nanoparticles would absorb more water and make the agglomeration phenomena easily accessible, leading to the formation of undisrupted pockets within the paste matrix and resulting in an increase in porosity of mortar.

Table 8.5: Internal pore distributions of the hardened mortars at 28 days with different dosages of NT.

Specimens	Total intruded volume (mL/g)	Mean radius/nm	Apparent density (g/cm^3)	Porosity/% ($2\ nm \leq d \leq 5\ \mu m$)	Pore size distributions/%		
					<10 nm	10-50 nm	>50 nm
ACM	0.082	16.2	2.46	22.6	4.08	15.3	3.22
AM2.5	0.076	14.2	2.34	18.2	4.36	12.7	1.14
AM3.5	0.056	15.4	2.41	19.6	4.14	13.2	2.26
AM5	0.057	17.9	2.53	23.4	2.18	17.1	4.12
AM10	0.057	18.7	2.49	23.9	2.44	17.4	4.06

8.4.6 Hydrophobicity test

To measure the change in hydrophobicity of the samples from the outer to the inner, wetting angle tests were carried out for the pure mortar sample and the mortar with different dosages of NT. Figures 8.19 (b) and (c) show the water contact angles from the outer to the inner for sample AM2.5 after 24 hours. It is noticeable that addition of 2.5wt% of NT increased the wettability of the sample surface compared to the control Mix as illustrated in Table 8.6. The contact angle decreased form outer (82 ± 2°) to the inner (32 ± 2°) as in Figure 8.19(a). The AM10 sample presented the highest contact angle at SV3 (92 ± 2°) amongst all the NT mortar and pure mortar specimens. Comparing with the AM2.5 sample, adding 10 wt% NT could increase the hydrophobicity of the sample by 11%. This is a significant improvement in the durability of cement mortars. Such a non-uniform distribution of porosity in the NT cement samples favoured the durability of the composite as surface area of the samples had much lower porosity. The results were also in line with the result of 3D volumetric porosity test performed in Section 4.4.1 as illustrated in Figure 8.19(a).

Table 8.6: contact angle from outer to inner

Specimens	Contact angle ∅°		
	SV1	SV2	SV3
ACM	0	0	0
AM2.5	32	46	82
AM5	37	49	87
AM10	52	51	92

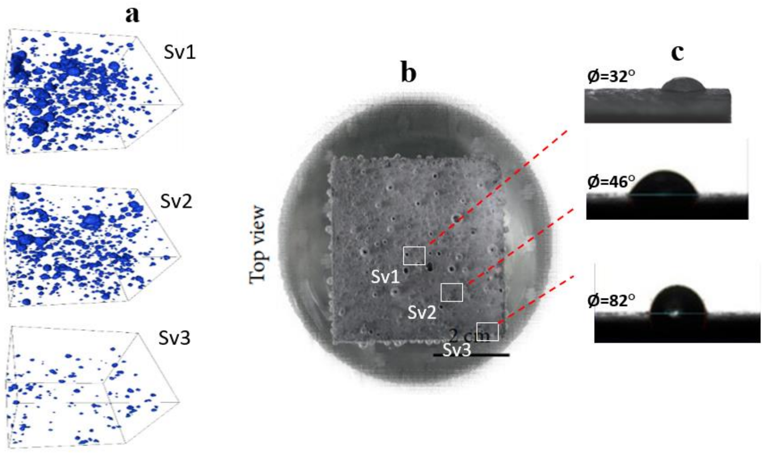

Figure 8.19(a), (b), (c): Positions of the three sub volumes “Sv1”, “Sv2”, “Sv3”, used to measure the relative 3D volumetric porosity and hydrophobicity.

8.5 Remarks

In this chapter, the physical and chemical characteristics of several NT cement mortars including the control mix were determined and studied. Novel XCT tests were conducted to quantify and characterised the development of steel corrosion and corrosion products as well as subsequent initiations and propagations of the cracks in the NT cement composites. SEM-EDS was used to evaluate the phases of the microstructures of the composite. The distributions of internal pore structures of hardened mortars at 28 days were measured by MIP method. Furthermore, the corrosion progression of a steel bar in concrete was investigated by X-ray computed tomography, i.e. XCT. Finally, the accelerated corrosion process of reinforcing steel with impressed current was traced by X-ray micro-computed tomography (μCT) with high accuracy and the mass losses of steel at different accelerated corrosion periods were analysed. Specifically, the main findings can be summarised as follows.

(1) The addition of 2.5 wt% NT refined pores and reduced capillary pores and their connectivity, hence reducing the absorption of sodium sulfate solution. Therefore, the mortars containing NT, i.e. NT ≤ 2.5 wt%, were less vulnerable to the formation of gypsum and ettringite and exhibited less expansion materials and variation in mass. The increases in the masses of the mortars may be due to absorption of sodium sulfate solution and precipitation of gypsum and ettringite in pores and cracks.

(2) Comparing with the AM2.5 sample, adding 10 wt% NT could increase the hydrophobicity of the sample by 11%.

(3) SEM-EDS spot analysis showed approximate Fe and O atomic percentages at different points, i.e. 1: Fe at ~87%, O at ~11%; at Point 2: Fe at ~38%, O at ~60%; and at Point 3: Fe at ~19%, O at ~78 %, see Figures 8.14 and 8.15. However, by adding 2.5wt% NT approximate Fe concentration detected reduced by 50%. Further increasing the amount of NT, i.e. 5 wt% and 10 wt%, the amounts of Fe concentration detected increased by 48.6 and 51%.

(4) The MIP results show that the total pore volume initially decreased but turned to increase after reaching a minimum with 2.5 wt% NT, where total pore volume decreased by 19.4%, harmless pores (d < 10 nm) increased by 6.4%, and harmful pores (d ≥ 50 nm) decreased by 64.6% compared with the reference sample, indicating that the pores of mortars mixed with 2.5% NT were significantly refined

by changing harmful pores to the nano-sized benign pores, leading to a much stronger durability of cement-based materials.

(5) Good linear relationships existed between the volume loss of steel, corrosion products, and corrosion-induced cracks. The mass loss of steel obtained by X-ray μCT measurement correlated well with the mass loss estimated by Faraday's law when compared with gravimetric results.

Chapter 9

Conclusions and Recommendations

9.1 Conclusions

Because of extensive use of concrete worldwide, it is essential to evaluate the environmental impact of this material. Additionally, to ensure the future affordability of concrete as a building material, it is necessary to improve the sustainability of concrete structures. Different approaches or potential opportunities for reducing the environmental impact and consumption of scarce resources have been already identified in the field of concrete construction, especially in the production of raw materials, concrete technology, and structures. One approach is to replace the percentage of Ordinary Portland Cement (OPC) with Supplementary cementitious materials (SCMs), to reduce the environmental consequences, mainly by reducing the CO_2-emissions. When these materials are combined with Portland cement through either pozzolanic or hydraulic activity, a contribution towards the properties of hardened concrete is made. As a result, the emission of greenhouse gases is reduced, whilst creating a more economical solution than Portland cement. As per engineering properties, it also increases the strength of the concrete over time, reduces permeability, increases durability, and minimises heat of hydration.

Another approach to reduce the environmental impact of concrete include the use of nano particles, which modify the hydration performance. By using nano particles in concrete, less steel reinforcement is required, and the concrete offers a lighter weight and longer serviceable life, which are all crucial issues in the eco-efficiency of construction materials. In this context, the environmental impact and sustainability of concrete were improved in this thesis by the use of Nano titanium combined with

Supplementary cementitious materials (SCMs). This allows the development of “green concretes” which are produced and used considering some of the approaches presented in Chapter 1. However, the implementation of these “green” concepts implies that certain parameters in the mix design process to obtain a sufficiently workable, strong, and durable concrete. The application of nanomaterials in cement and concrete has recently become an emerging topic of interest for research in cementitious composite materials. The nanomaterials can improve the performance of the cement-based materials in terms of physical, mechanical and durability properties. Amongst these materials, nano-TiO_2 (NT) has shown significant potential to be utilised in cementitious materials. The durability and sustainability of concrete are continuously becoming of increasing importance for the construction industry; nevertheless, only a limited amount of information can be found regarding the real changes in concrete properties when amorphous NT is added.

Although, different aspects of cement-based materials containing SCMs and NT particles separately have been reported in the literature, to the author's knowledge, there is no systematic study on the influence of NT in conjunction with these materials on the overall performance of cementitious materials. In particular, the effects of FA and MK as by-product materials and NT as a high surface area additive on the permeability, high brittleness, change in phase composition and pore structure properties of cementitious materials which lead to a decline in performance and service life of the building materials need to be studied in detail. This uncertainty casts doubt on the widespread application of the SCMs composites modified with NT particles. Therefore, this PhD thesis addressed this knowledge gap by investigating the permeability, porosity and change in phase composition of the FA and MK composites modified with NT particles.

In Chapter 1 a literature review of NT specification as well its applicability in concrete was addressed. The properties of the applied materials and the hardened cement matrix were characterized in Chapter 2. The mineralogical phases and chemical composition of the raw materials used were obtained from the X-ray diffraction (XRD) and X-ray fluorescence (XRF) analyses. The resulting characteristics, such as shape, particle size, specific surface area, density and pore-size distribution, were related and compared. The effects on the slump-flow test and the mechanical properties of mortars formulated with the NT were also discussed.

Chapter 3 addresses the theoretical background and experimental procedures and suitable test methods for evaluating the properties of NT cement composites using different techniques such as X-ray computed tomography (XCT), Brunauer-Emmett-Teller (BET), scanning electron microscopy (SEM), X-ray diffraction (XRD), thermogravimetric/derivative thermogravimetric analysis (TG/DTG), and energy-dispersive X-ray spectroscopy (EDAX®).

To determine the pore system of NT cement mortars across length scales with different NT dosages, X-ray computed tomography (XCT) was used to analyse the micro scale pore structures of NT mortars with NT percentages (Chapter 4). 3D pore structures of the NT mortars were obtained and evaluated. In addition, the scanning electron microscopy (SEM) was used to compare the morphologies of the samples with different NT inclusions. Meanwhile, elementary analysis was performed using an energy-dispersive X-ray spectroscopy (EDAX®). Moreover, the nanoscale surface areas and the nano pore volume and shapes of the NT mortar samples were obtained by Brunauer-Emmett-Teller (BET) and Barrett-Joyner-Halenda (BJH) analysis. Furthermore, the permeability of the NT mortars was measured using a high-pressure core holder with a sensitive and automated measurement capability.

In Chapter 5 the effects of NT on the crystalline phases of the cement mortar were investigated. The characterization of the cement hydration process, hydration products and morphology of the cement mortars were conducted by scanning electron microscopy (SEM) and X-ray diffraction (XRD) on the specimens with different NT inclusions. The changes in calcium silicate hydrates (C-S-H gel) and the other phases of cement mortars *e.g.* Ettringite, Portlandite, Alite and Belite, before and after the addition of NT in cement mortar specimens were detected using thermo-gravimetric method (TG). Derivative thermogravimetric (DTG) curves were plotted from the TG data to identify the extent of cement hydration and the exact boundaries of various phases or group of phases present in the hydrated samples.

The addition of NT as an additive in eco-concrete mixtures was addressed in Chapter 6. In particular, the effects of supplementary cementitious materials (SCM) such as FA and MK as by-product materials and NT as a high surface area additive on the permeability as well as pore structure properties of cementitious materials were studied in detail. The NT-modified cement samples were analysed by X-ray computed tomography (XCT) to examine the pore configuration in the matrix. 2D and 3D porosity calculations were carried out to find the pores and their exact size, position and distribution from the pore network using a Nikon XT H 225/320 LC X-ray computed tomography system. In addition, reconstructed tomography images were used to extract the main parameters of porosity. The number of pores in the scanned volume, and the volume and the shape of individual pores were determined. Finally, direct tensile tests were conducted in Chapter 7 to quantify and characterise the mechanical properties of the NT cement. Furthermore, the impacts of increasing the amount of NT on the mechanical properties of NT-modified cement were investigated. This test method covered the determination of the fracture energy (G_f) of composites using the disk-shaped compact tension geometry. Numerical results were validated with the existing experimental data specifically on the CMOD responses and von Mises stresses. It was found that the finite element results showed greater than 70% agreement with the experimental results. The present research is further summarized in the following.

9.1.1 Effect of NT in 2D and 3D Porosity

Several procedures and material characterization techniques have been discussed in Chapters 2 and 3 and later applied (Chapters 4-7) to obtain the main physical-chemical properties of the materials used in this research. In Chapter 4, the physico-chemical properties of different nano-titanium additives and their influence on the concrete properties were studied. This chapter attempts to determine the pore system of NT cement mortars across length scales with different NT dosages. X-ray computed tomography (XCT) was used to analyse the mesoscale pore structures of NT mortars with NT percentages of 0 wt%, 2.5 wt%, 3.5 wt%, 5 wt% and 10 wt%. To investigate the nature of the pore structure configurations of the NT-modified FA and MK composites, XCT tests were carried out.

Scans of 2.5 μm resolution were achieved at an operating voltage of 140 kV and a current of 120 μA, with 3141 projections recorded during one full rotation of the sample. It was observed that microscale pores (from 20μm to 200μm) of mortars mixed with 2.5 wt% NT were significantly refined. When the content of NT was more than 2.5 wt%, the total pore volume and the number of pores began to increase. However, when the amount of NT exceeded the optimal value, e.g. $2.5 < NT < 5\%$, the recorded 2D porosities (void area fraction) were still lower than the reference sample. It was also found that, replacing cement by combination of 2.5 wt% NT and 10 wt% FA was the optimal amount for improving the microstructure of the NT-modified fly ash samples, with 3D volumetric void fraction and 2D area void fraction reduced by 64.09% and

60.97%, respectively. However, replacing cement by combination of 2.5 wt% NT and 10 wt% MK reduced the 3D volumetric void fraction and 2D area void by 54.9% and 66.3%, respectively.

9.1.2 Effect of NT on permeability

Cement mortar samples containing different dosages of NT, i.e. 0 wt%, 2.5 wt%, 3.5 wt%, 5 wt% and 10 wt%, in cylindrical geometry with a diameter of 35 mm and a length of 70 mm were extracted from the samples using a diamond saw. In the second part of the experiment different percentages of OPC were replaced by combined use of NT, *i.e*. 0 wt%, 2.5 wt%, 5 wt% and 10 wt%, MK and FA within the range of 10 wt% to 30 wt%.

Similar to the experiment carried out in Chapter 4, the permeability measurement was performed under steady-state conditions. The vacuum saturated core sample was mounted in the core holder and then placed under a suitable confining pressure of 3 MPa to ensure a tight seal around the sample and minimal bypass of injected fluid around the sample. As it was concluded from the literature review (Chapter 2) and later confirmed by the findings presented in Chapters 4, 5 and 6, NT addition reduced the overall permeability of hardened concrete.

It may also be noted that, adding NT up to about 5 wt% could reduce the permeability of mortars. Higher than 5 wt% dosage of NT would lead to higher permeability of mortars. This could be caused by the fact that when the amount of NT exceeded the optimal value, *i.e*. NT > 2.5 wt%, the large specific surface area of the nanoparticles would absorb additional water and make the agglomeration phenomena easily reachable, leading to the formation of undisrupted pockets within the cement paste matrix and resulting in an increase in porosity of mortars. In summary, the resistance to the intrusion of water under pressure in the samples containing NT in the region of 2.5

wt% was improved due to the densification of the microstructure and the high specific surface area of the produced gel. Comparing with the pure mortar sample, adding 2.5 wt% NT could reduce the permeability by 32.1%. This is a significant improvement in the durability of cement mortars. Increasing the NT content up to 2.5 wt% and FA to 10 wt% led to a more reduction in permeability of the NT-modified fly ash composite compared with control mix with the permeability reduced by 44.1%. It has been suggested that the presence of FA, *i.e.* FA ≤ 10 wt%, could lead to a more preponderant precipitation of cement gel products in comparison to the CM. This would result in an efficacious blocking of pores and, thus, avail in reducing permeability.

In addition, pozzolanic reaction of FA could engender supplemental cementitious compounds that would block channels, fill pore space and, thus, further reduce the permeability of the hardened pastes. These effects enhanced the durability of the designed eco-concrete discussed in Chapter 6. When the amount of NT and FA exceeded the optimal values, *i.e.* NT > 2.5 wt% and FA > 10 wt%, the results showed clear trends of increasing permeability and porosity of specimens. In the third part of the experiment different percentages of OPC were replaced by combined use of NT, *i.e.* 0 wt%, 2.5 wt%, 5 wt% and 10 wt%, and MK within the range of 10 wt% to 30 wt%. Comparing with the pure mortar sample, adding 2.5 wt% NT and 10 wt% MK could reduce the permeability by 33.7%.

Increasing the NT content up to 2.5 wt% and MK to 20 wt% led to a more reduction in the permeability of the NT-modified MK composite compared with control mix, with the permeability reduced by 10.4%. When the amounts of NT and MK exceeded the optimal value, *i.e.* NT > 2.5 wt% and MK > 10/20 wt%, the results showed clear trends of increasing permeability and porosity of specimens. These results were shown and discussed in Chapter 6.

9.1.3 Effect of NT on microstructural morphology

In Chapter 5, the scanning electron microscopy (SEM) was used to compare the morphologies of the samples with different NT inclusions. Furthermore, SEM analyses were used to study the influence of FA and MK on the microstructure of the NT cement composite (Chapter 6). The objective of the microstructural analysis was to support the findings shown in the present research. It is important to notice that the performed microstructural analyses were qualitative, with the objective to give additional information that can explain the obtained results. The results shown and discussed in Chapter 5 demonstrated that increasing the NT content up to 2.5 wt% was linked with a more homogeneous microstructure compared to the reference mix. The possible reason is that NT could provide nucleation sites, which accelerated the precipitation of hydration products, made C-S-H disperse better, and limited the growth of $\mathrm{Ca(OH)_2}$, thus improving the density and homogeneity of cement matrix. On increasing the FA content to 10 wt%, the C-S-H gel remained homogeneous and comparable to the 2.5 wt% NT sample. However, the 10 wt% FA sample contained larger air-voids compared to the sample with 2.5wt%. Increasing the NT content up to 2.5 wt% and FA to 10 wt% led to a well compacted, uniform, denser pore structure with the least amount of unreacted fly ash grains compared to the reference sample. The absence of large, crystallized $\mathrm{Ca(OH)_2}$ confirmed that the addition of 2.5 wt% NT and 10 wt% FA caused a refinement of the microstructure (AM2.5 contained smaller air-voids) and probably induced the precipitation of medium sized C-S-H gel that normally had a high stiffness. This is due to interactions among the particles of FA with the calcium hydroxide, which resulted “in the formation of re-crystallized calcium carbonate in the cementitious matrix, causing the reduction in porosity of the matrix and the transition zone”.

This is in line with the high compressive strengths observed for this sample which were illustrated in Chapter 6. If the dosage of fly ash was too high (*i.e.,* FA >20 wt%), drying shrinkage distortions of mortars would be enlarged, leading to increase in the average pore radius size and causing internal defects to form in mortars, which would certainly influence the overall voids and the total porosity, due to the result that the microstructure became isolated and defective. In addition, when the amount of FA exceeded the optimal value, *i.e*. FA > 10 wt%, the unreacted or partially reacted FA particles created porosity in the matrix dispersed in small sized pores, so cavities were found from the spaces left after the dissolve of the FA particles.

Similarly, on increasing the MK content to 10 wt%, the C-S-H gel remained homogeneous and comparable to the 2.5 wt% NT sample. However, the 10 wt% MK sample now contained smaller air-voids. In addition, the unreacted or partially reacted MK particles visible within the structure. Increasing the NT content up to 2.5 wt% and MK to 20 wt% led to development of cracks alongside gypsum formation. Additionally, acicular (needle-shaped) structures were identified and possibly ettringite or other AFt phases that were rich in $CO3^{-2}$ (verified by EDS) as illustrated in Chapter 6.

On increasing the MK content to 30 wt%, the $Ca(OH)_2$ grains were now more visible than those with 10 wt% and 20 wt%. As explained in Chapters 5 and 6, the presence of significant amounts of $Ca(OH)_2$ resulted in a higher permeability and lower compressive strength. These findings were in line with the results of the mechanical and durability test discussed in Chapters 5 and 7.

9.1.4 Effect of NT on nanoscale pore system by BET and BJH analyses

The mechanical properties and durability of concrete depends mainly on the refinement of the microstructure of the hardened cement paste and the improvement of the paste aggregate interface zone (ITZ) and results in a decrease of the permeability (capillary porosity) of concrete. In this context, the BET data carried out on the powdered samples in Chapters 4 and 6 indicated that the isotherm measured was of Type IV (porous materials) according to the IUPAC nomenclature (IUPAC, 1985), signifying monolayer-multilayer adsorption in the early part of the curve with a type H3 hysteresis loop between adsorption and desorption and capillary condensation in mesopores (2 nm $< \phi <$ 50 nm) and macropores ($\phi >$ 50 nm). The presence of a hysteresis loop in the desorption isotherm showed that the samples were mesopores (materials with pores larger than 2 nm and smaller than 50 nm).

The lack of any limiting adsorption at high p/p^o suggests that the sample consists of plate-like particles giving rise to slit-like pores (Everett et al., 2002). There were clear trends of increasing surface area and pore volume of the NT cement composite with NT content, over the range of 0 wt% to10 wt% of the nanoparticles as illustrated in Chapter 4. This could stem from the formation of nanosized needle-shaped products in the presence of the nanoparticles.

The surface areas and the average pore diameter were calculated by the BET and BJH methods, respectively and were presented in Chapters 4 and 6. As it was concluded from the literature review (Chapter 2) and later confirmed by the findings presented in Chapters 4 and 6, the adsorption and desorption isotherms (BET) obtained on NT cement composite showed that the control mix containing 0 wt% NT had the lowest pore volume and surface area, and the sample containing 10 wt% NT had the highest pore volume and surface area among the specimens.

Another finding was that the pore diameter calculated for the samples with certain amount of NT, *i.e.* NT $>$ 5 wt%, was larger than the size of the primary particles (10 to 20.5 nm). As explanied in Chapter 4, probably this was due to the fact that the BJH method only considered the pore size distribution between the agglomerates. Additionally, the BJH method employed some approximations that were not valid for very small particles or could only be applied to a given part of the isotherm. The inert $\mathrm{TiO_2}$ nanoparticles, through the increased surface area and provision of heterogeneous nucleation sites, accelerated the hydration reaction and increased the formation of the C-S-H gel at the expense of Portlandite.

As it was concluded from the literature review (Chapter 2) and later confirmed by the findings presented in Chapters 4 and 6, beyond 5 wt%, there could be an agglomeration of the nanoparticles, so its impact on the properties of the composite would lessen. This was not revealed from the BET measurements which examined the nature of this interaction at the nanoscale level. Further, the pore volumes were evaluated using the BJH method from both nitrogen adsorption and desorption data and the results were presented in Chapter 4. The pore diameters and pore size distribution of the selected NT cement composites were calculated from the adsorption and desorption branches. It can be clearly seen that the sample with 10 wt% NT had considerably greater number of pores below 10 nm size than the ACM sample, *i.e.* pore volume was 0.005/$\mathrm{cm^3g^{-1}}$ compared to 0.002/$\mathrm{cm^3g^{-1}}$. For pores between 10 nm and 100 nm in size, the increase of pore volume was even higher when adding 10 wt% NT.

This is owing to the fact that NT promoted a higher extent of agglomeration of the NT particles that led to a larger pore volume, and a considerable amount of water was absorbed in the pores of the agglomerates, resulting in a reduction of water available to lubricate the granular system and for cement hydration, consequently leading to a lower flowability and a lower extent of hydration. This phenomenon showed that by adding NT in cement mortar, the nano pores (*i.e.*, mainly in the size of 1 nm to100 nm) were significantly increased.

Chapter 6 represents the pore diameters and pore size distribution of the selected NT cement composites with FA and MK inclusions, calculated from the adsorption and desorption branches. The surface areas and the average pore diameter were calculated by the BET and BJH method. The adsorption and desorption isotherms (BET) obtained on the specimens, representing the sample containing 0 wt% NT and 0 wt% FA which had the lowest pore volume and surface area, and the sample containing 0 wt% NT and 10 wt% FA which had the highest pore volume and surface area among the specimens, were presented in Chapter 6. This sample also had a type IV (H3) isotherm, mainly exhibited by highly agglomerated and very small primary particles (18.2 nm).

The pore volumes were evaluated using the BJH method from both nitrogen adsorption and desorption data and the results were also presented in Chapter 6 for the cement mortars with the highest and lowest pore volumes. The maximum volume of the adsorbed nitrogen was related to the pore volume of the samples. In general, a smaller particle size led to a larger pore volume. It can be clearly seen that the ACM sample had considerably greater number of pores below 10 nm size than the CM sample, *i.e*. pore volume was $0.01/cm^3g^{-1}$ compared to $0.002/cm^3g^{-1}$, as illustrated in Chapter 6. For pores between 10 nm and 200 nm in size, the increase of pore volume was even higher for sample ACM.

From the pore size distributions of the samples studied, it can be concluded that adding a certain amount of NT (*i.e.*, NT $\leq$ 2.5 wt%), FA (*i.e.*, FA $\leq$ 10 wt%) and MK (*i.e.*, MK $\leq$ 10 wt%) could modify the pore structure of cement mortars by changing the harmful microscale pores, permeability related (see XCT analysis) to the nano-sized benign pores (see BET analysis), leading to a much stronger durability of cement-based materials.

9.1.5 Identification of the formed hydrates using X-Ray diffraction analysis

Several procedures and material characterization techniques were discussed in Chapter 1 and later applied (Chapters 2-4) to obtain the main physical-chemical properties of the materials used in this research. In Chapter 5, the XRD analysis of NT-cement composites with different dosages of NT, at 7 and 28 days of curing, were studied. As it was concluded from the literature review (Chapter 2) and later confirmed by the findings presented in Chapters 5 and 6, increasing the NT content up to 2.5 wt%, increased the intensity of C-S-H. In general, C-S-H quantity increased first up to 2.5 wt% of NT inclusion and then decreased. This behaviour was attributed to the agglomeration of NT particles when exceeding the optimal value which could create more voids in concrete and decreased the calcium silicate phases (C_3S and C_2S) required for C-S-H gel formation.

Further the intensities of C_3S and C_2S increased when NT ≤ 2.5 wt%, and then gradually decreased when the dosage of NT increased beyond 2.5 wt%. As it was concluded from the literature review (Chapter 5), for hydration at 7 days, the intensities of AFt in mortars with 2.5 wt% NT were significantly greater than those without NT. However, AFt in mortars with 5 wt% NT was about the same as that with 2.5 wt% NT. For further increasing the dosage of NT to 10 wt%, the intensity of Aft decreased.

It can be seen from the XRD patterns (hydration at 7 days) that, compared with the control mix, there were no significant changes in the intensity of $Ca(OH)_2$ produced from cement hydration, when the added amount of NT increased to 2.5 wt%. Further increasing the NT content up to 5 wt% (AM5) would cause the intensity of $Ca(OH)_2$ to decrease slightly. It is concluded that for hydration at 28 days, the intensities of AFt in mortars with 2.5 wt% NT were significantly greater than those without NT. Further increasing the dosage of NT to 5 wt% and 10 wt% the intensity of AFt decreased. It can be seen from the XRD analysis in Chapter 5 (hydration at 28 days) that, compared with the control mix, there was a significant increase in the intensity of $Ca(OH)_2$, when the added amount of NT increased to 2.5 wt%. Further it was demonstrated in Chapter 5 that with increasing the NT to 5 wt%, compared with the control mix, there were no significant changes in the intensity of $Ca(OH)_2$.

On the contrary, when the added amount of NT increased to 10 wt%, there was a decrease in the intensity of $Ca(OH)_2$ produced from cement hydration. Chapter 6 presented the XRD analysis of the NT-modified fly ash and NT-modified metakaolin samples with different dosages, at 28 days of curing. As it was concluded from the literature review and later confirmed by the findings presented in Chapters 6, on increasing the NT to 2.5 wt%, the intensities of C_3S and C_2S increased and the increase in intensity of C-S-H was observed for both samples. On the contrary, no other new crystalline phase was found. It can be seen from the XRD analysis (chapter 6), compared with the control mix, there were no significant increases in the intensity of $Ca(OH)_2$ produced from cement hydration, when the added amount of NT increased to 2.5 wt%.

For the NT-modified MK samples, the generated amounts of AFt of each sample reached the maximum compared with the NT-modified fly ash. On increasing the NT to 2.5 wt%, and MK to 10 wt%, the intensities of C_3S and C_2S further increased and the increases in intensities of C-S-H reached the peak for hydration at 28 days. It should be noted that $Ca(OH)_2$ and Aft peak intensities increased for the samples containing FA and slightly decreased for the samples containing MK. As explanied in Chapter 6, FA lengthened the induction period of the hydration process.

The increased degree of hydration was presumably due to the enhanced dissolution and precipitation of hydration products upon FA, MK and NT incorporations.

When the added amount of FA and MK reached 20 wt% and 30 wt%, the intensities of C_3S and C_2S decreased, suggesting that the increased consumption of C_3S and C_2S phases and also increased formation of C-S-H phase compared with the control mix. Also, the decreases in the intensities of C-S-H and Aft were observed for both samples (Chapter 6). It can be seen from the XRD analysis that, compared with the control mix, there were no significant changes in the intensity of $Ca(OH)_2$ produced from cement hydration when the added amount of FA and MK increased to 20 wt%. However, when the amount of FA and MK reached 30 wt%, there was a significant decrease in the intensity of $Ca(OH)_2$.

9.1.6 Quantification of the formed hydrates through thermo-gravimetric analysis (TG/DTG)

In Chapter 5, thermogravimetric (TG) curves of the hydrated NT-cement composites, including the control, with different dosages of NT, *i.e.* 0 wt%, 2.5 wt%, 5 wt% and 10 wt%, were studied. Derivative thermogravimetric (DTG) curves were plotted from the TG data to identify the extent of cement hydration and the exact boundaries of various phases present in the hydrated samples. The changes in calcium silicate hydrates (C-S-H gel) and the other phases of cement mortars, *e.g.* Ettringite, Portlandite, Alite and Belite, before and after the addition of NT in cement mortar specimens were detected using thermo-gravimetric method (TG). Derivative thermogravimetric (DTG) curves were plotted from the TG data to identify the extent of cement hydration and the exact boundaries of various phases or group of phases present in the hydrated samples. The findings indicated the noticeable increase in the extent of bond formation between NT and free calcium hydroxide when the amount of NT was 2.5 wt% at 28 days curing. In addition, the total amount of $Ca(OH)_2$ and $CaCO_3$ for AM2.5 was 27.4%, which was also the smallest among all the samples, indicating the rising extent of bonding between NT and $Ca(OH)_2$ in AM2.5 in comparison to the bonding values in AM10, AM5 and CM, and also suggesting the difficulty of CO_2 penetration in AM2.5 due to the strength of bond formation and compact structure. These results were in good agreement with the result of compressive and tensile strengths observed in AM2.5. In Chapter 6, thermogravimetric (TG) curves of the hydrated NT-modified FA and MK samples, including the control, at 28 days of curing were studied.

The first DTG peaks of ACM appeared at 94 °C, corresponding to a 2.6% mass loss in C-S-H and AFt content. Similarly, the first DTG peaks of M2.5, AM2.5, BM2.5 and CM10 appeared between 64 °C and 107 °C where the highest C-S-H and AFt mass loss rate was observed for AM2.5. The second decomposition step of ACM occurred between 215 °C and 376 °C, and reached a maximum rate at 232 °C, resulting in a 0.31% mass loss in C_2AH_8 content. The second thermal decomposition steps of M2.5, AM2.5, BM2.5 and CM2.5 occurred in the same temperature range (~ 210–390 °C), where the corresponding mass losses were 0.35%, 0.31%, 0.91% and 0.82, respectively.

The third decomposition step of ACM, as well as those of M2.5, AM2.5, BM2.5 and CM2.5, occurred between 410 °C–550 °C. The mass loss rates observed at the third step of DTG showed the decreases in the rate of decomposition of $Ca(OH)_2$ in ACM and AM2.5 in comparison to that of M2.5, BM2.5 and CM2.5. The residues of M2.5, AM2.5, BM2.5 and CM10 at 850 °C, as well as the control were about 87-92% at 28 days of curing. Finally, the fourth decomposition step occurred between 550 °C and 740 °C. The mass loss rates observed at the fourth step of DTG showed a significant decrease in the rate of decomposition of calcium carbonate in M2.5 in comparison to that of ACM. The significant points of the TG–DTG analysis for the NT modified MK samples could be summarized as follows: the incline of the first step of the TG curve of

DM2.5 was very steep, the corresponding mass loss rate was the maximum (2.6 %.min^{-1}) and reached 5.2% mass loss at 109 °C, much greater than EM2.5 and FM2.5 due to the higher extent of C-S-H formation in DM2.5. The second step of decomposition of DM2.5 occurred between 220 °C and 380 °C, and reached a maximum rate at 242 °C, resulting in a 1.31% mass loss in C_2AH_8 content.

The mass losses at the third step of TG analyses for DM2.5, EM2.5 and FM2.5, related to the decomposition of $Ca(OH)_2$, were 2.4%, 1.2% and 1.2 respectively, which were all relatively higher than the NT cement mortars containing FA. The third thermal decomposition step of DM2.5 occurred considerably faster than those of ACM, M2.5, BM2.5, CM2.5, EM2.5 and FM2.5 as illustrated in Chapter 6. In the fourth decomposition step between 550 °C and 740 °C, the mass loss rate of FM2.5 observed was the smallest among all the samples.

Residues of DM2.5, EM2.5 and FM2.5 at 900 °C were 79.8%, 85.3% and 87.6%. In addition, the total amount of $Ca(OH)_2$ and $CaCO_3$ for M2.5 was 7.65%, which was also the smallest among all the samples, indicating the rising extent of bonding between NT and $Ca(OH)_2$ in M2.5 in comparison to bonding in other samples, suggesting the difficulty of CO_2 penetration in M2.5 due to the strength of bond formation and compact structure. These results were in good agreement with the results of compressive and tensile strengths observed in M2.5 (Tables 4 and 5). As seen in Table 6.13, the mass percent of free $Ca(OH)_2$, which did not enter the pozzolanic reaction, in the samples containing FA, was lower than those containing MK. Alternatively, the amount of free $Ca(OH)_2$ in BM2.5 was found the least among all the samples, i.e., 2.41%. These findings indicated the noticeable increase in the extent of bond formation between NT and free calcium hydroxide when the amount of NT was 2.5 wt% and FA was 20 wt% at 28 days of curing.

9.1.7 Results of the mechanical tests

In Chapter 7, load amounts in terms of CMOD with different percents of FA and MK particles in NT cement were studied. In addition, manually random sizes of particles were considered to simulate 2D section distribution of NT with FA and MK particles in the ABAQUS CAE Environment. In this simulation, by extracting properties of material with different percentages of particles from the RVE square and utilizing it in the numerical simulations, the behaviour of nano-cement containing different dosages of FA and MK was obtained. The results showed that the numerical and experimental results had similar trends, and the bearing load increased at first and decreased after that. In addition, the strengthening mechanism of NT cement with FA and MK was confirmed by simulation (XFEM). Thus, the results in the numerrical simulation may reflect macroscopic mechanical properties and simulation can become an effective way to predict the mechanical properties of nano-cement composites.

The results showed that the tensile strength increased with the increasing NT content up to 2.5 wt%. On increasing the NT (>2.5 wt%) and FA (>10 wt%) the tensile strengths increased by 56.3%. When the dosage of fly ash exceeded the optimal value, *i.e.* FA > 20 wt%, drying shrinkage distortions of mortars were enlarged, leading to the increase in average pore radius size and causing internal defects to form in mortars, which would certainly influence the overall voids and the total porosity, as the result the microstructure became isolated and defective. With increasing the NT (>2.5 wt%) and MK (>10 wt%), the tensile strength increased by 50.0%.

Similar to the NT-modified FA samples, when the amount of NT and MK exceeded the optimal values, *i.e.* NT > 2.5 wt% and FA > 10 wt%, the result showed a clear trend of decreasing the tensile strength of specimens. These results were in good agreement with the results of the 2D and 3D porosity analyses observed in Chapters 4 and 6. On increasing the NT (> 2.5 wt%) and MK (> 10 wt%), the fracture energy GF increased by 30.2%. However, once the percentage of MK increased to 20 wt% and 30 wt%, the fracture energy dramatically dropped. It can be concluded that adding a certain amount of NT (*i.e.*, NT ≤ 2.5 wt%), FA (*i.e.*, FA ≤ 10 wt%) and MK (*i.e.*, MK ≤ 10 wt%) can significantly increase GF, resulting sample to endure a greater load without exceeding the elastic limit. With increasing the amounts of FA and MK, due possibly to the rapid localization of micro-cracks the material became more brittle, which led to an increase in both width and number of cracks, hence decreasing CMOD or the ability of making deflection. On the other hand, the use of higher amount of FA and MK reduced the density of toughening mechanisms that were operational at the descending branch of the curve after the peak load.

9.1.8 Expansion and Mass Variation

In Chapter 8, the expansions of the NT cement mortars including control mix immersed in Na_2SO_4 solution at 25 °C and for 28 days of curing were studied. The results showed that the sample with 2.5 wt% NT presented the lowest expansion rate, *i.e.*, 0.31%, while the expansions in the OPC, 5 wt% and 10 wt% NT mortars were 0.38%, 0.43% and 0.57%, respectively, after 28 days.

Comparing with the pure mortar sample, adding 2.5 wt% NT could reduce the expansion rate by 18.4%, therefore causing more resistant to expansion. As the dosage of NT increased, the results showed a clear trend of increasing the expansion rate of the NT cement mortar with NT content, up to 10 wt%. Finally, the addition of 2.5 wt% NT refined pores and reduced capillary pores and their connectivity, hence reducing the absorption of sodium sulfate solution. Therefore, the mortars containing NT, *i.e.* NT ≤ 2.5 wt%, were less vulnerable to the formation of gypsum and ettringite and exhibited less expansion materials and variation in mass.

9.1.9 Reinforcement corrosion

In Chapter 8, the recorded 2D and 3D tomographies of the samples were provided. After the first accelerated corrosion session, corrosion products began to form on the lateral surface of the steel. At the same time, corrosion products protruded into the entrapped void near the steel face and the penetrated corrosion induced cracks. In addition, corrosion products penetrated much deeper into the cement pastes and cracks due to accelerated corrosion testing. After the third 460-s period, some corrosion products penetrated outward from the steel bar along the cracks. As shown in the reconstructed 3D tomographies of corrosion products (Chapter 8), the coverage area of corrosion products became wider and deeper under continued corrosion. In the end, the steel was almost covered by corrosion products.

The concentration of corrosion products was also identified based on variations in grey levels. The experimental results illustrated that the concentration of corrosion products was high near the steel surface but decreased with the distance from the steel surface. The SEM images of some selected morphological characteristics of the microstructure of the mortars in the naturally corroded sample, mixed with NT, *i.e.* 0 wt%, 2.5 wt%, 5 wt% and 10 wt%, at 28 days were presented in Chapter 8, showing that samples with different dosages of NT had obvious differences in morphology.

Corroded samples surfaces were examined by scanning electron microscopy (SEM) and the scanned surface areas were analysed by EDS to detect the observable chemical elements in the close to surface zones in depth of 1 µm. Various micro-cracks were formed on the surface of the mix with respect to the axes of the specimen, including perpendicular and diagonal. The presence of corrosion products was clearly linked to the presence of a macro-pore adjacent to the bar. The reference sample ACM contained a moderate number of small pores and medium size C-S-H structures. It had minor cracking on the surface, but nothing close to reinforcement. Sample AM2.5 did not contain significant cracks. It had an apparent dense structure and a relatively good ITZ. Samples AM5 and AM10 had cracks going from the surface until the reinforcement with an average size of 0.2 mm and 0.1 mm, respectively. SEM-EDS surface analyses were performed on intersection between rebar and cement matrix for all samples. The oxide was identified as some kind of mill-scale with an average chemical composition close to that of FeO. An example of such analysis was presented for sample ACM in Section 8.4.3. EDS spot analysis showed approximate Fe and O atomic percentages: at Point 1: Fe at ~87%, O at ~11 at%; at Point 2: Fe at ~38%, O at ~60%; and at Point 3: Fe at ~19%, O at ~78% as illustrated in Section 8.4.3. However, by adding 2.5wt% NT approximate Fe concentration detected decreased by 50%. Further increasing the amount of NT, *i.e.* 5 wt% and 10 wt%, the amount of Fe concentration detected increased by 48.6% and 51%.

9.1.10 Mercury intrusion porosimetry (MIP) and hydrophobicity

Chapter 8 described the distributions of internal pore structures of hardened mortars at 28 days, which were measured by MIP method. As shown, pores between 10-50 nm in diameter were found to make up most of the pore population among all samples. It was found that in the specimens with code nos AM2.5 and AM3.5, the majority of the pore volumes were 30.2% and 32.6%, respectively, and were contributed by pores ranging in size from 10-50 nm in diameter, while for other (larger) pore ranges the percentages were all smaller than the corresponding values. The majority of the pore volume ranging in size from 10-50 nm for the specimens with code nos AM5 and AM10 were 26.9% and 27.2%, respectively.

As can be seen from the Table 8.5, the total pore volume initially decreased but turned to increase after reaching a minimum with 2.5 wt% NT, where the total pore volume reduced by 19.4%, harmless pores (d < 10 nm) increased by 6.4%, and harmful pores ($d \geq 50$ nm) reduced by 64.6% compared with the blank sample, indicating that the pores of mortars mixed with 2.5% NT were significantly refined by changing harmful pores to the nano-sized benign pores, leading to a much stronger durability of cement-based materials.

When the content of NT was more than 2.5 wt%, the total pore volume and the number of harmful pores began to increase as illustrated in Section 8.4.5. This could be due to the fact that the crystallization process of hydration products could be controlled in an appropriate state by restraining the growth of CH crystal when the dosage of nanomaterials and the distance between particles were moderate. When the addition of NT was excessive, huge specific surface area of nanoparticles would absorb more water and make the agglomeration phenomena easily accessible, leading to the formation of undisrupted pockets within the paste matrix and resulting in an increase in porosity of mortar.

To measure the change in hydrophobicity of the samples from the outer to the inner, wetting angle tests were carried out on the pure mortar sample and the mortar with different dosages of NT. The results showed that addition of 2.5wt% of NT increased the wettability of the sample surface compared to the control mix as illustrated in Section 8.4.6. The contact angle decreases form outer (82 ± 2°) to the inner (32 ± 2°). The AM10 sample presented the highest contact angle at SV3 (92 ± 2°) amongst all the NT mortar and pure mortar specimens. Comparing with the AM2.5 sample, adding 10 wt% NT could increase the hydrophobicity of the sample by 11%. The results were also in line with the result of 3D volumetric porosity test performed in Section 4.4.1. This was a significant improvement in the durability of cement mortars. Such a non-uniform distribution of porosity in the NT cement samples favoured the durability of the composite as surface area of the samples had much lower porosity.

9.1.11 Effects of NT on the sustainability of concrete

Recent developments in the field of NT showed significant promise in addressing many of the challenges to produce an environmentally friendly concrete. Some of the approaches, previously discussed in Chapter 1 to obtain a "green concrete", were implemented later in this PhD thesis. In the last decade, TiO_2 cement has been applied in a number of laboratories and real civil engineering projects, *e.g.*, the Jubilee Church in Rome because of its ability to maintain its shiny white color. The decomposition of the pollutants leads to the formation of water, CO_2 and other harmless compounds which can be naturally washed away by rainwater and hence it is a completely green and environmental-friendly procedure. When mixing with cement, the "self-cleaning" property of TiO_2 can be utilised on a large-scale, *e.g.*, to help urban cities improve their air quality. Moreover, the white colour of titanium dioxide cement/concrete is generally appealing in terms of architectural needs. NT has been applied into concrete to promote the self-cleaning and air-purifying properties, as the TiO_2 can be activated by UV light and act as a catalyst in the photocatalytic oxidation of various air pollutants. When a structural element tends to crack under load, NT particles bridge the cracks. Such bridging action provides the nano concrete specimen greater ultimate tensile strength and, more importantly, huge toughness.

The main functions of the NT particles in members subjected to tension are to resist the opening of cracks due to micro-cracking, and increase the ability of the composite to withstand loads, and to allow large strains. The permeability of concrete is of significant concern and this is of particular concern in harsh and aggressive environments. Most durability problems, such as the corrosion of steel reinforcement, damage by freeze-thaw cycles, attack by sulphates and acids, and alkali aggregate reaction, are controlled or affected by the pore system of the concrete. In fact, due to the nano particle size and hydrophilic property, NT can change the pore system of cement paste across different length scales. The addition of NT particles into cement concrete is gaining an attention due to their high surface area and consequently high reactivity.

The influence of NT particles on the hydration of cementitious materials was examined and shown to enhance hydration due to the high specific surface area of NT particles, increasing the nucleation sites for the hydration reaction. Furthermore, the addition of NT particles was shown to improve the densification of the microstructure, thereby enhancing the durability of the cementitious materials. Another application of NT is the use as an additive in eco-concrete mixtures. The use of SCMs, such as fly ash (FA), silica fume (SF), hydrated lime (HL) and metakaolin (MK), currently represents a viable solution to partially substitute Portland cement clinker. When these materials are combined with Portland cement through either pozzolanic or hydraulic activity, a contribution towards the properties of hardened concrete is made. As a result, the emission of greenhouse gases is reduced, whilst creating a more economical solution than Portland cement. It was hypothesized that as NT had a high surface area to volume ratio and provided high reactivity, it could be employed as growth points to facilitate the SCMs hydration and modify the structure of hydration products at molecular level, which in turn improves the mechanical properties.

Finally, the use of NT makes the produced concrete financially more attractive and reduces the CO_2 footprint of concretes produced thereof. The applied NT will also improve the concrete properties, enabling the development of high-performance concretes for various constructions applications.

This results in concrete with better performance, lower costs, and improved ecological footprint. The final outcome is a methodology to design concrete and a practical framework which allow the optimum application of NT in concrete, given the available raw materials and the desired properties of the end-product.

9.2 Recommendations and Future Research

By using NT, the fundamental structure of the hydration products can be modified to enhance the concrete properties. NT in concrete does not only act as a nucleation site of C-S-H gel (accelerator) but also, as filler plugging the pores to decrease the void content of concrete, by changing the harmful microscale pores (permeability related) to the nano-sized benign pores, leading to a much stronger durability and strength of cement-based materials. However, in order to reach all the benefits produced in cement-based composites by the use of NT, future research should address the following issues:

(1) Agglomeration state and dispersion of NT is a major issue. Although various superplasticizers are available, their feasibility and effectiveness in presence of NT are still questionable. Thorough studies on the dispersion mechanism as well as the development of tailor-made superplasticizers are required. A further study can be taken on ultrasonication for the dispersion of nano-TiO_2.

(2) The author recommends casting a minimum number of three samples per mix design for all testing, to ensure accurate outcomes for the findings. It is an additional security towards the avoidance of lacking output data in case any specimen breaks or any test goes wrong. It gives the opportunity to work with a safety net and have the possibility to run the experiment several times.

(3) To accelerate the duration of compaction (vebe time), the addition of ‘superplasticiser’, such as ‘Gelnium’, can achieve the required time gain.

(4) Despite this research elucidates some effects of NT on the durability of concrete, other durability indicators have still not been investigated. Due to incorporation of the NT in concrete, the shrinkage behaviour (autogenous shrinkage) is influenced,

which needs to be studied. If the autogenous shrinkage is higher than acceptable, cracking during curing will occur. Further investigations on carbonation, corrosion resistance, acid resistance and sulfate resistance must be assessed as well.

(5) Distribution of the voids with different dimensions need to be performed using the technique of positron annihilation lifetime spectroscopy (PALS).

(6) This study concluded two fracture parameters. As an enhancement to the methodology and findings, a further study can be conducted on other fracture parameters as aforementioned in ‘Chapter 7’. For instance, some of the possible parameters that can be used are the fracture toughness, stress and crack length relationship and load against crack mouth opening displacement (CMOD) relationship. The study can be extended to examine the fracture properties of NT cement at different ages of 56, 90 and 365 days. According to several researches, as the age increases the mechanical properties improves.

(7) It is beneficial to programme the software of three point bending test to record stress and/or strain outputs against displacement. One must ensure the position of LVDT to record displacement measurement instead of the stroke outputs. Furthermore, additional fracture parameters can be included in the study, by measuring the crack length during the experiment to be compared with stress outputs.

(8) Even though positives results were obtained, further research is needed to study if this type of waste material can be supplied with stable physical and chemical properties. In addition, it is important to study the long-term effects on the concrete durability due to the high substitution level and the chloride content that was found in the sludge. The results demonstrate that the photovoltaic waste can be used as a potential silica-rich SCM to partly replace cement in concrete, thereby decreasing the CO_2 footprint of concrete and the environmental impact associated with landfill.

References

Abrams DA. Design of concrete mixtures. Structural materials research aboratory, Lewis Institute, vol. 1, 1919.

Agar-Ozbek A.S, Weerheijm J, Schlangen E and Breugel K. Investigating porous concrete with improved strength: testing at different scales, Construction and Building Materials, vol. 41, pp. 480–490, 2013.

Ahmaran S, Yaman I and Tokyay M. Transport and mechanical properties of self-consolidating concrete with high volume fly ash. Cem Concr Compos, vol. 31, pp. 99-106, 2009.
Aldea CM, Shah SP, and Karr A. The effect of cracking on water and chloride permeability of concrete, J. Mater. Civ. Eng. vol 11, no 3, pp. 181-187, 1999.

Al-Sulaimani GJ, Kaleemullah M, Basunbul IA, and Rasheeduzzafar. Influence of corrosion and cracking on bond behavior and strength of reinforced-concrete members, ACI Struct. J. 87 (2) (1990) 220–231.

Aly M, Hashmi MSJ, Olabi AG, Messeiry M, and Hussain AI. Effect of nano clay particles on mechanical, thermal, and physical behaviours of waste-glass cement mortars. Mater. Sci. Eng., vol. 528, pp. 7991–7998, 2011.

Aly M, Hashmi MSJ, Olabi AG, Messeiry M, Abadir EF, and Hussain AI. Effect of colloidal nano-silica on the mechanical and physical behaviour of waste-glass cement mortar. Materials Design. vol. 33, pp. 127-135, 2012.

Antoni M, Rossen J, Martirena F, Scrivener K. Cement substitution by a combination of metakaolin and limestone. Cement and Concrete Research, vol. 42, pp. 1579-1589, 2012.

Apostolopoulos CA, Demis S, and Papadakis VG. Chloride-induced corrosion of steel reinforcement – mechanical performance and pit depth analysis, Construct. Build. Mater. vol. 38, pp. 139-146, 2013.

Ashraf M, Khan A, Ali Q, Mirza J, Goyal A, and Anwar AM. Physico-chemical, morphological, and thermal analysis for the combined pozzolanic activities of minerals additives. Construction and Building Materials. vol. 23, pp. 2207-2213, 2009.

Askarinejad A, Pourkhorshidi AR, and Parhizkar T. Evaluation the pozzolanic reactivity of sonochemically fabricated nano natural pozzolan. Ultrason Sonochem. vol. 19, pp. 119-124, 2012.

ASTM. ASTM C117 Standard Test Method for Materials Finer than 75-μm (No. 200) Sieve in Mineral Aggregates by Washing. In Annual Book of ASTM Standards, vol. 04.02. American Society for Testing and Materials, Philadelphia, USA, 2004.

ASTM. ASTM C136 Standard Test Method for Sieve Analysis of Fine and Coarse Aggregates. In Annual Book of ASTM Standards, vol. 04.02. American Society for Testing and Materials, Philadelphia, USA, 2006.

ASTM. ASTM C293-94 Standard Test Method for Flexural Strength of Concrete (Using Simple Beam with Canter-Point Loading). ASTM Standard; p. 3, 1994.

ASTM. ASTM C469-94 Standard Test Method for Static Modulus of Elasticity and Poisson's Ratio of Concrete in Compression. ASTM Standards; p.4, 1994.

ASTM. ASTM C1012/C1012M-18a Standard Test Method for Length Change of Hydraulic-Cement Mortars Exposed to a Sulfate Solution American; ASTM C1012/C1012M-18a; American Society for Testing and Materials: West Conshohocken, PA, USA, 2018.

Ballari MM and Brouwers HJ. Full scale demonstration of air-purifying pavement. Journal of Hazardous Materials, vol. 254, pp. 406-414, 2013.

Barbhuiya SA, Barbhuiya JK, Russell M and Basheer PAM. Properties of fly ash concrete modified with hydrated lime and silica fume. Construction Build Mater, vol. 23, pp. 3233–3239, 2009.

Barenblatt EI, Entov VM, and Ryzhik VM. Theory of Fluid Flow through Natural Rocks. Kluwer Academic Publishers, Dordrecht, 1990.

Barret EP, Joyner LG, and Halenda PP. The determination of pore volume and area distributions in porous substances I. Computations from nitrogen isotherms. Journal of American Chemical Society, vol. 73, pp. 373-380, 1951.

Barros PJM, Sonebi M, and Tamimi AK. Workability, and rheology of fresh concrete: Compendium of tests. Report of RILEM TC 145-WSM, RILEM, Bagnios, 2002.

Bažant ZP. Concrete fracture models: testing and practice. Engineering Fracture Mechanics, vol. 69, pp. 165-205, 2002.

Beckhoff B, Kanngießer B, Langhoff N, Wedell R, and Wolff H. Handbook of Practical X-Ray Fluorescence Analysis. Fist ed. Springer Verlag, U.K., pp. 1-878, 2006.

Bentz DP, Halleck PM, Grader AS, and Roberts JW. Four-dimensional X-ray microtomography study of water movement during internal curing. In: Proceedings of the international RILEM conference—volume changes of hardening concrete: testing and mitigation, pp 11–20, 2006.

Biot MA. General theory of three-dimensional consolidation. Journal of Applied Physics, vol. 12: 155–164, 1941.

Bjornstrom J, Martinelli A, Matic A, Borjesson L and Panas I. Accelerating effects of colloidal nanosilica for beneficial calcium-silicate-hydrate formation in cement. Chemical Physics Letters. vol. 392, nos. 1-3, pp: 242-248, 2004.

Boukni A, Swamy RN, and Bali A. Durability properties of concrete containing 50% and 65% slag. Construct. Build. Mater., vol. 23, pp. 2836-2845, 2009.

Brunauer S, Emmet PH, and Teller E. Adsorption of gases in multimolecular layers. Journal of American Chemical Society 62, pp. 309-319, 1938.

BSI. BS EN 12620 Aggregates for Concrete, British Standards Institutions (BSI), 2008.

BSI. BS 410 Specification for Test Sieves. British Standards Institution (BSI), pp. 1-24.1986.

BSI. BS EN12350-2 Testing Fresh Concrete part 2 Slump-Test. British Standards Institution (BSI), 2009.

BSI. BS EN 12390 Testing Hardened Concrete. Part 1 Shape, Dimensions and other Requirements for Specimens and moulds, British standards Institution (BSI), 2012.

BSI. BS EN 12390 Testing Hardened Concrete Part 2 Making and Curing Specimens for Strength Tests, British standards Institution (BSI), 2009a.

BSI. BS EN 12390 Testing Hardened Concrete Part 3 Testing Compressive Strength of Test specimens, British standards Institution (BSI), 2009b.

BSI. BS EN 12390 Testing Hardened Concrete Part 5 Flexural Strength of Test Specimens, British Standards Institution (BSI), 2009c.

BSI. BS EN 197 Cement Part 1 Composition, Specifications, and Conformity Criteria for Common Cements, British Standards Institution (BSI), 2000.

BSI. BS EN 206 Concrete Part 1 Specification, Performance, Production, and Conformity, British Standards Institution (BSI), 2013.

BSI. BS EN 1015 Methods of Test for Mortar and Masonry Part 3 Determination of Consistence of Fresh Mortar (by Flow Table), British Standards Institution (BSI), 1999.

Chang CF, and Chen JW. The experimental investigation of concrete carbonation depth. Cement and Concrete Research. vol. 36, pp. 1760-1767, 2006.

Chen D, and Mahadevan S. Chloride-induced reinforcement corrosion and concrete cracking simulation, Cement Concr. Compos. vol. 30, no. 3, pp. 227–238, 2008.

Chen J, Kou SC, and Poon CS. Hydration and properties of nano-TiO_2 blended cement composites, Cement and Concrete Composites, vol. 34, no.5, pp. 641–649, 2012.

Chen J and Poon CS. Photocatalytic construction and building materials: From fundamentals to applications. Build. Environ. vol. 44, pp. 1899–1906, 2009.

Counto UJ. Effect of the elastic modulus, creep and creep recovery of concrete, Magazine of Concrete Research, vol. 16, pp. 129–138, 1964.

De Boer JH, and Lippens BC. Studies in pore system in catalysts II. The shape of pores in aluminium oxides systems. Journal of Catalysis, vol. 3, pp. 38-43, 1964.

Demeestere KJ, De Dewulf B, Witte BD, Beeldens A, and Van Langenhove H. Heterogeneous photocatalytic removal of toluene from air on building materials enriched with TiO_2, Building and Environment, vol. 43, no. 4, pp. 405–414, 2008.

Diamond S. Mercury porosimeter: an inappropriate technique for the measurement of pore size distributions in cement-based materials. Cem Concr Res, vol. 30, no. 10, pp. 1519-1524, 2000.

DIN. DIN ISO 9277 Determination of the Specific Surface Area of Solids by Gas Adsorption using the BET Method. German Institute of Normalization (DIN), pp. 1-19, 2005.

Diamond S, and Lachowski EE. Investigation of the composition and morphology of individual particles of Portland cement paste: 2. Calcium sulfoaluminates, Concrete Research, vol. 13, no. 3, pp. 334-339, 1983.

Dong B, Fang G, Liu Y, Dong P, Zhang J, Xing F, and Hong S, Monitoring reinforcement corrosion and corrosion-induced cracking by X-ray microcomputed tomography method, Cement Concr. Res. vol. 100, pp. 311–321, 2017.

Dong B, Shi G, Dong P, Ding W, Teng X, Qin S, Liu Y, Xing F, and Hong S. Visualized tracing of rebar corrosion evolution in concrete with x-ray microcomputed tomography method, Cement Concr. Compos. Vol. 92, pp. 102–109, 2018.

Drexler K. Molecular engineering: an approach to the development of general capabilities for molecular manipulation. Proceedings National Academic of Sciences, vol. 78, USA, pp. 5275-5278, 1981.

Duggal SK. Building Materials. New Age International (P) Ltd., Publishers. ISBN (13): 978-81-224-2975-6, 2008.

Erdogan ST, Quiroga PN, Fowler DW, Saleh HA, Livingston RA, Garboczi EJ, Ketcham PM, Hagedorn JG, and Satterfield SG. Three-dimensional shape analysis of coarse aggregates: new techniques for and preliminary results on several different coarse aggregates and reference rocks. Cement and Concrete Research, vol. 36, no. 9, pp. 1619–1627, 2006.

Erdoğan and Turhan Y. Materials of Construction. Ankara: METU Press Publishing Company, 2009.

Everett DH, Sing KSW, Haul RAW, Moscou L, Pierotti R A, Rouquerol J, and Siemieniewska. T. Reporting physisorption data for gas/solid systems with special reference in the determination of surface area and porosity, Pure & Appl. Chem, vol. 57, no. 4, pp. 602-618, 1985.

Fetter CW. Applied Hydrogeology. Merrill Publishing Co., Columbus, Ohio, 1988.

Feynman RP. There is plenty of room at the bottom. Engineering and Science, vol. 23, pp. 22-36, 1960.

Florence S and Konstantin S. Nanotechnology in concrete -A review. Construction and Building Materials. 24:20602071, 2010.

Freeze RA, and Cherry J.A. Groundwater. Prentice-Hall, Englewood Cliffs, N.J,1979.

Frias M, and Cabrera J. Influence of MK on the reaction kinetics in MK/lime and MK-blended cement systems at 20°C. Cement and Concrete Research, vol. 31, pp. 519-527, 2001.

Gaitero JJ, Campillo I, and Guerrero A. Reduction of the calcium leaching rate of cement paste by addition of silica nanoparticles. Concrete Research, vol. 38, pp. 1112-1118, 2008.

Gallucci E. Scrivener K, Groso A, Stampanoni M, and Margaritondo G. 3D experimental investigation of the microstructure of cement pastes using synchrotron X-ray microtomography. Cement and Concrete Research, vol. 37, no. 3, pp. 361-369, 2007.

Gdoutos EE. Fracture Mechanics. Dordrecht: Kluwer Academic Publishers, 1993.

Gregg S, and Sing KSW. Adsorption, Surface Area and Porosity. Academic Press, London, pp. 303, 1983.

Groen JC, Peffer LAA, and Perez-Ramirez J. Pore size determination in modified micro- and mesoporous materials. Pitfalls and limitations in gas adsorption data analysis. Microporous and Mesoporous Materials, vol. 60, pp. 1-17, 2003.

Gruyaert E, Van den Heede P, Maes M, De Belie N. Investigation of the influence of blast-furnace slag on the resistance of concrete against organic acid or sulphate attack by means of accelerated degradation tests. Cem. Concr. Res., vol. 42, pp. 173–185, 2012.

Güneyisi E, and Gesog lM. Properties of mortars with binary and ternary cementitious blends of fly ash and metakaolin. Mater Struct, vol. 41, no. 9, pp.1519–1531, 2008.

Güneyisi E, and Mermerdas K. Comparative study on strength, sorptivity, and chloride ingress characteristics of air-cured and water-cured concretes modified with metakaolin. Mater Struct, vol. 40, pp. 1161–1171, 2007.

Güneyisi E, Karaoğlu S, and Mermerdas K. Strength, permeability, and shrinkage cracking of silica fume and metakaolin concretes. Construction and Building Materials, vol.34, pp.120–130, 2012.

Güneyisi E, Karaboğlu S, and Mermerdas K. Corrosion behaviour of reinforcing steel embedded in chloride contaminated concretes with and without metakaolin. Composites B, vol.45, pp.1288–1295, 2013.

Güneyisi E, Gesoğlu M, and Mermerdas K. Improving strength, drying shrinkage, and pore structure of concrete using metakaolin. Mater Struct (in press). doi:10.1617/ s11527-007-9296-z, 2007.

Guth E. Theory of filler reinforcement, Journal of Applied Physics, vol. 16, pp. 20–25, 1945.

Haimson BC, and Doe TW. 1983. State of stress, permeability, and fractures in the Precambrian Granite of northern Illinois. Journal of Geophysical Research, vol. 88, pp. 7355–7371, 1983.

Halpin JC, Stiffness and expansion estimates for oriented short fibre composites, Journal of Composite Materials, vol. 3, pp. 732–734, 1969.

Halpin JC, and Tsai SW. Effects of environmental factors on composite materials, Tech. Rep. 67-423, AFML-TR., 1969.

Hammond GP and Jones CI. Embodied energy and carbon in construction materials. Proceedings of the Institution of Civil Engineers - Energy, 161 (2), pp. 87-98, 2008.

Hannesson G, Kuder K, Shogren R, and Lehman D. The influence of high volume of fly ash and slag on the compressive strength of self-consolidating concrete. Constr Build Mater, vol. 30, pp.161–168, 2012.

Harkins WD, and Jura G. Surfaces of Solids. XIII. A Vapor adsorption method for the determination of the area of a solid without the assumption of a molecular area, and the areas occupied by nitrogen and other molecules on the surface of a solid. Journal of the American Chemical Society, vol. 66, pp. 1366-1373, 1944.

Heidrich C, Feuerborn H-J, and Weir A. Coal combustion products, a global perspective, 2013 World of Coal Ash (WOCA) Conference, Lexington, USA, 2013.

Hewlett PC. Lea's Chemistry of Cement and Concrete. 3rd edition JohnWiley & Son Inc., New York, 1053 p., 2004.

Hou PK, Kawashima S, Wang KJ, Corr DJ, Qian JS, and Shah SP. Effects of colloidal nano silica on rheological and mechanical properties of fly ash–cement mortar. Cement Concr Compos, vol. 35, no.1, pp. 12–22, 2013.

Hüsken G. A multifunctional design approach for sustainable concrete: with application to concrete mass products. PhD thesis, Eindhoven University of Technology, the Netherlands, 243.p., 2010.

Hunger M, Husken G, and Brouwers HJ. Photocatalytic degradation of air pollutants - From modelling to large scale application. Cement and Concrete Research, vol. 40, no. 2, pp. 313-320, 2010.

Hüsken G, and Brouwers HJH. A new mix design concept for earth-moist concrete: A theoretical and experimental study. Cement and Concrete Research, vol. 38, pp. 1246-1259, 2008.

Irassar EF, Gonzelaz M, and Rahhal V. Sulfate resistance of type V cements with limestone filler and natural pozzolana. Cement and Concrete Composites, vol. 22, no. 5, pp. 361-368, 2000.

ISO. ISO 3310 Test Sieves -Technical Requirements and Testing Part 1 Test Sieves of Metal Wire Cloth. International Organization for Standardization, CH-1211 Genève 20, Switzerland, pp. 1-15, 2000.

IUPAC. Reporting data for gas/solid systems with special reference to the determination of surface area and porosity. International Union of Pure and Applied Chemistry IUPAC. Pure and Applied Chemistry, vol. 57, no. 4, pp. 603-619, 1985.

Jayapalan AR, Lee BY, and Kurtis KE. Effect of nano-sized titanium dioxide on early age hydration of Portland cement. Nanotechnology in Construction, vol. 3, pp. 267-273, 2009.

Jayapalan AR, Lee BY, Fredrich SM, and Kurtis KE. Influence of Additions of Anatase TiO_2 Nanoparticles on Early-Age Properties of Cement-Based Materials. Transp. Res. Rec. J. Transp. Res. Board. 2141, pp. 41–46, 2010.

Joint Committee on Powder Diffraction Standards; JCPDS-International Centre for Diffraction Data: Newtown Square, PA, USA, 2000.

Karihaloo B. What is quasi-brittle fracture and how to model its fracture behaviour. International Magazine on Engineering Structural Integrity, vol. 4, no. 4, pp. 18-20, 2010.

Kawashima S, Hou P, Corr DJ, and Shah SP. Modification of cement-based materials with nanoparticles. Cement and Concrete Composites, vol. 36, pp. 8-15, 2013.

Kim HS, Lee SH, and Moon HY. Strength properties and durability aspects of high strength concrete using Korean metakaolin. Construction and Building Materials, vol. 21, pp. 1229-1237, 2007.

Kim K, Hoe Y, Kang S, and Lee J. Effect of sodium silicate- and ethyl silicate-based nano-silica on pore structure of cement composites. Cement and Concrete Composites, vol. 49, pp. 84-91, 2014.

Kjellsen KO, and Lagerblad B. Hollow-shell formation-an important mode in the hydration of Portland cement. Journal of Materials Science, vol. 32, no. 11, pp. 2921-2927, 1997.

Kruth J-P, Carmignato S, Schmitt R, De Chiffre L, and Weckenmann A. Computed tomography for dimensional metrology CIRP Ann. Manuf. Techn., vol. 60, no.2, pp. 821-841, 2011.

Lee BY, and Kurtis KE. Influence of TiO_2 nanoparticles on early C_3S hydration. J. Am. Ceram. Soc, vol. 93, pp. 3399–3405, 2010.

Lee BY, Jayapalan AR, Fredrich SM, and Kurtis KE. Influence of Additions of Anatase TiO_2 Nanoparticles on Early-Age Properties of Cement-Based Materials. Transp. Res. Rec. J. Transp. Res. Board. 2141, pp. 41–46, 2010.

Lee BY, Jayapalan AR, and Kurtis KE. Effects of nano- TiO_2 on properties of cement-based materials. Mag. Concr. Res, vol. 65, pp. 1293–1302, 2013.

Leng Z, Feng D, Xie N, Gong C, Xiao H, and Li H. Portland cement paste modified by TiO_2 nanoparticles: A microstructure perspective. Ind. Eng. Chem. Res, vol. 52, pp. 11575–11582, 2013.

Li G. Properties of high-volume fly ash concrete incorporating nano-SiO_2. Cem Concr Res, vol. 34, no. 6, pp. 1043–1049, 2004.

Li H, Xiao HG, and Ou JP. A study on mechanical and pressure-sensitive properties of cement mortar with nanophase materials. Cement and Concrete Research, vol. 34, pp. 435-438, 2004a.

Li H, Xiao HG, Yuan J, Ou JP. Microstructure of cement mortar with nanoparticles. Composites Part B: Engineering, vol. 35, pp. 185-189, 2004b.

Lothenbach B, and Wieland E. A thermodynamic approach to the hydration of sulphate resisting Portland cement. Waste Management, vol. 26, pp. 706-719, 2006.

Lu S, Landis E, and Keane D. X-ray microtomographic studies of pore structure and permeability in Portland cement concrete. Mater Struct, vol. 39, no. 6, pp. 611–620, 2006.

Ma B, Li H, Mei J, Li X, and Chen F. Effects of nano- TiO_2 on the toughness and durability of cement-based material. Adv. Mater. Sci. Eng. 583106, 2015.

Masad E, Saadeh S, Al-Rousan T, Garboczi E and Little D. Computations of particle surface characteristics using optical and X-ray CT images. Computational Materials Science, vol. 34, no. 4, pp. 406–424, 2005.

Mechling J, Lecomte A, and Diliberto C. Relation between cement composition and compressive strength of pure pastes. Cement and Concrete Composites, vol. 31, no. 4, pp. 255-262, 2009.

Michell BS. An Introduction to Materials Engineering and Science for Chemical and Materials Engineers. John Wiley & Sons, Inc., Hoboken, New Jersey, 968 p., 2004.

Mindess S, Young JF, and Darwin D. Concrete. 2nd edition, Prentice Hall, 2002.

Myers RJ, Bernal SA, and Provis JL. A thermodynamic model for C-(N)A-S-H gel: Deviation and validation. Cement and Concrete Research, vol. 66, pp. 27-47, 2014.

Nadeem A, Memonb SA, and Lo TY. Mechanical performance, durability, qualitative and quantitative analysis of microstructure of fly ash and Metakaolin mortar at elevated temperatures. Construction and Building Materials, vol.38, pp. 338–347, 2013.

Nazari A. The effects of curing medium on flexural strength and water permeability of concrete incorporating TiO_2 nanoparticles. Mater. Struct, vol. 44, pp. 773–786, 2011.

Nazari A, Sh R, Shamekhi SF, and Khademno A. Influence of AL_2O_3 nanoparticles on the compressive strength and workability of blended concrete. Journal of American Science, vol. 6, no. 5, pp. 6-9, 2010.

Nazari A, Shamekhi F, Riahi S, Riahi S, Seyedeh, and Khademno A. Assessment of the effects of the cement paste composite in presence TiO_2 nanoparticles. Journal of American Science, vol. 6, no. 4, pp. 43-45, 2010.

Neville AM. Properties of Concrete, 4th ed., Prentice Hall/Pearson, Harlow, U.K., pp. 537-576, 2002.

Neville AM. The confused world of sulfate attack on concrete. Cement and Concrete Research, vol. 34, pp. 1275-1296, 2004.

Nossoni G, and Harichandran R. Current efficiency in accelerated corrosion testing of concrete, Corrosion, vol. 68, no. 9, pp. 801–809, 2012.

Odler I. Hydration, setting and hardening of Portland cement. In Lea's Chemistry of Cement and Concrete. London: Arnold, Ed. Hewlett PC, pp. 241–84, 1998.

Oltulu M, and Sahin R. Single, and combined effects of nano-SiO_2, nano-AL_2O_3 and nano-Fe_2O_3 powders on compressive strength and capillary permeability of cement mortar containing silica fume. Materials Science & Engineering A, Structural Materials: Properties, Microstructure and Processing, vol. 528, pp. 7012-7019, 2011.

Paiva H, Velosa A, Cachim P, and Ferreira VM. Effect of metakaolin dispersion on the fresh and hardened state properties of concrete. Cement and Concrete Research, vol.42, pp.607–612, 2012.

Palomo A, Grutzeck MW, and Blanco MT. Alkali-activated fly ashes: a cement for the future. Cem Concr Res, vol. 29, pp. 1323–1329, 1999.

Pascoe kJ. An Introduction to the Properties of Engineering Materials, Van Nostrand Reinhold, London, UK, 3rd edition,1978.

Ponikiewski T, Katzer J, Bugdol M, and Rudzki M. X-ray computed tomography harnessed to determine 3D spacing of steel fibres in self compacting concrete (SCC) slabs. Construction and Building Materials, vol. 74, pp. 102–108, 2015.

Poon CS, Kou SC, and Lam L. Compressive strength, chloride diffusivity and pore structure of high performance metakaolin and silica fume concrete. Construction and Building Materials, vol. 20, pp. 858-865, 2006.

Proske T, Hainer S, Rezvani M, and Graubner CA. Eco-friendly concretes with reduced water and cement contents-Mix design principles and laboratory tests. Cement and Concrete Research, vol. 51, pp. 38-46, 2013.

Østergaard L. Early-Age Fracture Mechanics and Cracking of Concrete Experimental and Modelling. Denmark: DTU-Tryk, 2003.

Raki L, Alizadeh R, Makar JM, and Sato T. Cement and concrete nanoscience and nanotechnology. Materials, vol. 3, pp. 918-942, 2010.

Ramezanianpour AA, and Jovein H.B. Influence of metakaolin as supplementary cementing material on strength and durability of concretes. Construction and Building Materials, vol.30, pp.470–479, 2012.

Ramachandran VS, Paroli RM, Beaudoin JJ, and Delgado AH. Handbook of Thermal Analysis of Construction Materials. William Andrew Publishing, Norwich, New York, U.S.A., pp. 1-680, 2002.

Rao GA. Generalization of Abrams' law for cement mortars. Cement and Concrete Research, vol. 31, pp. 495-502, 2001.

Rattanasak U, and Kendall K. Pore structure of cement / pozzolan composites by X-ray microtomography. Cement and Concrete Research, vol. 35, no. 4, pp. 637-640, 2005.

Rice JR, and Cleary MP. Some basic stress diffusion solutions for fluid-saturated porous media with compressible constituents. Reviews of Geophysics and Space Physics, vol. 14, pp. 227–241, 1976.

Richardson IG. The calcium silicate hydrates. Cement and Concrete Research, vol. 38, no. 2, pp. 137-158, 2008.

Richardson IG, and Groves GW. The incorporation of minor and trace elements into calcium silicate hydrate (C-S-H) gel in hardened cement pastes. Cement and Concrete Research, vol. 23, no. 1, pp. 131-138, 1993.

Sabir B.B, Wild S, and Bai J. Metakaolin and calcined clays as pozzolans for concrete: A review. Cement and Concrete Composites, vol. 23, pp. 441-454, 2001.

Sabir BB, Wild S, and Khatip JM. On the workability and strength development of metakaolin concrete. In: Dhir RK, Dyer TD (eds) Concrete for environmental enhancement and protection. (E&FN Spon), pp 651–656, 1996.

Sanchez F, and Sobolev K. Nanotechnology in concrete - A review. Construction and Building Materials, vol. 24, pp. 2060-2071, 2010.

Santhanam, M, Cohen MD, and Olek J. Mechanism of sulfate attack: a fresh look Part 1. Summary of experimental results. Cement and Concrete Research, vol. 32, pp. 915-921, 2002.

Santhanam M, Cohen MD, and Olek J. Sulfate attack research – whither now? Cement and Concrete Research, vol. 31, pp. 845-851, 2001.

Scrivener KL, Fullmann T, Gallucci E, Walenta G, and Bermejo E. Quantitative study of Portland cement hydration by X-ray diffraction/Rietveld analysis and independent methods. Cement and Concrete Research, vol. 34, no. 9, pp. 1541-1547, 2004.

Selvadurai APS, and Yue ZQ. On the indentation of a poroelastic layer. International Journal of Numerical and Analytical Methods in Geomechanics, vol. 18, pp. 161–175, 1994.

Shaikh F, Supit S, and Sarker PA. Study on the effect of nano silica on compressive strength of high volume fly ash mortars and concretes. Mater Des, vol. 60, pp. 433–442, 2014.

Shi C, Fernández Jiménez A, and Palomo A. New cements for the 21st century: the pursuit of an alternative to Portland cement. Cement and Concrete Research, vol. 41, pp. 750-763, 2011.

Sing KWS. Characterization of porous materials: Past, present, and future. Colloids Surface A, Physicochemical Engineering Aspects, vol. 241, pp. 3-7, 2004.

Sobolev K, Flores I, and Hermosillo R. Nanomaterials, and nanotechnology for high-performance cement composites. In Proceedings of ACI Session on "Nanotechnology of

Concrete: Recent Developments and Future Perspectives". American Concrete Institute, 7 November, Denver, U.S.A., pp. 91-118, 2006.

Spiesz PR. Durability of concrete with emphasis on chloride migration. PhD thesis, Eindhoven University of Technology, the Netherlands, 232 p., 2013.

Stutzman PE. Cement clinker characterization by scanning electron microscopy, Cement, Concrete, and Aggregates, vol. 13, no. 2, pp. 109-114, 1991.

Taylor HFW. Cement Chemistry, 1st Edition, London: Academic Press, 1990.

Taylor HFW. Cement Chemistry, 2nd Edition, Thomas Telford, London, 1997.

Taylor R, Richardson IG, and Brydson RMD. Composition and microstructure of 20-year-old ordinary Portland cement-ground granulated blast-furnace slag blends containing 0 to 100% slag, Cement and Concrete Research, vol. 40, no. 7, pp. 971-983, 2010.

Teychenne DC, Franklin RE, and Erntroy HC. Design of Normal Concrete Mixes. 2nd ed. Herts: Construction Research, 1997.

Thiele G, Poston M, and Brown R. A case study in sizing nanoparticles. Micromeritics Analytical Services, pp. 1. Available at www.micromeritics.com, 2007.

Thomas JJ, Jennings HM, Allen AJ. The surface area of cement pastes as measured by neutron scattering: evidence for two C-S-H morphologies. Cement and Concrete Research, vol. 28, no. 6, pp. 897-905, 1998.

Tobón JI, Payá JJ, Borrachero MV, and Restrepo OJ. Mineralogical evolution of Portland cement blended with silica nanoparticles and its effect on mechanical strength. Construction and Building Materials, vol. 36, pp. 736-742, 2012.

Van Tittelboom K, De Belie N, and Hooton RD. Test methods for resistance of concrete to sulfate attack—A critical review. In Performance of Cement-Based Materials in Aggressive Aqueous Environments; Springer: New York, NY, USA, pp. 251–288, 2013.

Wang S and Li VC. Engineered cementitious composites with high-volume fly ash. ACI Mater J, vol. 104, pp. 233–241, 2007.

Wong HS, Zhao YX, Karimi AR, Buenfeld NR, and Jin WL. On the penetration of corrosion products from reinforcing steel into concrete due to chloride-induced corrosion, Corrosion Sci. vol. 52, no. 7, pp. 2469–2480, 2010.

Young JF, and Hansen W. Volume relationships for C-S-H formation based on hydration stoichiometries. Materials Research Society, vol. 85, pp. 313-314, 1987.

Yu C, Sun W, and Scrivener K. Mechanism of expansion of mortars immersed in sodium sulfate solutions. Cem. Concr. Res., vol. 43, pp. 105-111, 2000.

Zhang G, Chang L, and Schlarb AK. The roles of nano-SiO_2 particles on the tribological behavior of short carbon fiber reinforced PEEK. Compos. Sci. Technol, vol. 69, pp. 1029–1035, 2009.

Zhang M. H, and Islam J. Use of nano-silica to reduce setting time and increase early strength of concretes with high volumes of fly ash or slag. Constr Build Mater, vol. 29, pp. 573–580, 2012.

Zhang MH, and Li H. Pore structure and chloride permeability of concrete containing nanoparticles for pavement. Constr Build Mater, vol. 25, no. 2, pp. 608–616, 2011.

Zhang MH, and Malhotra VM. Characteristics of a thermally activated alumino-silicate pozzolanic material and its use in concrete. Cem Concr Res., vol. 25, no. 8, pp. 1713– 1725, 1995.

Appendix 1

Cement chemistry notation

C = CaO

S = SiO_2

H = H_2O

A = Al_2O_3

F = Fe_2O_3

S = SO_3

C = CO_3

M = MgO

This leads to the following most common abbreviations for anhydrous and hydrates phases:

C_3S	$3CaO.\ SiO_2$	Tricalcium silicate (Alite)
C_2S	$2CaO.\ SiO_2$	Dicalcium silicate (Blite)
C_4AF	$4CaO.\ Al_2O_3.\ Fe_2O_3$	Ferrite
C_3A	$3CaO.\ Al_2O_3$	Tricalcium aluminate
CSH_2	$CaSO_4.\ 2H_2O$	Gypsum
CC	$CaCO_3$	Calcium carbonate
C-S-H	$x\mathrm{CaO}.\ y\mathrm{SiO}_2.\ z\mathrm{H}_2\mathrm{O}$	Calcium silicate hydrate
C-A-S-H	$a\mathrm{CaO}.\ b\mathrm{Al}_2\mathrm{O}_3.\ c\mathrm{SiO}_2.\ d\mathrm{H}_2\mathrm{O}$	Calcium silicate aluminate hydrate
AFt phase	$3CaO.\ Al_2O_3.\ CaSO_4.\ 32H_2O$	Ettringite

Journal publications

Shafaei D, Yang S, Berlouis L, Minto J. (2020). Multiscale pore structure analysis of nano titanium dioxide cement mortar composite. Materials Today Communications. 22 (2020) 100779.

Shafaei D, Yang S, Berlouis L, Saafi M. (2020). Enhanced Durability Properties of Nano-Titanium Dioxide/Fly Ash Cement Composites. ACI Material Journal, in review.

Shafaei D, Yang S, Berlouis L, Saafi M. (2020). Microstructural Characterization of Phases and Interfaces of Cement Mortars Containing Nano Titanium Dioxide. In preparation.